





Estudios de adsorción-desorción de fármacos sobre fibras de carbón activado

Ana Claudia Pina Riveiro

Tesis de Doctorado

Presentada como uno de los requisitos para el título de **Doctor**

Programa de Posgrado en Química de la Facultad de Química
Universidad de la República

Programa de Desarrollo de Ciencias Básicas

Mayo 2025

Adsorption—desorption studies of pharmaceutical compounds on activated carbon fibres

Tribunal

Presidente, Dr. Elen Leal da Silva Pontificia Universidade Católica do Rio

Grande do Sul – Instituto do Petróleo e dos

Universidad de Lisboa, Lisboa, Portugal

Recursos Naturais, Brasil

Integrante, Dr. Ana Paula Carvalho

Integrante, Dr. Ricardo Faccio

Facultad de Química Udelar

Directores de Tesis

Dr. Alejandro Amaya Facultad de Química Udelar

Dr. M. Concepción Ovin Ania CEMHTI, CNRS, Orléans, Francia

Dr. Néstor Tancredi Facultad de Química, Udelar



Carpe Diem

Don't allow the day to end without having grown a bit, without being happy, without feeding your dreams.

Don't be defeated by discouragement.

Don't allow anyone to take away your right to express yourself, which is almost a duty.

Don't abandon the desire to make something extraordinary of your life.

Don't stop believing that words and poetry can change the world.

No matter what happens, our essence is intact.

We are beings filled with passion.

Life is both desert and Oasis.

It knocks us down, it hurts us, it teaches us, it turns us into the protagonists of our own stories.

Even if the winds blow against us, the powerful masterpiece continues:

You can add a stanza.

Never stop dreaming,
Because in Dreams Man can be free.
Don't fall into the most fatal of errors: Silence.
The majority live in a frightful silence.
Don't resign yourself to this, flee.....

"I emit my screams from the roofs of this world", says the poet.

Value the beauty of the simple things.

One can make beautiful poetry about little things.

Don't betray your beliefs,
because we can't row against our own selves:

That turns life into hell.

Enjoy the panic provoked by having your life in front of you.

Live it intensely, without mediocrity.

Remember that the future is within you, so face your duties with pride and without fear.

Learn from those who can teach you.

From the experiences of those that preceded us, our "Dead Poets",

They will help you walk through life.

The society of today is us:

The "Living Poets"

Don't allow life to get by you without living it.....

Attributed to Walt Whitman

Dedicated to my children. • • •

Carpe Diem

No dejes que termine el día sin haber crecido un poco, sin haber sido feliz, sin haber alimentado tus sueños.

No te dejes vencer por el desaliento.

No permitas que nadie te quite el derecho a expresarte, que es casi un deber.

No abandones las ansias de hacer de tu vida algo extraordinario.

No dejes de creer que las palabras y las poesías pueden cambiar el mundo.

Pase lo que pase nuestra esencia está intacta.

Somos seres llenos de pasión.

La vida es desierto y es oasis.

Nos derriba, nos lastima, nos enseña,

nos convierte en protagonistas de nuestra propia historia.

Aunque el viento sople en contra,

la poderosa obra continúa:

Tú puedes aportar una estrofa.

No dejes nunca de soñar, porque sólo en sueños puede ser libre el Hombre. No caigas en el peor de los errores: el silencio. La mayoría vive en un silencio espantoso. No te resignes, huye...

"Emito mis alaridos por los tejados de este mundo", dice el poeta.

Valora la belleza de las cosas simples.

Se puede hacer bella poesía sobre pequeñas cosas,

No traiciones tus creencias,

porque no podemos remar en contra de nosotros mismos:

Eso transforma la vida en un infierno.

Disfruta del pánico que te provoca tener la vida por delante.

Vívela intensamente, sin mediocridad.

Piensa que en ti está el futuro,
entonces encara tus deberes con orgullo y sin miedo.

Aprende de quienes puedan enseñarte.
Las experiencias de quienes nos precedieron,
de nuestros "Poetas Muertos",
Ellos te ayudarán a caminar por la vida.
La sociedad de hoy somos nosotros:
Los "Poetas Vivos".
No permitas que la vida pase de largo
sin vivirla.....

Atribuido a Walt Whitman

Dedicado a mis hijos.

AGRADECIMIENTOS

Este camino, quienes lo han transitado, saben cuán ingrato puede volverse. Las amarguras se hacen rutina y el cansancio, un compañero constante. Sin embargo, cada día se elige seguir adelante. No es una decisión al azar, sino una que se sostiene en el apoyo incondicional de quienes están presentes: afectos que acompañan y resisten, siempre.

A mi familia, el pilar fundamental de mi vida, y a mis amigos, que aun desde la distancia supieron ofrecer su oído cuando la presión se hacía sentir. A mis colegas, tanto los de siempre como los más recientes, con quienes compartí no solo trabajo, sino también risas. A todos ellos, les extiendo mi más profundo agradecimiento.

En primer lugar, gracias a mi familia: Steven, Dante, Santina y Emma, por su amor y apoyo incondicional durante estos años. Este doctorado lo hicimos en familia. Realicé mi estancia en el exterior con mis hijos, quienes llegaron a un país desconocido, sin siquiera hablar el idioma. No solo lo aprendieron, sino que completaron el año escolar con excelentes calificaciones. Vivieron la pandemia encerrados durante tres meses, lejos de su hogar, su familia y sus amigos. Por todo ello, mi primer agradecimiento es para ellos, y para su padre, que quedó solo con la angustia de tenernos lejos, sin poder hacer nada en un mundo que había cerrado sus puertas.

A mis directores de tesis, los Dres. Alejandro Amaya, Néstor Tancredi y Conchi Ania: su acompañamiento constante fue esencial para que este trabajo pudiera concretarse. Alejandro, gracias por tu fe y paciencia infinitas; valoro enormemente tu palabra, incluso en el disenso, y más aún tu amistad. Néstor, mentor excepcional y profesor inolvidable, me siento afortunada de haber trabajado a tu lado y compartido tantas experiencias. Conchi, más que una tutora, fuiste un sostén en Francia, una tía para mis hijos y, sin duda, una hermana para mí. Tu calidez humana y generosidad son invaluables. A los tres, gracias por estar, enseñar y acompañar.

Al Dr. Jossano Marcuzzo, por su hospitalidad en São José dos Campos y por compartir generosamente sus conocimientos sobre fibras. A la Ing. Kana Maïga, por las horas compartidas de trabajo y risas en Orléans; imposible olvidarte. A mi familia en Orléans: el Dr. Ignacio Cameán, la Dra. Verónica Pozas, el Dr. Vianney Díaz y la Lic. Fernanda Villalonga. Hoy separados por tres continentes, pero siempre unidos por esa ciudad que nos acogió y nos hizo sentir en casa. Al Dr. Getaneh Diress, por tantas horas de trabajo compartidas, por su risa contagiosa y su humor inquebrantable. Yo lo torturaba con Metallica y él a mí con música etíope. Ortodoxo cristiano, compartíamos un vino mientras contaba que temía más a la ira de su madre que a la de Dios. A la Dra. Ilhem Rassas, que intentó que practicara el ayuno del Ramadán; no aguanté ni una mañana.

Extraño nuestras conversaciones en esa mezcla de inglés y francés que solo nosotras entendíamos, y su cuscús tunecino.

A Laura García, amiga incondicional y hermana de la vida, que siempre está, sin importar cómo ni cuándo. A mis amigas de toda la vida: Leticia, Gabriela, Fernanda, Fer Bianchi y Mónica, un grupo de mujeres maravillosas con historias suficientes para llenar varias enciclopedias. A la Dra. Mirian Casco, con quien la vida me cruzó en Gijón, y hoy seguimos compartiendo trabajo y amistad.

A mis compañeros de Fisicoquímica, por todos estos años compartidos. A los Dres. Andrés Cuña y Jorge Castiglioni: en uno de los momentos más difíciles de mi estancia en el exterior, sus mensajes fueron como un abrazo a la distancia. No olvido esas palabras que, sin saberlo, fueron una brújula en medio del desasosiego. Nunca lo dije en su momento, pero les estoy inmensamente agradecida.

A la Facultad de Química, mi segundo hogar. Al personal del CEMHTI en Orléans, por su esfuerzo y paciencia con mi francés. A mis colegas de la UCU, por hacer del trabajo un lugar donde también se cultiva la amistad.

A los organismos que financiaron este proyecto: el Programa de Desarrollo de las Ciencias Básicas (PEDECIBA), la Agencia Nacional de Investigación e Innovación (ANII), la Comisión Académica de Posgrado (CAP) y la Comisión Sectorial de Investigación Científica (CSIC).

A mi hermano, la única persona con quien puedo hablar de cualquier cosa sin sentido durante horas y reírnos hasta frustrar a quienes nos rodean. Dos locos felices. A mi abuela Amanda, que hubiera deseado ser marino y recorrer el mundo. Sus consejos: "No te quedes en tu casa solo teniendo hijos", y el inmortal "Que nunca nadie te vea llorar".

Y, por último, pero no menos importante, a mis padres. Lo que soy y donde estoy, se los debo a ellos.

Montevideo, 25 de mayo 2025

ACKNOWLEDGEMENTS

Anyone who has walked this path knows how harsh it can be. Bitterness often becomes part of daily life, and exhaustion a constant companion. Still, we choose to move forward — not by chance or accident, but by the steady support of those who stand by us. It is their presence, their unwavering affection, that sustains us.

To my family, the cornerstone of my life, and to my friends, near or far, who always offered a listening ear when the pressure felt overwhelming. To my colleagues, old and new, with whom I've shared not only long hours of work but also many moments of laughter. To all of you, I extend my deepest gratitude.

First and foremost, I thank my family — Steven, Dante, Santina, and Emma — for their endless support throughout these years. This PhD has truly been a family endeavour. I spent my research stay abroad with my children, who arrived in a country where they didn't even speak the language. Not only did they learn it, but they also completed the school year with outstanding grades. They lived through the pandemic, confined for three months without being able to go outside, far from home, family, and friends. For all of this, my first thank you goes to my children and to their father, who stayed behind, carrying the worry of having his family far away in a world that had closed its doors.

To my thesis advisors, Drs. Alejandro Amaya, Néstor Tancredi, and Conchi Ania — this work would not have been possible without your continuous support and guidance. Alejandro, thank you for always believing in me, your endless patience, and your words, even when we disagreed. Above all, thank you for your friendship. Néstor, an exceptional mentor and former professor, I feel fortunate to have worked by your side and shared so many memorable experiences. And Conchi — more than just a supervisor — you welcomed me in France, supported me at every moment, became an aunt to my children, and truly, a sister to me. You are an extraordinary human being, not only for your knowledge but also for your kindness and generosity. I feel privileged to have crossed paths with you. Thank you all, for being there, for teaching me, and for believing in me. To Dr. Jossano Marcuzzo, thank you for your hospitality during my stay in São José dos Campos and for sharing your expertise in fibre research — your support was invaluable. Engineer Kana Maïga, thank you for the long working hours and laughter we shared in Orléans. It was unforgettable—and she even shares a birthday with my daughter. To my Orléans family — Dr. Ignacio Cameán, Dr. Verónica Pozas, Dr. Vianney Díaz, and Lic. Fernanda Villalonga—though now scattered across three continents, we will always be united by that city that welcomed us and made us feel at home.

To Dr. Getaneh Diress, for the hours of lab work, your infectious laughter, and ever-cheerful spirit. I made him listen to Metallica; he made me listen to Ethiopian bands. A devout Orthodox Christian who drank wine with us while joking that he feared his mother's disapproval more than God's wrath. To Dr. Ilhem Rassas, who once invited me to try fasting for Ramadan — I didn't last a morning. I miss our conversations in that quirky mix of English and French that only we could understand, and I miss her Tunisian couscous, too.

To Laura García, a true friend and life sister, no matter what, she's always there, supporting and listening. To my lifelong friends - Leticia, Gabriela, Fernanda, Fer Bianchi, and Mónica - a remarkable group of women with enough stories to fill an encyclopedia. To Dr. Mirian Casco, life brought us together in Gijón, and we've continued sharing work and friendship ever since.

To my fellow researchers in the Physical Chemistry Department, for all these years of shared experience. To Drs. Andrés Cuña and Jorge Castiglioni — during one of the saddest moments of my stay abroad, your messages were like a warm embrace across the distance. You sent exactly the words I needed to hear, guiding me when I felt lost. I never thanked you then, but I would like to take this opportunity to say how significant your gesture was.

To the Faculty of Chemistry, my second home. To the staff of CEMHTI in Orléans, thank you for your efforts in understanding my French. To my colleagues at UCU, for making the workplace a community of friends.

To the institutions that funded this research — the Program for the Development of Basic Sciences (PEDECIBA), the National Agency for Research and Innovation (ANII), the Academic Graduate Commission (CAP), and the Sectoral Commission for Scientific Research (CSIC).

To my brother, the only person with whom I can talk nonsense for hours and laugh uncontrollably. We frustrate those around us, but we're just two happy lunatics. To my grandmother Amanda, who once said that had she been born a man, she would have been a sailor — to travel the world and never settle. Her last advice to me: "Never let anyone see you cry."

And finally — though certainly not least — my heartfelt thanks to my parents. Who I am and where I am today, I owe entirely to them.

Montevideo, 25 May 2025

RESUMEN

El desarrollo sostenible es uno de los desafíos más importantes de nuestra generación. Indudablemente, el cambio climático global y la degradación ambiental son el resultado de una sociedad basada en una economía lineal enfocada en producir, consumir y desechar, que prioriza las ganancias económicas por sobre los factores sociales o ambientales. Este panorama genera una presión significativa sobre el medio ambiente y los recursos naturales, los cuales se vuelven cada vez más escasos y contaminados. Esto subraya la necesidad urgente de cambiar hacia un modelo económico circular basado en criterios de producción y consumo sostenibles que limite el uso de recursos no renovables y promueva la utilización, reutilización y reciclaje de los recursos disponibles. Por otro lado, la sociedad está tomando conciencia de los desafíos que representan los contaminantes emergentes en los recursos hídricos. La presencia de estos contaminantes y su resistencia a los métodos convencionales de tratamiento del agua han impulsado el desarrollo de alternativas para abordar este problema.

Esta tesis doctoral se ha centrado en abordar los problemas mencionados anteriormente mediante la exploración de la síntesis de un producto de alto valor añadido (fibras de carbón activado) utilizando un precursor natural, fibra de lana. Esta materia prima natural es abundante y económica en Uruguay (uno de los mayores productores mundiales), donde se producen toneladas de fibras de lana cada año. Un objetivo principal fue optimizar las condiciones para el tratamiento del precursor de lana para obtener fibras de carbono y fibras de carbón activado. Debido a la composición y estructura compleja del precursor , uno de los mayores desafíos de esta tesis fue lograr las mejores condiciones de estabilización para mantener la morfología fibrosa. Otro desafío fue lograr las condiciones óptimas de activación necesarias para preservar la morfología fibrosa después de la activación.

Los resultados obtenidos indican que un pretratamiento de estabilización oxidativa de las fibras de lana permite que el material sea expuesto a pasos de tratamiento posteriores a altas temperaturas sin comprometer la morfología fibrosa. Se obtuvieron fibras de carbono con redes de poros variadas mediante protocolos de activación tanto química como física de las fibras estabilizadas, pero solo la activación física permitió mantener la morfología fibrosa.

Un segundo objetivo fue evaluar las potencialidades de las fibras de carbón activado como adsorbente para la eliminación de compuestos farmacéuticos de soluciones acuosas. Se realizaron estudios con soluciones monocomponente y mezclas binarias de dos contaminantes.

Los experimentos de adsorción en fase líquida para la eliminación de compuestos farmacéuticos demostraron que, independientemente de la morfología fibrosa, los materiales activados mostraron buenas capacidades de adsorción para los contaminantes estudiados. Las captaciones de las soluciones monocomponente y de las mezclas binarias se vieron afectadas por la fuerza iónica de la solución; la magnitud de este impacto dependió de la naturaleza del contaminante (es decir, el estado de ionización, el tipo de grupos funcionales superficiales). Dado que los materiales preparados están destinados a aplicarse como tratamiento terciario en plantas de tratamiento de agua, es importante comprender y controlar los parámetros operativos clave para tener en cuenta el rendimiento general.

El mecanismo de adsorción de los compuestos farmacéuticos seleccionados es complejo, incorporando varias interacciones de naturaleza claramente diferente que un modelo de adsorción de Langmuir y un modelo cinético dependiente de la concentración pueden describir. Por otro lado, la adsorción de ambos compuestos farmacéuticos seleccionados en mezclas binarias sigue un Modelo de Langmuir Modificado Multicomponente con Factores de Interacción (η) y el mismo comportamiento cinético que en soluciones monocomponente. Los parámetros operativos críticos, como el pH de la solución o la fuerza iónica, afectaron igualmente la captación en las mezclas binarias, en comparación con la retención en soluciones monocomponente. El efecto competitivo en la capacidad de retención de ambos contaminantes en soluciones acuosas fue claramente observado, dando lugar a una disminución en la captación de metronidazol (siendo el sulfametoxazol preferentemente adsorbido en las fibras de carbón activado). No se pudo establecer una predicción general sobre el comportamiento de adsorción competitiva, ya que los modelos necesitan tener en cuenta las interacciones entre los contaminantes.

En resumen, el trabajo realizado en esta tesis doctoral demuestra que se pueden preparar fibras de carbón activado derivadas de fibras de lana natural (un precursor no convencional) y que los materiales preparados muestran un rendimiento adecuado como adsorbentes de moléculas farmacéuticas.

ABSTRACT

Sustainable development is one of the significant challenges of our generation. Undeniably, the current global climate change and environmental degradation are the result of a society based on a linear economy focused on producing, consuming, and discarding, which prioritises economic gain over social or environmental factors. This panorama generates significant pressure on the environment and natural resources, which become increasingly scarce and polluted. It underscores the urgent need to shift towards a circular economic model based on sustainable production and consumption criteria that limits the use of non-renewable resources and promotes the utilisation, reuse and recycling of the available resources. On the other hand, society is becoming aware of the challenges posed by emerging pollutants in water resources. The occurrence of these contaminants and their resistance to conventional water treatment methods have triggered the development of alternatives to tackle this issue.

This PhD thesis has focused on addressing those problems mentioned above by exploring the synthesis of a high-added value product (activated carbon fibres) using a natural (waste) precursor (wool fibres). This natural raw material is abundant and inexpensive in Uruguay (one of the major worldwide producers), where tons of uncommercialised wool fibres are produced as waste every year. A primary objective focused on optimising the conditions for treating the wool precursor to obtain carbon fibres and activated carbon fibres. Owing to the wool precursor's complex composition and structure, one of this thesis's most significant drawbacks was achieving the best stabilisation conditions to maintain the fibrous morphology. A second objective focused on evaluating the potentialities of the activated carbon fibres as adsorbents for the removal of pharmaceutical compounds from aqueous solution. Studies from single-component solutions and binary mixtures of two selected pollutants were conducted to assess this. Another challenge was to achieve the optimal activating conditions necessary to preserve the fibrous morphology after activation.

The results obtained indicate that an oxidative stabilisation pretreatment of the wool fibres enables the material to be exposed to subsequent treatment steps at high temperatures without compromising the fibrous morphology. Carbon fibres with varied pore networks were obtained by both chemical and physical activation protocols of the stabilised fibres, but only physical activation allowed the fibrous morphology to be maintained.

The liquid phase adsorption experiments for the removal of the pharmaceutical compounds demonstrated that regardless of the fibrilar morphology, the activated materials displayed good adsorption capacities for the studied pollutants. The uptakes from single-component solutions and binary mixtures were affected by the ionic strength of the solution; the extent of this impact depended on the nature of the pollutant (i.e., ionisation state, type of surface moieties). Since the prepared materials are intended to be applied as a tertiary treatment in water treatment plants, it is important to understand and control key operating parameters to account for the overall performance.

The adsorption mechanism of the selected pharmaceutical compounds is complex, incorporating various interactions of distinctly different nature that a Langmuir adsorption model and a concentration-dependent kinetic model can describe. On the other hand, the adsorption of both selected pharmaceutical compounds in binary mixtures follows a competitive Modified Langmuir Multicomponent Model with Interaction Factors (η) and the same kinetic behaviour as in single-component solutions. Critical operating parameters such as the solution pH or ionic strength equally affected the uptake in the binary mixtures, compared to the retention from single component solutions. The competitive effect in the retention capacity of both pollutants in aqueous solutions was clearly observed, giving rise to a fall in the uptake for metronidazole (being sulphamethoxazole preferentially adsorbed in the activated carbon fibres). A general prediction about the competitive adsorption behaviour could not be established, as the models need to account for the interactions between the pollutants.

In summary, the work carried out in this PhD thesis demonstrates that activated carbon fibres derived from natural wool fibres (an unconventional precursor) can be prepared and that the prepared materials show adequate performance as adsorbents for pharmaceutical molecules.

Index	
Agradecimientos	xi
Acknowledgements	xiii
Resumen	XV
Abstract	xvii
List of Tables	XXV
List of Figures	xxxi
List of Symbols and Abbreviations	xiviii
1. INTRODUCTION	1
1.1 Contamination of water resources, an actual concern	4
1.2 The presence of pharmaceutical compounds in the aquatic envir	ronment 7
1.3 Situation in Uruguay	12
1.4 Methods of remediation	14
1.5 Why the use of Wool, an ancient and still novel material?	18
1.6 Thesis main and specific goals	23
1.7 Thesis structure	24
2. ACTIVATED CARBON MATERIALS	27
2.1 Structure of activated carbons	30
2.2 Porosity	32
2.3 Surface chemistry	33
2.4 Precursors	35
2.5 Synthesis of active carbon (AC)	36
2.5.1 Pre-treatment	37
2.5.2 Carbonisation	38
2.5.3 Chemical activation	39
2.5.3.1 Thermal or physical activation	40
2.5.3.1 Chemical activation	44
2.6 Types of AC and applications	47
2.7 Regeneration	49
2.8 Activated Carbon Fibers (ACF)	50

	2.8.1	Stabilisation	54
3	3. ADS	SORPTION FROM THE LIQUID PHASE	55
3.1	Funda	mentals of liquid phase adsorption	57
3.2	Adsor	ption isotherms from monocomponent solutions	62
	3.2.1	Langmuir model	62
	3.2.2	Freundlich model	63
	3.2.3	Elovich model	64
3.3	Isother	rm models applied to multicomponent adsorption	64
	3.3.1	Non-competitive adsorption system (NC)	65
	3.3.2	Langmuir Multicomponent (LM)	65
	3.3.3	Modified Langmuir Multicomponent with δ (MLM δ)	66
	3.3.4	Extended Langmuir Multicomponent (ELM)	67
	3.3.5	Modified Langmuir Multicomponent with Interaction Factor (η) (MLM η)	67
3.4	Kineti	c models	68
	3.4.1	Pseudo-first order (PFO)	68
	3.4.2	Pseudo-second order (PSO)	69
	3.4.3	Film diffusion (FD)	69
	3.4.4	Intraparticle diffusion (ID)	70
3.5	The ch	nemistry of the aqueous solution	71
	3.5.1	The effect of solution pH on the adsorption	71
	3.5.2	Ionic strength effect	72
2	4. MA	TERIALS AND CHARACTERISATION TECHNIQUES	73
4.1	Worki	ng strategy	75
4.2	Materi	als and treatments	76
	4.2.1	Precursor	76
	4.2.2	Stabilised material	76
	4.2.3	Active carbon materials	78
		4.2.3.1 Physical activation	78
		4.2.3.2 Chemical activation	79
	4.2.4	Pharmaceutical compounds (PhCs)	80

4.3	Chemic	al and struct	ural characterisation	82
	4.3.1	Textural ch	aracterisation	82
		4.3.1.1 A	dsorption-desorption isotherms	83
		4.3.1.2 B	ET equation	88
		4.3.1.3 D	ubinin – Radushkevich equation	89
		4.3.1.4 Po	ore size distribution: Density Functional Theory	90
	4.3.2	Elemental a	analysis	91
	4.3.3	Thermal sta	ability and oxidative resistance	91
	4.3.4	Thermal de	composition couple with mass spectrometry	92
	4.3.5	Fourier tran	asformed infrared spectroscopy	92
	4.3.6	Raman spec	ctroscopy	93
	4.3.7	Scanning el	lectronic microscopy	94
	4.3.8	X-ray diffra	action	95
	4.3.9	pH at the po	oint of zero charge	97
	4.3.10	Potentiome	tric titration	97
4.4	Liquid	phase adsorp	otion experiments	98
	4.4.1	Kinetic stud	dies	98
	4.4.2	Thermodyn	namic studies	100
	4.4.3	Binary syst	em studies	100
	4.4.4	Solution's p	pH effect	101
	4.4.5	The ionic st	trength effect	102
4	CTI	DV AND OI	PTIMISATION OF THE STABILISATION STEP	103
5.1			the precursor	105
3.1	5.1.1		lectronic microscopy	105
	5.1.2	Elemental of	•	103
	5.1.3		asformed infrared spectroscopy	106
	5.1.4		tabilisation of the precursor	100
	3.1.4		hermogravimetric studies	108
			alorimetric studies	110
5.2	Stabilio	ation treatme		110
J.∠	DiaUIIIS	uuvu uvaliill	~11tD	114

5.3	Charac	terisation	of the stabilised material	113
	5.3.1	Thermog	gravimetric studies	113
	5.3.2	Element	al content	115
	5.3.3	$pH_{pzc} \\$		116
	5.3.4	Fourier t	transformed infrared spectroscopy	117
	5.3.5	Thermal	decomposition couple with mass spectrometry	119
	5.3.6	Raman s	spectroscopy	129
	5.3.7	Scanning	g electronic microscopy	131
	5.3.8	X-ray di	ffraction	133
5.4	Partial	conclusion	ns	134
				105
			OF THE ACTIVATION VARIABLES	137
6.1		• 1	es of the char in CO ₂ and Ar	140
6.2		7 1	es in KOH	142
6.3	Textur	al and mor	rphology characterisation	143
	6.3.1	Repeatal	bility of the activation methods	144
		6.3.1.1	Repeatability of the chemical activation procedure	144
		6.3.1.2	Repeatability of physical activation method controlled by	145
			Chemical Reaction	
		6.3.1.3	Repeatability of physical activation method controlled by	146
			Diffusion	
	6.3.2	Activation	on method comparison (Physical vs Chemical)	147
	6.3.3	Control	method comparison (Diffusion vs Chemical Reaction)	153
	6.3.4	Effect of	f the activation time	158
6.4	Chemi	cal charact	terisation	163
	6.4.1	Element	al composition	163
	6.4.2	Surface	charge	164
	6.4.3	Protons'	exchange capacity in aqueous solution	165
	6.4.4	Function	nal groups	166
6.5	Partial	conclusion	ns	168

,	7. ADS	SORPTION IN MONOCOMPONENT SYSTEMS	171
7.1	Adsor	otion in aqueous solution	173
7.2	Kineti	c studies	173
	7.2.1	SMX adsorption kinetics	173
	7.2.2	MNZ adsorption kinetics	178
	7.2.3	AMP adsorption kinetics	183
7.3	Equili	brium adsorption	186
	7.3.1	SMX adsorption thermodynamics	186
	7.3.2	MNZ adsorption thermodynamics	199
	7.3.3	AMP adsorption thermodynamics	210
7.4	Ionic s	trength studies	211
7.5	pH vai	riation studies	213
7.6	Partial	conclusions	215
;	8. ADS	SORPTION IN BINARY SYSTEMS	219
8.1	Adsor	ption in complex mixtures	221
8.2	Adsor	ption experiences (1:1, molar ratio)	222
8.3	Comp	etition models	233
	8.3.1	Non-competitive adsorption system model	233
	8.3.2	Langmuir Multicomponent model	235
	8.3.3	Modified Langmuir Multicomponent model with discount factor $\boldsymbol{\delta}$	238
	8.3.4	Extended Langmuir Multicomponent	240
	8.3.5	Modified Langmuir Multicomponent with Interaction Factor	241
8.4	Compa	arison among competition models	245
8.5	Ionic s	trength studies	246
8.6	pH vai	riation studies	247
8.7	Comp	etition under other molar ratios	249
	8.7.1	Competition under 1:1.5 (SMX:MNZ) molar ratio conditions	251
	8.7.2	Competition under 1.5:1 (SMX:MNZ) molar ratio conditions	252
	8.7.3	Competition under 1:2 (SMX:MNZ) molar ratio conditions	254
	8.7.4	Competition under 2:1 (SMX:MNZ) molar ratio conditions	256
8.8	Compa	arison among binary mixtures for the MLMη model	258

	Index
8.9 Partial conclusions	261
9. CONCLUSIONS	263
9.1 Overall conclusions	265
9.2 Perspectives	268
10. BIBLIOGRAPHIC REFERENCES	269
Annex I	
Complementary data	299
Annex II	
Articles	309
Annex III	
Expositions	313
Annex IV	
Photographic documentation	319

Concentrations of PhAC found at Río de la Plata River in the Montevideo region, separated by therapeutic class.	12
Chemical composition, wt. %, and dry-ash-free basis of virgin wool.	22
Classification of CF (SJ. Park 2015).	52
Physicochemical characteristics of the selected drugs for this work.	81
HPLC working conditions for monocomponent solutions.	100
HPLC working conditions for binary solutions.	101
Chemical composition (wt. %, dry-ash free basis) of the pristine	106
wool (average values plus the standard deviation).	
List of stabilisations under air atmosphere tested.	112
The virgin wool's chemical composition (wt.%, dry-ash free basis)	115
and the samples obtained after oxidative stabilisation at various	
temperatures and times (average values plus the standard deviation).	
pHPZC values for stabilised materials (average values plus the standard deviation).	116
Quantifying the amounts of CO and CO2 released was obtained by	125
integrating the m/z 28 and 44 peaks in the TPD profiles.	
Raman parameters for 275 and 300 series.	131
Structure parameters of X-ray diffraction for SF series of selected	134
samples.	
List of the carbonised samples developed for the present work.	139
	Montevideo region, separated by therapeutic class. Chemical composition, wt. %, and dry-ash-free basis of virgin wool. Classification of CF (SJ. Park 2015). Physicochemical characteristics of the selected drugs for this work. HPLC working conditions for monocomponent solutions. HPLC working conditions for binary solutions. Chemical composition (wt. %, dry-ash free basis) of the pristine wool (average values plus the standard deviation). List of stabilisations under air atmosphere tested. The virgin wool's chemical composition (wt.%, dry-ash free basis) and the samples obtained after oxidative stabilisation at various temperatures and times (average values plus the standard deviation). pHPZC values for stabilised materials (average values plus the standard deviation). Quantifying the amounts of CO and CO2 released was obtained by integrating the m/z 28 and 44 peaks in the TPD profiles. Raman parameters for 275 and 300 series. Structure parameters of X-ray diffraction for SF series of selected samples.

Table 6.2	Main textural parameters obtained from the nitrogen adsorption-	145
	desorption isotherms at -196 °C for the chemically activated	
	samples.	
Table 6.3	Main textural parameters obtained from the nitrogen adsorption-	146
	desorption isotherms at -196 °C for the physically activated	
	samples under chemical reaction control regime (CR).	
Table 6.4	Main textural parameters obtained from the nitrogen adsorption-	147
	desorption isotherms at -196 °C for the physically activated	
	samples under diffusion control regime (D).	
Table 6.5	Main textural parameters of selected samples obtained from the N_2	150
	and CO ₂ adsorption isotherms analysis at -196 and 0 °C,	
	respectively.	
Table 6.6	Main structural parameters obtained from the XRD pattern analysis	153
	for ACF-240-CR and ACF-KOH.	
Table 6.7	The Main textural parameters of selected samples synthesised by	154
	physical activation under Diffusion (D) and Chemical Control (CR)	
	conditions were obtained from N2 and CO2 adsorption-desorption	
	isotherms at -196 and 0 C, respectively.	
Table 6.8	Apparent kinetic constant value as a result of Equation 2.2	156
	integrated expression (n and α : kinetic parameters, see Chapter II,	
	section 2.4.3.1).	
Table 6.9	Regime flow and hydraulic residence time for both methods.	157
Table 6.10	The main textural parameters of samples synthesised by physical	160
	activation under Chemical Control (CR) conditions were obtained	
	from N2 and CO2 adsorption-desorption isotherms at -196 and 0	
	C, respectively.	
Table 6.11	Crystalline parameters obtained from XRD patterns of samples	162
	ACF-120-CR and ACF-240-CR.	
Table 6.12	Elemental analysis on a dry-ash free basis (wt.%) of the wool	164
	precursor (WF) and the ACFs obtained by different methods	
	(average values and standard deviations are presented).	

Table 6.13	pHpzc measures average values for ACFs obtained by physical and	165
	chemical activation	
Chapter VII		
Table 7.1	Kinetic fitting comparison for SMX (1.0 mmolL-1) adsorption onto	178
	ACF obtained under chemical and physical activation (D and CR	
	methods) and different times for CR control.	
Table 7.2	Kinetic fitting comparison for MNZ adsorption onto ACF obtained	181
	under CR and D method, chemical and physical activation, and	
	different times for CR control.	
Table 7.3	Kinetic fitting comparison, for the first 15 minutes of the process,	183
	for MNZ adsorption onto ACF obtained under the CR and D	
	methods, chemical and physical activation, and different times for	
	CR control.	
Table 7.4	Kinetic fitting for AMP adsorption onto ACF-30-D.	185
Table 7.5	Kinetic features comparison among SMX, MNZ and AMP	186
	adsorbates for the same adsorbent ACF-30-D.	
Table 7.6	Isotherms fitting comparison for SMX adsorption onto ACF	189
	obtained under chemical and physical activation (D and CR	
	methods) and different times for CR control.	
Table 7.7	Fitting parameters for the SMX uptake at an equilibrium	194
	concentration of 0.1 mmolL-1 as a function of the pore size	
	distribution for pores of selected ranges.	
Table 7.8	Fitting parameters to different adsorption models of the	202
	experimental equilibrium adsorption data for MNZ on the series of	
	ACF obtained under chemical and physical activation (D and CR	
	control regimes) and different activation times for CR control	
	regimes.	
Table 7.9	Fitting parameters for the MNZ uptake for Ceq 0.1 mmolL-1 as a function	208
	of the volume of pores plots for 0.7, 1.5, 2.0 and 3.0 nm.	
Table 7.10	Isotherms fitting comparison for SMX adsorption onto ACF	211
	obtained under physical activation under Diffusion control.	

Chapter VIII

Table 8.1	Percentage deviation (% D) between the predicted and the	235
	experimental uptakes of SMX and MNZ in equimolar (1:1) binary	
	mixtures.	
Table 8.2	Percentage deviation between the experimental and the predicted	238
	molar uptakes of MNZ and SMX from equimolar (1:1) binary	
	mixtures using the LM models for similar (s) and different (d)	
	adsorption capacities.	
Table 8.3	Percentage deviation between the predicted adsorption capacity	240
	and the experimental data for the adsorption of SMX and MNZ	
	from equimolar (1:1) binary mixtures using the (MLM δ) adsorption	
	model.	
Table 8.4	Percentage deviation between the predicted adsorption capacity	241
	and the experimental data for the adsorption of SMX and MNZ in	
	equimolar (1:1) binary mixtures onto ACF-30-D adsorbent for	
	(ELM) adsorption model (1:1 molar ratio).	
Table 8.5	Interaction factors for each component depending on the ACF.	242
Table 8.6	Percentage deviation between the experimental and the predicted	245
	molar uptake by the (MLM $\!\eta 0$ adsorption model of MNZ and SMX	
	from equimolar (1:1) binary mixtures for the studied samples.	
Table 8.7	Comparison of the respective percentage Deviation (%D) for each	246
	model applied to the adsorption data obtained from the binary	
	mixtures.	
Table 8.8	Comparison of the respective (%) Deviation for each model applied	252
	to the adsorption data obtained under binary conditions for	
	solutions (1:1.5 SMX:MNZ molar ratio) for ACF-30-D sample.	
Table 8.9	Comparison of the respective percentage Deviation (%) for each	254
	model applied to the adsorption data obtained for a binary mixture	
	(1.5:1 SMX:MNZ molar ratio) for sample ACF-30-D.	
Table 8.10	Comparison of the respective (%) Deviation for each model applied	256
	to the adsorption data obtained under binary conditions for	
	solutions (1:2 SMX:MNZ molar ratio) for ACF-30-D sample.	

Table 8.11	Comparison of the percentage Deviation (%) for each model	258
	applied to the adsorption data obtained under binary solutions (1:2	
	SMX:MNZ molar ratio) for sample ACF-30-D.	
Table 8.12	Interaction factors for each component depending on the molar	260
	ratio (SMX:MNZ) for the ACF-30-D adsorbent.	
Annov I		
Annex I		
Table AI.1	Parameters used in the calculation of the dimensionless Reynolds	275
	number.	
Table AI.2	SMX adsorption isotherms data (average data from three	275
	experiments).	
Table AI.3	MNZ adsorption isotherms data (average data from three	276
	experiments).	
Table AI.4	AMP adsorption isotherms data (average data from three	277
	experiments).	
Table AI.5	Kinetic fitting comparison for SMX (0.4 mmolL ⁻¹) adsorption onto	278
	ACF obtained under chemical and physical activation (D and CR	
	• •	
	methods) and different times for CR control.	

Chapter I		
Figure. 1.1	Water distribution on Earth (credit: Timothy Bralower © Penn State University is licensed under (CC BY-NC-SA 4.0).	4
Figure 1.2	Water cycle, main issues affecting water quality and quantity, from European Environment Agency 2018 (EEA).	5
Figure 1.3	Annual baseline water stress.	6
Figure 1.4	UN symbol for the Sustainable Development Goal 12.	6
Figure 1.5	Locations of studied rivers/catchments for the global assessment. (Wilkinson et al., 2022).	8
Figure 1.6	Cumulative API concentrations quantified across 137 studied river catchments organised by descending cumulative concentration (ngL ⁻¹). Black lines mark percentiles. The cumulative concentrations reported here are calculated as the average sum concentration of all quantifiable API residues at each sampling site within respective river catchments.	10
Figure 1.7	Concentrations of PhAC found at Río de la Plata River, in Montevideo and Buenos Aires's regions, separated by therapeutic class. Comparison between coasts.	13
Figure 1.8	Schematic layout of the five steps involved in the WWTP from O.S.E.	15
Figure 1.9	UN symbol for the Sustainable Development Goal 12.	19
Figure 1.10	Bonds in wool from The Chemical & Physical Structure of Merino Wool (CSIRO 2015).	20
Figure 1.11	Schematic diagram of the structure and morphology of a Merino wool fibre (Source: CSIRO).	21
Chapter II		
Figure 2.1	Drinking fountain that dates from the 18 th century (Domaine national de Chambord – Chambord Castle – France).	30
Figure 2.2	Schematic representation of the microstructure of the AC (R. Bansal, Donnet, and Stoeckli 1988).	31

Figure 2.3	Diagram that models the structural changes which occur during the	31
	heat treatment of graphitisable carbon.	
Figure 2.4	Schematic illustration of the structure of AC: (a) readily undergoing	32
	graphitisation, and (b) undergoing graphitisation to a small degree.	
Figure 2.5	Schematic representation of the porous structure of an AC.	33
Figure 2.6	Schematic representation of the principal O-, N-, and S-containing	34
	surface groups in activated carbons, including free edge sites and	
	carbon-hydrogen complexes.	
Figure 2.7	General scheme of the activation process.	37
Chapter III		
Figure 3.1	Lennard-Jones-type diagrams: potential energy versus distance.	58
Figure 3.2	Model of the double-layer structure of the adsorbent-adsorbate	59
	interface with examples of specific and nonspecific ion adsorption.	
Figure 3.3	Schematic representation of methylene blue adsorption on AC.	60
Figure 3.4	Adsorption mass transfer steps.	61
Figure 3.5	Schematic representation of adsorption processes and mechanisms.	62
Chapter IV		
Figure 4.1	Working scheme.	75
Figure 4.2	Image of the as received Wool-fibres.	76
Figure 4.3	Stainless steel hollow cylindrical mesh that was placed inside the THF.	76
Figure 4.4	Scheme of the temperature treatment under an oxidising atmosphere.	77
Figure 4.5	Stainless steel hollow cylindrical mesh that was placed inside the	77
	muffle.	
Figure 4.6	Scheme of the temperature treatment under an oxidising atmosphere;	77
	the cooling is carried out outside the equipment at room temperature.	
Figure 4.7	Activation under diffusion control.	78
Figure 4.8	Activation under chemical reaction control.	79
Figure 4.9	Chemical activation process.	80
Figure 4.10	Chemistry structure and UV spectra of AMP.	81
Figure 4.11	Chemistry structure and UV spectra of SMX.	81

Figure 4.12	Chemistry structure and UV spectra of MNZ.	82
Figure 4.13	Schematic representation of the different pore types established by	83
	IUPAC for activated carbon.	
Figure 4.14	Classification according to IUPAC of the gas's adsorption isotherms.	84
Figure 4.15	Classification of hysteresis loops.	86
Figure 4.16	X-ray diffraction spectrum of Graphene, Graphite and AC (data	96
	provided by NaFMAT group, CEMHTI, CNRS).	
Figure 4.17	Graphic representation of the parameters L _c , L _a and d ₀₀₂ .	96
Figure 4.18	Multipoint stirring plate where the experiments were left stirring at	99
	room temperature.	
Chapter V		
Figure 5.1	SEM images of the pristine wool fibres.	106
Figure 5.2	The infrared spectrum of the wool fibre used as a carbon fibre's	107
	precursor in this study.	
Figure 5.3	Vibrational modes of the amide group.	108
Figure 5.4	Thermogravimetric profiles (mass evolution and derivative weight)	109
	under inert and air atmosphere of the pristine wool fibres.	
Figure 5.5	Differential Scanning Calorimetry of pristine wool under nitrogen	111
	and air atmosphere a), under air atmosphere (full scale) b).	
Figure 5.6	Deconvolution of the 220 – 300 °C peak under air atmosphere.	112
Figure 5.7	Thermogravimetric profile under an inert atmosphere of the wool	114
	fibres stabilised in the air at several temperatures for (a) 60 and 120	
	minutes and (b) 30 minutes.	
Figure 5.8	The virgin wool's chemical composition (wt.%, dry-ash free basis)	116
	and the samples obtained after oxidative stabilisation at various	
	temperatures and times.	
Figure 5.9	Infrared spectra of the pristine wool fibre and the series of samples	118
	stabilised at 60 and 120 minutes at various temperatures.	
Figure 5.10	The second derivative of the FTIR transmittance spectra of (A) WF	119
	and SF-60 and 120 minutes series, (B) SF-300 60 and 120 minutes	
	samples.	

Figure 5.11	TPD-MS profiles of selected m/z for the pristine and stabilised	121
	wool fibres. Insets illustrate differentiated emission zones for WF	
	and SF-300-60.	
Figure 5.12	The total areas of the profiles correspond to 44, 28, 18, and 2 m/z	123
	signals obtained from TPD-MS data.	
Figure 5.13	Evolution of the peak deconvolution for signal m/z 64.	126
Figure 5.14	Evolution of the peak deconvolution for signal m/z 46.	127
Figure 5.15	Evolution of the peak deconvolution for signal m/z 44.	128
Figure 5.16	Evolution of the peak deconvolution for signal m/z 28.	129
Figure 5.17	Raman spectra of selected stabilised samples.	130
Figure 5.18	SEM images of the pristine (WF) and stabilised (series SF-T-t)	132
	wool fibres at various temperatures (magnification of the pictures:	
	x270; magnification of insets: x2000).	
Figure 5.19	SEM image of the stabilised material at 400 °C for 30 minutes,	132
C	where the fibres collapse can be observed.	
Figure 5.20	XRD spectra of WF, SF-250 and upper series	133
Chapter VI		
Figure 6.1	Thermogravimetric analysis for SF-300-120 under Ar and CF	142
	obtained at 800 and 1000 °C under CO ₂ .	
Figure 6.2	Reactivity profiles for SF-300-120 under Ar, and CF obtained at	142
	800 and 1000 °C under CO ₂ .	
Figure 6.3	Thermogravimetric analysis under Ar atmosphere for the samples	143
	impregnated with KOH.	
Figure 6.4	DTG analysis under Ar atmosphere for the samples impregnated	143
	with KOH.	
Figure 6.5	N ₂ adsorption-desorption isotherms at -196 °C of three batches of	145
	chemically activated material.	
Figure 6.6	N_2 adsorption-desorption isotherms at -196 °C of three batches of	146
	physically activated material, all of them under the same working	
	conditions (240 minutes at 950 °C).	

Figure 6.7	N ₂ adsorption-desorption at -196 °C of three batches of physically	147
	activated material obtained by D control.	
Figure 6.8	Nitrogen adsorption/desorption isotherms at -196C of samples	148
	ACF-KOH (600°C, 60 min), ACF-60-CR (875°C, 60 min) and	
	ACF-240-CR (875°C, 240 min).	
Figure 6.9	Magnification of the low-pressure region of the N2 adsorption	148
	isotherms at -196C of samples ACF-KOH and ACF-60-CR.	
Figure 6.10	Magnification of the low-pressure region of the N2 adsorption	148
	isotherms at 196C of samples ACF-KOH and ACF-240-CR.	
Figure 6.11	Pore size distribution for selected samples obtained from the	150
	2DNLDFT-HS method applied to the N2 adsorption isotherms at -	
	196C; (left) derivative pore volume; (right) cumulative pore	
	volume.	
Figure 6.12	SEM image of ACF-KOH, 70x.	151
Figure 6.13	SEM image of ACF-240-CR, 100x.	151
Figure 6.14	SEM image of ACF-KOH, 1000x.	151
Figure 6.15	SEM image of ACF-240-CR, 1000x.	151
Figure 6.16	SEM image of ACF-60-D, 200x.	152
Figure 6.17	SEM image of ACF-60-D, 1000x.	152
Figure 6.18	XRD patterns of ACF-240-CR and ACF-KOH, where the lack of	153
	significant differences between plots is observed.	
Figure 6.19	N ₂ adsorption-desorption isotherm at -196C of selected samples	154
	synthesized by physical activation under Diffusion (D) and	
	Chemical Control (CR) conditions.	
Figure 6.20	SEM image of ACF-30-D sample, 500x.	155
Figure 6.21	SEM image of ACF-30-CR sample, 500x.	155
Figure 6.22	SEM image of ACF-30-D sample, 3000x.	156
Figure 6.23	SEM image of ACF-30-CR sample, 4000x.	156
Figure 6.24	Material's behaviour under the PCM kinetic model.	158
Figure 6.25	The material's behaviour under the UCM kinetic model is based on	158
	the model proposed by Levenspiel (Levenspiel, 2001).	

Figure 6.26	N ₂ adsorption-desorption isotherms plots for samples obtained by	159
	CR control at different treatment times.	
Figure 6.27	Nitrogen adsorption/desorption isotherms at -196C of samples	159
	(ACF-30-CR and ACF-240-CR) prepared by the physical	
	activation method under the CR regime.	
Figure 6.28	Nitrogen adsorption/desorption isotherms at -196C of samples	159
	(ACF-180-CR and ACF-240-CR) prepared by the physical	
	activation method under the CR regime.	
Figure 6.29	Correlation between the textural parameters and the physical	160
	activation time under CR control. Data are plotted in different axes	
	for clarity.	
Figure 6.30	Correlation between the burn-off and the activation time for	161
	samples treated under CR control regime (the inset shows the fitting	
	parameters).	
Figure 6.31	Correlation between the burn-off and the micropore volumes for	161
	samples treated under CR control regime.	
Figure 6.32	Correlation between the burn-off and the mesopore volume for	162
	samples treated under CR control regime.	
Figure 6.33	XRD pattern plots for ACF-120-CR and ACF-240-CR samples.	163
Figure 6.34	The virgin wool's chemical composition (wt.%, dry-ash free basis)	164
	and the ACFs obtained by different methods (chemical, physical-	
	D, and physical-CR).	
Figure 6.35	Charge exchange during a potentiometric titration with NaOH 0.1	166
	M for the sample ACF-300-D and its replica.	
Figure 6.36	FTIR spectra for all the different activation methods followed in	167
	this work.	
Figure 6.37	ACF structures for both activations, (A) ACF-CR series where the	168
	disulphur bridge that sustains the morphology can be seen, and (B)	
	ACF-KOH.	

Chapter VII		
Figure 7.1	SMX normalised concentration variation graph as a function of	175
	time for ACF samples from the different activation methods	
	(chemical and physical under D and CR regimes).	
Figure 7.2	Concentration decay curve of SMX as a function of time for	175
	samples with similar textural features.	
Figure 7.3	Comparison between the absolute removal of SMX (percentage),	175
	the normalised specific surface area and the micropore volume	
	(percentage), for selected samples obtained under physical -CR, D	
	control regimes- and chemical activation.	
Figure 7.4	Concentration decay curve of SMX as a function of time for the	176
	physically activated samples. The similar equilibrium time of the	
	samples is marked.	
Figure 7.5	Speciation diagram of SMX in aqueous solution and the	177
	deprotonation equilibrium due to pH changes.	
Figure 7.6	Concentration decay curve of MNZ as a function of time for ACF	179
	samples from the different activation methods (chemical and	
	physical under D and CR regimes).	
Figure 7.7	Speciation diagram of MNZ in aqueous solution and the species	179
	present depending on the medium pH.	
Figure 7.8	MNZ's molecule, the dashed circle englobes the structure's planar	180
	section.	
Figure 7.9	Comparison between the absolute removal of MNZ (percentage),	181
	the normalised specific surface area and the micropore volume	
	(percentage), for selected samples obtained under physical -CR, D	
	control regimes- and chemical activation.	
Figure 7.10	Speciation diagram for AMP in aqueous solution the species	184
	present depending on the medium pH.	

AMP normalised decay concentration curve as a function of time

Figure 7.11

for ACF-30-D sample.

185

Figure 7.12	SMX adsorption isotherms for ACF samples from the different	187
	activation methods (chemical and physical under D and CR	
	regimes).	
Figure 7.13	SMX adsorption isotherms for ACF-KOH and ACF-240-CR	188
	samples.	
Figure 7.14	Isotherms comparison between samples activated under CR and D	188
	regimes for 30 minutes.	
Figure 7.15	Comparison of SMX adsorption capacities against the microporous	190
	volume calculated by DR (for all the samples obtained under	
	different conditions).	
Figure 7.16	Comparison of SMX adsorption capacities against the microporous	191
	areas (calculated by DR for all the samples obtained under different	
	conditions).	
Figure 7.17	Comparison of SMX adsorption capacities against the $S_{\mbox{\scriptsize BET}}$ values	192
	for all the samples obtained under different conditions.	
Figure 7.18	SMX spatial structure and size (Serna-Carrizales et al. 2023).	192
Figure 7.19	Correlation between the uptake of SMX for an equilibrium	194
	concentration of 0.1 mmolL ⁻¹ as a function of the size of the pores:	
	(a) up to 0.7 nm, (b) up to 1.5 nm, (c) up to 2.0 nm, and (d) up to	
	3.0 nm. Pore volumes were evaluated from the nitrogen adsorption	
	isotherms at 77K of the ACF using the 2D-NLDFT-HS method.	
Figure 7.20	Contour plot of the coefficient of determination of the uptake of	195
	SMX at various equilibrium concentrations and the pore sizes.	
Figure 7.21	Evolution of the solution pH at different concentrations of SMX	197
	before (squares) and after the adsorption on samples ACF-KOH	
	(triangles) and ACF-240-CR (circles). 20 mg of adsorbent have	
	been used for all the adsorption assays.	
Figure 7.22	SMX removal efficiency evolution for all the samples obtained	198
	under different activation conditions vs the initial SMX	
	concentration (20 mg of adsorbent per analysis).	

Figure 7.23	Representation of the operating lines (dotted lines) from the kinetic	199
	data on the equilibrium adsorption isotherms for samples ACF-	
	KOH, ACF-240-CR, and ACF-60-CR, for the adsorption of SMX.	
Figure 7.24	MNZ adsorption isotherms for samples prepared upon different	200
	activation methods (chemical and physical under D and CR	
	regimes).	
Figure 7.25	MNZ spatial structure and size (Serna-Carrizales et al. 2023).	201
Figure 7.26	Evolution of the solution pH at different MNZ concentrations	203
	before (squares, initial concentration) and after the adsorption for	
	samples ACF-KOH (triangles) and ACF-240-CR (circles). 20 mg	
	of adsorbent were used in all cases.	
Figure 7.27	MNZ removal efficiency evolution for all the samples obtained	204
	under different activation conditions vs the initial MNZ	
	concentration (20 mg of adsorbent per analysis).	
Figure 7.28	Correlation between the MNZ adsorption capacities and the	205
	micropore volumes, calculated by the DR formulism applied to N ₂	
	and CO ₂ adsorption isotherms.	
Figure 7.29	Correlation between the MNZ adsorption capacities and the	206
	micropore surface area calculated by the DR formulism applied to	
	N ₂ and CO ₂ adsorption isotherms.	
Figure 7.30	Correlation between the MNZ adsorption capacities and the	206
	specific surface area $(S_{\mbox{\scriptsize BET}})$ calculated by the BET equation from	
	the N ₂ adsorption isotherms.	
Figure 7.31	MNZ uptake for equilibrium concentrations of 0.1 mmolL ⁻¹ as a	207
	function of the volume of pores below (a) 0.7 nm, (b) 1.5 nm, (c)	
	2.0 nm, and (d) 3.0 nm.	
Figure 7.32	Contour plot of the coefficient of determination of the uptake of	208
	MNZ at various equilibrium concentrations and the pore sizes.	
Figure 7.33	Representation of the operating lines (dotted lines) from the kinetic	209
	data on the equilibrium adsorption isotherms for samples ACF-	
	KOH, ACF-240-CR, and ACF-120-CR, for the adsorption of	
	MNZ.	

Figure 7.34	AMP adsorption isotherms for ACF-30-D, fitting data in Annex II.	210
Figure 7.35	Evolution of the solution pH at different pharmaceutical compound	211
	concentrations before (black squares, initial concentration) and	
	after the adsorption for sample ACF-60-D (red circles) (20 mg of	
	adsorbent per analysis).	
Figure 7.36	Equilibrium adsorption isotherms of SMX and MNZ on sample	212
	ACF-KOH, showing the response in solutions with varied ionic	
	strength: NaCl 10 and 100 mmol.	
Figure 7.37	Equilibrium adsorption isotherms of AMP in sample ACF-30-D,	213
	showing the response in solutions with varied ionic strength: NaCl	
	10 and 100 mmol.	
Figure 7.38	SMX and MNZ effect of the solution's pH on the adsorption	214
	capacity (for clarity reasons, the pH values were marked for one	
	experience, while the others follow the same criteria).	
Figure 7.39	The effect of the solution's pH on the AMP's adsorption capacity.	215
Figure 7.40	Schematic representation of the mechanisms involved in the SMX	216
	adsorption.	
Figure 7.41	Schematic representation of the mechanisms involved in the MNZ	217
	adsorption.	
Figure 7.42	Schematic representation of the mechanisms involved in AMP	217
	adsorption.	
Chapter VIII		
Figure 8.1	Comparative uptakes of SMX and MNZ in monocomponent	223
	solutions and equimolar (1:1) binary mixtures for sample ACF-	
	KOH at various initial concentrations.	
Figure 8.2	Evolution of the solution pH at different concentrations of the	223
	equimolar (1:1) binary mixture before (black squares) and after	
	(blue triangles and red dots) reaching the adsorption equilibrium on	
	sample ACF-KOH. 20 mg of adsorbent have been used for all the	
	adsorption assays.	

Figure 8.3	Comparative uptakes of SMX and MNZ in monocomponent	224
	solutions and equimolar (1:1) binary mixtures for sample ACF-	
	240-CR at various initial concentrations.	
Figure 8.4	Evolution of the solution pH at different concentrations of the	225
	equimolar (1:1) binary mixture before (black squares) and after	
	(blue triangles and red dots) reaching the adsorption equilibrium on	
	sample ACF-240-CR. 20 mg of adsorbent have been used for all	
	the adsorption assays.	
Figure 8.5	Comparative uptakes of SMX and MNZ in monocomponent	226
	solutions and equimolar (1:1) binary mixtures for sample ACF-	
	120-CR at various initial concentrations.	
Figure 8.6	Evolution of the solution pH at different concentrations of the	227
	equimolar (1:1) binary mixture before (red dots) and after the	
	adsorption on sample ACF-120-CR (triangles). 20 mg of adsorbent	
	have been used for all the adsorption assays.	
Figure 8.7	Comparative uptakes of SMX and MNZ in monocomponent	228
	solutions and equimolar (1:1) binary mixtures for sample ACF-30-	
	D at various initial concentrations.	
Figure 8.8	Evolution of the solution pH at different concentrations of the	228
	equimolar (1:1) binary mixture before (red dots) and after the	
	adsorption on sample ACF-30-D (triangles). 20 mg of adsorbent	
	have been used for all the adsorption assays.	
Figure 8.9	Evolution of the uptake of SMX in an equimolar (1:1) binary	229
	mixture for different adsorbents with the corresponding	
	equilibrium concentrations of both pollutants.	
Figure 8.10	Evolution of the uptake of MNZ in an equimolar (1:1) binary	230
	mixture for different adsorbents with the corresponding	
	equilibrium concentrations of both pollutants.	
Figure 8.11	Pore size distribution for samples utilised for binary adsorption	231
	experiences, obtained from the 2D-NLDFT-HS method applied to	
	the N ₂ adsorption isotherms at -196 °C.	

Figure 8.12	Correlation between the cumulative total pore volume and the	231
	uptake of SMX and MNZ in binary solutions (1:1 molar ratio,	
	initial concentrations of 0.4 and 0.6 mgL ⁻¹).	
Figure 8.13	Contour plot of coefficient of determination for the dependence of	232
	the uptake of SMX in binary mixtures at various equilibrium	
	concentrations and pore sizes.	
Figure 8.14	Contour plot of the coefficient of determination for the dependence	233
	of the uptake of MNZ in binary mixtures at various equilibrium	
	concentrations and pore sizes.	
Figure 8.15	Comparison between the experimental and the predicted molar	234
	uptakes by the NC adsorption model for the adsorption of MNZ	
	and SMX from equimolar (1:1) binary solutions for ACF-KOH and	
	ACF-240-CR and ACF-120-CR samples, ACF-30-D sample (inset).	
Figure 8.16	Comparison between the experimental and the predicted molar	236
	uptakes by the Langmuir Multicomponent adsorption model for the	
	adsorption of MNZ and SMX from equimolar (1:1) binary mixtures	
	for ACF-KOH and ACF-240-CR samples.	
Figure 8.17	Comparison between the experimental and the predicted molar	237
	uptakes by the Langmuir Multicomponent adsorption model for the	
	adsorption of MNZ and SMX from equimolar (1:1) binary mixtures	
	for ACF-120-CR and ACF-30-D samples.	
Figure 8.18	Comparison between the experimental and the predicted molar	239
	uptakes by the (MLM\delta) adsorption model for the adsorption of	
	MNZ and SMX from equimolar (1:1) binary mixtures for ACF-	
	KOH and ACF-240-CR samples, ACF-120-CR and ACF-30-D	
	(inset).	
Figure 8.19	Comparison between the experimental and the predicted molar	241
	uptakes by the ELM adsorption model for the adsorption of MNZ	
	and SMX from equimolar (1:1) binary mixtures for sample ACF-	
	30-D.	
Figure 8.20	Comparison between the experimental and the predicted molar	244
	uptakes by the MLM ₁ adsorption model for the adsorption of MNZ	

	and SMX from equimolar (1:1) binary mixtures for ACF-KOH,	
	ACF-240-CR and ACF-120-CR samples, ACF-30-D sample	
	(inset).	
Figure 8.21	Evolution of the SMX and MNZ uptake in the presence of various	247
	concentrations of sodium chloride.	
Figure 8.22	Evolution of the SMX adsorption capacity with the solution pH	248
	variation in equimolar (1:1) binary mixtures at different initial	
	concentrations.	
Figure 8.23	Evolution of the MNZ adsorption capacity with the solution pH	248
	variation in equimolar (1:1) binary mixtures at different initial	
	concentrations.	
Figure 8.24	Comparison of the SMX adsorption capacity onto sample ACF-30-	250
	D under different conditions: monocomponent solution and binary	
	mixtures SMX:MNZ at various molar ratios. Uptakes are	
	normalised towards the adsorption capacity in the monocomponent	
	solution.	
Figure 8.25	Comparison of the MNZ adsorption capacity onto sample ACF-30-	250
	D under different conditions: monocomponent solution and binary	
	mixtures SMX:MNZ at various molar ratios. Uptakes are	
	normalised towards the adsorption capacity in the monocomponent	
	solution.	
Figure 8.26	Comparison between the experimental and the predicted molar	251
	uptakes by the ELM and MLM $\!\eta$ adsorption models, NC, LM-s, and	
	$MLM\delta$ inset, for the adsorption of MNZ and SMX from binary	
	solutions (1:1.5 SMX:MNZ molar ratio) for ACF-30-D sample.	
Figure 8.27	Comparison between the experimental and the predicted molar	253
	uptakes by the ELM and MLM $\!\eta$ adsorption models, NC, LM-s, and	
	$MLM\delta$ inset, for the adsorption of MNZ and SMX from binary	
	solutions (1.5:1 SMX:MNZ molar ratio) for ACF-30-D sample.	
Figure 8.28	Comparison between the experimental and the predicted molar	255
	uptakes by the ELM and MLMn adsorption models for the	

	adsorption of MNZ and SMX from binary solutions (1:2	
	SMX:MNZ molar ratio) for ACF-30-D sample.	
Figure 8.29	Comparison between the experimental and the predicted molar	255
	uptakes by the LM-s, and MLMo adsorption models for the	
	adsorption of MNZ and SMX from binary solutions (1:2	
	SMX:MNZ molar ratio) for ACF-30-D sample.	
Figure 8.30	Comparison between the experimental and the predicted molar	257
	uptakes by the MLMη and MLMδ adsorption models for the	
	adsorption of MNZ and SMX from binary solutions (2:1	
	SMX:MNZ molar ratio) for ACF-30-D sample.	
Figure 8.31	Comparison between the experimental and the predicted molar	257
	uptakes by the NC and LM-s adsorption models for the adsorption	
	of MNZ and SMX from binary solutions (2:1 SMX:MNZ molar	
	ratio) for ACF-30-D sample.	
Figure 8.32	%D between the experimental adsorption uptake and the model's	259
	prediction for every working condition when using ACF-30-D as	
	adsorbent.	
Annex I		
Figure AI.1	Carbon dioxide adsorption/desorption isotherms at 0 °C of samples.	271
Figure AI.3	Pore size distribution of samples.	271
Figure AI.4a	Infrared spectrum of ACF-KOH sample.	272
Figure AI.4b	Infrared spectrum of ACF-240-CR sample.	273
Figure AI.4c	Infrared spectrum of ACF-120-CR sample.	273
Figure AI.4d	Infrared spectrum of ACF-60-CR sample.	274
Figure AI.4e	Infrared spectrum of ACF-30-CR sample.	274
Figure AL4f	Infrared spectrum of ACF-30-D sample.	275

A Absorbance (a.u.)

AC Active Carbon

ACF Activated Carbon Fibre

AMP Acetaminophen

AMPA Aminomethylphosphonic acid

API Active pharmaceutical ingredients

BET Brunauer-Emmet-Teller model

 $C(\lambda)$ Wavelength-dependent pre-factor

CAF Banco de Desarrollo de América Latina y el Caribe

CARU Comisión Administradora del Río Uruguay

C_{BET} BET equation parameter related to the energy of monolayer adsorption

Ce The solute equilibrium concentration (mmolL-1)

CF Carbon Fibre

CIC Comité Intergubernamental Coordinador de los Países de la Cuenca del Plata

CMF Ceramic membrane filter
CMS Carbon molecular sieves
COD Chemical oxygen demand

CODIA Conferencia de Directores Iberoamericanos de Agua

d₀₀₂ Average interlayer spacing

D_e¹ Effective diffusion coefficient (cm²min⁻¹)

DFT Density Functional Theory
DOC Dissolved organic carbon
DR Dubinin - Radushkevich

Ds Intraparticle diffusion coefficient
DSC Differential scanning calorimetry

Ea Activation Energy (kJmol⁻¹)

EA Elemental Analysis

EC European Commission

EDA Electron donor-acceptor

EDLC Electric double layer capacitor
EEA European Environment Agency

EF Electro-flocculation

EGA Evolved gas analysis

ELM Extended Langmuir Multicomponent adsorption model

EP Emerging Pollutants

EPA Environmental Protection Agency (USA)

F Fractional approach for the ID model

FD Film Diffusion kinetic model

FTIR Fourier Transform Infrared Spectroscopy

FWHM Full width at half-maximum

G Gibbs energy (kJmol⁻¹)
GAC Granular Active Carbon

HM High modulus

HPLC High-performance liquid chromatography

HSDM Homogeneous Solid Diffusion Model

HTS High-tensile-strength

ICTAC International Confederation for Thermal Analysis and Calorimetry

ID Intraparticle Diffusion model

 I_D Intensity of the disordered Raman band I_G Intensity of the graphitic Raman band

IHP Inner Helmholtz plane
IM Intermediate modulus

IS Ionic strength

IUPAC International Union of Pure and Applied Chemistry

IWTO International Wool Textile Organisation

k The rate constant of adsorption for the ID model (min⁻¹)

K' Adsorption equilibrium constant for the FD model

K_F Freundlich equilibrium constant (molL⁻¹)

K_f Mass transfer coefficient

K_{int} Intraparticle diffusion constant

K_L Langmuir Equilibrium constant (Lmmol-1)

L Accessible pore width (nm)
La Crystalline surface size (nm)

Lc Apparent crystallite thickness (nm)

LDF Linear Driving Force

LM Langmuir Multicomponent model

LM-d Langmuir Multicomponent Model with different adsorption capacities in

single component solutions

LM-s Langmuir Multicomponent Model with similar adsorption capacities in

single component solutions

m/m Mass percentage (%)

MB Methylene Blue

MLM δ Modified Langmuir Multicomponent model with discount factor δ

MLM η Modified Langmuir Multicomponent model with Interaction Factor (η)

MNZ Metronidazole

MW Molecular weight (gmol⁻¹)

n Freundlich exponent

NC Non-competitive model

OEA Organización de Estados Americanos

OHP Outer Helmholtz plane

OSE Obras Sanitarias del Estado

p/po Partial pressure
Pa Pascal (Nm⁻²)

PAC Powdered Active carbon

PAN Polyacrylonitrile

PFAS Per- and poly-fluoroalkyl substances

PFO Pseudo First Order kinetic model

PhAC Pharmaceutical Active Compounds

PhC Pharmaceutical Compounds

 pH_{pzc} pH at the point of zero charge

p_{Ka} Acid dissociation constant

po Solid saturation pressure

PSO Pseudo Second Order kinetic model

PT Potentiometric titration

q Quantity of adsorbate adsorbed per carbon mass unit (mmolg⁻¹)

Q Net charge concentration (molg⁻¹)

QDF Quadratic Driving Force

qe Quantity of adsorbate adsorbed at the equilibrium per carbon mass unit

(mmolg⁻¹)

qm Maximum adsorption capacity for the adsorbent to adsorb the working

adsorbate (mmolg-1)

qt Quantity of adsorbate adsorbed per carbon mass unit at a determined time

(mmolg⁻¹)

R Total particle radius fir ID model

R¹ Diffusion constant of the liquid film (min⁻¹)

Raman peak areas ratio

r_o Adsorbent particle radius (cm)

 R_p , $_{ID/IG}$ Raman peak intensities ratio S_{BET} Specific surface area (m^2g^{-1})

SDG Sustainable Development Goals

SDG12 Sustainable Development Goals - Sustainable Consumption and Production

SDG6 Sustainable Development Goals - Clean water and sanitation

SEM Scanning electronic microscopy

SF Stabilised Fibres
Smi Surface area (m²g⁻¹)
SMX Sulfamethoxazole

S_o Particle surface area of the solid per volume unity

SOL Solubility (mgmL⁻¹)

SUL Secretariado Uruguayo de la Lana

TG Thermogravimetry

TGA Thermogravimetric Analysis
THF Tubular horizontal furnace

TPD Thermal Programmed Desorption

TPD-MS Thermal Programmed Desorption coupled with Mass Spectroscopy

TT Tylosin tartrate
UHM Ultrahigh modulus
UN United Nations

UN Water United Nations Water

UNESCO Organización de las Naciones Unidas para la Educación, la Ciencia y la

Cultura

UV Ultraviolet

VTP $_{(0.97 \text{ p/p0})}$ Total pore volume at 0.97 (p/po) (cm³g⁻¹)

W Volume (cm³g⁻¹)

w/w weight ratio
WF Wool Fibres

WHO World Health Organization

WISE Water Information System for Europe Freshwater

Wo Total micropore volume (cm³g⁻¹)

wt.% Weight percentage (%)

WWTP Waste Water Treatment Plants

XRD X-ray Diffraction YM Young's modulus

zi Ionic charge of the electrolyte

α Carbon conversion degree

β Affinity factor adsorbate-adsorbent in the Dubinin – Radushkevich equation

 ΔH Enthalpy variation (kJmol⁻¹)

 Δr_o Film thickness (cm) η Interaction Factor θ Bragg angle (°)

 λ Wavelength of the radiation (cm⁻¹) Extent of the activation reaction

% D Percentage deviation (%)

2D-NLDFT-HS Non-local density functional theory

2θ XRD incident radiation angle



"La biblioteca se defiende sola, insondable como la verdad que en ella habita, engañosa como la mentira que custodia."

El nombre de la Rosa

Humberto Eco

"Water is the source of life"

Even though this statement can be considered the utmost truth, it is also true that water is the perfect medium to transfer pathogens and any pollutants quickly. Circa 4000 – 2000 B.C., several methods were already used to improve water quality, like boiling, keeping the liquid under the sun, filtering through sand or wood charcoal, and storing the water inside copper containers. The main interest of these treatments was to improve organoleptic characteristics, but the relationship between human health and water safety was not yet established. It was not until several thousand years later that the connection was set. The unprecedented levels and rates of urban growth coupled with our current model of consumer society triggered a massive need for a clean water supply. That fact, along with the indiscriminate utilisation of water sources, has caused their scarcity, and the few that still exist are contaminated.

For this reason, academia is constantly working with the industry to improve the cleaning water processes that ensure quality. However, developing new materials and technologies for water treatment can be considered a never-ending field, which is, in fact, always located several steps behind compared to the incidence of the appearance of novel contaminants.

The United Nations (UN), during the 108th General Assembly on 28 July 2010, adopted the resolution 64/292 (and subsequent modifications): *The human right to water and sanitation*. The document expresses deep dismay that approximately 884 million people lack access to safe drinking water. More than 2.6 billion do not have access to basic sanitation, and outrageously, about 1.5 million children under five years of age die, and 443 million school days are lost each year due to water- and sanitation-related diseases. The document specifies, among other points:

- 1. Recognizes the right to safe and clean drinking water and sanitation as a human right that is essential for the full enjoyment of life and all human rights;
- Calls upon States and international organisations to provide financial resources, capacity-building, and technology transfer through international assistance and cooperation, in particular to developing countries, to scale up efforts to provide safe, clean, accessible, and affordable drinking water and sanitation for all (United Nations 2010).

1.1 Contamination of water resources an actual concern

Water is a scarce natural resource, essential for life in all its expressions, for the existence of ecosystems and the biodiversity associated, and for human activities; its accessibility has become a genuine concern nowadays. From the Industrial Revolution onward, society has suffered exponential development and growth, and these events caused rapid and alarming degradation of water quality.

Global water use has increased by six over the past 100 years. It grows steadily at about 1% per year due to increasing population, economic development, and shifting consumption patterns (UNESCO and UN-Water 2020). The average use of water at a global scale is not equally distributed. Agriculture currently accounts for 69% of global water withdrawals, mainly used for irrigation but also includes water used for livestock and aquaculture. This ratio can reach up to 95% in some developing countries. Industry (including energy and power generation) accounts for 19%, while municipalities are responsible for the remaining 12% (Schmidt 2019).

Furthermore, water distribution on the Earth's surface is highly uneven. Only 3% of the water on the surface is fresh (Figure 1.1); the remaining 97% resides in the ocean. Of freshwater, 69% resides in glaciers, 30% underground, and less than 1% is in lakes, rivers, and swamps. In other words, only one per cent of the water on the Earth's surface is usable by humans, and 99% of the usable quantity is underground (Bralower and Bice, n.d.).

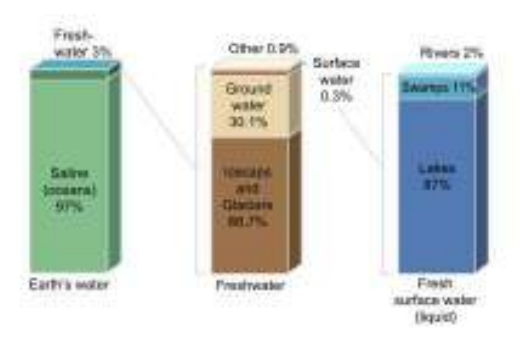


Figure. 1.1 Water distribution on Earth (credit: Timothy Bralower © *Penn State University is licensed under CC BY-NC-SA 4.0*)

Moreover, water pollution increases throughout the water cycle (Figure 1.2). This increment in water pollution has many actors involved, helped by inefficient wastewater treatments. If this trend continues without adequate control measures and reuse policies,

it is expected that by 2050, more than 40 % of the worldwide population will live under hydric stress; this last is measured as water use as a function of available supply (Schmidt 2019). An annual baseline of water stress is established (Figure 1.3); under this categorisation, most of the South American region is under low stress, with specific zones under arid and high water stress. Baseline water stress measures the ratio of total water withdrawals to available renewable water supplies. Water withdrawals include domestic, industrial, irrigation, and livestock consumptive and non-consumptive uses. Available renewable water supplies include surface and groundwater supplies and consider the impact of upstream consumptive water users and large dams on downstream water availability. Higher values indicate more competition among users (Schmidt 2019).

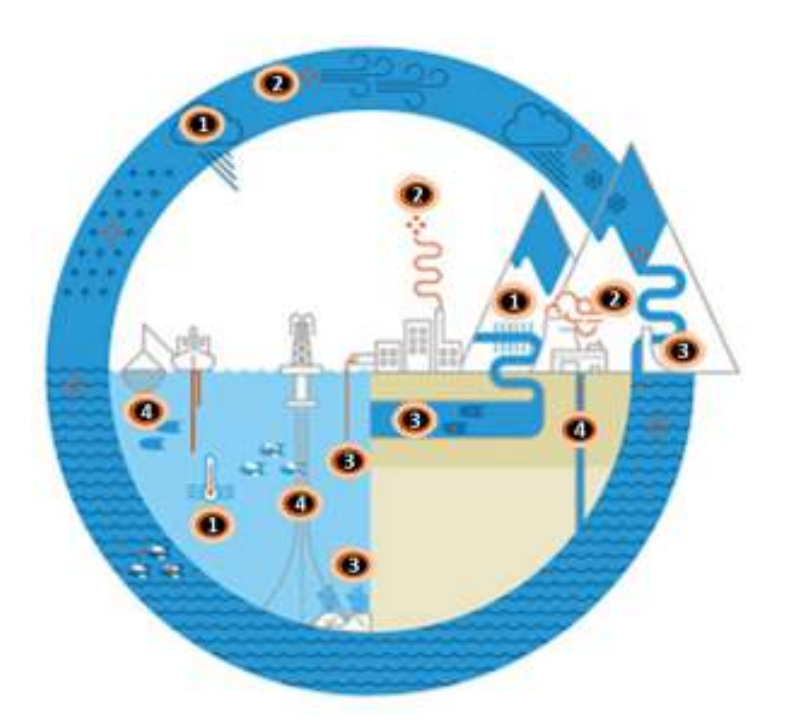


Figure 1.2 Water cycle, main issues affecting water quality and quantity, from European Environment Agency 2018 (EEA), 1- Climate change, 2- Pollution, 3- Physical alteration, and 4- over-exploitation.

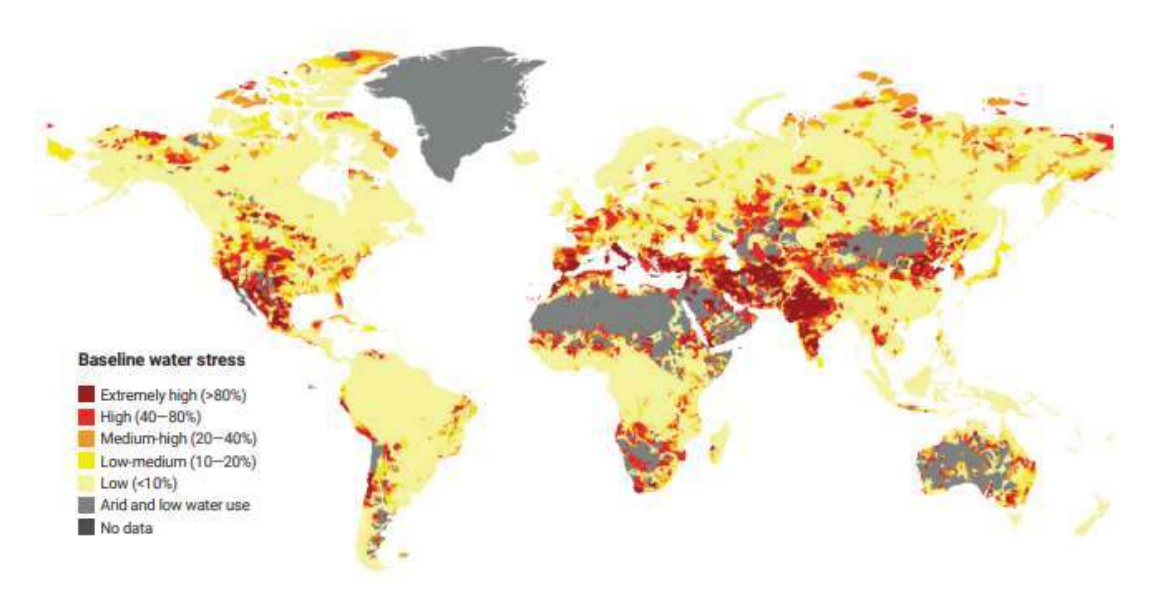


Figure 1.3 Annual baseline water stress (Schmidt 2019).

In a worldwide effort to reverse the trend, all the United Nations (UN) states in 2015 were part of the 2030 Agenda for Sustainable Development, which set out a 15-year plan to achieve 17 Sustainable Development Goals (SDG). Among these goals, SDG6 (Figure 1.4) refers to Clean Water and Sanitation: by 2030, universal and equitable access

to safe and affordable drinking water for all (UN-A/RES/70/1 2016).

Within Uruguay's borders, the law regarding water quality is governed by the 253/79 decree (Decreto Nro. 253/979 1979) and the Digest of Quality by the binational Commission: Comisión Administradora del Río Uruguay (caru.org.uy).

Regarding the Guaraní Aquifer, a Mercosur document was drafted that establishes the necessity of



Figure 1.4 UN symbol for the Sustainable Development Goal 12.

controlling and protecting this water reservoir, ratified by all the member countries (Mercosur 2010). Interestingly, despite the previous laws, the Plan Nacional de Aguas (National Water Plan) has existed in Uruguay since 2016, which contemplates several aspects regarding current and future consumption needs and water quality (Decreto Nro.205/017 2017).

1.2 The presence of Pharmaceutical compounds in the aquatic environment

In recent years, the incidence of drugs in aquatic environments has increased alarmingly. Improvement in detection analysis has made it possible to detect potentially dangerous drugs that, until now, went unnoticed. These microcontaminants are known as Pharmaceutical Active Compounds (PhAC), and their emerging interest is due to their potential adverse impact on ecosystems. Multiple types of drugs can be found within the former classification, such as antibiotics, synthetic hormones, analgesics, and antiinflammatories, as well as several metabolites and transformation products (Sabater et al. 2008). Since PhACs are prescribed to treat different types of illnesses, they are therefore designed with the capacity to cause biological effects (Comerton et al. 2009). Consequently, they pose traits of genotoxicity and endocrine disruption (Evgenidou et al. 2015) in addition to physicochemical properties similar to those of xenobiotic substances, which have a natural tendency to accumulate in the lipids of organisms (Halling-Sorensen et al. 1998). Unfortunately, these emerging pollutants (EP) can remain throughout wastewater treatments, and since these treated fluent are discharged into water bodies, they can easily be found in receiving surface waters. They do not necessarily need to be persistent to cause adverse effects; in some cases, the massive consumption, such as painkillers, is enough to trigger the damage.

In this regard, a recent study englobes a global-scale assessment of API (Active Pharmaceutical Ingredients) in 258 rivers around the globe, depicting the environmental influence of 471.4 million people across 137 geographic regions. The samples were collected from 1,052 locations in 104 countries (Figure 1.5). This work involves several researchers and institutions, where two nationals participated on behalf of Uruguay, Dr. Horacio Heinzen from the Faculty of Chemistry and Dr. Andrés Pérez-Parada from North Regional, both from Udelar (Universidad de la República) (Wilkinson et al. 2022). The results of this survey established that the most contaminated sites were in low- to middle-income countries and were associated with areas with poor wastewater and waste management infrastructure and pharmaceutical manufacturing. The most frequently detected APIs were carbamazepine, metformin, and caffeine (a compound also arising from lifestyle use), recorded at over half of the sites monitored. Concentrations of at least one API at 25.7% of the sampling sites were higher than concentrations considered safe for aquatic organisms or which are of concern in terms of selection for antimicrobial resistance. At the same time, the highest mean cumulative concentration of API was

observed in Lahore, Pakistan, at 70.8 μgL⁻¹, with one sampling site reaching a maximum cumulative concentration of 189 µgL⁻¹. Followed by La Paz, Bolivia (68.9 µgL⁻¹mean, 297 μgL⁻¹maximum) and Addis Ababa, Ethiopia (51.3 μgL⁻¹ mean, 74.2 μgL⁻¹maximum). The most polluted sampling site was in the Rio Seke (La Paz, Bolivia), with a cumulative API concentration of 297 µgL⁻¹. This sampling site was associated with untreated sewage discharge and rubbish disposal along the river's bank. Four APIs were detected across all continents, all of them over-the-counter APIs: caffeine (stimulant), nicotine (stimulant), acetaminophen/paracetamol (analgesic), and cotinine (a stimulant metabolite). Additionally, 14 APIs were detected in all continents except Antarctica: atenolol (βcarbamazepine (antiepileptic), cetirizine (antihistamine), blocker), citalopram desvenlafaxine (antidepressant). (antidepressant). fexofenadine (antihistamine). gabapentin (anticonvulsant), lidocaine (anesthetic), metformin (antihyperglycemic), (anti-inflammatory), (antihyperglycemic), naproxen sitagliptin temazepam (benzodiazepine for insomnia treatment), trimethoprim (antimicrobial), and venlafaxine (antidepressant).

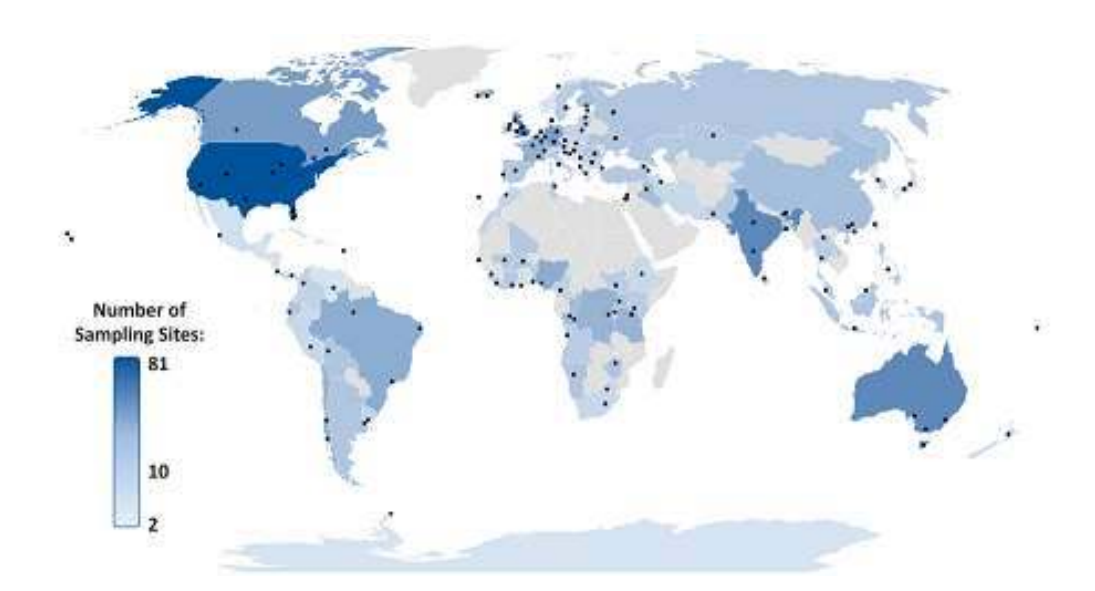


Figure 1.5 Locations of studied rivers/catchments for the global assessment. Points indicate groups of sampling sites across respective river catchments and countries, which are shaded based on the total number of sampling sites (Wilkinson et al., 2022).

One of the aspects to highlight of this work is that all the nations that participated in this experiment entailed the first monitoring for 36 of them, including Uruguay. The

plot below shows the overall situation, where the cumulative concentration is classified by percentiles (Figure 1.6); unfortunately, Montevideo is among those at the highest percentile (eleventh position starting from the left). The contaminants with the highest concentrations were paracetamol, caffeine, metformin, fexofenadine, sulfamethoxazole (antimicrobial), metronidazole (antimicrobial), and gabapentin. Analgesic, antibiotic, and anticonvulsant classes showed the most significant global concentration range. The relative affordability and differences in regulatory oversight likely contribute to the largest API concentrations the study found for some substances. The income differences also play an essential role in the API distribution, where the highest concentrations were found at lower-middle income (World Bank income classification). The explanation for this, although speculative, is that these countries have low connectivity to wastewater infrastructure (UNESCO and UN-Water 2020) while also tending to have improved access to larger numbers of medicines relative to low-income countries with lower healthcare expenditures (Ewen et al. 2017).

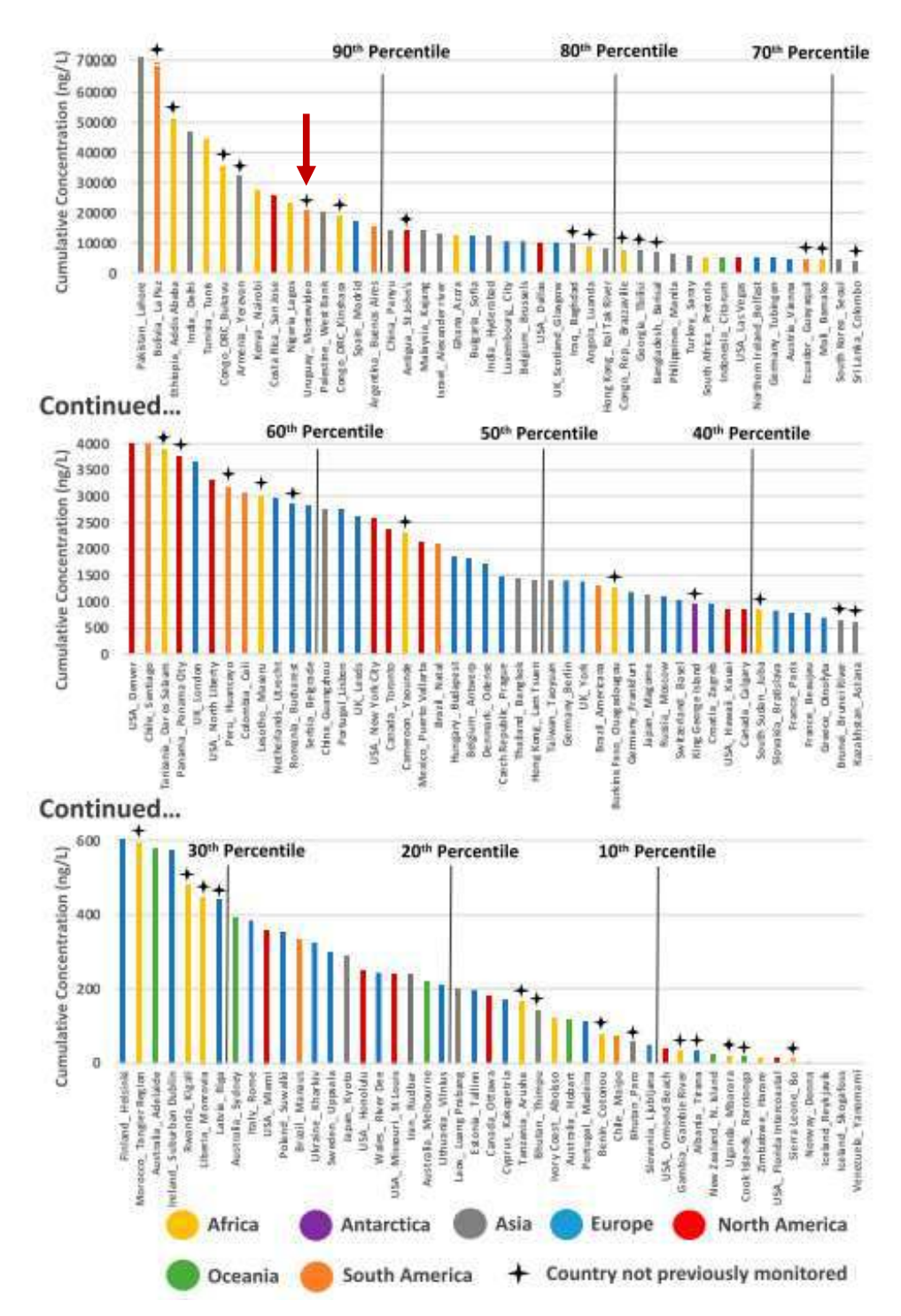


Figure 1.6 Cumulative API concentrations quantified across 137 studied river catchments organised by descending cumulative concentration (ngL⁻¹). Black lines mark percentiles. The cumulative concentrations reported here are calculated as the average sum

concentration of all quantifiable API residues at each sampling site within respective river catchments (Wilkinson et al. 2022).

In recent years, due to the information mentioned earlier, several organisations have started to control and regulate the quantities of chemical substances present in water bodies that do not represent a risk to natural life and human beings.

In this sense, the World Health Organization (WHO) has established water quality as a critical research field since the accessibility to drinking water has been declared as one of the fundamental human rights. Several agencies worldwide have been working to reverse and prevent the incidence of these EP's, like the Environmental Protection Agency (EPA) from the United States. This agency continuously updates the list of drugs and the methods available for detection. Also, the European Environment Agency (EEA) works under their Water Information System for Europe Freshwater (WISE freshwater) program to improve water quality.

In 2022, the European Commission (EC) adopted a proposal to revise the list of priority substances in surface water (COD 2022/0344 2022), proposing to add 24 substances as well as a standard for total pesticides. The proposal stated that the listed substances pose well-documented risks to nature and human health. The list includes PFAS - a large group of "forever chemicals" used in cookware, clothing and furniture, fire-fighting foams, and personal care products; a range of pesticides; bisphenol A, a plasticiser and a component of plastic packaging; and several pharmaceuticals used as painkillers, anticonvulsants or antibiotics. The latest European Watch List dated August 2020, where several substances are considered a risk to human health (Decision 2020/1161/E.U. 2020).

Our region does not have an organism that englobes all the countries under the same law regarding water course contamination, much less control over the presence of pharmaceutical substances in water. However, there is a conscience regarding the problem. For that reason, we can find forums like CODIA (Conferencia de Directores Iberoamericanos de Agua), where those responsible for water policies for each country share their experiences. The OEA (Organización de Estados Americanos) organisation, along with CAF (Banco de Desarrollo de América Latina) and CIC (Tratado de la cuenca del Plata 1969) had launched a program under the project CIC-OEA-CAF/GEF. This project aims to prepare the field to implement an actionable strategic plan. Five countries participated in this initiative: Argentina, Bolivia, Brazil, Paraguay, and Uruguay.

However, this enterprise still does not consider the feasible presence of PhAC in water, although it is worried about preserving its bio-systems and overall quality since there is neither presence recognition nor a law framework to handle it.

Summarising, the existence of PhAC in water courses is a well-documented fact that cannot be ignored. The latter, along with the fact that wastewater treatments are not as effective as they should be (Evgenidou et al. 2015), allows the presence of dangerous substances that could eventually end up in our glass of water. The growing concern about this led to the construction of watch lists and guides to analyse and control its presence; however, these are separate local initiatives, disregarding that water is connected all over the globe and should be treated as one unit regardless.

1.3 Situation in Uruguay

Uruguay is not oblivious to the mentioned situation; the study showed that our case is compromised since we are at the highest percentile regarding the cumulative concentration of substances (Figure 1.5). The quantities found are distributed among several groups of substances (Table 1.1).

Table 1.1 Concentrations of PhAC found at Río de la Plata river in the Montevideo region, separated by therapeutic class (Wilkinson et al. 2022).

Substance	Total pharmaceutical concentrations by therapeutic class (ngL ⁻¹)
Analgesics	4920
Antibiotics	741
Anticonvulsants	654
Antidepressants	121
Antihyperglycemic	7650
Antihistamines	190
β-blockers	220
Stimulants	7960
Other	373

Comparing the records for the same river but at a different sampling site (Buenos Aires), it is remarkable that the Uruguayan coast recorded higher figures for most of the substances (Figure 1.7). Although speculative, these figures could be an effect of the currents and not what each city dumps into the river. However, independently of the origin, the fact is that this river needs action to reverse this tendency. Notwithstanding that, it is the same river, and the difference in population between these two cities is remarkable; the contamination is higher on the Uruguayan coast.

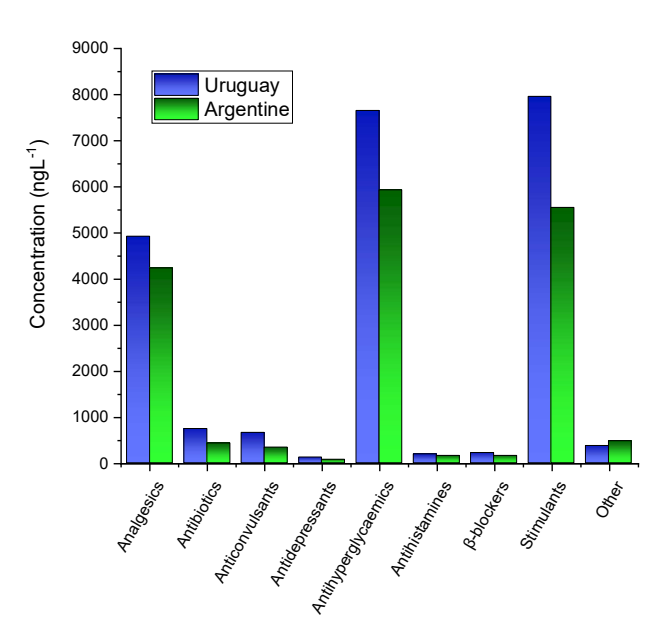


Figure 1.7 Concentrations of PhAC found at Río de la Plata River, in Montevideo and Buenos Aires's regions, separated by therapeutic class. Comparison between coasts.

An interesting work to mention studied the incidence of PhAC contamination in three important species of edible fish (*Megaleporinus obtusidens*, *Salminus brasiliensis*, and *Prochilodus lineatus*) from the Uruguay River. This work was a collaboration among several institutions from Argentina, Spain, and Uruguay, where the muscle accumulation of 17 PhAC was investigated. Fish were sampled in fall and spring from 8 localities distributed along 500 Km of the Uruguay River. The study established that the concentrations found in the muscle evidenced that fish are exposed to PhAC at different levels depending on the compound. Atenolol and carbamazepine were the most frequently detected PhAC (>50 %), but at concentrations consistently below 1 µg/kg wet weight

(w/w). Hydrochlorothiazide, metoprolol, venlafaxine, propranolol, codeine, and the carbamazepine metabolite, 2-hydroxy carbamazepine, were accumulated at higher levels, showing maximum concentrations between 1 and 10 μ g/kg (w/w), but infrequently (<50 %). The other PhACs were consistently below 1 μ g/kg (w/w) and at frequencies lower than 50 % (Rojo et al. 2019). Although this work concluded that the concentrations found did not pose a risk for human consumption, they were identified as a potential risk, which is why it is a call to action.

We have the already mentioned Plan Nacional de Aguas (Water National Plan) at a national level. This ambitious plan contemplates many aspects related to the quality and care of water sources, including groundwater. Among other actions, the program establishes the need to assess the presence of agrochemicals but not human PhAC. Moreover, the document reported that the norm that applies today needs to be actualised but refers to agrochemicals. Not only that, but also recorded positive results for the presence of AMPA (primary metabolite of glyphosate, aminomethylphosphonic acid), atrazine, and glyphosate, all with values under the standard according to the report (but with the allowed standard figures not informed) (Decreto Nro.205/017 2017). Also, the Plan Ambiental de Desarrollo Sostenible (Environmental Plan for Sustainable Development) in their Objective 1.3, establishes guidelines to preserve water quality, conserve continental aquatic ecosystems, and maintain hydrological processes, through models of sustainable management of basins and aquifers (Decreto Nro.222/019 2019). In addition, prioritising actions in the drinking water supply basins were set: Santa Lucía, Laguna Del Sauce, and Laguna Del Cisne, whereas The Río Negro and San Salvador basins were also prioritised on potentially impactful activities.

Different initiatives are working towards better managing this natural resource, aiming to reach the 2030 global goals. Essentially, Uruguay already accuses the presence of PhACs in their water courses, which can become a potential risk for its quality. Although the national plans implemented so far do not specifically recognise the presence of this type of contaminant, the existence of international reports stating this fact is a good starting point from which to work.

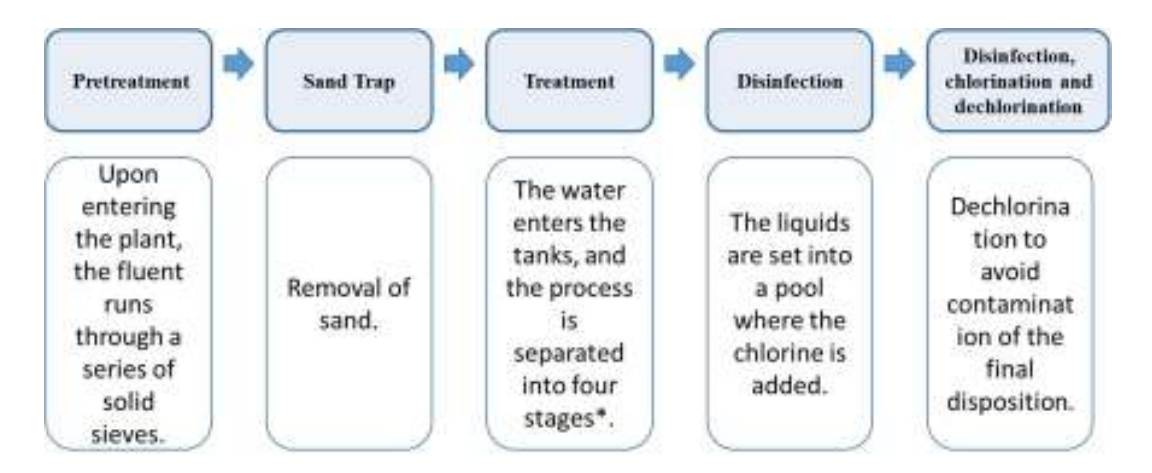
1.4 Methods of Remediation

The presence of PhAC in sewage is unavoidable since the organism cannot wholly assimilate a wide variety of substances, excreting the remnants. Therefore, this is a global

problem regardless of the development degree of the country in question since, up until now, the technology of Waste Water Treatment Plants (WWTP) has failed to remove the PhAC that comes into the sewage effectively (Yang et al. 2022; Kim et al. 2020; Couto et al. 2019). This lack of effectiveness of the WWTP to remove the PhAC contributes to the subsequent increase in the latter's concentration in water courses, inducing an increment of drug-resistant pathogens and endangering the environment (Jo et al. 2021). Hence, developing efficient technologies to remove or degrade these pollutants from wastewater and, eventually, from water bodies is essential.

Different types of Waste Water Treatment Plants (WWTP) exist depending on the nature of the contaminants present in the fluent -household sewage differs from that of the industry; however, they all share a typical treatment layout. Generally, the process is composed of a first stage of physical separation where different sieves are used to retain the solid particles; then, the fluent is subjected to treatments that differ depending on the WWTP technology to be finally disinfected.

In Uruguay, the agency in charge of the sewage treatment is Obras Sanitarias del Estado (State Sanitation Work Office, OSE), with 46 treatment plants around the territory where the sewage undergoes a five-step treatment (Figure 1.8).



*Stages: Gas: is burned; Foam: goes back to the pretreatment; Liquids: the conditions inside the reactor favour the regeneration of bacteria population that consumes the organic matter, improving the liquid quality; Sludge: they are dehydrated in a centrifuge and go to final disposal, the dehydration water go back to pretreatment.

Figure 1.8 Schematic layout of the five steps involved in the WWTP from O.S.E. (http://www.ose.com.uy/saneamiento/tratamientos).

The process follows this sequence: Pretreatment, Primary treatment, Secondary treatment, Tertiary treatment, Sludge treatment, and fluent Final disposition.

- Pretreatment: It consists of physical processes for removing coarse solids, sand, and grease (roughing, grit removal, degreasing, in that order) so that it does not affect and facilitate the other purification processes so that the pretreatment units will be the first to the treatment scheme.
- Primary treatment: Its purpose is to remove suspended and floating matter. The
 most common system is a settler equipped with a bottom sweeper and a surface
 sweeper. These units do not remove colloidal suspensions or dissolved solids.
 Primary sedimentation does not always occur in a treatment plant, depending on
 the characteristics of the liquid and the type of secondary treatment applied.
 Assisted primary treatment: some systems can be helped by dosing chemical
 products to promote sedimentation.
- Secondary treatment: The main objective is to reduce the concentration of organic matter. Usually, biological oxidation process treatments are used for domestic liquids. There are a wide variety of processes. The most common is Trickling filters, Activated sludge: conventional or extended aeration, Lagoons: aerated, facultative, Anaerobic Reactors, and Oxidation Ditches.
- Tertiary treatment: It is the treatment that allows the removal of nutrients such as phosphorus and nitrogen. In the case of phosphorus, this process is usually carried out by chemical precipitation and settling. At the same time, nitrogen is generally removed through biological processes (nitrification/denitrification), a sequence of aerobic and anoxic reactors. On the other hand, the disinfection process is also known as tertiary treatment, and among the currently used are UV disinfection, chlorination, dechlorination, and maturation lagoons.
- Sludge treatment: Some sludge generated in secondary treatments, such as activated sludge with extended aeration, only requires one dewatering stage. Otherwise, digesters stabilise them (an anaerobic biological process), and pilot experiences of vermicomposting are carried out in some localities. Vermicomposting is an organic matter bio-oxidation and stabilisation process mediated by the combined action of earthworms and microorganisms, from which a stabilised final product with compost characteristics is obtained. Once treated, the sludge goes to its final disposal.

 Final disposition: According to environmental regulations, the treated fluent leaves the WWTP through discharges towards receiving bodies. (http://www.ose.com.uy/saneamiento/tratamientos).

From the previous description, there is no need to remark that the process does not contemplate a step specifically designed to treat PhAC. This fact is practically the norm worldwide since this is a relatively recent problem. Moreover, the presence of PhAC has proved to be persistent in water bodies, and they can remain even after being treated in WWTP; this establishes the need to apply different tertiary techniques aiming to prevent this from happening. Not only that, but also, because of the complexity and variety of substances present in the aquatic media, a simple treatment that manages to eradicate all types of functional groups does not exist. Therefore, depending on the drug's nature, specific stand-alone techniques can remove the substance or, in some cases, in combination with others. The remediation methods can be classified as biological, applied for sludge and wastewater treatment, and physicochemical (ozonation, nanofiltration, advanced oxidation, and adsorption) for wastewater and surface water treatments.

Works regarding different methods applied to different types of drugs, sometimes even working with a combination of techniques, can be found in the literature. For instance, in a recent study, the researchers combined electro-flocculation (EF) and catalytic ozonation (CO) in combination with the novel catalyst Ni-Co-Zeolite 5A° followed by ceramic membrane filtration (CMF). This hybrid process removes veterinary antibiotics in pharmaceutical wastewaters (Enrofloxacin, EFC - and Tylosin tartrate-, TT). The efficiencies reported were 33% and 93 % for EFC and TT, respectively (Masood et al. 2023). Other work based on ozone-driven oxidation of refractory organic matter utilising potassium ferrate to catalyse the reaction was applied in a pharmaceutical factory effluent of a WWTP. To assess the method's efficacy, they analysed the dissolved organic carbon by ultraviolet absorption (UV254) and fluorescent organics. The technique demonstrates an increment of 14.9 % in the DOC removal rate and 29.03 % in the UV254 removal (Wang et al. 2022).

Nanofiltration is another technique that removes substances to treat cancer. A pilot scale study tested this method's effectiveness in removing three anticancer drugs from wastewater effluents by installing a pilot unit with a Desal 5DK membrane at a domestic WWTP; the results confirmed that it is a promising method (Cristóvão et al. 2022).

However, organic matter can foul the membrane surface, affecting its performance. Considering this, another group tested three nanofiltration membranes to remove Triclosan (a personal care product), and another eight selected PhAC (Caffeine, Diazepam, Diclofenac, Ibuprofen, Naproxen, Sulfamethoxazole, and Trimethoprim) and tried to elucidate their dependency on the working conditions. The removal efficiencies of target compounds proved to be primarily dependent on the pH of the media (Garcia-Ivars et al. 2017). An alternative option to remove PhAC is to apply a pretreatment to the wastewater, like heterogeneous Fenton. In this case, the PhAC is pre-oxidized by hydroxyl radical-based advanced oxidation. However, the wastewater characterisation before and after Fenton treatment reveals that Fenton oxidation increases in inorganics. Therefore, an additional treatment step is needed to reduce further the chemical oxygen demand (COD) and inorganics (Scaria et al. 2022). One of the most extended methods is adsorption because of its simplicity and relatively low cost compared with other techniques. Active carbon (AC) is the most widely used adsorbent material. However, several works regarding modified AC can be found to improve the adsorption performance in terms of time and capacities (Couto et al.2019). In this sense, a new magnetic AC was developed and tested in the adsorption of Carbamazepine, Sulfamethoxazole, and Ibuprofen. Nonetheless, according to the Langmuir model, its capacity does not differ so much from that already reported in previous works with AC not functionalised (Pereira et al. 2023).

Although biological treatments at WWTP have been applied for a while, such as anaerobic, anoxic, and aerobic treatments with different configurations, typical municipal WWTPs such as these are not designed to mitigate pharmaceuticals but only for organics and nutrients treatment (Son et al. 2022).

Therefore, despite ongoing efforts to develop efficient systems to remove these hazardous substances from water, science is still in the early stages of solving the problem.

1.5 Why the use of Wool, an ancient and still novel material?

We have been describing the difficulty related to clean and safe water access worldwide and the undeniable presence of PhAC, a problem already knocking at our door. What is hard to see is the connection between this worry and the use of wool.

There is no doubt that along with the water accessibility problem, the final disposition of industrial waste is another issue to be solved and goes hand in hand with the former. The current panorama of global climate change and environmental degradation results from a society based on a linear economy oriented towards producing, consuming, and discarding, and that privileges economic gain over any other factor (social or environmental). This situation creates significant pressure on the environment and natural resources -increasingly scarce and polluted- and makes it urgently necessary to introduce changes toward a circular economic model. This economic model is based on sustainable production and consumption criteria restricting the utilisation of nonrenewable materials and favouring the use, reuse, and recycling of available resources. The 2030 Agenda, mentioned before, is the UN roadmap to achieve a balance between society, environment, economy, and technological development, and it includes responsible consumption and production in one of its sustainable development goals (SDG 12, Figure 1.9). This goal establishes the need to use resources and natural materials efficiently through recycling and reuse activities, reducing the impact of their transformation on the environment (UN-A/RES/70/1 2016). A good practice to achieve

this focuses on transforming agroindustrial waste into high-added-value products, using efficient and environmentally friendly production processes. In this sense, the knowledge and management of local waste become a vital strategy to promote and follow this transition path toward a sustainable society. Hence, the first approach is to detect each country's priority sectors and identify the local opportunities.



Figure 1.9 UN symbol for the Sustainable

In this sense, the sheep sector is one of Uruguay's economic development engines. It is the fifth exporting

country of sheep meat in the world and the third in combed wool, with a wool export market in 2022 of circa 180 million U.S. dollars, slowly recovering from the COVID-19 pandemic (Reporte Exportaciones 2023). In any case, although the figures are not yet those of times before the pandemic, the production of wool waste is high, and its use and recycling into high-value-added products have become a key strategy to promote the country's circular economy.

Wool is a commodity traded globally; the variety of its markets is very large and constantly expanding. It can be found in many sectors: clothing and fashion, sporting

goods, carpets, interior use, aviation, architecture (thermal insulation, humidity regulator), the manufacturing industry, medical use, and protective clothing. However, despite all the positive attributes of wool, its price is falling worldwide. This price decline will likely lead to fewer farmers turning to wool production, which means job losses. For this reason, new and innovative applications of this raw material must be sought (Reporte Exportaciones 2020). Wool fibre is the hairiness covering sheep's body (*Ovis aries*). However, the generalisation of this denomination to other types of animals of the camelid family (Camelidae) is widespread, such as the alpaca, vicuña, guanaco, and llama. Wool fibre structure mainly comprises fibrous proteins.

Fibrous proteins are included in the subgroup of keratins. They are characterised by having a high sulphur content. The keratin macromolecule has a long chain of amino acids, one of the most important of which is cystine. This amino acid defines many chemical and physical wool properties due to the -S-S- disulphide bridges (Figure 1.10) in its structure. These bonds are of great importance for the union of polypeptide chains, being, together with hydrogen bonds, those responsible for fibres's stability. The polypeptide chain has a helical configuration, where the aliphatic and aromatic residues of the keratin side chains, valine, leucine, and phenylalanine, conform to hydrophobic zones due to their non-ionic character (Jones et al. 2009). The cysteine side bridges are not evenly distributed throughout the fibre structure. In the root zones, a part of the cystine residue is reduced. It will later recombine to form disulphide bridges during keratinisation (fibre growth), thereby increasing the chemical attack fibre resistance. Therefore, to modify the structure of wool, the disulphide bond is broken and then regenerated in another position upon oxidation. Once the disulphide bridge is broken, the fibre loses its characteristic shape. The structure can be recomposed using an oxidising agent (Millington et al. 2017).

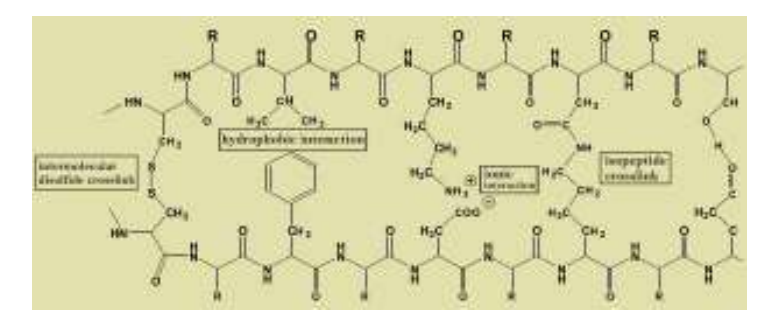


Figure 1.10 Bonds in wool from *The Chemical & Physical Structure of Merino Wool* (CSIRO 2015).

Several classes of wool fibre can be found, which leads to a significant variation in fineness, length, and curl values, depending directly on the breed, food, health, and climate. The apparent diameter of the fibre varies from 16 µm, for the Merino breed up to 40 µm for thicker Rommey Marsh-type wool. The fibre length varies from 7-8 cm for the finest and 70-150 cm or more for the thickest. The physical and chemical structure features of wool fibre give it unique textile material characteristics (for example, the felting capacity). The properties used to set the fibre quality for the international market are diameter, length, resistance, and colour (Elvira 2009). The fibre can be described as a complex biopolymer where different sections can be identified in its structure as follows (Figure 1.11):

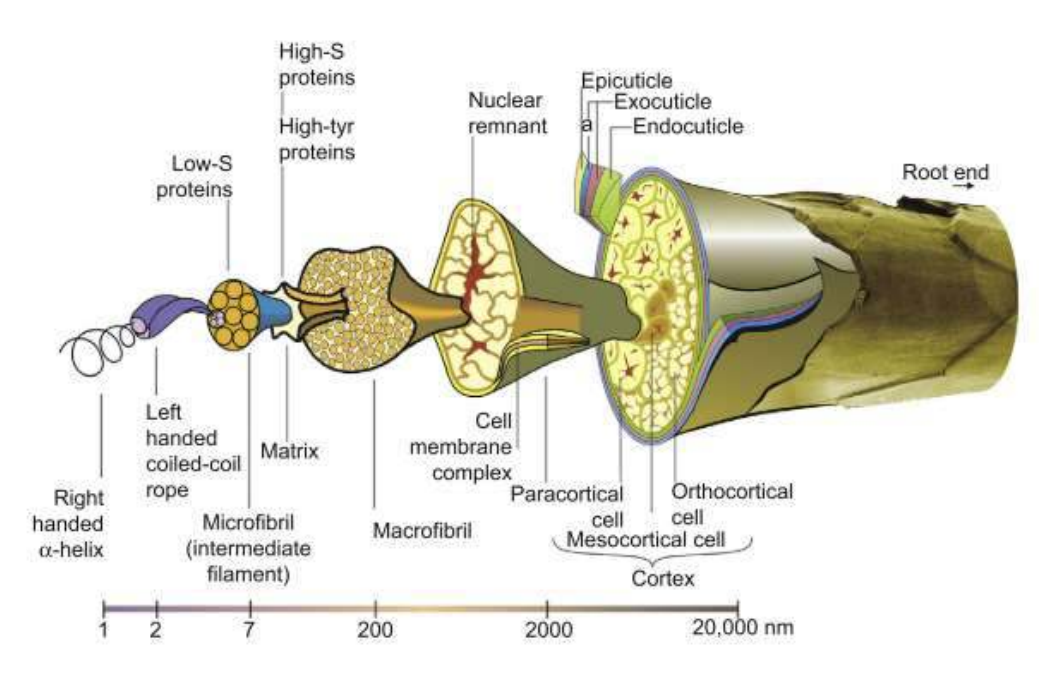


Figure 1.11 Schematic diagram of the structure and morphology of a Merino wool fibre (Source: CSIRO).

The fibre structure has two well-differentiated areas: the medulla (or "cortex"), which constitutes most of the fibre, and an external section called the cuticle (Jones et al. 2009). The cuticle resembles a protective layer of overlapping scales arranged similarly to the bark on a palm tree trunk (Figure 1.9). It represents approximately 10% by weight of the total fibre. Its cells have a thickness corresponding to a normal cell, except where they overlap one another and are oriented towards the end of the fibre. These cells have

a hardness and chemical structure that acts as a protective fibre barrier. In addition, a waxy layer on them prevents liquid water from penetrating the wool fibre; nevertheless, it can quickly absorb water vapour. They are also responsible for "felting," in which the fibres are subjected to friction between them in conditions of controlled humidity, high temperature, and, in some cases, extreme pH. As a result, a fibre of greater thickness and shorter length and width is obtained (Millington et al. 2017).

The medulla (or "cortex") constitutes 90% of the weight of the fibre and comprises two types of cells: the orthocortex and the paracortex. Both parts have different chemical properties. The marrow cells have a "cell membrane complex" that acts as "cement" between them and separates them from the cuticle. The marrow cells are spindle-shaped, generally 95 μ m long and 5 μ m in diameter. Cylindrical microfibrils of high crystallinity form them, 10 μ m long and 0.3 μ m in diameter, packed in an amorphous or low crystallinity matrix. Microfibrils are made up of low sulphur protein molecules, containing clusters of two or three polypeptide chains, α -coils twisted together Lotay et al. 1977). The matrix, on the other hand, is made up of keratin with high sulphur content. Keratin is a protein rich in sulphur; this element is not found in any other fibre and comes from the catabolism process, that is, by degradation of the proteins that constitute living matter. Keratin is mainly comprised of C, H, O, N, and S, averagely in the following proportions (Table 1.2):

Table 1.2 Chemical composition, wt %, and dry-ash-free basis of virgin wool (Pina et al. 2021; Chen et al. 2013; Speakman 1985).

Element	%
Carbon	45 - 50
Oxygen	20 - 25
Nitrogen	12 - 16
Hydrogen	5 – 7
Sulphur	3-4

On the other hand, the material also has fat in its structure, a secretion produced by the animal's sebaceous glands. Wool fat is comprised of a large number of components mixture, which can be set into three main groups: free fatty acids (4 to 10%), free fatty alcohols (1 to 3%), and esters of fatty acids and alcohols (87 to 95%).

In summary, wool is distinguished by having the following characteristics: a complex and highly versatile chemical structure and a complex physical structure, including a scaly surface. These characteristics, together, give the fibre a high capacity to absorb moisture (it can absorb up to 50% of its weight) and repel water and, or liquids on the surface (hydrophobicity). In addition, the material has durability, natural undulation or "crimp", high fire resistance (it is a fire retardant material), excellent thermal insulation, low generation of static electricity, and high elasticity and recovery capacity (Millington et al. 2017).

For the reasons above, using wool waste to develop a value-added material is an exciting opportunity to explore. Thus, if we think of designing an adsorbent material for water treatment from wool wastes, we would be attacking two problems, water pollution and the reuse of industrial waste, both of which target part of the 2030 Agenda SDG6 and SDG12. On the other hand, despite Uruguay being one of the major worldwide producers, there is a stock that is left unsold, and this is raising concerns among breeders. According to the last economic report, approximately 40 million kilograms could not be commercialised (Reporte Exportaciones 2023). This surplus entails new efforts to reverse this situation by developing new add-value materials.

1.6 Thesis main and specific goals

The current doctoral thesis addresses two main topics: the adsorption performance in the liquid phase under two working conditions, monocomponent and binary mixtures, of a novel wool-based adsorbent material and the development of the adsorbent itself. As well as trying to understand the reactions and transformations that occur during the process.

The primary main goal was the material development, an activated carbon fibre (ACF), and keeping the morphology after the treatment was the critical problem. Thus, several obtention techniques and conditions were assessed, always using sheep wool as an adsorbent precursor. The election of wool was based on the fact that it is a waste from a national industry of relevance for our economy, supported by the accessibility to find it in our media at a relatively low cost.

Two specific objectives arise from this first part: first, the study and optimisation of the stabilising conditions for the fibre - an unavoidable step for fibrous materials before the treatment itself. Testing various temperature and treatment time conditions under an oxidising atmosphere to achieve the stabilised material with the best morphological features was needed to keep the morphology. The second specific goal was the obtention of the adsorbent material (ACF) to be used in the adsorption experiments. Two activation techniques, physical and chemical, were carried out, and a treatment time pool was tested.

Likewise, all the obtained materials were extensively characterised to relate the chemical composition and textural features with the techniques applied.

The second objective, the adsorption studies, was carried out for monocomponent and binary mixtures to assess the material's behaviour when competition is involved and when it is not. Different medium conditions, varying pH and ionic strength, were tested to better understand the processes involved. The specific goals for this study were the establishment of the adsorption models — kinetic and thermodynamic — for monocomponent adsorption. And establish the thermodynamic model that best fits the binary mixture to elucidate which type of interference could be expected when working with the presence of a second substance. The models applied in this work are generally used for the adsorption of heavy metals, so this is a novel approach to elucidate the mechanisms involved in PhAC adsorption.

1.7 Thesis structure

Details of the thesis structure and the information that will be found in the document are as follows:

Chapter I: This chapter is dedicated to explaining the actual concern regarding water accessibility and the challenges that our society faces in securing the world's safe drinking water. It provides a brief overview of the state of water bodies worldwide regarding PhAC contamination, the WWTP technologies available to combat this, and novel strategies to address the problem. A description of the proposed working material can also be found here.

Chapter II: This section displays all the information related to active carbon, including its use along history, different obtention strategies and the factors that affect the material during the obtention, structure and chemistry, presentations, and uses in our daily lives.

Chapter III: This chapter describes the kinetic and thermodynamic models applied for adsorption in an aqueous solution. This includes models for both working conditions, monocomponent and binary solutions. Also, the pH and ionic strength effects regarding the adsorption performance of the adsorbent material are depicted.

Chapter IV: This chapter depicts the materials, equipment, and techniques used for this work, including a subsection explaining the method utilised for the adsorption experiments.

Chapter V: This chapter is exclusively dedicated to studying the stabilisation step, a necessary treatment to allow the material to be subsequently exposed to higher temperatures without compromising the morphology. The effects on the fibre suffered under an oxidising atmosphere are discussed at length from different angles, and techniques such as infrared spectroscopy and thermal programmed desorption coupled with mass spectra are used, among others.

Chapter VI: This chapter discusses the characteristics of the adsorbent materials obtained using different methods from various perspectives. The comparison is made by considering the modified parameters, such as different treatment times under the same gas flow, the same time but different flow, or directly different activation treatments (physical vs. chemical). The data used for this were those recorded from the ACF characterisation, the textural analysis, the main one, but by no means the only one.

Chapter VII: This chapter discusses the results recorded for monocomponent adsorption. It also analyses and discusses the kinetic behaviour and isotherm experiments, considering the drug and the material features. Several ACFs with different characteristics were used for these experiments, and the respective results were compared with each other; the effect of pH and ionic strength is also discussed here.

Chapter VIII: The recorded data for binary mixture adsorption are discussed in this chapter. Like in Chapter VI, several ACFs with different characteristics were used, and the respective results were compared; the effect of pH and ionic strength is also discussed here. The kinetic behaviour and the isotherms experiments are analysed, and several adsorption models are applied to elucidate what type of interference would be expected for this situation.

Chapter IX: Although each chapter has its sector of partial conclusions, it gives an overview of the results obtained and the general findings to which they lead.

Chapter X: This chapter collects all the references used in this work.

Annexe I: Complementary results are shown here to help readers better understand the previous chapters.

Annexe II: Works published in peer-reviewed international scientific journals are attached to this section.

Annexe III: List of national, regional, and international events where this work or part of it was shown.



"Para aquellos que no encuentran su destino,
Y se pierden en los recodos del camino,
Recuerden que el diablo siempre espera
Más no desespera
Esperando tu presencia
Hacia el final de...
La Ruta Eterna"
La ruta eterna
Emma Villarreal

Activated carbons (AC) include a wide range of carbon-based materials that typically have an amorphous structure -despite microcrystalline sections- (Bansal et al. 2005) and present a highly developed porosity and an extended interparticle area. The synthesis of activated carbons involves two main steps: carbonisation under an inert atmosphere and activation (these will be further discussed in the following sections). According to this, any carbonaceous precursor can be treated to produce AC, although the final material's properties strongly depend on many factors.

The International Union of Pure and Applied Chemistry (IUPAC) defines AC as porous carbon, a char, which has been subjected to reaction with gases, sometimes with the addition of chemicals, e.g. ZnCl₂, before, during, or after carbonisation to increase its adsorptive properties (Fitzer et al. 1995). Other definitions can be found depending on the bibliography consulted; all of them refer to amorphous carbon materials that exhibit a high degree of porosity and an extended superficial interparticle (Marsh et al. 2006; Bansal et al. 1988). In contrast, recent material chemistry advances have enabled new preparation methods of porous carbons that do not necessarily include an activation step with an activating agent (e.g., polycondensation reactions, photoinduced and solvothermal approaches). The resulting porous carbon material is typically referred to as nanoporous carbon in these cases (Ania et al. 2019).

The earliest recorded uses for this material date back as far as 3750 BC when the Egyptians utilised charcoal (resulting from burning wood) as a reducing agent for copper and other materials or as a smokeless fuel. Later, ca. 1500 BC, they started to use it for medical applications (Przepiórski 2006). Despite this, it was not until the 18th century that the adsorptive capacities of this carbonaceous material were fully exploited. Swedish chemist Carl W. Scheele, who in 1773 measured the volume of gases adsorbed by charcoal, achieved this milestone (Rouquerol et al. 2015). That work led to another research study in which Johann T. Lowitz (1776) proved that charcoal could be used to solve decolourisation problems (Thorburn et al. 2014). Industrial production of AC started in Europe in the early 19th century and was primarily utilised for sugar refining (Bansal et al. 1988). The first patent was registered in 1854, while the first carbon filters used successfully to purify air and drinking water were recorded in 1862 (Jagtoyen et al. 1993). Afterwards, the application of this product to remove organic dyes and other pollutants from wastewater that originated in the textile industry was expanded (Robinson et al. 2001). Von Ostrejko patented the use of CO₂ as an activating agent for the obtention

of AC in 1901 (Jagtoyen et al. 1993). Despite this, it was not until World War I that the demand for this product significantly increased due to its ability to adsorb warfare gases. In this regard, AC became an essential material for industrial protection against hazardous gases. Reinforced by the accelerated development of society during the 20th century, the use of this adsorbent spread to different fields; not only this, but new applications were also discovered. To this day, examples of the early use of carbon materials for drinking water treatment can be seen (Figure 2.1).



Figure 2.1 Drinking fountain that dates from the 18th century (Domaine national de Chambord – Chambord Castle – France). Once delivered to the kitchen, the water was placed in a filtering fountain: a sizeable metallic vessel partially filled with coal or charcoal. It was used to filter the impurities from water, thereby rendering it drinkable.

2.1 Structure of Activated Carbons

From a structural point of view, AC is composed of distorted graphene-like layers of sp2 domains of carbon atoms also rich in defects (free edge sites), heteroatoms located at the edges (predominantly) or inserted in the basal planes, and carbon atoms in sp³ configurations (Guo et al. 2012). The distorted graphene layers (or microcrystals) are stacked by weak Van der Waals forces, either in an ordered or turbostratic structure, with different degrees of planarity depending on the graphitization extent of the materials (Figure 2.2). The free sites are associated with armchair (carbine-like) and zigzag (carbene type) configuration carbon atoms (rather than H-terminated or free radicals as generally assumed for a long time) and account for the surface reactivity of carbons in gasification reactions or to chemisorb heteroatoms and create stable surface functionalities (Radovic et al. 2005).



Figure 2.2 Schematic representation of the microstructure of the AC (Bansal et al. 1988).

Each microcrystal is typically formed by ca. 5 to 15 crystalline layers or basal planes. These microcrystalline structures build up during the carbonization process and achieve an interlaying spacing of circa 0.34 – 0.35 nm (0.335 nm for graphite). The microcrystalline layers in AC are randomly oriented, as opposed to the ordered structure of graphite (Figure 2.3) (R. C. Bansal and Goyal 2005; Biscoe and Warren 1942).

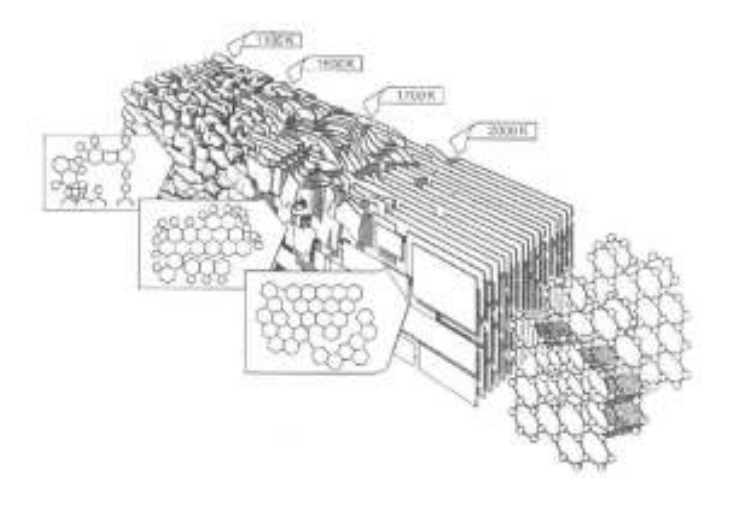


Figure 2.3 Diagram that models the structural changes which occur during the heat treatment of graphitisable carbon (Marsh 1982).

Carbon materials can be classified into two types based on their graphitising ability (Franklin 1951): graphitising and non-graphitizing carbons, upon their capacity to be transformed into crystalline graphite upon the thermal rearrangement of the crystallites by thermal heating at high temperatures. Due to the well-developed microporous structure, activated carbons typically belong to the non-graphitizing category (Figure 2.4).

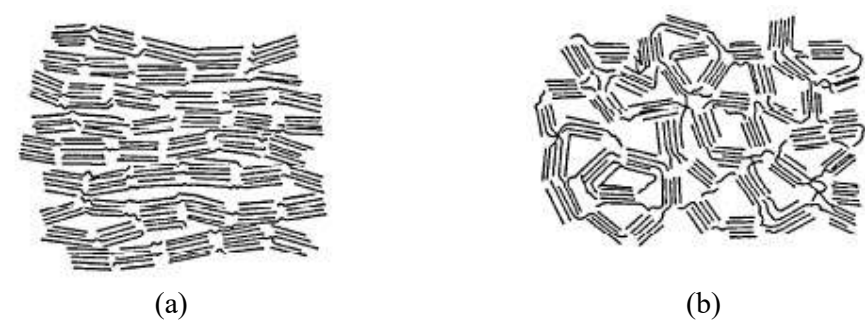


Figure 2.4 Schematic illustration of the structure of AC: (a) readily undergoing graphitisation, and (b) undergoing graphitisation to a small degree (Franklin 1951).

2.2 Porosity

The porous structure formed during the carbonisation process is further developed during the activation process, where the carbonaceous material and tar between the crystallites and some carbons belonging to the crystallite structure are removed. This treatment enhances the volume and enlarges the diameters of the pores (Bansal et al. 2005). The activation also removes disorganised carbon, exposing the crystallites to the action of the activating agent and leading to the development of the microporous structure. The structure of the pores and their pore size distribution are conditioned by the nature of the precursor (raw material) and their carbonisation conditions. A microporous AC is obtained when the degree of eliminated material (burn-off) is less than 50 %, and a macroporous AC is when the extent of burn-off is greater than 75 % (Dubinin 1960). The range in between results in a material with a varied porous structure and contains all types of pores. AC has a strongly developed internal surface; the inner surface is defined as the surface of all pore walls, but in the presence of microporosity, it has become customary to define the external surface as the non-microporous surface (Thommes et al. 2015). In this sense, IUPAC, in its recommendation guide, classified the pores according to their diameter as follows (Sing et al. 1985):

- Pores with widths exceeding 50 nm are called macropores.
- Pores of widths between 2 nm and 50 nm are called mesopores.
- Pores with widths not exceeding about 2 nm are called micropores.

Dubinin first proposed this classification (Dubinin, 1960) and later adopted it by IUPAC (revisited in 2015, Thommes et al. 2015). The porous width represents the

distance between a slit-shaped pore's walls or a cylindrical pore's radius. The **Micropores** generally constitute about 95 % of the total surface area of the AC, and their volume is circa 0.15 to 0.70 cm³g⁻¹. Besides, they can be subdivided into two subcategories: *ultramicropores*, for narrow pores with a width < 0.7 nm, and *supermicropores*, for wide micropores, meaning a width > 1.4 nm (Thommes et al. 2015). The **Mesopores**, also known as transitional pores, have a volume that usually varies between 0.1 and 0.2 cm³g⁻¹. The surface area of these pores does not exceed 5 % of the total surface area of the AC (Bansal et al. 2005). However, if mesoporosity is needed, it can be reached by applying specific methods, attaining a volume of 0.2 to 0.65 cm³g⁻¹. Other synthetic methods have been proposed if a greater extent of mesoporosity is aimed (Ania et al. 2019) at attaining mesopore volumes of ca. 0.2 to 0.65 cm³g⁻¹. **Macropores** have a meagre contribution to the surface area, only 0.5 m²g⁻¹, with a pore volume between 0.2 and 0.4 cm³g⁻¹. They act as transport channels for the adsorbate into the micro and mesopores. The interconnection among the different pores can be visualised as follow (Figure 2.5):

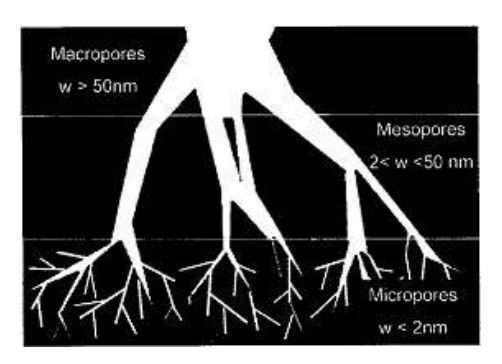


Figure 2.5 Schematic representation of the porous structure of an AC (Menéndez-Díaz et al. 2006).

2.3 Surface chemistry

As important as the structure is the nature of the functional groups on the material's surface. It plays a fundamental role in its chemical reactivity. For AC materials, the disturbances in the elementary microcrystalline structure, due to the presence of imperfect or partially burnt graphitic layers in the crystallites, cause a variation in the arrangement of electron clouds in the carbon skeleton and result in the creation of unpaired electrons and incompletely saturated valences. These disturbances influence the adsorption properties of AC, especially for polar and polarisable compounds.

Oxygen-containing functionalities are by far the most common surface groups present on all types of carbon surfaces, mainly due to the strong affinity of carbons to interact with oxygen when exposed to air (O₂ chemisorption occurs even at low temperatures) (Radovic et al. 2005; Henning 1966). Although they can also be incorporated from the chemistry of the precursor. Depending on the nature of the precursor, other heteroatoms, such as nitrogen, sulphur, and halogens, can also be present in activated carbons. It has been shown that these heteroatoms are bonded to the edges and corners of the aromatic sheets of carbon atoms at defect positions and give rise to surface groups or surface complexes. Most common structures corresponding to oxygen, nitrogen, and sulphur-containing functional groups in activated carbons are shown (Figure 2.6).

These active sites are responsible for the capacity of the AC to undergo halogenation reactions, hydrogenation, oxidation and/or act as a catalyst in several chemical reactions. Despite their importance, the surface sites associated with functional groups represent a tiny proportion of the total surface area. Nevertheless, this small presence plays a vital role in its adsorption capacity.

Figure 2.6 Schematic representation of the principal O-, N-, and S-containing surface groups in activated carbons, including free edge sites and carbon-hydrogen complexes.

For O- groups of carbon materials: (a) carboxyl groups, (b) lactones, (c) hydroxyl, (d) carbonyl, (e) quinone, (f) ether, (g) epoxide, (h) carboxylic anhydride, (i) chromene, (j) lactol, (k) electron density on carbon basal planes, (l) pyrone, (m) carbine, and (n) carbene sites. For N-groups: (a) pyrrole-like group, (b) nitrile, (c) secondary amine, (d) nitro group, (e) nitroso group, (f) tertiary amine, (g) primary amine, (h) pyridine-like group, (i) imine, (j) amide, (k) lactam, (l) pyridone, (m) quaternary amine, (n) pyrazine, and (o) nitrogen bridge in furanic groups. For S-groups: (a) sulphide, (b) thiophenol, (c) disulphide, (d) thioquinone, (e) sulphoxide, (f) thiolactone, (g) sulphonic, (h) thiophene. Adapted from Ania CO, Surface chemistry of green carbons, in Green Carbon materials; Advances and Applications (Bandosz et al. 2006).

Two significant effects arise from surface chemistry: the hydrophobic/hydrophilic and the acidic/basic characters. This material has a hydrophobic nature, but polar oxygen-containing surface groups can increase the hydrophilicity since water molecules can form hydrogen bonds with the oxygen on the carbon surface. The other significant effect is their influence on the acidic or basic character of the carbons. AC materials have acidic and basic groups coexisting on their surface; therefore, they are naturally amphoteric. Consequently, if the pH of the medium is higher than the pKa of carbonyl, hydroxyl, and lactone groups, they will behave as acidic groups. On the other hand, the basic nature can be attributed to pyrone and chromene-like groups, as well as the delocalised π -electrons of the basal planes (Montes-Morán et al. 1998). Also, some nitrogen-containing groups can behave as basic sites. However, if the acidic groups are more numerous, or their acidic strength is bigger than the basic groups, then the carbon will have an acidic nature.

2.4 Precursors

Precursors such as wood, coconut shells, fruit stones, coals, lignites, petroleum coke, etc., are all inexpensive and have high carbon content, which makes them suitable for producing AC (Marsh et al. 2006a). However, due to excessive demand for AC, there is a shortage of materials such as coconut shells and charcoal, and owing to this, the market prices have increased (Market Report, 2020). The cost of the precursor is critical to keeping a stable and affordable final product at a price that can compete in the international market. In this regard, because of the important industrial development of society, tons of solid waste are generated daily, jeopardising air and water quality. Indeed, growing environmental concerns and awareness have led to settling stricter national laws

and international guidelines. These new political visions aim to stimulate the re-utilization of those residues.

Since transport plays an essential role in the final cost, it is almost mandatory that industrial plants use local wastes as raw materials to avoid undesirable increases in the product price, guaranteeing a constant supply. For this reason, while coconut shell stands for 60 % of the AC market in Asia, their presence decreases to 12 % in Europe. Another critical requirement is low inorganic matter content. The adsorption is measured per mass unit, and inorganic matter is non-porous, so their presence reduces the adsorption capacity (Mufioz-Guillena et al. 1992). The lignocellulosic precursors are the most frequently used material; it stands for 45 % (m/m) of worldwide production. These are materials with low inorganic content, allowing to obtain AC with low ash content (Menéndez-Díaz and Martín-Gullón 2006).

The production yield of AC from biomass is meagre (circa 5 to 10 % of AC comes from wood) because of their high mass loss during the thermal treatment, adding to the high production cost (Menéndez-Díaz et al. 2006). For this reason, low-cost agricultural and industrial wastes become the ideal precursor materials. Considering the problem mentioned earlier regarding the need to find a new use for agricultural wastes, their low cost reinforces the concept that they are a suitable choice.

2.5 Synthesis of AC

Activated carbons are produced at an industrial scale by so-called conventional activation methods (i.e., physical and chemical activation). Most processes start with a carbonisation (pyrolysis) or an oxidation step of the precursor, followed by the carbonised material (charcoal) exposure to a reactive atmosphere in the presence of an activating agent that allows the development of a porous structure. Extensive work has been done to enhance the porosity of the resulting carbon adsorbents by the use of different activating agents, the choice of precursors, the optimisation of the activation conditions (temperature, heating rate, gas flow), and the usage of various impregnation methods (soaking, stirring) (Marsh et al. 2006b). In general, the process scheme can be outlined as follows (Figure 2.7):

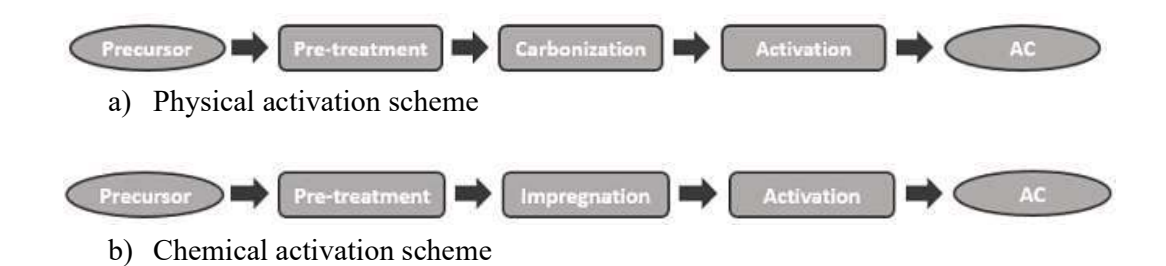


Figure 2.7 General scheme of activation process (in b: dry and washing steps are not considered).

The *Thermal* or *Physical Activation* is carried out in two consecutive steps in the same oven, changing the working atmosphere. This procedure usually needs higher temperatures than *Chemical Activation*, portraying a disadvantage in energy costs. *Chemical Activation* implies a step where the precursor is left in contact with the activating agent, the mixture can be dry or in an aqueous phase, and in the latter, the sample is left stirring for at least 24 hours and then drying before carrying out the activation. This technique has the advantage of lower working temperatures than those used in *Thermal Activation*. Even with this, there is still the inconvenience that this technique implies, as well as more steps and the use of large quantities of water. Both procedures are further explained in the corresponding sections of this chapter (2.4.3.1 and 2.4.3.2).

2.5.1 Pre-treatment

Frequently, before the treatment to obtain AC, the raw material needs to be prepared; this includes different actions taken to get a clean, homogeneous material with the desired particle size. These *Pre-treatments* take place before the carbonisation/activation of the raw material. For example, sometimes the sample needs to be homogenised, solid impurities removed, or in other cases, like powdered and granular carbons, the pre-treatment consists of crushing and sieving to acquire the desired size. Specific precursors need a previous wash with water or acid solutions to clean the material and to reduce mineral matter; as explained before, it is imperative to reduce the presence of inorganics that strongly affect the AC performance. On the other hand, if the raw material is a fibre, a pre-oxidation treatment, generally known as stabilisation (see 2.8.1), will be required.

The variety of treatments depends on the nature and conditions of the raw material. There is no straightforward technique for a specific precursor; therefore, it will be up to each case.

2.5.2 Carbonisation

Carbonisation occurs following pre-treatments, which is critical to AC synthesis. Carbonisation involves the thermal decomposition of the carbonaceous material, eliminating non-carbon species and producing a fixed carbon mass and a rudimentary pore structure (Bansal et al. 1988). This treatment is carried out in an oven under an inert gas flow, typically Nitrogen or Argon. The parameters that affect the structure, quality, and yield of the produced carbon are the heating rate, the final temperature reached for the thermal treatment, the residence time, and the nature of the raw material. Considering all these parameters, the experiment is designed to achieve a carbonised version with the desired features. A low heating rate during pyrolysis results in lower volatilisation and higher char yield because of increased dehydration and better stabilisation of the polymeric components (Mackay et al. 1982). The terms carbonisation and pyrolysis are used indistinctly, and in fact, these two thermal treatments are practically identical; essentially, the difference lies in the final objective for both processes. However, in both cases, the main products from the decomposition of the macromolecular structure are a gaseous fraction (rich in hydrogen, light hydrocarbons, and tar) and a solid fraction rich in carbon called char. The main goal of pyrolysis is to recover the gas products and volatiles that evolved during the treatment. Consequently, the working parameters like temperature and residence time, among others, are set to favour the release of gaseous products (Marsh et al. 2006c). On the other hand, the objective of carbonisation is the production of coal, especially the development of a primary microporous network with adequate hardness and density, among other characteristics that make the final quality of the material (Marsh et al. 2006c). In this case, the working parameters will be set to achieve the desired solid material without considering the volatiles evolved.

In the overall production of CA, carbonisation is a critical step where the microporous structure of the final material starts to build prior to the activation. At this stage, the main parameters to control are the heating rate, the final temperature, and the residence time; the slightest change in one of these parameters will make the final product different. Compared with the precursor, the char formed is enriched in relative carbon

content and aromaticity. Because much mass evolved during carbonisation, this increase in aromaticity is accompanied by increased incipient microporosity since many functional groups and bridge chains evolved, yielding void spaces (Marsh et al. 2006b). The carbonization-heating rate is crucial in establishing the final textural characteristics of the char. If a high heating rate is used, the solid obtained will have a well-developed meso and macropore network, low density, and a low abrasion and hardness index due to a very quick devolatilisation. On the other hand, low heating rates lead to a slow devolatilisation, disfavouring the development of a large meso and macro network; consequently, both features, density and hardness, are higher than those obtained at high heating rates. However, the incipient microporosity is unaffected whether the heating rate is high or not. Henceforth, a low heating rate treatment at not very high temperatures and long residence times seems to provide the best conditions to produce chars that, upon activation, give rise to dense and hard AC (Menéndez-Díaz et al. 2006).

2.5.3 Activation

After carbonisation, the material only has an incipient porous structure. Consequently, it is not ready to be used as an adsorbent until its porous network is enhanced or *activated*. As previously explained, two main methods are used to achieve activation: thermal, physical, and chemical. The former implies a process at high temperatures, normally between 800 – 1000 °C, under a reactive (oxidant) atmosphere (CO₂, O₂, H₂O vapour, and air). The latter implies the treatment of the material with a dehydrating agent (H₃PO₄, ZnCl₂, KOH, among others) at temperatures between 400 – 1000 °C, followed by extensive washing to secure the absence of the activating agent.

Both methods have advantages and weaknesses; their main difference is the working temperature and the number of steps. The chemistry activation requires lower temperatures; therefore, higher yields are gained compared with the physical method. Usually, it is presented as a one-step technique, but that only refers to the thermal treatment, not the entire method. The last wash is not only another stage in the process but a significant one since the activated material needs to be cleaned from the activating agent and/or their products of degradation, because otherwise, its performance will be affected. Also, the water used for cleaning must be treated, allowing it to be reused or returned to the water system. The physical method needs higher temperatures, which means higher costs, reinforced by higher energy bills and lower carbon yields. Those are

the main drawbacks of this technique; nevertheless, it has the advantage that it does not need water for cleaning.

2.5.3.1 Thermal or physical activation

In a simplified way, *Thermal* or *Physical Activation* refers to the development of porosity by the gas phase. It can be described as a selective process of gasification (removal) of individual carbon atoms. The process is selective since the reactivity of the carbon atoms depends on their position on the carbonaceous skeleton; the reaction is generally carried out at elevated temperatures (between $750-1100\,^{\circ}\text{C}$) and proceeds through the formation of surface oxygen complexes. A detailed review of the understanding of the chemical reactions, thermodynamics, and kinetics of the physical activation with these gases can be found in "*Activated Carbon*" (Marsh et al. 2006). The objective of the activation process is to enlarge and open the incipient porosity developed during the carbonisation. This is carried out under a reactive atmosphere in the Presence of oxidants such as oxygen (or air), steam, and carbon dioxide, according to (Reactions 2.1-2.3):

$$C + CO_2 \rightarrow 2CO$$
 $\Delta H = +159 \, kJmol^{-1}$ Reaction 2.1
 $C + H_2O \rightarrow CO + H_2$ $\Delta H = +117 \, kJmol^{-1}$ Reaction 2.2
 $C + O_2 \rightarrow CO_2$ $\Delta H = -406 \, kJmol^{-1}$ Reaction 2.3

The activation kinetic is conditioned by the characteristics of the carbonised material and the reactive gas selected. Moreover, the extent of the gasification, known as burn-off, will also depend on the nature of the reactive gas and the temperature selected to carry out the treatment (Bansal et al. 1988). The gasification of chars under CO₂ and steam (and their mixtures) is preferred over oxygen (air) due to the high exothermic enthalpy of the latter, making the reaction temperature challenging to control. As a result, oxygen does not penetrate the char particles, and fast gasification occurs on the external surface, leading to the complete burn-out of the carbon material rather than the formation of pores. Due to this, it is impossible to achieve a well-developed porosity network with this gas, and it is rarely used in industry. In the case of CO₂ or steam, the reactions are endothermic; thus, an external heat supply is required, allowing accurate control of the experimental conditions (Marsh et al. 2006). Although steam and carbon dioxide have slower kinetics

than oxygen, their reactions with the carbon are endothermic, which allows accurate control of the process conditions. Consequently, they are the most widely employed gases for physical activation.

The choice of the gasification temperature is not arbitrary and depends on the reactivity of the precursor under CO₂ and steam. It is important to keep a moderate reactivity to assure a diffuse regime control of the reaction and prevent the fast gasification of the external surface of the materials (leading to a non-porous material). A simple approach to measuring the gasification rate consists of carrying out a thermal profile of the char under a CO₂ or steam atmosphere and evaluating the mass loss rate with the temperature. This test provides an idea of the onset temperature of the reactivity for the oxidising gas chosen and allows comparing the reactivity rate of different precursors. Additionally, for specific precursors (e.g., coals), a peroxidation step is recommended to favour the formation of an incipient porosity in the char (Parra et al. 1996), and a well-developed microporosity after the gasification.

The reactions of carbon dioxide, steam, and molecular oxygen, as well as producing gaseous reaction products, also result in the formation of chemisorbed oxygen, called *the surface oxygen complexes*, which possess a broad range of chemical functionality and stabilities (Marsh et al. 2006a). The chemistry of these complexes is a function of the formation's temperature and subsequent thermal treatments. In general terms, this reaction can be described as (Reaction 2.4):

$$C_f + CO_2 \leftrightarrow CO + C(O)$$
 Reaction 2.4

where C_f is fixed carbon, and C(O) describes surface oxygen complexes without any reference to their chemistry. During the activation, these oxygen complexes behave in two ways: as reaction intermediates in the carbon gasification and as retarders (inhibitors) thereof (Marsh et al. 2006a). The C(O) initially formed becomes stable under the reaction conditions, and this provokes that the complex acts as a retardant by blocking the reaction site (Reaction 2.5):

$$C(0) \rightarrow C - 0$$
 Reaction 2.5

However, it may decompose, leaving the site as CO (Reaction 2.6), leaving a free surface carbon atom available for the reaction:

$$C(0) \rightarrow C0$$
 Reaction 2.6

Similar behaviour is recorded for the reaction between the carbon and steam, where the hydrogen inhibits the reaction rate by forming C(H) surface complexes. However, since the hydrogen surface complexes are more stable than those formed by carbon dioxide, the inhibitor effect is remarkably more substantial for the former. Nevertheless, the inhibitory effect of these two gases may not necessarily be harmful since they have a kinetic almost one hundred times slower compared to air and oxygen, which allows controlling gasification and, therefore, the development of porosity.

The activation process takes two steps; during the first one, the disorganised carbon is burned out, preferentially when the burn-off does not exceed 10 %, which leads to the opening of blocked pores. During the second stage, the carbon of the aromatic ring system starts burning, producing active sites and broader pores. Activation with carbon dioxide promotes external oxidation and the development of larger pores compared to steam. The extension of external and internal oxidation depends on how developed the pores are in the carbonised material (Bansal et al. 1988).

The kinetic expression for the activation processes under carbon dioxide is:

$$\frac{d\alpha}{dt} = \left(\frac{k_1 e^{\left(-\frac{E_a}{RT}\right) P_{CO_2}}}{1 + k_2 e^{\left(-\frac{E_2}{RT}\right) P_{CO_2} + k_3 e^{\left(-\frac{E_3}{RT}\right) P_{CO_2}}}}\right) (1 - \alpha)^n$$
 Equation 2.2

Where α is the carbon conversion degree (mass of reacted carbon vs. mass of initial carbon). The expression inside the parentheses is the apparent kinetic constant, as an expression of the Langmuir-Hinshelwood type (Walker et al. 1959) where k_i is the Arrhenius-type preexponential factor, Ea is the activation energy, E2 and E3 are the adsorption enthalpies, and Pi is the partial pressure. Finally, n is the reaction order and can have the following values (Heek et al. 1991):

- n = 0 is very unusual; in this case, the reaction rate is independent of the degree of carbon conversion.

- *n* = 1, in this case, the reaction proceeds under chemical reaction control, which means the reactive agent first diffuses through the pore network and later reacts at any active site.
- n = 0.67, the reaction is under diffusion control, implying that the oxidising agent reacts only on the surface because it does not have enough time to diffuse internally. Therefore, the particle size becomes smaller as the degree of conversion increases.

Depending on the partial pressure of the reagents and products, the temperature at which the transition occurs is around 1123 K (or lower) when the reaction rate is not very high. Under chemical control, the porosity development attained is as high as that obtained with steam (Rodríguez-Reinoso et al. 1995). Consequently, porosity development is poor under diffusion control, giving rise to external particle burning (Wigmans 1989). Generally, low carbon dioxide mass flow vs. mass of carbon operates under chemical control, whereas high carbon dioxide mass flow vs. mass of carbon falls under diffusion control.

The activation under CO₂ and H₂O renders materials with different porosity. Comparison is not straightforward since the chars react differently to the oxidising gases. Based on studies performed on the same precursor using CO₂ and steam at similar gasification rates, it may be concluded that CO₂ activation produces activated carbons with a narrow distribution of micropores. In contrast, steam activation generates carbons with a wider micropore size distribution and a slightly more significant development of mesopores (Rodríguez-Reinoso et al. 1995). In any case, both gases produce low functionalisation activated carbons due to the high gasification temperatures. However, CO₂ activation creates more stable oxygen groups than steam (Molina-Sabio et al. 2004).

Among other parameters, the effect of the flow rate of the activating agent is also important. Slow rates (ca. below 10 mLmin⁻¹) favour the development of microporosity due to homogeneous gasification through the whole carbon particle network (Ania et al. 2019). At high CO₂ or steam flow rates, the gas does not penetrate deeper into the material, and the burn-off on the external surface of the carbon particle becomes more important than the generation of internal porosity. As a result, the carbon yield decreases, the activated carbons display low total pore volumes, and the porosity mainly comprises macropores. This is an acute difference with chemical activation, where fast rates favour

the development of microporosity, as will be addressed below. The particle size is also important, with smaller particle sizes leading to denser carbon materials, more developed surface areas, and narrow micropores.

Regarding the porous features, as a rule, burn-off degrees lower than ca. 50 wt.% render microporous activated carbons, with total pore volume and surface areas increasing with the burn-off, regardless of the nature of the precursor (Rodríguez-Reinoso et al. 1995). Additionally, at high levels of burn-off, the ablation of the carbon particles becomes essential; thus, the industrial gasification of chars rarely goes beyond 40 - 50 wt. % (Marsh et al. 2006b).

2.5.3.2 Chemical activation

The second procedure to obtain AC involves a reaction between the carbon precursor and a chemical reagent followed by a thermal treatment. This technique is known as Chemical activation and is considered a one-step method because the porosity and the transformations take place simultaneously. Chemical activation has recognised advantages for producing activated carbons with highly developed porosity, as it leads to higher yields and allows the use of lower temperatures than physical activation. However, as explained before, the disadvantages of chemical activation include its extreme corrosivity and unavoidable washing process (Dai et al. 2018). Additionally, the activation mechanisms are different in both processes and so is the porosity of the resulting activated carbon. A detailed review of the mechanism of the different chemical activation reactions for various activating agents can be found in (Marsh et al. 2006b).

The main factors affecting the activation process include the activating agent, mixing method, mass ratio precursor-chemical reagent, and heating method (Sevilla et al. 2014). In all cases, the temperatures required for treatment range from 623 to 1173 K. Regarding the selection of the activating agent, its chemical nature must be considered. According to the acid-basic theory and activation mechanism, activating agents can be classified into four categories: alkaline, acidic, neutral, and self-activating (Marsh et al. 2006c). The chemical agents most frequently used are phosphoric acid (acidic), zinc chloride (neutral), potassium hydroxide, sodium hydroxide (strong alkaline), K₂CO₃ (Kim et al. 2020) and Na₂CO₃ for middle alkaline activating agents (Marsh et al. 2006c, and references therein). However, the list is extensive; therefore, several works can be found

in the literature where other chemical reagents were used. These chemical reagents produce quite a different pore development in the precursor material, in a molar ratio precursor-reagent that usually varies between 1:1 and 1:4. The feasibility of the chemical agent is strongly dependent on the recovery of the reagent for recycling. The impregnation can be carried out in two ways: in an aqueous solution under stirring for at least one hour, followed by thermal treatment at 373 K to evaporate the excess water, or by a solid mixture. In both cases, after the impregnation, the material is treated at a high temperature under an inert atmosphere, and the temperature will depend on the chemical reagent selected. This step is critical for the subsequent steps; during this stage, the activating agent molecules will gradually merge with the internal structure of the carbon precursor. The mixing time needs to be long enough to ensure that the reagent reaches the inner layers and not only the shallow layer (Danish et al. 2018). Generally, the wet method is preferable to the dry method for acidic activating agents (Gao et al. 2020), while for alkaline and neutral activating agents, both wet and dry methods can be used indistinctly (Khan et al. 2020; Spessato et al. 2019). The advantage of mixing in an aqueous solution is that it allows uniform contact between the precursor and the chemical agent. However, the drawback of this method is the consumption of water followed by a drying procedure, which consumes time and energy. Independently of the impregnation method and the thermal treatment, the last step will always be an extensive wash until a constant pH value.

Zinc chloride was the principal activating agent up to 1970 and is still used in China. Its action is effective upon materials with high volatile matter, and oxygen content, such as lignocellulosic materials. Low recovery efficiencies, corrosion problems, and the need to reduce emissions have led to their replacement for phosphoric acid (Menéndez-Díaz et al. 2006). The temperatures for the thermal treatment range between 773 and 1073 K, giving rise to a broad and open microporosity that favours the material for adsorption in liquid-phase applications.

Phosphoric acid can produce high surface area carbons depending on the precursor, the impregnation ratio selected, and the thermal treatment conditions. As with zinc chloride, this reagent is adequate for precursors with high content of volatile matter; for this reason, it is widely used for wood and some agricultural by-products. The temperature used for the treatment oscillates between 673 and 773 K. The material activated by this method presents a better-developed mesoporosity compared to thermal

activation. The precursor-reagent impregnation ratio frequently used is 1.5; during this stage, the acids attack the hemicellulose, and lignin hydrolysing the glycosidic linkage to produce polysaccharides, cleaving the aryl ether bonds of the lignin (Jagtoyen et al. 1998). It has been reported that using nitrogen during the thermal treatment gives the best porosity and carbon yield results. Nevertheless, this reagent also represents an environmental problem associated with eutrophication derived from phosphorous compounds.

During the 1970s, AMOCO Corporation, USA researchers developed a process that obtains high surface area carbons (approximately 3000 m²g⁻¹) by chemical activation. Later, in the 1980s, Anderson Development Company first commercialised the product (Menéndez-Díaz et al. 2006). This new method uses alkaline hydroxides as activating reagents. Unlikely the previous chemicals, this does not need high volatile matter; on the contrary, the most appropriate materials are those with low volatile matter and rich carbon content. The precursor-alkaline hydroxide ratio is usually between 2 and 4, and temperatures required are higher than those needed for zinc chloride and phosphoric acid, with at least one hour at a maximum temperature (Menéndez-Díaz et al. 2006). The way that KOH acts upon the precursor differs from the previous reagents; in this case, the agent reacts with the carbon skeleton, producing solid and gaseous products while producing a rise in porosity. According to experimental data, the chemical reaction proposed for this method (Lillo-Ródenas et al. 2004) is as follows (Reaction 2.7):

$$6KOH + 2C \leftrightarrow 2K + 3H_2 + 2K_2CO_3$$
 Reaction 2.7

Where the potassium carbonate decomposes further, producing K₂O and CO₂. Thermodynamically, the mentioned reaction is feasible above 873 K. The primary influence on the final activated material features is in the precursor-KOH impregnation ratio and much less in the final temperature treatment. In general, the activation with KOH produces materials with extremely narrow microporosity and high adsorption capacity without the presence of mesopores at all (Menéndez-Díaz et al. 2006). Large specific surface areas can be attained with this method from 1500 up to 3000 m²g⁻¹, depending on the impregnation ratio. However, high impregnation ratios can destroy the carbon structure, disintegrating the powder granules of carbon (Marsh et al. 2006a). The gas regime in the oven, where the carbonisation takes place, strongly influences the porosity development; a high carrier gas flow secures the presence of microporosity. Therefore,

the flow is vital for treatments carried out at low temperatures (ca 973 K) and low precursor-KOH ratios due to the dilution of reaction products, favouring the chemical reaction (Lozano-Castelló et al. 2007).

In recent years, other chemical activating agents, such as alkaline carbonates (K₂CO₃, Na₂CO₃), were used to replace KOH as an activating agent (Kwiatkowski et al. 2013; Mestre et al. 2007). Like the latter, they also allow the development of AC with high specific surface areas and micropore volumes. However, they need treatment temperatures above 800 °C to achieve this, which is a drawback in energy consumption.

2.6 Types of AC and applications

Several forms of AC can be found in the market, excluding the textural characteristics; depending on the features of the application, the presentation that best suits the working conditions will be chosen. The differences encompass characteristics as diverse as morphology (size and form of the particle) and surface chemistry.

- Powdered activated carbon (PAC): this type of carbon presents a particle size smaller than 0.177 mm as defined by ASTM D2862-16 (American Society for Testing and Materials); thus, they have a larger surface area-to-volume ratio. PAC is used mainly to remove a wide range of organic contaminants that influence colour, odour, and taste from wastewater, potable water, and water required in industrial processes. Hence, the most common application for PAC is in water treatment (Campinas et al. 2021; C. Kim et al. 2014). However, in recent years, the cosmetic industry has used this presentation for skincare creams (Lee et al. 2018).
- Granular activated carbon (GAC): among activated carbon materials, GAC is the dominant segment owing to the high demand for the product from several enduse industries such as water treatment, air, and gas purification (Advanced Materials / Activated Carbon Market). Their particle size ranges between 1 5 mm (Menéndez-Díaz et al. 2006), and it is usually used in fixed bed adsorbers in continuous processes and with low-pressure drops in both liquid and gas phase purifications (Tröger et al. 2020; Hijnen et al. 2010).

- Activated carbon fibres (ACF): these materials are basically carbonised fibres that are subsequently activated by different means (further details in 2.7)
- Carbon fabrics and felts: to meet specific requirements for some applications such as adsorption, catalyst supports, and gas separation, the AC can be manufactured in the form of fabric or felt (P. Dai et al. 2020; Sohrabi et al. 2020; Pina et al. 2018a; Pina et al. 2018b). They are usually lighter in weight and very versatile in their disposition because of their structure.
- Monolithic structures: Two types of monolithic structures can be distinguished: coated monoliths and integral monoliths. The former comprises a monolithic backbone and a support layer coated onto or in the structure. The monolithic structure is usually either a ceramic or a metallic monolith that supplies mechanical and geometrical properties, whereas the support layer provides the adsorptive and/or catalytic properties. The second type is made of support material, which must provide mechanical, geometric, and adsorptive properties all by itself. This kind of configuration has the potential to overcome many of the limitations of conventional granular beds in terms of substantially reducing the pressure drop, enhancing renewability, and eliminating dusting and attrition (Menéndez-Díaz et al. 2006). They are commonly used for processes based on adsorption and catalysis (Vergunst et al. 2001).
- Carbon films: molecular separations based on molecular size and shape differences are significant for gas separation, such as CO₂/CH₄ or N₂/O₂ mixtures. The layer in this kind of membrane must be thin (<50.10-6 m) and be able to present good mechanical properties to facilitate handling and fixing. Two types of membranes can be found: unsupported and supported. The unsupported materials provide high selectivities but suffer from extreme fragility. This drawback can be avoided by forming carbon layers on support media such as porous graphite, sintered stainless steel, and ceramic supports (Qian et al. 2020; Huang et al. 2018).

2.7 Regeneration

As the adsorption process goes on, the adsorption capacity of the material diminishes because of the pore filling by the adsorbate molecules. This will proceed until the AC is exhausted, meaning all the pore sites are blocked, and the fluid concentration remains constant. At this point, the AC needs to be replaced, and there are two main options: replace it with a new one and dispose of the discarded by incineration or use it for landfilling. The second option is the regeneration of the exhausted AC, thereby reducing the consumption of this material.

Regeneration is often the most appealing option due to its distinct advantages, including the potential to recover adsorbed products of economic value, depending on the characteristics of the process (Menéndez-Díaz et al. 2006). Although this is an attractive alternative, it is not always conceivable since, on some occasions, the cost associated with this process is very high compared with the cost of the adsorbent material. In addition, most regeneration techniques give rise to AC with smaller adsorption capacities than the original AC (Menéndez-Díaz et al. 2006); for this reason, it is commonly used for GAC but not PAC. Despite this, assessing the material's regeneration viability is imperative. Therefore, different regeneration strategies have been developed.

- Thermal regeneration: is the most extensively used technology for regenerating exhausted carbons. It consists in heating the material at a temperature and residence time that guarantees the elimination of the adsorbates. For this purpose, different oven configurations can be used, such as a rotary oven, multiple hearths, a fluidised bed, and even a microwave (Oladejo et al. 2020). The thermal method is very versatile but is not exempt from drawbacks. This type of regeneration requires high energy consumption and causes considerable carbon loss (circa 5 15 %) due to attrition, burn-off, and washout (Ania et al. 2004; Sabio et al. 2004). In some cases, the regeneration must be carried out under activating conditions like CO₂ (Oladejo et al. 2020), steam, or air (Márquez et al. 2021), known as reactivation.
- Steam regeneration: usually performed on-site (Jareteg et al. 2021) and is very useful for adsorbates with low boiling points. The advantage and the difference with the thermal method is that this requires a lower temperature. Once the carbon is saturated and exposed to a counter-current of steam, the steam can desorb the

- adsorbate due to its high heat content. The drawback resides in the fact that it is pointless for compounds soluble in water unless an additional process is applied that allows the recovery of the adsorbate.
- Advanced oxidation processes involve the generation of highly reactive hydroxyl radicals to initiate a series of chain reactions for pollutant degradation. Hydrogen peroxide/ozonation (H₂O₂/O₃), Fenton's reagent, and hydrogen peroxide under ultraviolet illumination (H₂O₂/UV) and UV light can be found, among other techniques that apply oxidation processes to recover the carbon material (Bury et al. 2021; Santos et al. 2020; Horng et al. 2008; Velasco et al. 2014).
- Extraction with solvents: the regeneration is carried out by passing a stream of the solvent through a bed that contains the AC. The solvent needs to be recovered after use because they are costly (Larasati et al. 2022). Another option is extraction using supercritical fluid regeneration: fluids under critical conditions help extract substances from exhausted active carbons. The most widely used ones are carbon dioxide and water. The technique is based on the fact that in these conditions, the fluids exhibit densities similar to those of gases, enabling them to dissolve and/or desorb contaminants from the carbon surface (Chihara et al. 1997).

2.8 Activated Carbon Fibres (ACF)

ACFs are porous carbons with a fibre shape and a well-defined porous structure that can be prepared with a high adsorption capacity (Linares-Solano et al. 2008). The ACF is a CF that was afterwards activated by the already reported methods (2.4.3); the main difference with an AC is the need to stabilise the precursor before the carbonisation step (2.7.1).

The earliest known commercial use of carbon fibres was in carbonising cotton and bamboo fibres for incandescent lamp filaments. In 1879, Thomas Alva Edison used carbon fibre filaments (testing materials) for the first time in his early incandescent light bulb experiments, which used electricity to heat a thin strip of material, called a filament, until it glowed. Later, carbon fibres were discovered in 1880, and he patented the use of carbon fibres as filament materials for his electric lamp. The practical commercial uses of carbon fibres, such as reinforcement, came into being in the 1960s when it became apparent that those materials, which contributed significantly to the strength and stiffness of structural products, could be developed. During World War II, the Union Carbide

Corporation (UCC) investigated the fabrication of carbon fibres analogously to manufacture rayon and polyacrylonitrile (PAN); both processes were developed in 1959 and 1962, respectively (Park 2015). However, these two have a meagre carbon yield. This is defined as the ratio between the mass of the sample as measured at the pyrolysis temperature (Wb) by the dry mass measured at the end of the drying period at 105 °C (Wa) according to (Equation 2.8) (Hassan et al. 2015):

Carbon yield (%) =
$$\left(\frac{W_b}{W_a}\right) * 100$$
 Equation 2.8

In 1963, pitch-derived carbon fibres were invented; due to the low price and high yield compared with those mentioned above, the manufacture of this material has increased considerably (Linares-Solano et al. 2008). Moreover, until now, many precursor materials such as polyesters, polyamides, polyvinyl alcohol, polyvinylidene, poly-p-phenylene, and phenolic resins have been investigated for manufacturing carbon fibres, and there are a few works focused on the utilisation of natural materials as a precursor of CF, mainly composites (Borukati et al. 2019; Yang et al. 2016).

CF are classified based on the fibre structure and degree of crystallite orientation: ultrahigh-modulus (UHM), high-modulus (HM), intermediate-modulus (IM) (these three are related to the Young's modulus*), high-tensile-strength** (HT), and isotropic CF. The UHM and HM carbon fibres are highly graphitised and characterised by a high modulus. The UHM carbon fibres are characterised by a modulus greater than 500 GPa. In comparison, the HM carbon fibres are characterised by a modulus greater than 300 GPa and a strength-to-modulus ratio of less than 1 %. The IM and HT carbon fibres have high strength and low modulus owing to the heat treatment at lower temperatures. The IM carbon fibres have a modulus of up to 300 GPa and a strength-to-modulus ratio of >1 × 10^{-2} . The HT carbon fibres are characterised by a strength greater than 3 GPa and a strength-to-modulus ratio between 1.5 and 2 × 10^{-2} . Finally, the isotropic carbon fibres show a random orientation of the crystallites and possess a modulus as low as 100 GPa combined with low strength (Park 2015). Their main advantage is low cost. The type of CF is directly related to the carbonisation temperature (Table 2.1).

Carbon fibre	Carbonisation temp. (°C)	Long-distance order	Classification
I high modulus	≥ 2000	High	UHM / HM / IM
II high strength	≈ 1500	Low	HT / IM
III Isotropic	< 1000	Very low	Isotropic

Table 2.1 Classification of CF (Park 2015).

* Young's modulus (YM) is a numerical constant that describes the elastic properties of a solid undergoing tension or compression in only one direction, as in the case of a metal rod that returns to its original length after being stretched or compressed lengthwise. YM is a measure of the ability of a material to withstand changes in length when under lengthwise tension or compression. Sometimes referred to as the modulus of elasticity, it is equal to the longitudinal stress divided by the strain (Equation 2.9).

$$YM = \frac{stress}{strain} = \frac{FL_0}{A(L_n - L_0)}$$
 Equation 2.9

Where F (N) is the force that is pulled at each end of the fibre, A (m²) is the cross-sectional area, Lo (m) is the original length, and Ln (m) is the final length (Li et al. 2021; Müssig et al. 2010).

** Tensile strength is the maximum stress a material can withstand while being stretched or pulled before necking, which is when the specimen's cross-section begins to contract significantly. Tensile strength is the opposite of compressive strength, and the values can differ. The stress is measured as force per unit area. For some non-homogeneous materials (or for assembled components), the tensile strength can be reported as a force or as a force per unit width. In the SI system, the unit of tensile strength is Pascal (Pa) (or a multiple thereof, often mega pascals MPa) or, equivalently, Newton per square meter (Nm⁻²) (Park 2015; Müssig et al. 2010).

Although ACF is an up-and-coming material, its use is not as widespread as AC, mainly due to CF cost of production. The main features and advantages of the ACF are as follows (Linares-Solano et al. 2008):

- Arge apparent surface area and adsorption capacity.
- Fibre shape with a small diameter (circa 10 and 40 μm); this characteristic is significant for applications that require higher packing density, like gas storage.
- Low density.
- Ability to be woven into different fabrics.
- The pore size distribution of the ACF, specifically microporous materials, is narrow and uniform, although mesoporous ACF can also be prepared.
- The narrow diameter eliminates mass transfer limitations, with high-speed adsorption-desorption rates.

Essentially, the applications of ACF do not differ from those of AC; however, owing to the former's characteristics, some uses have advantages over conventional AC.

For instance, for adsorption processes, in gas and liquid phases, ACF contains microporosity readily available to the adsorbate, and the mass transfer limitations due to the diffusion within meso and macroporosity are absent (Suzuki 1994), making the adsorption process faster (Shmidt et al. 1997; Brasquet et al. 1997). Regarding water treatment, ACF was also studied as an antibacterial material, where the fibre-supported Ag (Tang et al. 2017; Park et al. 2003).

ACF and CF have also been studied and used as Carbon Molecular Sieves (CMS) for separating gas mixtures such as CO₂/CH₄ and N₂/O₂ (Pina et al. 2018a; De La Casa-Lillo et al. 1998). CF can be useful for this application because of its narrow microporosity, while ACF can be tailored by cracking hydrocarbons to develop good-quality CMS (Linares-Solano et al. 2008).

Another use for this material is as a catalyst and catalyst support; the versatility of the carbon materials, like porosity and surface chemistry, along with the morphology, makes these materials rather interesting for this kind of application (Hsiao et al. 2021; Li et al. 2020).

In recent years, with the increasing need to find alternative fuel sources, using porous materials for gas storage (H₂ and CH₄) has been thoughtfully studied (Conte et al. 2020; Burchell et al. 2017). Utilising those gases has a positive environmental impact, hence the importance of finding suitable storage devices. The advantage of ACF over AC is their essentially microporous character and higher packing density, although the higher cost of the former is detrimental (Linares-Solano et al. 2008).

Finally, another use for ACF as an electrode material for supercapacitors has also been reported. Due to their high surface area and other properties, such as electrochemical stability and high electrical conductivity, carbon materials are the most widely used materials for EDLC electrodes (Pina et al. 2018b)Although different commercial devices already exist on the market, some issues remain, like increasing the amount of stored energy. In this respect, carbon materials are a promising alternative.

2.8.1 Stabilisation

One of the main drawbacks of synthetic and cellulosic fibres is that during a thermal treatment, they fuse, decompose, or degrade, losing mechanical strength and morphology (Hassan et al. 2015b). Hence, the natural fibres' thermal processing pathway will control the resulting material's features. A standard procedure for preparing material with fibre morphology and controlled mechanical strength is based on performing an oxidative thermal stabilisation of the fibre precursor at a mild temperature prior to the carbonisation. The oxidative stabilisation reactions involve mostly cyclising nitrile groups (when using polyacrylonitrile as a precursor) and dehydrogenating saturated C–C bonds (for synthetic and cellulosic fibres). The original fibres are transformed into a cross-linked cyclised network of carbon-nitrogen rings. This new spatial disposition prevents the fusion of the fibres during further thermal treatments at high temperatures (Torres-Canas et al. 2020).

This step is critical to obtain carbon fibres and could take up to several hours, depending on the temperature, precursor diameter, and precursor fibre characteristics. Proper conditions, such as heating rate, time, and temperature, should be established for the optimum stabilisation of each precursor (Park 2015). The temperature is usually in the 200 - 300 °C range, notwithstanding.



"Éste es el Diablo, de quién hablábamos hace un momento. Jesús miró a uno, luego al otro y vio que, salvo las barbas de Dios, eran como gemelos, cierto es que el Diablo parecía más joven, menos arrugado, pero sería una ilusión de los ojos, o un engaño por él inducido."

El Evangelio según Jesucristo

José Saramago

3.1 Fundamentals of liquid phase adsorption

The term "Sorption" describes the attachment of a substance to a surface throughout an interaction. Depending on the type of interaction between the sorbate (compound that is adsorbed) and the sorbent (material where the adsorption takes place), sorption can be divided into physical, chemical, or electrostatic (Sahoo et al. 2020).

Physical sorption or physisorption involves the formation of weak physical interactions where no exchange of electrons is observed. Weak van der Waals forces are typically between the surface and the sorbate. Since the forces involved are weak, this sorption can be easily reversed (for example, by heating). The physisorption energy ranges from 15 to 30 kJmol⁻¹ and is stable at temperatures below 150 °C (Wandelt 2016).

Chemical sorption or chemisorption implies the formation of chemical bonds between the sorbate and the surface site. In chemical sorption, an exchange of electrons occurs between the adsorbed molecule and the surface site. A high interaction energy characterises this sorption mechanism, equivalent to strong chemical bonds (≥100 kJmol¹), and therefore, it is more stable at higher temperatures than physisorption.

Electrostatic sorption involves the formation of Coulomb attractions between adsorbed ions and charged functional groups. The term "electrostatic sorption" is explicitly used to indicate ion exchange (Sahoo et al. 2020).

The term "Adsorption" is used to describe the enrichment of an adsorbate (gaseous, liquid, or solid) on external or internal surfaces of solids; in the same sense, it can be described as the accumulation of a substance in the interphase of a surface (IUPAC 2009). According to the second law of thermodynamics, the adsorption of substances on solids takes place to reduce the free surface energy of the solid (Sahoo et al. 2020). The energy associated with the chemical bond formation on the solid surface can be depicted by means of Lennard-Jones potential energy curve (Lennard-Jones 1932). Therefore, Lennard-Jones potential can be used to explain the energetic phenomenon occurring during an adsorption or desorption process (Figure 3.1).

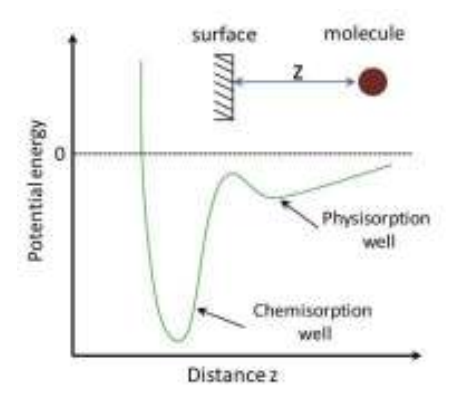


Figure 3.1 Lennard-Jones-type diagrams: potential energy versus distance (Sahoo et al. 2020). Represents the molecule's energy as a function of the distance (z) from the mass centre of the molecule to the surface.

The adsorption potential well can be seen as the result of the balance of two forces: van der Waals attraction and the repulsion between the electron clouds at the surface and that of the adsorbed molecule. When the adsorbate reaches the well, it is adsorbed (trapped) by this potential energy until it acquires enough energy to be desorbed. Hence, the lower the energy of the adsorbate, the easier it will be for him to fall and stick in the chemisorption well. The chemisorption well is located below the physisorption one because the bonds formed are short-ranged and stronger for the former.

According to thermodynamics, any system will behave to reduce its energy until it reaches the lowest value of Gibbs energy (G). For an adsorption process that takes place at a constant temperature, the expression for the energy is given by the following expression (Equation 3.1):

$$\Delta G = \Delta H - T \Delta S$$
 Equation 3.1

Where ΔH and ΔS are, respectively, the changes in enthalpy and entropy during the adsorption, a spontaneous process is always accompanied by decreased Gibbs energy (ΔG < 0). In terms of enthalpy, this process is always exothermic for adsorption in the liquid phase, which implies a negative ΔH value.

Liquid adsorption occurs at an interface surrounded by solvent molecules that can be firmly adsorbed and must be displaced from the surface to allow the adsorbate to reach the site. In the case of aqueous solutions, and when working with ion adsorbates, the accumulation of ions near the surface can be described by models based on the double-layer structure, the oldest the one developed by Helmholtz in 1874 (Kolb 2002). The model states that an atomic distance separates two layers of opposite charge form at the adsorbent-adsorbate interface. The model was afterwards modified by Gouy and Chapman, who introduced the creation of a diffuse layer. Later on, Stern combined the two previous models, defining two regions of ion distribution, the inner (IHP) and outer (OHP) Helmholtz planes (Figure 3.2), which can be represented as follows:

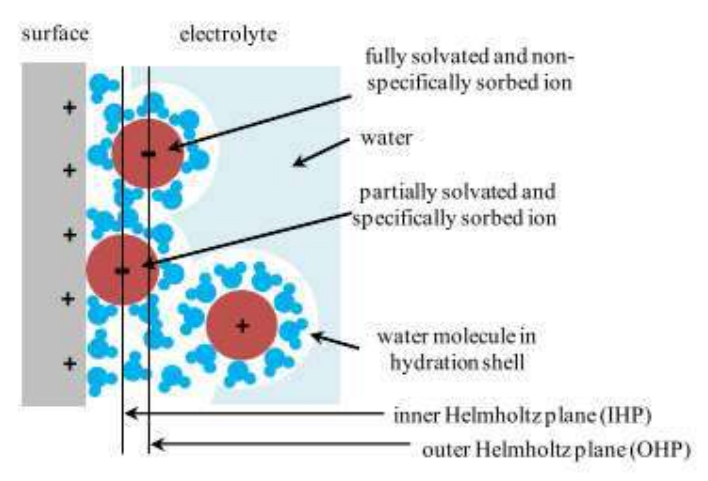


Figure 3.2 Model of the double-layer structure of the adsorbent-adsorbate interface with examples of specific and nonspecific ion adsorption (Kolb 2002).

A layer of solvent molecules surrounds all particles in the solution; therefore, the interaction is not only with the adsorbent surface but also with the solvent. Two types of adsorptions can be identified depending on the specificity of the process. When the particle can be adsorbed at a well-defined geometry pore, this type of chemisorption is called specific adsorption. This leads to the need to discard, at least partially, the solvent molecules that surround the particle to be adsorbed. In order to achieve that, the bond energy between the ion and the surface may overcome the energy of partial desolvatation. If the solvent-ion interactions are stronger than ion-surface interactions, ions preserve their hydration shell. In this case, adsorption is nonspecific (Sahoo and Prelot 2020), and sorbed ions are principally bound by electrostatic attraction, known as physisorption, where weak forces are involved. Specifically, adsorbed ions form the inner Helmholtz plane, whereas non-specifically sorbed ions form the outer Helmholtz plane.

Depending on the adsorbent surface properties, the pollutant's characteristics, and the physicochemical conditions, there are many different types of interactions (Thomas et al. 2002). Electrostatic interactions and ion exchange, surface complexation (sorption of reactive solute occurs on specific sites of the adsorbent), dissolution (when solid is partially dissolved in suspension), co-precipitation (when released ions react with species in the solution and precipitate on the surface), surface precipitation (at variance with the former), π - π interactions, H-bonding, Lewis acid-base interactions, hydrophobic interactions, n- π electron donor-acceptor (EDA), etc. The organic molecule's interactions (pesticides, drugs, dyes, etc.) are mainly governed by hydrophobic and π - π interactions (Sahoo et al. 2020). Hence, the interactions involved are usually complex; an example of this is the mechanism between methylene blue (MB) and an AC derived from chitosan hydrogel-coated tea saponin (Figure 3.3) involving electrostatic attraction, H-bond, π - π interactions, and van der Waals forces (Ma et al. 2021).

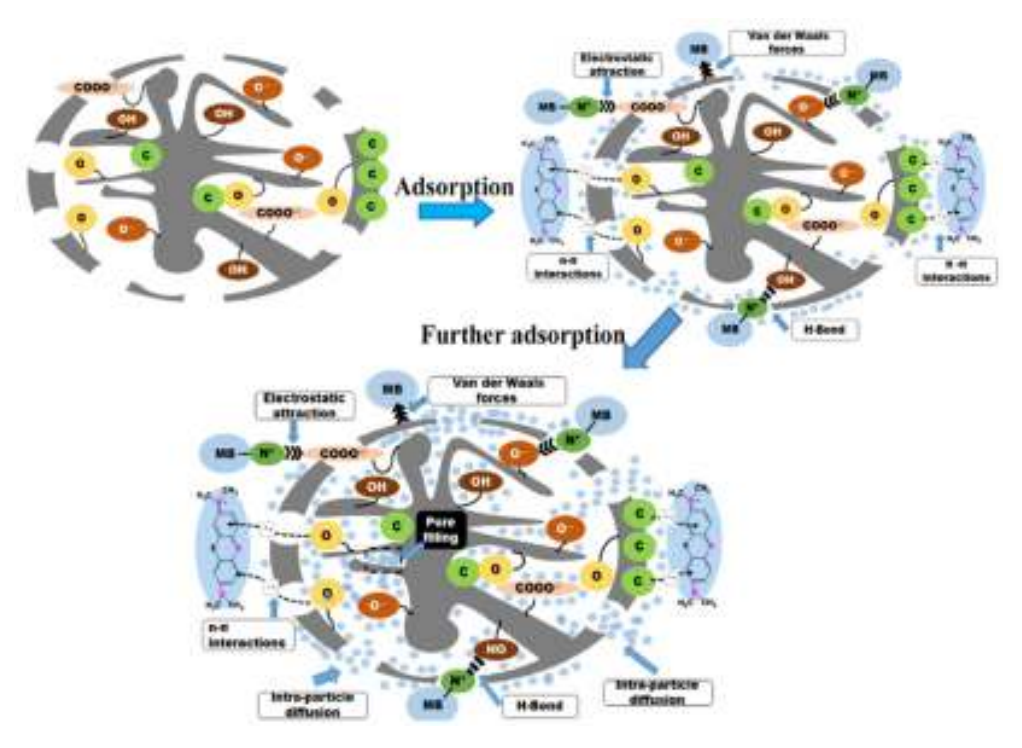


Figure 3.3 Schematic representation of methylene blue adsorption on AC (Ma et al. 2021).

The adsorption in the liquid phase strongly depends on many factors, covering the nature of the adsorbent and the reaction medium. Those parameters include the textural properties of the adsorbent, the dosage, physicochemical properties and chemistry composition of the adsorbent, chemistry and physical properties of the adsorbate, as well as the concentration and characteristics of the liquid phase, like pH and ionic strength

(IS). In addition to that, the experimental procedure is also critical since the process implies a mass transfer. Features like contact time, stirring speed, and mixing method must be carefully optimised. This has an impact on the kinetics, as well as the intrinsic properties of the materials. They significantly influence kinetic parameters, such as intraparticle and external (film) mass transport processes (Figure 3.4), and thus affect the design of an adsorbent system.

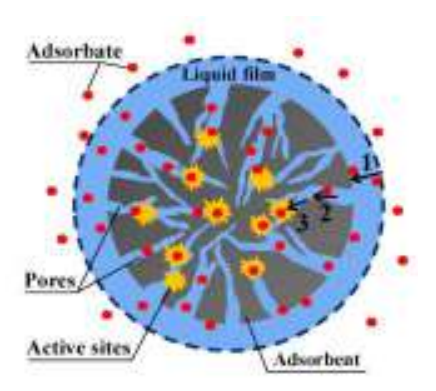


Figure 3.4 Adsorption mass transfer steps (1- external diffusion, 2- internal diffusion, 3- adsorption on active sites) (Wang et al. 2020).

In summary, the adsorption process encompasses two main aspects: the kinetic and the thermodynamic (this last contemplates the adsorption mechanism), and both need to be studied in separate ways. In all cases, the whole process entails four steps:

- 1 Bulk solution transport.
- 2 Film diffusion transport.
- 3 Pore/surface transport.
- 4 Adsorption.

As already mentioned, the adsorption mechanism will depend on the adsorbate and adsorbent natures (Figure 3.5). However, it is also intimately connected with the working conditions. In this regard, all the parameters affecting the adsorption process have been considered throughout this work, and each will be studied in detail.

Several adsorption and kinetic models were studied, and their rationale is explained here (following sub-sections).

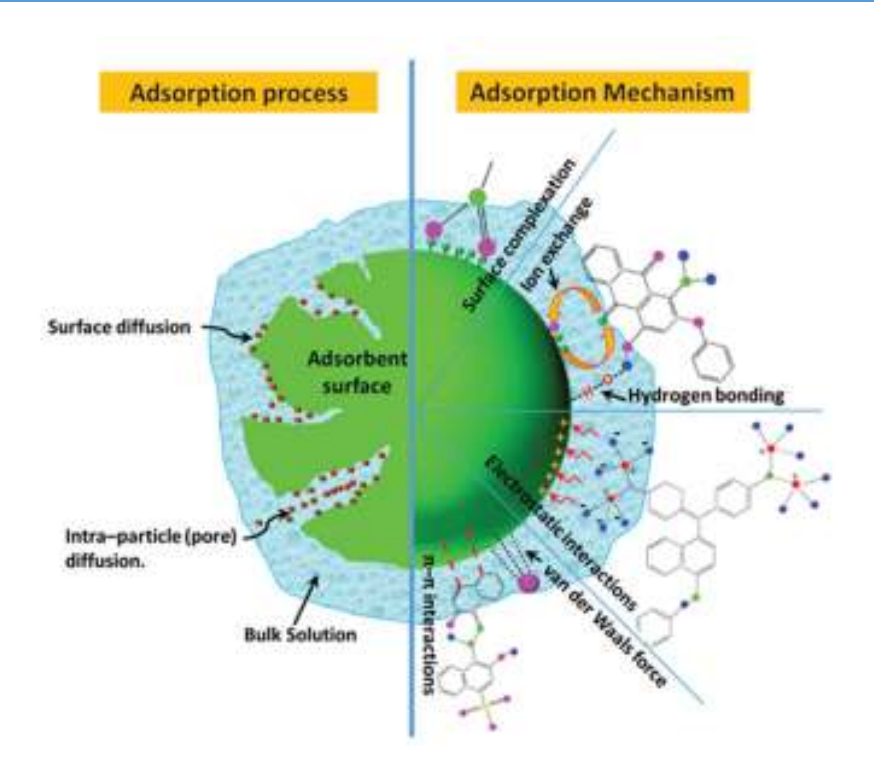


Figure 3.5 Schematic representation of adsorption processes and mechanisms (Dutta et al. 2021)

3.2 Adsorption isotherms from monocomponent solutions

The isotherm is the graphical representation of the mathematical relationship between the amount of adsorbate adsorbed per carbon mass unit and the concentration of the solute once the equilibrium reaches a constant temperature. Among the more widely applied models are Langmuir, Freundlich and Elovich (Cooney 1998). This section presents a brief description of each model and its considerations.

3.2.1 Langmuir model

The Langmuir isotherm equation (Langmuir 1918) is the first theoretically developed adsorption isotherm and still has an essential position in physisorption as well as chemisorption theories (Bansal et al. 2005). This theory is based on certain assumptions that are:

- The adsorbed entities (atoms, molecules, or ions) are attached to the surface at definite localised sites.
- Each site accommodates one and only one adsorbed entity, which leads to the formation of a monolayer.

• The energy state of each adsorbed entity is the same at all sites on the surface, independent of the presence or absence of other adsorbed entities at neighbouring sites. Thus, the Langmuir model assumes that the surface is perfectly smooth and homogeneous and that the lateral interactions between the adsorbed entities are negligible.

This model establishes a dynamic equilibrium where both processes, adsorption and desorption, take place with the same kinetic. This implies that the velocity at which the molecules are adsorbed is the same with which the molecules leave the surface. The mathematical expression (Equation 3.2) for the model:

$$q = \frac{q_m K_L C_e}{1 + K_L C_e}$$
 Equation 3.2

Where q (mmolg⁻¹) is the quantity of adsorbate adsorbed per carbon mass unit, q_m (mmolg⁻¹) is the maximum adsorption capacity for the adsorbent to adsorb the working adsorbate, C_e (mmolL⁻¹) is the concentration of solute at the equilibrium, K_L (Lmmol⁻¹) is the constant of Langmuir that relates the affinity between adsorbate and adsorbent, it is therefore considered as the equilibrium constant of sorption interaction. Thus, it would be related to the binding energy of adsorption (Aksu 2005).

3.2.2 Freundlich model

In many cases, the adsorption follows the behaviour predicted by the Freundlich model, which assumes the existence of many types of sites acting simultaneously, each with a different free energy of sorption, and that there is a large number of available sites (Freundlich 1926). The empirical expression (Equation 3.3) for this model:

$$q = K_F C_e^n$$
 Equation 3.3

where K_F (molkg⁻¹) (molL⁻¹)⁻ⁿ is the Freundlich constant, and n is the Freundlich exponent related to the adsorption intensity. It usually applies to a small range of concentrations and, in particular, to dilute solutions. The Freundlich model assumes that many sites act simultaneously, each with a different free energy of sorption and that many available sites exist. The Freundlich exponent is related to the diversity of free energies associated with the solute sorption by the multiple components of a heterogeneous sorbent (Weber 1996).

For n = 1, the isotherm is linear, and constant free energy of sorption can be assumed for all sorbate concentrations (in this case, K_F can be seen as a partition coefficient between the solution and the solid phase) (García-Zubiri et al. 2009). However, n < 1 values depict adsorption where the sorption intensity decreases as the concentration increases, and on the contrary, n > 1 means that intensity and concentration follow the same tendency (Singh 2016).

3.2.3 Elovich model

The Elovich isotherm model assumes that adsorption sites increase exponentially with adsorption, which implies multilayer adsorption (Hamdaoui et al. 2007). The linearised form of the Elovich isotherm model (Equation 3.4) shows that the slope and intercept of the plot ln (qe/Ce) versus qe give maximum adsorption capacity (qm) and Elovich equilibrium constant K_E (Lmg⁻¹), respectively (Manjunath et al. 2017):

$$In\left(\frac{q_e}{C_e}\right) = InK_E q_m - \frac{1}{q_m} q_e$$
 Equation 3.4

3.3 Isotherm Models Applied to Multicomponent Adsorption

For a multi-component system, all the components of the solution may be likely to be adsorbed. However, elucidating the adsorption behaviour is not simple since the process could follow different routes. The adsorption can be unspecific, known as Noncompetitive (Chang et al. 2015), or the surface of the adsorbent may show a preference for one of the components depending upon the nature of the solid surface as well as the nature of the adsorbates present in the solution. This implies that there is competition among the adsorbates for the adsorbent surface. Thus, the adsorption in this situation is commonly called *Competitive Adsorption* (Bansal et al. 2005). Among the latter, several models predict the adsorption capacity of the adsorbent regarding the working adsorbate, assuming different types of interferences.

For this work five models were study regarding the adsorption of the binary mixture SMX-MNZ, Non-competitive (NC), Langmuir Multicomponent (LM), Modified Langmuir Multicomponent with discount factor δ (MLM δ), Extended Langmuir Multicomponent (ELM), and Modified Langmuir Multicomponent with Interaction Factor (η) (MLM η) (Apiratikul et al. 2006).

3.3.1 Non-competitive adsorption system (NC)

Non-competitive adsorption is the product of the nonspecific selectivity of the adsorption sites in a multicomponent system (Chang et al. 2015). In a binary adsorption system, it is assumed that adsorption sites are mutually or partially independent and that there is no adsorption interference by the adsorbates (Bonomo et al. 2003). The empirical expression (Equation 3.5) of the isotherm according to Langmuir is written as follows:

$$q_{e,i} = \frac{q_{max,i} K_{L,i} C_{e,i}}{1 + K_{L,i} C_{e,i}} + \frac{q_{max,j} K_{L,j} C_{e,i}}{1 + K_{L,j} C_{e,j}} + \cdots$$
 Equation 3.5

where, $q_{e,i}$ (mmolg⁻¹) is the equilibrium adsorption capacity of the adsorbate of interest per adsorbent mass unit; $q_{max,i}$ (mmolg⁻¹) is the maximum adsorption capacity of i in single component system (Equation 3.2), $K_{L,i}$ is the Langmuir constant for the adsorption of the adsorbate of interest in single component solution, C_e (mmolL⁻¹) is the equilibrium concentration of the multicomponent adsorption for each component present in the medium that presents adsorption onto the adsorbent material.

3.3.2 Langmuir Multicomponent (LM)

The Langmuir single adsorption isotherm can be extended for use in a system with N adsorbates, the empirical expression (Equation 3.6) for this situation:

$$q_{e,i} = \frac{q_{m,i}K_{L,i}C_i}{1 + \sum_{j=i}^{N} K_{L,j}C_j}$$
Equation 3.6

where, $q_{e,i}$ is the adsorbate uptake of the component i once the equilibrium was reach, N is the number of the components that can be adsorbed, C_j (j = 1, 2, ..., n) is the equilibrium concentration of each component, while $q_{m,i}$ and $K_{L,i}$ are the Langmuir constants as obtained from the corresponding single component sorption isotherms. This model assumes that competition between different components depends exclusively on the concentration ratio and can be applied to predict the adsorption behaviour of a material in a multi-component system using the single components parameters (Papageorgiou et al. 2009). However, this model was reported to function correctly as long as the adsorption capacity for both compounds is similar (Al-Asheh et al. 2000). Other authors

assumed that some adsorption occurs without competition because not all sites are available to all solutes (Leyva-Ramos et al. 2001). They modified the bi-solute Langmuir isotherm for systems in which the $q_{m,i}$ values of components are different (Jain et al. 1973), proposing the following isotherm for the solute with the higher $q_{m,i}$ (Equation 3.7):

$$q_{e,i} = \frac{(q_{m,i} - q_{m,j})K_{L,i}C_i}{1 + K_{L,i}C_i} + \frac{q_{m,j}K_{L,i}C_i}{1 + K_{L,j}C_j}$$
Equation 3.7

The expression for the compound with the lower q_m is the same as represented in Equation 3.5. The constants are from single solute Langmuir isotherms. In Equation 3.7, the difference between the maximum molar uptakes is the number of sites with non-competitive adsorption.

In this work, both models were applied depending on the results of the single solute isotherms.

3.3.3 Modified Langmuir Multicomponent with discount factor δ (MLMδ)

This model adds the term δ to the binary Langmuir isotherm (Garke et al. 1999). The correspondent modified isotherm (Equation 3.8) expression is as follow:

$$q_{i} = \frac{K_{Li}C_{i}[(1+K_{Lj}C_{j})q_{m,i}-K_{Lj}C_{j}q_{m,j}\delta]}{1+K_{Li}C_{i}+K_{Lj}C_{j}+(1-\delta)K_{Li}C_{i}K_{Lj}C_{j}}$$
Equation 3.8

with
$$\delta = \frac{q_{m,i}}{q_{m,j}}$$

where values q_m , K_L and C come from the corresponding single solution. In a two-component system, competition for a particular site is only relevant if both molecules have physical access. If molecule 1 is larger than molecule 2, only a fraction of the adsorption sites for molecule 2 are available to molecule 1, which is expressed as $0 < \delta \le 1$. Hence, this model considers the exclusion effects of pore size, defining a discount factor (δ) .

3.3.4 Extended Langmuir Multicomponent (ELM)

This model assumes uniform pore size distribution, leading to the competition of the adsorbates for the same adsorption sites since they are equal in terms of energy (Yang 1987). The model is described as follow (Equation 3.9):

$$q_{i=\frac{q_{max}K_{L,i}c_{i}}{1+\sum_{j=i}^{N}K_{L,j}c_{j}}}$$
Equation 3.9

where q_{max} and K_L are the Langmuir multicomponent parameters, which are obtained by correlating the equilibrium data for each component in the multicomponent system. In this model q_{max} represents the adsorbent's maximum adsorption capacity for the N adsorbates present in the medium.

3.3.5 Modified Langmuir Multicomponent with Interaction Factor (η) (MLMη)

This model incorporates an interaction factor (η) that corrects the Langmuir isotherm considering competitive effects. This interaction factor is specific to each compound in a given system and depends upon the other compounds present (Leyva-Ramos et al. 2001; Srivastava et al. 2006). The empiric expression (Equation 3.10) for this model is as follows:

$$q_i = \frac{q_{m,i} K_{L,i} \left(\frac{c_i}{\eta_i}\right)}{1 + \sum_{j=i}^{N} K_{L,j} \left(\frac{c_j}{\eta_j}\right)}$$
Equation 3.10

where q_{mi} , $K_{L,i}$ and $K_{L,j}$ are the constants that comes from the single isotherm adsorption and ηi is the interaction factor. The value of η allow to identify which compound show a bigger competitive effect, since while bigger the value, smaller is the affinity of the adsorbent surface for the compound in liquid phase.

Another form to express the interaction is establishing a factor that considers the interaction between adsorbates, it is represented as $\eta_{i,j}$ (Equation 3.11) (Leyva-Ramos et al. 2001):

$$q_i = \frac{q_{m,i} K_{L,i} \left(\frac{c_i}{\eta_{ii}}\right)}{1 + \sum_{j=i}^{N} K_{L,j} \left(\frac{c_j}{\eta_{ij}}\right)}$$
Equation 3.11

3.4 Kinetic models

There are several models that describe the adsorption process kinetic that envisage different aspects regarding the mechanism. Those studies, allow to stablish the residence conditions that are required for the system to reach equilibrium, which implies that the adsorbent material adsorbed the maximum adsorbate quantity for the working conditions stablished. The kinetic models can be divided into two main groups: the Reaction Models originated from the chemistry reaction kinetic models (Pseudo-first Order (PFO), Pseudo-second Order (PSO), and Elovich). The second group encompass the Diffusion models, these are always built on the base of three consecutive steps. The first step involves diffusion throughout the liquid film surrounding the adsorbent particles, known as External Diffusion or Film Diffusion. The second instance implies the diffusion inside the liquid within the pore, known as Internal Diffusion or Intraparticle Diffusion. The last step involves the adsorption and desorption of the adsorbate at the active site, known as Mass Action (Qiu et al. 2009). This last instance is very fast for processes that involve physisorption; for this reason, the first two steps generally rule the kinetic.

3.4.1 Pseudo-first order (PFO)

The PFO model is derived from the linear rate model, assuming that the equilibrium amount is constant throughout the experiment and equal to the final concentration in the solid (Brandani 2021). Lagergren first proposed this model in 1898 (Equation 3.12) with the following expression:

$$\frac{dq_t}{dt} = k_1(q_e - q_t)$$
 Equation 3.12

Integrating the equation as mentioned earlier for the conditions of $q_0 = 0$, $t_0 = 0$ and linearising the expression yields (Equation 3.13):

$$In(q_e - q_t) = Inq_e - k_1 t$$
 Equation 3.13

The PFO parameter qe is the equilibrium adsorption amount, and k_1 is the parameter frequently used to describe how fast the adsorption equilibrium is achieved. It has been reported that the PFO model was theoretically consistent and equalled to the linear driving force (LDF, see equation 3.17) model when the linear model (Equation 3.14) could represent the adsorption isotherm (Rodriguez and Silva – Wang).

$$q_e = KC_e$$
 Equation 3.14

3.4.2 Pseudo-second order (PSO)

The pseudo-second-order (PSO) model is derived from the quadratic driving force (QDF) model (Equation 3.15).

$$\frac{dq_t}{d_t} = k_{QDF}(q_e - q_t)^2$$
 Equation 3.15

Equation 3.14 is a kinetic model with a rate of adsorption that decreases monotonically in time since (qe – qt) constantly decreases throughout the experiment. The QDF model can be seen as a concentration-dependent LDF model where the mass transfer coefficient goes to zero at equilibrium. The QDF expression could physically represent a particular chemisorption process; however, it does not represent the physisorption situation where the mass transfer coefficient is not zero at equilibrium (Brandani 2021). The PSO model is obtained if the equilibrium concentration is assumed constant and equal to the final value (Equation 3.16).

$$\frac{dq_t}{d_t} = k_2(q_e - q_t)^2$$
 Equation 3.16

This equation can be solved using the initial conditions $q_t = 0$ when t = 0, and the resultant expression is normalised (Equation 3.17).

$$\frac{1}{q_t} = \frac{1}{k_2 q_e^2} \frac{1}{t} + \frac{1}{q_e}$$
 Equation 3.17

As in the PFO model, the k₂ parameter is a magnitude that reflects how fast the adsorption process is.

3.4.3 Film Diffusion (FD)

Within a solid/liquid adsorption system, the solute accumulation degree on the solid surface is equal to the solute transfer through the liquid film, according to the mass balance law (Equation 3.18):

$$\frac{\delta \bar{q}}{\delta t} = K_f S_0(C - C_i)$$
 Equation 3.18

C and C_i represent the solute concentration at the surface and within the liquid, respectively, K_f is the mass transfer coefficient at the film, and S_o is the particle surface

area of the solid per volume unity. Equation 3.17 is known as the *Linear Driving Force* (LDF).

Another expression for this model uses the equation that represents the mass transfer at the film (Equation 3.19):

$$In\left(1 - \frac{q_t}{q_e}\right) = -R^1 t$$
 Equation 3.19
$$R^1 = \frac{3D_e^1}{r_0 \Delta r_0 k'}$$

 R^1 (min⁻¹) is the diffusion constant of the liquid film, D_e^1 (cm²min⁻¹) is the effective diffusion coefficient, r_o (cm) is the adsorbent particle radius, Δr_o (cm) is the film thickness and k' is the adsorption equilibrium constant. This model has been tested in several liquid/solid systems for phenol adsorption, for instance, using a polymeric adsorbent (Qiu et al. 2009).

3.4.4 Intraparticle Diffusion (ID)

A typical intraparticle diffusion model is the so-called homogeneous solid diffusion model (HSDM), which can describe mass transfer in an amorphous and homogeneous sphere. A simplified and linearised equation can be applied as follows (Equation 3.20), being generally valid in a short experience time (Cooney 1999).

$$In\left(1 - \frac{\bar{q}}{q_m}\right) = \frac{-D_S \pi^2}{R^2} t + In\frac{6}{\pi^2}$$
 Equation 3.20

 D_s is the intraparticle diffusion coefficient, R is the total particle radius, and \bar{q} represents the average value for the quantity adsorbed by a spherical particle at any time. Equation 3.19 is valid for short times since it assumes a constant concentration at the surface of the solid.

A second expression for this model was raised by Weber-Morris (Weber 1963), where the degree of solute adsorption onto the adsorbent varies proportionally with $t^{1/2}$ in place of t (Equation 3.21).

$$q_t = k_{int}t^{1/2} + B$$
 Equation 3.21

Where k_{int} is the intraparticle diffusion constant, and B represents the boundary layer thickness.

Finally, *Dumwald-Wagner* proposed another model for the ID (Equation 3.22), and it has proved to work properly for several systems (Wang 2004):

$$log(1 - F^2) = -\frac{\kappa}{2.303}t$$
 Equation 3.22

Where F is the fractional approach to equilibrium and K (min⁻¹) the rate constant of adsorption. A plot of $log(1 - F^2)$ versus t should be linear (Aniagor et al. 2023).

3.5 The chemistry of the aqueous solution

Several factors effectively affect the adsorption process, like the nature and characteristics of the adsorbent, the nature of the adsorbates and the environmental conditions. Two significant effects are related to the solvent chemistry, pH and ionic strength. Hence, both parameters have been considered and studied separately and studied separately.

3.5.1 The effect of solution pH on the adsorption

The pH of the working solution directly affects the adsorption behaviour of the carbon adsorbent since it can alter the surface charge of the adsorbent and the existing form of the adsorbate, depending on its structure. The hydrated carbon surface exhibits ion exchange properties, and there is a correlation between ion exchange capacity and the net surface charge carried by the solid. This behaviour is pH-dependent because the surface can function as a Brønsted acid or base. Therefore, a negative net charge leads the solid to function as a cation exchanger, while a positive net charge results in an anion exchanger behaviour. In this sense, a surface's propensity to either positively or negatively charge as a function of the pH is the pH value at which the surface carries zero net charge. This value is designated as the point of zero charge, pHpzc (Noh et al. 1989). According to this, the surface of the adsorbent presents a positive charge in solutions with pH values below the pHpzc and a negative charge above it (De Rezende et al. 2019).

In addition to the effect mentioned earlier, the adsorbate molecule can also be affected by the pH value, depending on the capacity of the functional groups to exchange protons. Thus, electrostatic attraction or repulsion is feasible to influence the adsorption process.

3.5.2 The ionic strength effect

Ionic strength (IS) is one of the significant factors affecting adsorption; the extent varies depending on the physicochemical characteristics of the adsorbent and adsorbate (Bernal et al. 2020). The expression that quantifies the IS is as follows (Equation 3.23):

$$I = \frac{1}{2} \sum z_i^2 c_i$$
 Equation 3.23

Where I is IS, z_i and c_i represent the ionic charge and concentration of ion i, respectively. The presence of electrolytes (neutral or charged) in an aqueous solution containing an organic adsorbate is expected to affect the adsorption capacity throughout the interactions established between the different molecules (solvent-solute and solute-adsorbent). Depending on the nature of the molecules involved in a particular system, the adsorption capacity may increase or decrease (Kyriakopoulos et al. 2006). For instance, the adsorption of heavy metals decreases with the concentration of Na ions due to the binding between these ions and negative charges on the adsorbent surface (in biomass), the same sites that bind the heavy metals. However, the protein adsorption increases with the concentration of Na and Ca ions due to the formation of π -cation interactions with graphene layers, creating positively charged surface sites which then bind to negative charges in the adsorbate molecules and enhance the adsorbed amount (Zhang et al. 2019). Structure-making salts like NaCl or any other salt consisting of small ions enhance the structuring of aqueous phases and, thus, the cohesive energy in water due to their strong interactions with water dipoles. The increase in structure has several effects on the properties of the aqueous solutions, such as an increment in viscosity (Endo et al. 2012).

On the other hand, the salting out must be considered due to the effect on the solubility of nonelectrolytes in water. The salting-out is induced by the movement of solvent from the hydration layer of nonelectrolytes to the hydration layer of ions with great polarity or affinity for water (Zhang et al. 2019).



"La risa mata el miedo, y sin el miedo no puede haber fe, porque sin miedo al Diablo ya no hay necesidad de Dios."

El nombre de la rosa

Umberto Eco

4.1 Working strategy

The strategy followed for the experimental work organisation is summarised below (Figure 4.1) for clarity purposes. The following sections describe the details of each step.

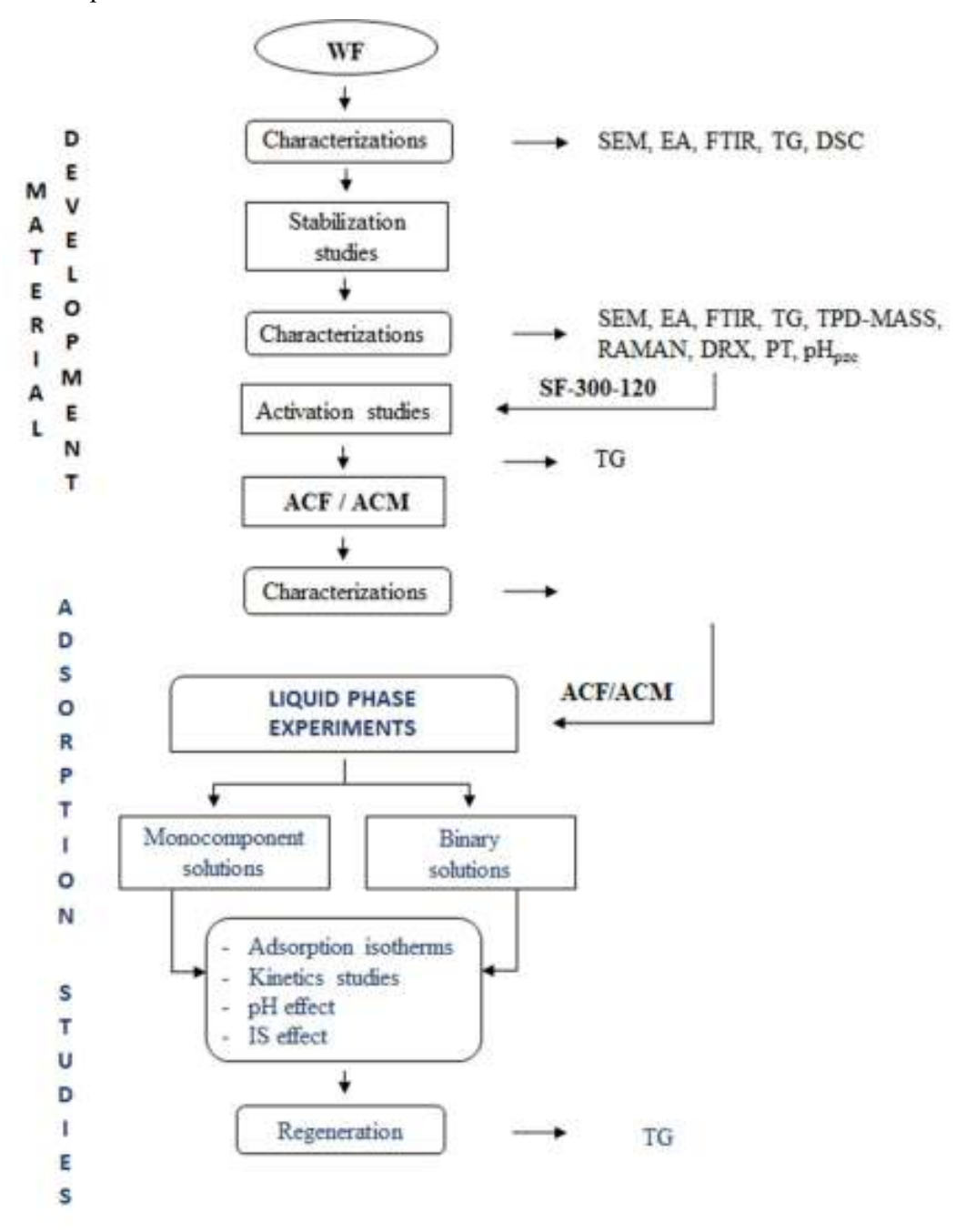


Figure 4.1. Working scheme.

4.2 Materials and treatments

The as-received wool fibres underwent several treatments, turning them into different materials in the process; each is described in this section. The drugs used for this work and their physicochemical features are also displayed here.

4.2.1 Precursor

Sheep Merino wool fibres (WF) provided by the Uruguayan wool secretariat (SUL by its Spanish initials) were used as precursors. The as-received WF (ca. 29 µm diameter) were already clean and spun (Figure 4.2).



Figure 4.2 Image of the received Wool-fibres.

4.2.2 Stabilised material

An oxidative treatment was obtained from the stabilised fibres (SF) used in this work. Two protocols were followed for this:

Protocol 1: wool fibres (WF) were placed inside a tubular horizontal furnace (THF, CARBOLITE FURNACES) by rolling them up around a stainless steel hollow cylindrical mesh (ca. 4 cm diameter, 23 cm length, Figure 4.3) under an air atmosphere.



Figure 4.3 Stainless steel hollow cylindrical mesh that was placed inside the THF.

After the stabilisation, the samples were cooled down to room temperature under N₂ atmosphere flow (ca. 100 mL min⁻¹), as shown (Figure 4.4).

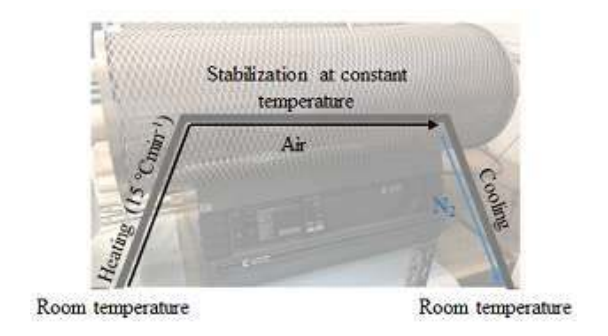


Figure 4.4 Scheme of the temperature treatment under an oxidising atmosphere.

Protocol 2: WF samples were placed inside a muffle, NABERTHERM, under an air, atmosphere rolled up around a stainless steel hollow cylindrical mesh (ca. 20 cm diameter, 15 cm length, Figure 4.5). After the stabilisation, the samples were removed from the muffle and left at room temperature to cool down (Figure 4.6).



Figure 4.5 Stainless steel hollow cylindrical mesh that was placed inside the muffle.

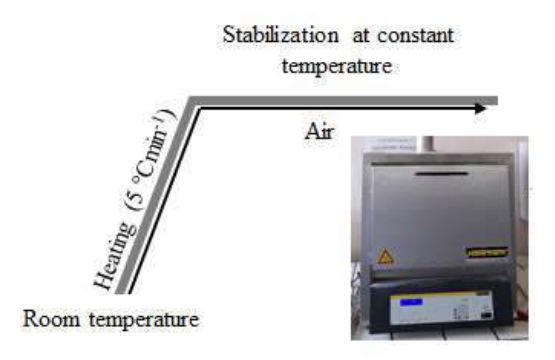


Figure 4.6 Scheme of the temperature treatment under an oxidising atmosphere; the cooling is carried out outside the equipment at room temperature.

In both cases, the oxidative stabilisation was carried out under an air atmosphere (100 mL min⁻¹), varying the final temperature and time of exposure according to the thermogravimetric analysis carried out in the WF (for the temperature and time selection, see Chapter V, Table 5.2) (heating rate 5 °C min⁻¹). All the experiences were carried out in triplicate to assess the replicability of the method.

4.2.3 Activated carbon materials

The stabilised carbon fibres were activated (applying physical and chemical activation) to assess the most suitable procedure.

4.2.3.1 Physical Activation

First, the stabilised fibres were carbonised at 800 °C under N₂ flow, 100mLmin⁻¹, for 30 min to obtain the carbon fibres (CFs). Subsequently, the CFs were physically activated under different conditions by varying temperatures and CO₂ flow. This allows a comparison of the porosity development in two operating conditions: chemical- and diffusion-controlled processes (for the control descriptions, see Chapter II).

Physical activation by diffusion control: the CFs were activated under CO_2 flow, 200 mLmin⁻¹ (diffusion control), at 950 °C testing different activation times (from 30 min up to 4 hours) and finally were left cooling until room temperature under N_2 flow (Figure 4.7). The activation temperature was selected based on the reactivity profile of the CF under the CO_2 atmosphere (for the temperature selection, see Chapter VI, section 6.1). The nomenclature for these samples is ACF-d-t-D, where d stands for date, t for time and D for diffusion control.

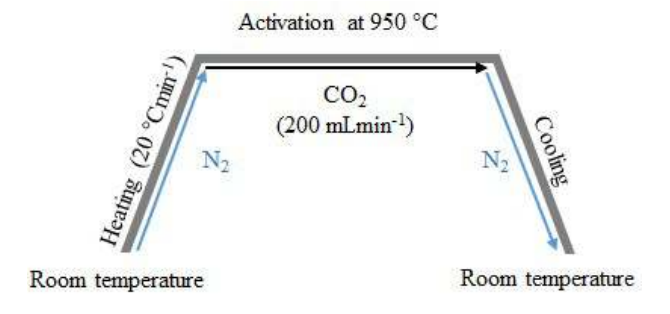


Figure 4.7 Activation under diffusion control.

Physical activation by chemical reaction control: the CF were activated at 875 °C under a CO_2 flow of 10 mLmin⁻¹, testing different activation times (from 30 min up to 4 hours); the above cooling method was used (Figure 4.8). The activation temperature was selected based on the reactivity profile of the CF under the CO_2 atmosphere (for the temperature selection, see Chapter VI, section 6.1). The nomenclature assigned to these samples is ACF-d-t-CR, where d stands for the date, t for time, and CR for chemical reaction.

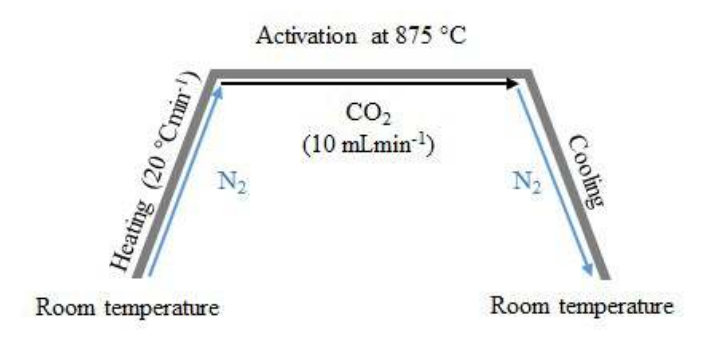


Figure 4.8 Activation under chemical reaction control.

4.2.3.2 Chemical activation

The SFs were activated with KOH (Merck, 90 %) using the solution impregnation described elsewhere (Mestre et al. 2019; Gomis-Berenguer et al. 2017). Briefly, the activating agent was dry mixed with the SF (weight ratio 1:1); subsequently, the minimum quantity of distilled water was added to the mixture and was left stirring at 60 °C until the presence of liquid was not visually detected. The mixture was then dried at 90 °C for 24 hours to allow the evaporation of the moisture. The dry mixture was thermally treated at 600 °C for one hour under an N₂ atmosphere, 100 mLmin⁻¹ (Marsh et al. 2006). Finally, the sample was washed with distilled water at 60 °C until constant pH (Figure 4.9). The samples were labelled ACF-KOH-d-, where *d* stands for the date. The chemical agent selected is known because it leads to high adsorption capacity carbons of extremely narrow microporosity and no mesopores (Marsh et al. 2006). Therefore, to compare both techniques, physical and chemical, the carbons should share similar features.

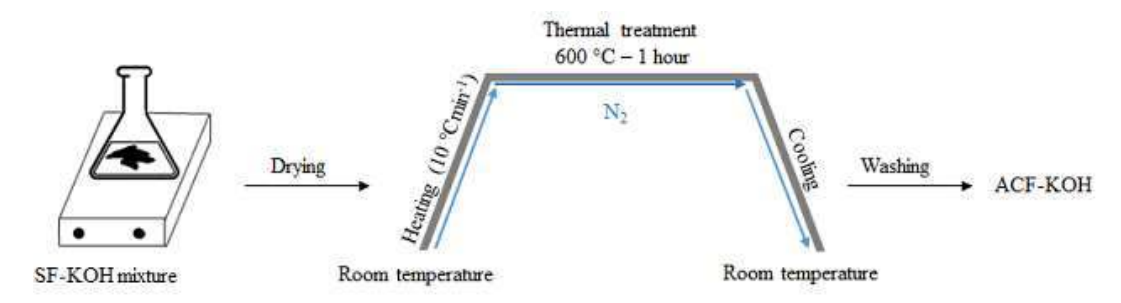


Figure 4.9 Chemical activation process.

A THF (CARBOLITE) was used for all the thermal treatments, coupled with a gas mass flow controller. The gases used for this work were all of the certified quality.

4.2.4 Pharmaceutical compounds

As indicated in Chapter I, three pharmaceutical compounds (PhCs) were investigated in this PhD work as water pollutants (Table 4.1), Acetaminophen (AMP), Sulfamethoxazole (SMX) and Metronidazole (MNZ).

AMP is an analgesic drug (Figure 4.10) used alone or combined with opioids for pain management. It is also used as an antipyretic agent and is characterised by massive consumption worldwide.

SMX (Figure 4.11) is an oral sulphonamide antibiotic, combined with trimethoprim, used to treat various infections of the urinary tract, respiratory system, and gastrointestinal tract. Since 2020, it has been on the European Watch list for its persistent presence in watercourses (Decision 2020/1161/EU 2020).

MNZ (Figure 4.12) is a commonly used antibiotic in the nitroimidazole class. It is frequently used to treat gastrointestinal infections and parasitic infections such as trichomoniasis, giardiasis, and amebiasis. MNZ has been used as an antibiotic for several decades, and its added antiparasitic properties set it apart from many other antibacterial drugs, allowing it to treat a wide variety of infections.

SMX and MNZ are persistent pollutants in watercourses. All the chemicals were purchased from Sigma Aldrich.

(www.drugbank.ca - fdasis.nlm.nih.gov)

Table 4.1 Ph	ysicochemical	characteristics	of the selected	drugs for this work.

Contaminant	Formula	MW	Sol.	pKa	CAS N°
		(gmol ⁻¹)	(mgmL ⁻¹)	(298 K)	
			14,000		
AMP	C ₈ H ₉ NO ₂	151,16	(25 °C)	9.4	103-90-2
			610	1.7 (pK ₁)	
SMX	$C_{10}H_{11}N_3O_3S$	253,26	(60 °C)	5.6 (pK ₂)	723-46-6
			9500		
MNZ	$C_6H_9N_3O_3$	171,15	(25 °C)	2.62	443-48-1

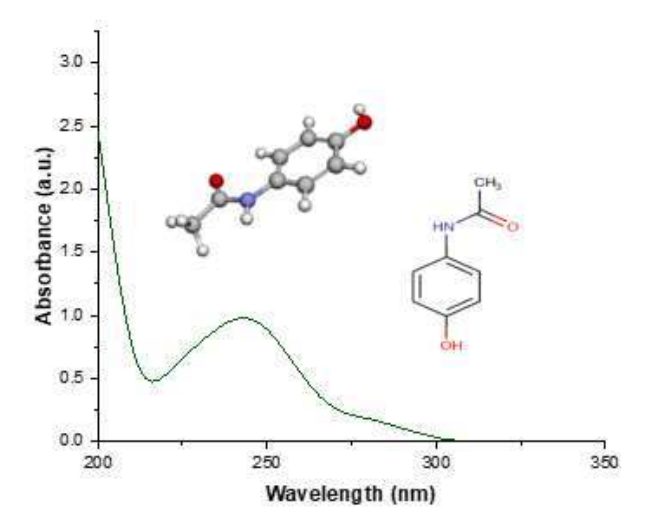


Figure 4.10 Chemistry structure and UV spectra of AMP.

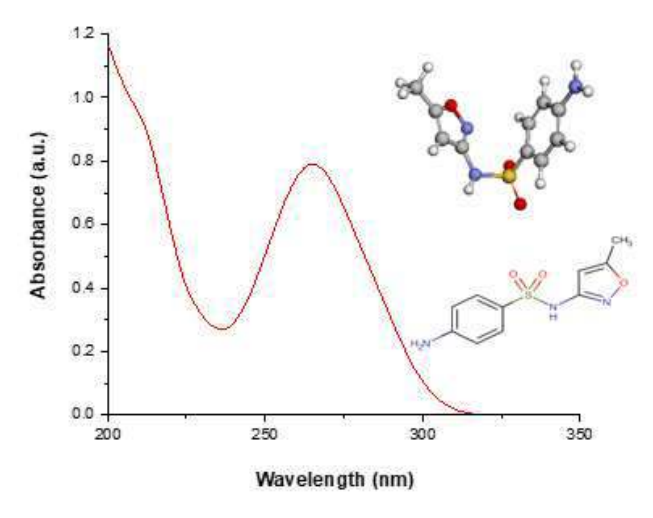


Figure 4.11 Chemistry structure and UV spectra of SMX.

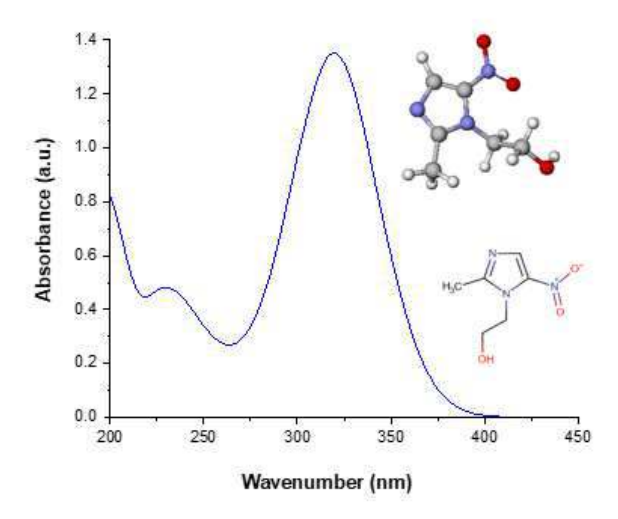


Figure 4.12 Chemistry structure and UV spectra of MNZ.

4.3 Chemical and structural characterisation

When developing novel materials and using a new activated carbon material as an adsorbent, the user must have the most accurate knowledge of the surface's chemistry and the structure's morphology. These features strongly influence the adsorption processes, so studying the material in detail is crucial. Several of the available techniques were applied in this work and will be briefly described in this section.

4.3.1 Textural characterisation

The International Union of Pure and Applied Chemistry (IUPAC) defines "Texture" as the geometry of the hollow space inside the particles (Thommes et al. 2015a). The study of the textural properties of the material comprehends several aspects as following detail:

- Specific surface area is the specific surface area per mass unit of the solid.
- Specific volume of the pores is the total volume of the pores per mass unit of the solid.
- Pore width, assuming a specific geometry.
- Distribution of pore sizes is a measure of the volume of pores for a particular pore size.

The pore width represents the distance between the walls of a slit pore or the diameter of a cylindrical pore (Figure 4.13). According to the pore width, they are

classified into one of three categories: macro, meso or micropores (for the description of the pore sizes classification, see Chapter II, section 2.1).

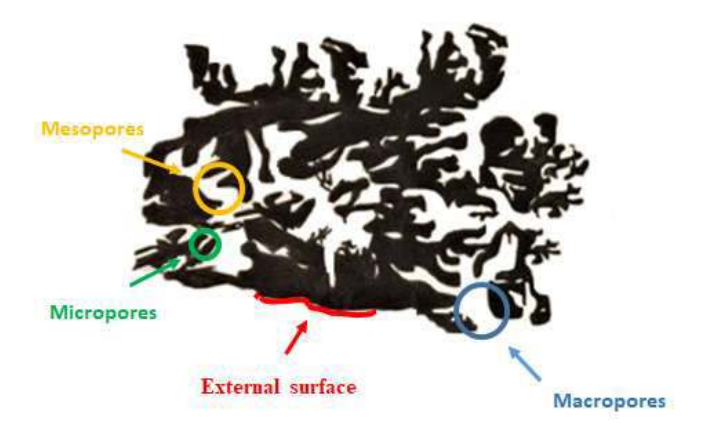


Figure 4.13 Schematic representation of the different pore types established by IUPAC for activated carbon (reproduced by Santina Villarreal).

4.3.1.1 Adsorption-desorption isotherms

The physical adsorption of gases is one of the most widely used techniques to study the structure of solids. When a solid is exposed to gas while confined in a closed space, it adsorbs gas until it reaches equilibrium. Therefore, the pressure of the gas decreases while, at the same time, the mass of the solid increases. The amount of gas the material will adsorb depends on the amount of solid, gas and adsorbent natures, working temperature, and pressure. For a specific adsorbent-adsorbate pair at constant temperature and below the critic temperature for the gas, the moles of gas adsorbed by the solid can be established by the following expression that represents the isotherm of adsorption (Equation 4.1):

$$n = f\left(\frac{p}{p_o}\right)_{T,gas,s\'olido}$$
 Equation 4.1

where p_0 is the solid saturation pressure at the working temperature, and p/p_0 is the partial pressure (Haul 1969). From the recorded gas data, it is possible to estimate the apparent specific surface area, total pore volume, micropore volume and pore size distribution, all by applying the corresponding models. It should be pointed out that by analysing the shape of the gas adsorption isotherm and considering the IUPAC mentioned above classification, it is possible to obtain a first approach regarding the porous characteristics of the studied material (Figure 4.14).

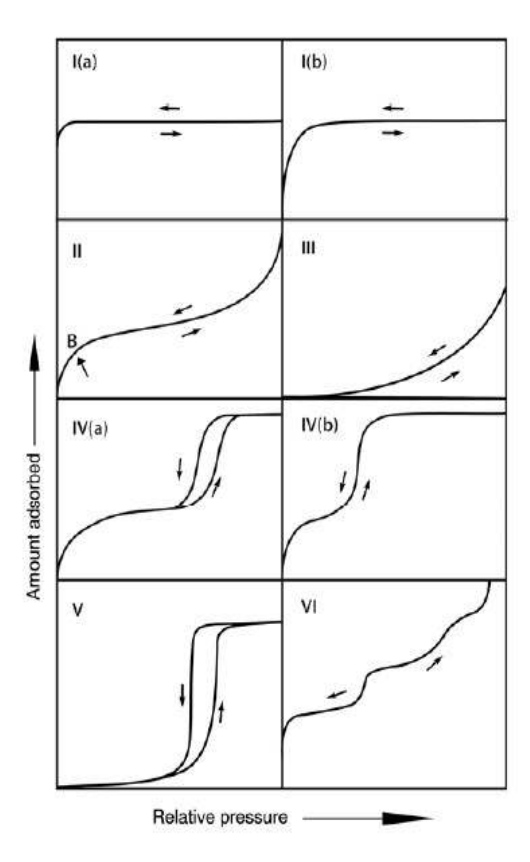


Figure 4.14 Classification according to IUPAC of the gases adsorption isotherms (Thommes et al. 2015).

Reversible type I(a) isotherms are given by microporous solids having relatively small external surfaces (e.g., some activated carbons, molecular sieve zeolites and certain porous oxides). The isotherm is concave to the abscissa, where there is a large filling at low relative pressures and a rapid slope up to a constant value. The former is due to enhanced adsorbent-adsorptive interactions in narrow micropores (micropores of molecular dimensions), resulting in micropore filling at very low p/p_o. For nitrogen and argon adsorption at 77 K and 87 K, Type I(a) isotherms are given by microporous materials having mainly narrow micropores (of width $< \sim 1$ nm). Reversible type I(b) isotherms are found with materials having pore size distributions over a broader range, including wider micropores and possibly narrow mesopores ($< \sim 2.5$ nm).

In the case of type *II* isotherms, these are given by the physisorption of most gases on non-porous or macroporous adsorbents. The shape results from unrestricted monolayer-multilayer adsorption up to high relative pressure. If the knee is sharp, Point B, the beginning of the middle section, usually corresponds to the completion of

monolayer coverage. A more gradual curvature (i.e., a less distinctive Point B) indicates a significant overlap of monolayer coverage and the onset of multilayer adsorption.

Type *III* isotherm does not show an identifiable point B; therefore, it is impossible to establish at which relative pressure the monolayer is formed. The adsorbent-adsorbate interaction is weak, and the adsorbed molecules are clustered around the most favourable sites on the surface of a non-porous or macroporous solid.

The adsorbent determines the adsorption behaviour in mesopores- adsorptive interactions and also by the interactions between the molecules in the condensed state. Mesoporous adsorbents give type IV isotherms (e.g., many oxide gels, industrial adsorbents and mesoporous molecular sieves). In this case, the initial monolayer-multilayer adsorption on the mesopores walls is followed by pore condensation (a phenomenon whereby a gas condenses to a liquid-like phase in a pore at a pressure p less than the saturation pressure p_0 of the bulk liquid). Type IV(a) also shows hysteresis when the pore width exceeds a certain critical width. This behaviour depends on the adsorption system and temperature (e.g., for nitrogen and argon adsorption in cylindrical pores at 77 K and 87 K, respectively, hysteresis starts to occur for pores wider than ~ 4 nm) (Thommes et al. 2014). With adsorbents with smaller mesopores width, completely reversible Type IV(b) isotherms are observed; these are given by conical and cylindrical mesopores that are closed at the tapered end.

The type V isotherm shape is similar to that of Type *III* at low relative pressures; this behaviour can be attributed to weak adsorbent-adsorbate interactions. At higher values, molecular clustering is followed by pore filling. These isotherms are observed for water adsorption on hydrophobic microporous and mesoporous adsorbents.

The reversible stepwise Type VI isotherm represents layer-by-layer adsorption on a highly uniform, non-porous surface. The step height now represents the capacity for each adsorbed layer, while the step's sharpness depends on the system and the temperature.

Adsorption *Hysteresis* arises when the adsorption and desorption curves do not coincide. Several factors can lead to the appearance of this phenomenon, but are generally associated with capillary condensation. In complex pore structures, the desorption path often depends on network effects and various forms of pore blocking. Many different

shapes of hysteresis loops have been reported, and based on that, they were classified into five categories (Figure 4.15).

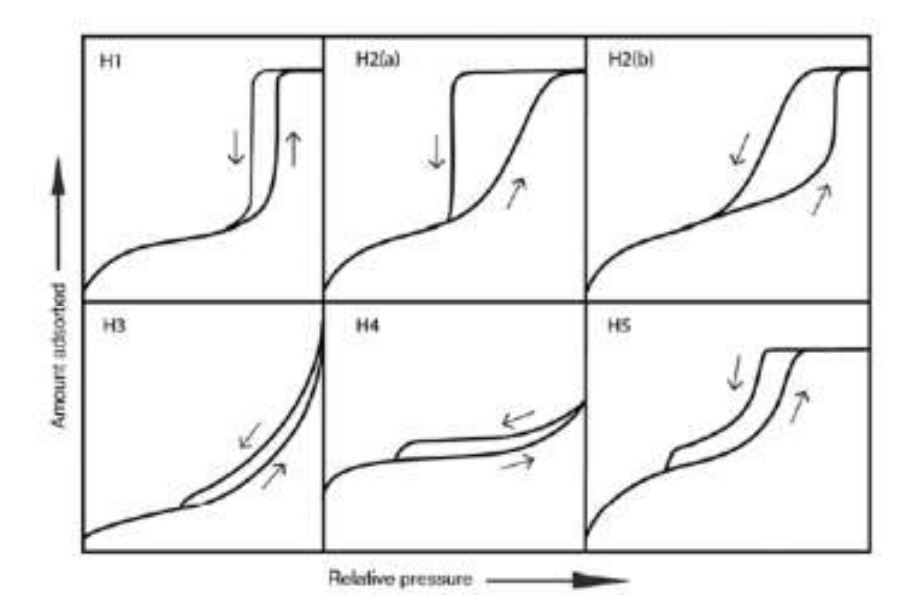


Figure 4.15 Classification of hysteresis loops (Thommes et al. 2015b).

The type H1 loop is found in materials that exhibit a narrow range of uniform mesopores, for instance, in templated silica, some controlled pore glasses and ordered mesoporous carbons. Usually, network effects are minimal, and the steep, narrow loop is a sign of delayed condensation on the adsorption branch.

More complex pore structures give hysteresis loops of Type H2 with significant network effects. The steep desorption branch, a characteristic feature of H2(a) loops, can be attributed to pore-blocking/percolation in a narrow range of pore necks or cavitation-induced evaporation. H2(a) loops are given by many silica gels, some porous glasses, and some ordered mesoporous materials. The Type H2(b) loop is also associated with pore blocking, but the size distribution of neck widths is much larger. This type of hysteresis loop has been observed with mesocellular silica foams and specific mesoporous ordered silica after hydrothermal treatment.

There are two distinctive features of the Type H3 loop: (i) the adsorption branch resembles a Type II isotherm, and (ii) the lower limit of the desorption branch is usually located at the cavitation-induced p/p. Loops of this type are given by non-rigid aggregates

of plate-like particles (e.g., certain clays), but also if the pore network consists of macropores which are not entirely filled with pore condensate.

The H4 loop is somewhat similar, but the adsorption branch is now a composite of Types I and II, the more pronounced uptake at low relative pressure associated with micropores filling. These loops are often found with aggregated crystals of zeolites, some mesoporous zeolites, and micro-mesoporous carbons.

Although the Type H5 loop is unusual, it has a distinctive form associated with specific pore structures containing open and partially blocked mesopores (e.g., plugged hexagonal templated silica.

In this work, the textural material features were obtained by the physical adsorption of N_2 and carbon CO_2 at -196 and 0 °C, respectively. Combining both gases allows estimation of the apparent specific surface area, the total pore volume, micropore volumes, and the pore size distribution. Although both gases have similar molecular dimensions (0.36 and 0.33 of diameter for N_2 and CO_2 , respectively), the difference in adsorption temperature (-196 and 0 °C) implies faster adsorption kinetics for CO_2 . Due to the low working temperature for N_2 , the gas has a low diffusion rate; therefore, micropores with dimensions near the molecular diameter (circa 0.4 nm) cannot be filled (Rodriguez-Reinoso et al. 1984). The adsorption of CO_2 at 0 °C allows determining the microporous pore volume, while the adsorption of N_2 gives the total pore volume information; for this reason, the need to use both gases to have all the information required. The N_2 isotherm is used concerning micro and mesoporous information, while the CO_2 isotherm is used to obtain information about narrow micropores (width < 0.7 nm) (Rouquerol et al. 2015).

The relationship between the internal surface and the pore diameter width is shown as follows (Eq. 4.2):

$$S_{mi} = \frac{2 \times 10^3 W}{L}$$
 Equation 4.2

Where S_{mi} is the surface area in m²g⁻¹, W is the volume in cm³g⁻¹, and L is the accessible pore width in nanometres calculated from the Stoeckli-Ballerini equation (Stoeckli et al. 1990).

Volumetric analysers were used to measure the adsorption of N_2 at -196 °C and CO₂ at 0°C (3FLEX and TRISTAR 3020, MICROMERITICS). All samples were previously outgassed under vacuum (ca. 10 – 1 Pa) at 120 °C (heating rate of 2 °Cmin-1) for 17 h to obtain reproducible and accurate data (Figini-Albisetti et al. 2010). Each isotherm was recorded at least in duplicate on fresh sample aliquots to guarantee the accuracy and reproducibility of the experiments (the error was below 2 %). The specific surface area (S_{BET}) was calculated using the BET equation applied to the N_2 adsorption isotherms at -196 °C. The total pore volume (V_{total}) was calculated as the volume of gas adsorbed at a relative pressure of 0.97 in the N_2 adsorption isotherms at – 196 °C, expressed in terms of cm3g-1, using the density of liquid gas to convert the amount of gas adsorbed in standard temperature and pressure (STP) conditions with the expression (Equation 4.3):

$$V_{TOTAL\ PORES}(cm^3g^{-1}) = V_{gas\ adsorbed}(cm^3g^{-1}, STP) * 0.00154643$$
 Equation 4.3

Micropore volumes were determined by Dubinin Radushkevich's formulism, either to the nitrogen adsorption data (total micropore volume, Wo, N₂) or to the CO₂ adsorption data to assess the narrow microporosity (Wo, CO₂). For the pore size distribution, the 2D-NLDFT-HS approach was used. Further details of these equations are described below.

4.3.1.2 BET equation

The Brunauer-Emmet-Teller (BET) method (Brunauer et al. 1938) is one of the most widely used to determine the apparent specific surface area (S_{BET}). This model was developed for mesoporous solids, but its application was extended to a vast number of materials. So, the use of the term "apparent" since not all the materials fit the conditions required to apply this method. This theory calculates the surface area using the relative pressure range corresponding to the monolayer filling. The BET equation considers van der Waals as the unique attraction force responsible for the adsorption process. The model also considers a surface energetically uniform where all the active sites are equivalent. At the same time, it assumes that the heat of adsorption of each layer above the first is equal, and its value coincides with the latent heat of condensation. The equation is commonly expressed in the linear form (Equation 4.4) (Rouquerol et al. 2015):

$$\frac{p/p^{o}}{n(1-\frac{p}{p^{o}})} = \frac{1}{n_{m}c_{BET}} + \frac{c_{BET}-1}{n_{m}c_{BET}}(p/p^{o})$$
 Equation 4.4

Where n is the specific amount adsorbed at the relative pressure p/p° and n_m is the specific monolayer capacity. The parameter C_{BET} is exponentially related to the energy of monolayer adsorption. It is generally agreed that the value of C_{BET} instead gives a valuable indication of the shape of the isotherm in the BET range. Thus, if the value of C_{BET} is at least ~ 80 , the knee of the isotherm is sharp, and Point B is reasonably well-defined (Thommes et al. 2015b). Equation 4.4 has several linearised forms, one proposed by Parra (Parra et al. 1995) and used for this work (Equation 4.5).

$$\frac{X}{n(1-X)} = \frac{1}{n_m c_{BET}} + \frac{1}{n_m c_{BET}} \left[\frac{1-X}{X} \right]$$
 Equation 4.5

Where *X* is the relative pressure.

This linearisation facilitates the election of the experimental interval in which the BET equation is applied. With this method, the CBET value is more precise since the determination of the application range is more precise and restrictive, avoiding negative values for this parameter and complying with the IUPAC recommendations for calculating the surface area by applying the BET equation (Thommes et al. 2015; Rouquerol et al. 2015). Particularly, the analysis is suitable for microporous solids, where applying the traditional method is more problematic (Parra et al. 1995).

4.3.1.3 Dubinin – Radushkevich equation

In 1947, Dubinin and Radushkevich (DR) proposed an equation for the characteristic curve regarding the fractional filling of the micropore volume. This empirical equation considers the distinct adsorption energies and assumes that the micropore size follows a Gaussian distribution. The linear DR equation (Equation 4.6) is given as follows:

$$InW = InW_o - \left(\frac{RT}{\beta E_o}\right)^2 In^2 \left(\frac{p^o}{p}\right)$$
 Equation 4.6

where W (cm³g⁻¹) is the condensed volume inside the pores at T temperature and p/po relative pressure. Wo (cm³g⁻¹) is the total pore volume that is accessible to the adsorbate; β is an affinity factor adsorbate-adsorbent (this factor takes the value 1 for benzene), for nitrogen takes a value of 0.34 and 0.36 for carbon dioxide (Guillot et al. 2001). The graphical representation of In W vs In²(p°/p) turns into a linear function where the

intersection with the ordinate axis will be In Wo. From the slope, the value of E_o related to the average pore width can be deduced.

This PhD thesis applied the DR formulism to N_2 adsorption data (Wo, N_2) and CO_2 adsorption data (Wo, CO_2).

4.3.1.4 Pore size distribution: Density Functional Theory

The Density Functional Theory (DFT) is widely used to calculate pore size distributions of porous materials. The method assumes that an experimental isotherm can be expressed as the sum of the isotherms of individual pores forming the porous solid structure (Evans et al. 1984; Lastoskie et al. 1993). The mathematical expression (Equation 4.7) is as follows:

$$n(p) = \int_{w_{min}}^{w_{max}} f(w)\rho(p, w)dw$$
 Equation 4.7

where n(p) is the quantity of gas adsorbed at a pressure p, the terms w_{min} and w_{max} are the width of the minimum and maximum pores; f(w) is the distribution of pore volume as a function of the pore width, and $\rho(p,w)$ is the molar density of the adsorbate at pressure p in a pore with width w.

The first approaches using DFT to evaluate the pore size distribution made simplistic assumptions concerning the functional form of the size distribution. More recently, a generalisation was accomplished by numerical deconvolution of the isotherm data using a set of pore shape-dependent model isotherms; each set member represents a unique, narrow range of pore sizes. Nowadays, more sophisticated methods based on NLDFT have determined the pore size distribution in the entire range of pore sizes accessible by the adsorptive molecule. This new method incorporates concepts related to the dimensionality of the pores, the heterogeneity surface energy and geometrical corrugation in the equation (2D-NLDFT-HS) (Jagiello et al. 2013a; 2013b).

In this thesis, the 2D-NLDFT-HS approach was used to obtain the distribution of pores sizes.

4.3.2 Elemental analysis

The elemental analysis (EA) includes assessing carbon, hydrogen, nitrogen, sulphur and oxygen content based on the norm ASTM D-5373. The technique consists of burning the sample in the presence of oxygen at a high temperature (~ 1200 °C). The combustion products, such as CO₂, H₂O, N₂, and SO₂, are typically measured using infrared spectroscopy. In the case of oxygen, the sample is heated up to 1070 °C under an inert atmosphere, provoking the liberation of different gas molecules (CO, CO₂, and H₂O). This gas mixture is passed through a bed of graphite powder to reduce it to CO, then CO is oxidised to CO₂ in a CuO catalyst, and a chatarometric detector detects it. In this PhD thesis, the determination of the most common heteroatoms in carbon materials (i.e., C, H, N, S and O) was carried out by an analyser (THERMO SCIENTIFIC FLASH 2000). For comparative purposes, all samples were previously dried under an air atmosphere for 12 hours at 105 °C.

4.3.3 Thermic stability and oxidative resistance

A thermal analysis studies the relationship between a sample property and its temperature as the sample is heated or cooled in a controlled manner. A thermogravimetric analysis (or thermogravimetry) measures the sample mass during the temperature increment (Lever et al. 2014). Therefore, when heated, the material weight change is the basis of the thermogravimetric (TG) method. This technique continuously records sample weight changes while the material is subjected to a controlled temperature program (Bottom 2008). The data obtained identifies different events that lead to weight loss, and depending on the nature of the events involved, in some cases, it is possible to identify the beginning and the end of the process. However, the thermogravimetric parameters are not intrinsic to the material since they depend on the heating program, working atmosphere, material and geometry of the crucible, mass used for the analysis, particle size and reaction heat.

In this work, two different atmospheres were used to identify the events provoked by the heating from those produced by the oxidant agent (redox reactions). In this sense, all the samples were analysed on 6-25 mg of the material in a thermobalance SHIMADZU TGA-50 and SETARAM LABSYS under air and inert atmospheres (N₂), flow 50-100 mLmin⁻¹, and heating rate 10 °Cmin⁻¹.

4.3.4 Thermal decomposition coupled with mass spectrometry

This technique is classified as an EGA (evolved gas analysis) according to the International Confederation for Thermal Analysis and Calorimetry (ICTAC). This terminology involves a family of techniques where the nature and, or amount of gas or vapour evolved is determined (Lever et al. 2014). The term evolved gas detection (EGD) has also been used where the nature of gas is not determined. Thermal Programmed Desorption (TPD) is a suitable technique for characterising surface functional groups of carbon materials (Bandosz et al. 2006a). It is well known that carboxylic functional groups decompose by heating (decarboxylation reaction) into carbon dioxide and water vapour at temperatures below 400 °C. Functional groups like quinone or phenol decompose at temperatures between 400 – 800 °C into carbon monoxide and water vapour (decarbonylation reaction).

For this work, a thermobalance NETZSCH STA 409 DC coupled with a mass spectrometer that allowed the analysis of the evolved gas from the sample heating was used. The thermogravimetric profiles were recorded under the Ar atmosphere, and selected m/z signals were recorded and quantified (e.g., m/z 2, 18, 28, 44, 46, 64). Assignments of the m/z signals were carried out upon analysis of the relative intensities of the mass fragments of the whole mass spectrum and comparison with theoretical spectra of pure gases given by the NIST Library. The quantification of the CO and CO₂ gases was carried out using oxalate as a reference.

4.3.5 Fourier transform infrared spectroscopy

Fourier Transform Infrared Spectroscopy (FTIR) is based on the molecular vibration. An infrared spectrum is commonly obtained by passing infrared radiation through a sample and determining which fraction of the incident radiation is absorbed at a particular energy. The peak energy in an absorption spectrum corresponds to the vibration frequency of a part of a sample molecule. Still, for a molecule to show infrared absorptions, it must possess a specific feature, i.e. the electric dipole moment of the molecule must change during the vibration (Stuart 2005). Therefore, FTIR allows the recognition of functional groups as long as the molecule is infrared active (Figure 4.16). These studies were carried out with a BRUKER VERTEX 80v, using materials dispersed in –and pressed with- dry KBr (spectroscopic grade) in a 1:1000 ratio (w/w).

Transmission spectra were carried out between 4000 and 350 cm⁻¹ (64 scans collected, resolution 4 cm⁻¹). Spectra data were recorded under a vacuum to avoid the interference of ambient moisture and CO₂. The spectra were corrected using the KBr pellet as background. At least two pellets of each sample were measured to attain the consistency of measurements. An online database provided by Michigan State University was used to identify the different moieties based on the IR bands.

https://www2.chemistry.msu.edu/faculty/reusch/virttxtjml/spectrpy/infrared/infrared.htm

4.3.6 Raman spectroscopy

Raman spectroscopy has become one of the most popular techniques for characterising carbon materials (e.g., fullerenes, nanotubes, diamonds, carbon chains). The spectrum contains information about atomic structure and electronic properties (Ferrari et al. 2013). Therefore, it is a very effective method for investigating the intimate bonding structure of carbon. However, there are still discussions on the exact relationship between the Raman spectra and atomic vibration (Baek et al. 2017). Regardless, a consensus exists about the carbonaceous material's principal spectra features, namely the "disordered" or D band around 1350 cm⁻¹, the "graphitic" or G band around 1580 cm⁻¹, and a series of second-order Raman modes found in the vicinity of 2700 cm⁻¹ (Dietzek et al. 2010). The former is related to the combination of sp³-hybridised and sp²-hybridised carbon, while the second, G-band, is ascribed to the vibration of sp²-hybridised carbon (Baek et al. 2017).

This technique, applied to carbon materials, was introduced by Tuinstra and Koenig (Tuinstra et al. 1970), who reported that the Rp (ID/IG) varied inversely with the crystalline surface size (La). Knight and White (Knight et al. 1989) developed the equation even further by the dependence of the wavelength λ_L , assuming the following correlation (Equation 4.8) between La and the Rp (ID/IG):

$$\frac{I_D}{I_G} = \frac{C(\lambda)}{L_a}$$
 Equation 4.8

Where $C(\lambda)$ is a wavelength-dependent pre-factor (the wavelength dependency of C, valid for 400 nm $< \lambda < 700$ nm) (Wang et al 1990), on the other hand, Ferrari and Robertson (Ferrari et al. 1969) reported that La could exhibit a proportional relation with area intensity ratio, Ra (ID/IG), if La is around 2 nm size. For minimal values of L_a , the

previous equation (Equation 4.7) does not work, generating a new expression (Equation 4.9):

$$\frac{I_D}{I_C} = C(\lambda) L_a^2$$
 Equation 4.9

Where $C(\lambda)$ represents the wavelength-dependent pre-factor.

Raman spectra were recorded in ambient conditions in a spectrometer RENISHAW INVIA REFLEX equipped with a 355 nm laser and using an optical microscope with an x50 long LEICA DM2500 working-distance objective (ca. 10 mm). Each spectrum was recorded with an integration time of 5 s in the 500–2400 cm⁻¹ wavenumber range; the data presented represents the average of three measurements. Deconvolution of Raman spectra was carried out by a fitting procedure using a linear baseline and Gaussian/Lorentzian functions by the Origin program.

4.3.7 Scanning electron microscopy

Scanning electron microscopy (SEM) is routinely used to generate high-resolution images that reveal information regarding the material's external structure and to show spatial variations in chemical compositions. The technique involves bombarding the surface with an electron beam; as a result of the interaction, a wide variety of signals will be emitted, making it possible to compose the topography of the material, its physical properties, and chemical composition.

An electronic microscope is a device that generates a high-energy electron beam (circa 5 – 30 keV), shapes and sizes the beam, focuses on the surface, and can vary the focal point in any of the three spatial dimensions. Each point-induced excitation's answer by the electron beam enables the registration of the material's image. Different signals can be obtained depending on the detector used; the widely utilised ones are the secondary electrons, the retro-dispersed Auger electrons, and the characteristic X-rays. Each signal reveals information regarding topography, physical properties, and chemical composition. The resolution of the obtained SEM images depends on the type of signal recorded; however, these are characterised by high resolution (up to 10 nm) and significant depth of field (Ivanova et al. 2016).

In this PhD work, the samples were evaluated using a JEOL JSM 5900L Scanning Electron Microscope; samples were observed as prepared with a metallic coating.

4.3.8 X-ray diffraction

X-rays are magnetic radiation with a very low wavelength ranging between 10^{-2} and 10 nm. As in other electromagnetic radiation, the interaction between the electric vector and the material's electrons generates dispersion. For solid crystalline structures, the overlapping of the different wavefronts diffracted by subsequent layers of atoms can lead to constructive and destructive interactions as a function of inter planes distances of the network (di), of the wavelength of the radiation (λ) and of the angle of incidence of radiation on the surface of the solid (θ i). Early during the XX century, Bragg (Bragg 1913) demonstrated that for constructive interaction, this condition needs to be accomplished (Equation 4.10):

 $n\lambda = 2d\sin\theta$ Equation 4.10

Where n is an integer number, the space between layers of atoms (di) has to be the same, and the wavelength of the radiation and the dispersion centres must be regularly distributed.

A diffractogram is a radiation intensity representation after the interaction with the sample. It depends on the incident angle (commonly 2θ) and is characteristic of every crystal. X-ray Diffraction (XRD) technique helps establish whether the solid has a crystalline structure and the disposition of the atoms inside the network (Skoog et al 2001). Materials derived from graphene show two characteristic peaks in their X-ray diffraction spectrum (Figure 4.16): the [001] peak is circa 10°, and the [100] peak is between 40 and 50°. In contrast, the graphite spectrum shows a characteristic peak [002] between 20 and 30° (Lavín 2017).

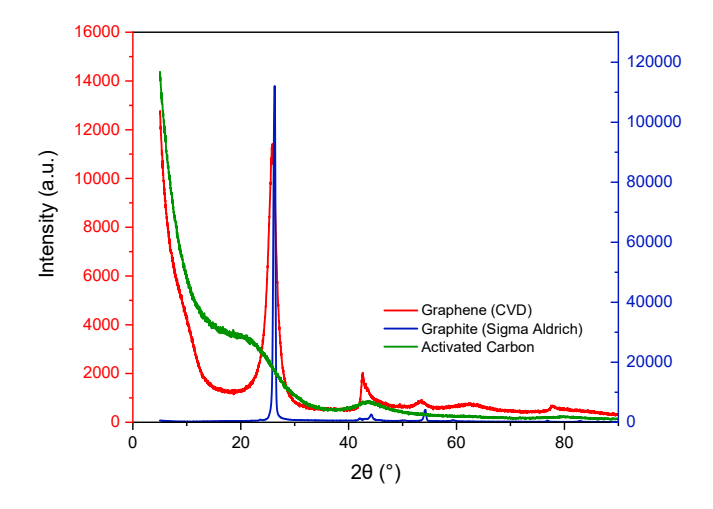


Figure 4.16 X-ray diffraction spectrum of Graphene, Graphite and AC (data provided by NaFMAT group, CEMHTI, CNRS).

For this work, crystalline phase evolution with the different thermal treatments was studied by using RIGAKU ULTIMA IV equipment and Cu K α radiation. The apparent crystallite thickness (L_c), apparent layer-plain length parallel to the fibre axis (L_a), and average interlayer spacing (d₀₀₂) (Figure 4.17) were calculated using Bragg and Scherrer equations (Equations 4.11 and 4.12).

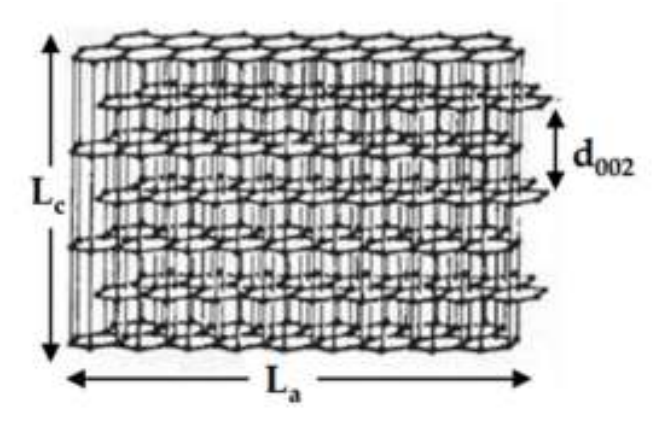


Figure 4.17 Graphic representation of the parameters L_c, L_a and d₀₀₂.

$$d_{002} = \frac{\lambda}{2\sin\theta}$$
 Equation 4.11

$$L_{a,c} = \frac{\kappa\lambda}{\beta\cos\theta}$$
 Equation 4.12

where θ is the Bragg angle (°), λ is the wavelength of the X-rays (λ = 0.154 nm), β is the FWHM of the peak (radian), and K is the form factor (0.89 for L_c and 1.84 for L_a).

4.3.9 pH at the point of zero charge

The pH at the point of zero charges (pH_{PZC}) is defined as the pH at which the surface charge of the material (inner and exterior) takes zero value; this means that the material has the same quantity of positive and negative charges (Noh et al. 1989). The pH_{PZC} determination allows knowing the tendency of the material to get positively or negatively charged as a function of the medium conditions, like, for example, the pH of the working solution.

The pH_{PZC} for each sample was determined by the mass titration method (Ania et al. 2007), which records the pH value depending on the solid concentration. A certain amount of sample is put in contact with distilled water under an inert atmosphere and is left stirring until it reaches equilibrium (commonly 48 hours). After this, the pH is measured using a conventional glass electrode. Subsequently, a known quantity of water is added to the medium, obtaining a new dilution, and the previous proceeding is repeated. Usually, the technique starts with a 16% sample weight solution and is gradually diluted up to 1 %. The theory poses that the pH should increase until it reaches a constant value, which corresponds with the point of zero charge for pure samples without unspecific adsorption.

4.3.10 Potentiometric titration

Potentiometric titration (PT) is broadly used for the acid-base nature identification of the functional groups on the surfaces of several materials. The technique is based on the acid-base titration of a material suspension in an inert electrolyte solution to establish the sample's capacity to exchange protons with the environment. The experimental data obtained is the solution pH as a function of the volume of base added; nonetheless, this information must be expressed as net charge concentration (Q), which is calculated by (Equation 4.13):

$$Q(molg^{-1}) = \frac{V_i(c_a - c_b) + \Delta V N_t(V_i + \Delta V)\{[H^+] - [OH^-]\}}{m}$$
 Equation 4.13

Where V_i is the dissolution volume at every instant (cm³). C_a and C_b are acids and initial base concentrations (molL⁻¹), ΔV is the cumulative volume of titrant volume solution (cm³), N_t is the titrant solution concentration expressed as normality (moles_{solute}.Kg_{solvent}), and m is the mass of the material to study (g). The protons concentrations [H⁺] and hydroxide ions [OH⁻] are calculated from the pH measures and the Davies equation for the activity coefficients (γ) (Equation 4.14):

$$\log \gamma = -0.5115Z^2 \left(\frac{\mu^{\frac{1}{2}}}{1 + \mu^{\frac{1}{2}}} \right) - 0.3\mu$$
 Equation 4.14

where μ is the ionic force for every point of the solution, and Z is the charge of the ions.

The technique consists of putting 100 mg of the sample and 50 mL of NaNO $_3$ 0.01 M (strong electrolyte) under an inert atmosphere with continuous stirring until equilibrium is reached; this usually takes 17 hours. Once the solution is at adequate conditions, the pH is measured with a conventional glass electrode; depending on the result, the pH has to be adjusted to a value of 3, or minor, by using HCl 0.1 M (Contescu et al. 1993). Once the medium is at pH 3, the conditions are established, and the acid-base titration with a NaOH 0.1 M solution begins. For this analysis, an automatic titrator METROHM - TITRINO 848, was used, and a fixed quantity of 2 μ L per drop was established for the titration solution up to pH 12.

4.4 Liquid phase adsorption experiments

Adsorption experiments were planned to study the adsorption capacity of the ACF in batch conditions for both the monocomponent solutions and the binary mixtures. The problem-solution pH was not buffered for all the cases since the values remained within the allowed limits for draining to public sewer collectors (Decreto Nro. 253/979 1979).

4.4.1 Kinetic studies

These experiments were carried out in batch conditions where 50 mL of the working solution, with an initial concentration of 0.8 mmolL⁻¹ of the PhC, was poured into a conical flask along with 20 mg of ACF and was left stirring (400 rpm) at room temperature, in a multipoint agitation plate, POLY, CIMAREC (Figure 4.18). After vacuum filtering, the samples were withdrawn from the flasks at regular intervals and analysed to determine the remnant drug concentration using a Millipore nylon membrane

 $0.45 \mu m$. All PhC solutions were prepared with ultra-pure water obtained from MILLI-Q equipment, MILLIPORE Corp. (Table 4.2).



Figure 4.18 Multipoint stirring plate where the experiments were left stirring at room temperature.

The concentrations were determined by UV-spectrophotometry using a UV-2700, SHIMADZU equipment, establishing the remnant concentration at the maximum absorbance (242 nm for AMP, 266 for SMX and 320 for MNZ) according to the Bouguer-Beer law (Equation 4.15):

$$A = \varepsilon bC$$
 Equation 4.15

where A (a.u.) is the absorbance, ε is the molar absorptivity coefficient, and b is the thickness of the tray.

The PhC's concentration was also measured using high-performance liquid chromatography HPLC equipment, AZURA-KNAUER, fitted with a UV-Vis variable wavelength detector. Working conditions are listed below (Table 4.2). The expression used to calculate PhC uptake is as follows (Equation 4.16):

$$q_t = \frac{(c_0 - c_t)V}{W}$$
 Equation 4.16

Where qt (mmolg-1)is the amount of PhC adsorbed at time t, Co and Ct are the PhC concentration at the beginning of the experience and at time t (mmolL⁻¹), respectively. V is the volume of PhC solution (L), and W is the dried adsorbent (g) weight.

Table 4.2 HPLC working conditions for monocomponent solutions.

	Pollutants		
Conditions	SMX	MNZ	
Mobile phase (MeOH/H ₂ O) v/v	50:50	50:50	
Column	C18	C18	
Flow rate (mLmin ⁻¹)	0.5	0.5	
UV detector (wavelength, nm)	237, 257, 263, 266	254, 275, 300,320	
Retention time (min)	12:48	6:45	
Temperature (°C)	35	35	
Sample injection (µL)	10	10	

4.4.2 Thermodynamic studies

Batch-mode equilibrium adsorption experiments were conducted under similar operating conditions, varying the initial concentration of the PhC. The contact time needed to reach the equilibrium was previously established with the kinetic data. At the end of the experiment, the solutions were filtered and analysed to establish the equilibrium concentration using the same technique as the one cited in 4.4.1. The adsorption capacity q_e (mmolg⁻¹) of the ACF at equilibrium was calculated as given in the equation (Equation 4.17):

$$q_e = \frac{(c_0 - c_e)V}{W}$$
 Equation 4.17

Where q_e (mmolg⁻¹) is the amount of PhC adsorbed at equilibrium, Co and Ce are the PhC concentrations at the beginning of the experiment and equilibrium (mmolL⁻¹), respectively. V is the volume of PhC solution (L), and W is the dried adsorbent (g) weight.

4.4.3 Binary system studies

The same working conditions and the technique and analysis procedure described in 4.4.1 were used to study binary solutions. The PhC mixtures were prepared by varying the molar ratio of SMX-MNZ, and the working conditions are listed below (Table 4.3).

Table 4.3 HPLC working conditions for binary solutions.

	Pollutants		
Conditions	SMX/MNZ		
Mobil phase (Acetonitrile/H ₂ O) v/v	80:20		
Column	C18		
Flow rate (mLmin ⁻¹)	0.8		
UV detector (wavelength, nm)	237, 263, 266, 320		
Retention time (min)	11:12 - 6:17		
Temperature (°C)	35		
Sample injection (μL)	10		
Molar rates SMX/MNZ	1/1, 1/1.5, 1.5/1, 1/2, 2/1, 1/10, 10/1		

HPLC-grade Methanol and Acetonitrile were purchased from MERCK, Germany, and used for the mobile phase solutions. The overall analysis time was 14 minutes, carried out by an AZURA, KNAUER HPLC equipment with a diode array detector, D2 lamp, 190-700 nm, max. 100.

4.4.4 Solution's pH effect

To assess the pH influence on the adsorption capacity, batch-mode equilibrium adsorption experiments were conducted under operating conditions similar to those used for the monocomponent experiments. However, the working pH varied in these cases.

Two isotherm adsorption points from the monocomponent and binary experiences were selected for the experiment (same PhC initial concentration), and the solution pH was set by adding acid and basic solutions (HCl and NaOH, 0.1 M). In both cases, the volume added was in the order of μ L; therefore, the ionic strength can be assumed constant. The pH range was set between 5 to 10, per the values the national decree allowed (Decreto Nro. 253/979 1979). The adsorption recorded data was plotted in the isotherm (without pH correction) to assess the detour due to the pH.

4.4.5 The ionic strength effect

Like the pH effect experiments, the ionic strength was tested by selecting two points from the adsorption isotherm (same PhC initial concentration) and adding a strong electrolyte to the medium. For the experiment, NaCl was selected, and the influence of two concentrations, 10 and 100 mmolL-1, was tested. The adsorption recorded data was plotted in the isotherm (without pH correction) to assess the detour due to the ionic strength.



"Mais je suis plus puissant que le doigt d'un roi, dit le serpent."

Le petit prince

Antoine de Saint-Exupéry

One of the main drawbacks of fibrous materials, regardless of their nature (synthetic, cellulosic or protein), is that during the thermal treatment, they fuse, decompose, or degrade, losing mechanical strength and morphology (Hassan et al. 2015b). A standard procedure to avoid this is to expose the material to a mild temperature pre-heat stabilisation under oxidative conditions. Several reactions are involved during this treatment, mainly the cyclisation of nitrile groups (when using polyacrylonitrile as a precursor) and the dehydrogenation of saturated C-C bonds (for synthetic and cellulosic fibres). The original fibre's molecular structure is transformed into a cross-linked cyclised network of carbon-nitrogen rings. This new spatial disposition prevents the fusion of the fibres during further thermal treatments at high temperatures (Torres-Canas et al. 2020). The mechanisms involved during the oxidative stabilisation of wool fibres are not yet clarified, with only one previous work focused on their use for porous activated carbon fibre preparation from fabrics (Hassan et al 2015a).

In this chapter, the criteria for selecting temperature-time parameters to be studied are first shown. Subsequently, extensive characterisation of the obtained samples according to the previously established conditions is described. The chapter ends with a discussion regarding which stabilisation conditions best fit the main goal: keeping the fibre structure.

5.1 Characterisation of the precursor

5.1.1 Scanning electron microscopy

As mentioned before, this study used natural wool fibres as a precursor to synthesise carbon fibres. The scanning microscopy images of the raw precursor show the characteristic tubular morphology of the material (Broda et al. 2016), where the cellular arrangement of the cuticle disposition is recognisable (Figure 5.1).

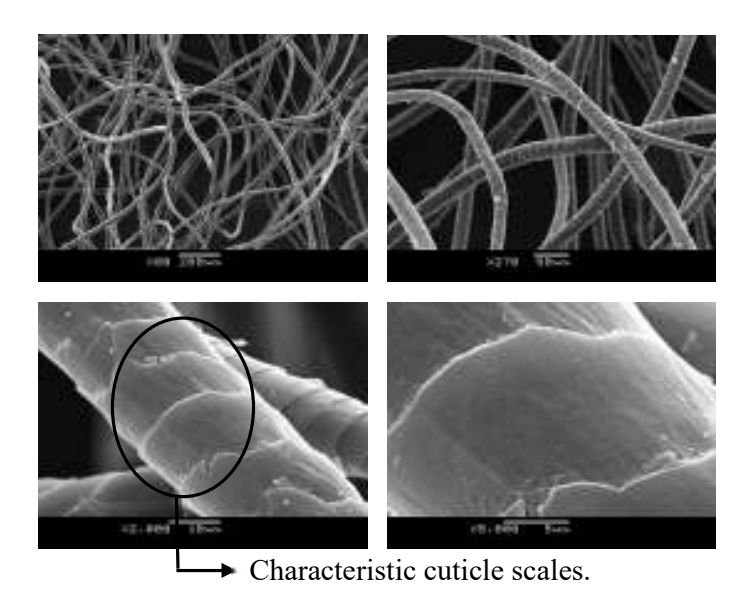


Figure 5.1 SEM images of the pristine wool fibres.

5.1.2 Elemental content

The chemical composition of the material shows a protein molecular structure rich in sulphur and nitrogen (Table 1).

Table 5.1 Chemical composition (wt. %, dry-ash free basis) of the pristine wool (average values plus the standard deviation).

Sample	N	C	Н	S	0
WF	15.45 ± 0.14	49.03 ± 0.09	6.97 ± 0.15	3.04 ± 0.04	25.52 ± 0.15

5.1.3 Fourier-transformed infrared spectroscopy

On the other hand, the infrared spectrum of the fibre (Figure 5.2) shows the typical absorption bands reported for wool material (Chandwani et al. 2016; Broda et al. 2016). The broadband between 4000 and 3000 cm⁻¹ can be interpreted as two contributions corresponding to N–H stretching vibration (~3300 cm⁻¹), amide A moieties, and O–H stretching (~3200 cm⁻¹). The former is associated exclusively with the NH group vibration and is thus insensitive to the conformation of the polypeptide backbone. Its wavenumber position depends on the strength of the hydrogen bond (Barth 2007). The frequency registered corresponds to H-bonded groups (Pakkaner et al. 2019). Amide B (Fermi resonance doublet ~ 3100 cm⁻¹) peak, also related to N–H stretching vibrations, can also be identified, and Amide I features (C=O stretching band ~ 1650 cm⁻¹). Amide II (out-of-phase combination of the NH in-plane bend and the CN stretching vibration ~ 1500 cm⁻¹

¹) and Amide III (in-phase combination of the NH bend and the CN stretching vibration, \sim 1235 cm⁻¹) (Barth 2007). It is important to note that the previous bands are related to different vibrations of the same functional group (Figure 5.3). The exact wavenumber of the amide I vibration depends on the nature of hydrogen bonding involving the C=O and N–H groups. This vibration is determined by the particular secondary structure adopted by the protein being considered. According to the data reported and the wavenumber recorded, the conformation is assigned mainly to the α-helix structure (Stuart 2005). The disulfide bond stretching vibration band was observed at 522 cm⁻¹, in agreement with data reported in the literature (Stuart 2005).

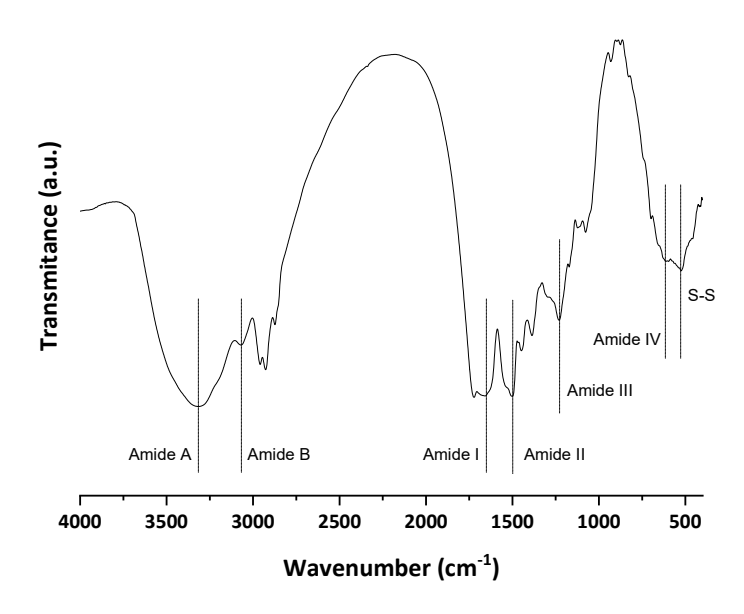


Figure 5.2 The infrared spectrum of the wool fibre used as a carbon fibre's precursor in this study.

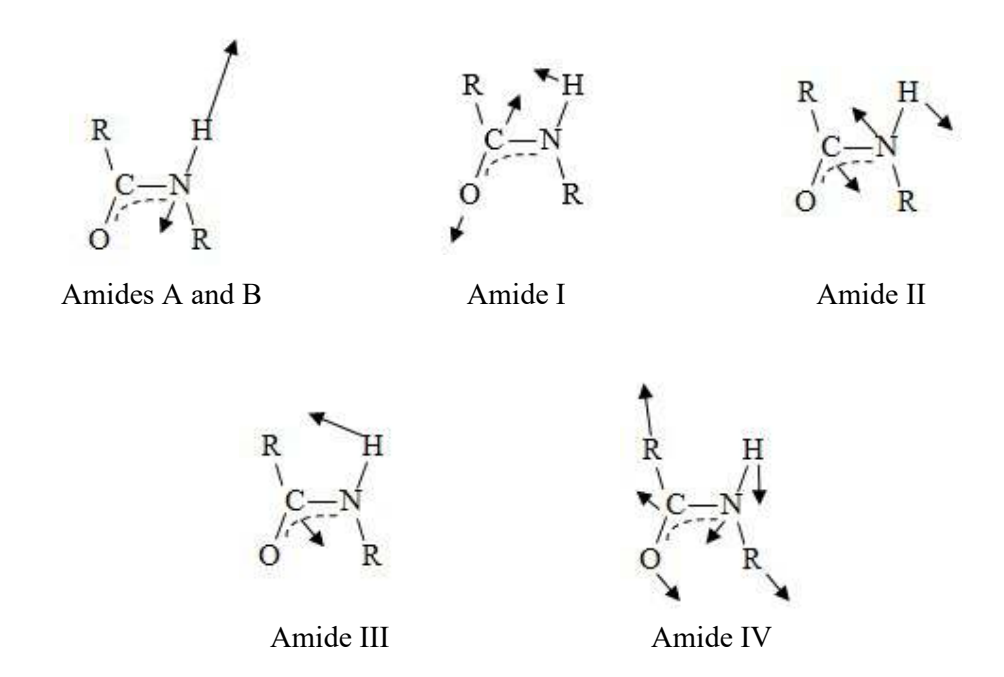


Figure 5.3 Vibrational modes of the amide group (Bandekar 1992)

5.1.4 Oxidative stabilisation of the precursor

5.1.4.1 Thermogravimetric studies

To select the best conditions for oxidative stabilisation, the thermal features of the pristine wool fibres (WF) were studied in a thermobalance under an oxidising and inert atmosphere (Figure 5.4). This study was carried out in both atmospheres (N₂ and air) to discriminate the effect of temperature mass loss from those related to the oxidising atmosphere.

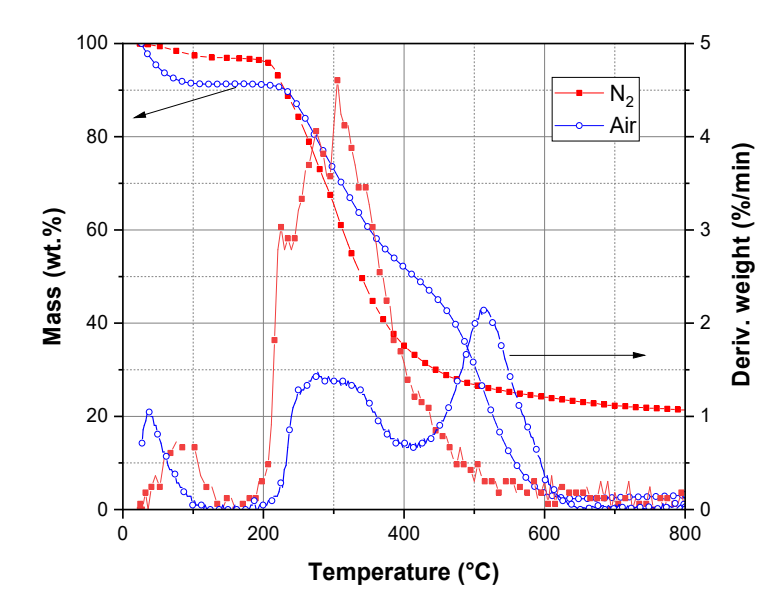


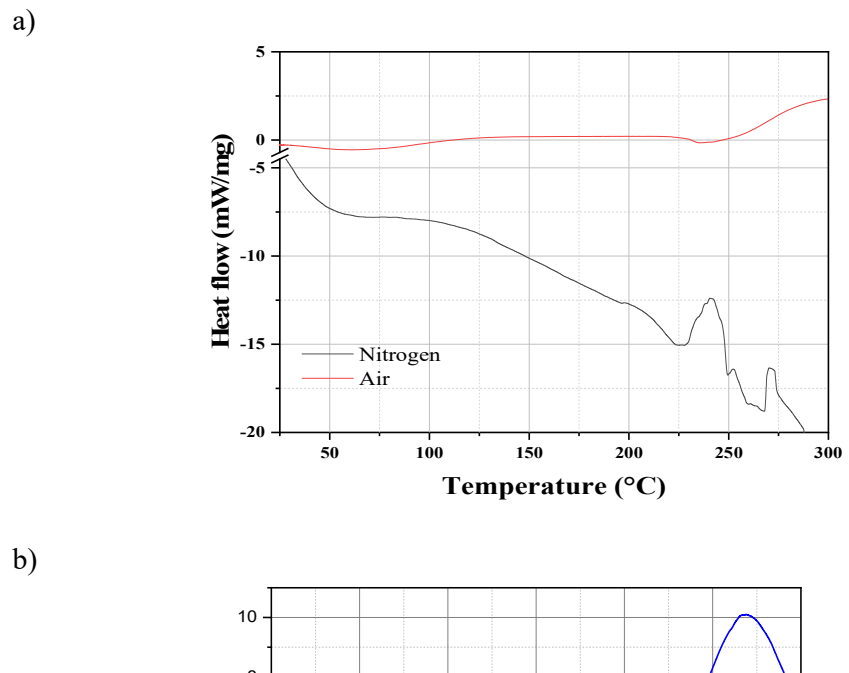
Figure 5.4 Thermogravimetric profiles (mass evolution and derivative weight) under inert and air atmosphere of the pristine wool fibres.

A first mass loss below 100 °C observed in both atmospheres corresponds to the wool fibre's moisture (ca. 1-3 wt.%). Under an inert atmosphere, a sharp mass loss is observed between 200-500 °C, accounting for a ca. 60 wt. % of total mass loss (Figure 5.4, red plot). This feature is associated with the rupture of the hydrogen bonds of the wool fibres' peptide structure and loss of the secondary structure, thereby undergoing condensation reactions, rendering a solid to a melted phase change (Hassan et al. 2015). The temperature range agrees with other studies reporting the thermal decomposition of wool (Chen et al. 2013; Pakkaner et al. 2019). In contrast, the profile in the air showed two distinct thermal events in the range of 200-400°C (Figure 5.4, blue plot). Below 200°C, the mass loss was negligible, pointing out the threshold oxidative temperature of the WF; a similar thermal fingerprint has been reported for several natural fibres (Torres-Canas et al. 2020). The mass loss in the air between 225-375 °C accounted for ca. 40 wt.% of the overall mass loss. This has been associated with cyclisation and saturation reactions (Park 2015). Above 480 °C, the mass loss rate increased (ca. 1.5 times faster compared to the first thermal event below 400 °C), reaching a complete mass loss, characteristic of a combustion reaction. Previous works reported that this step could be carried out at 180-300 °C (Paiva et al. 2003); however, other authors affirm that the optimum range is between 200-300 °C (Ko 1991; Dalton et al. 1999). Even temperatures beyond 300 °C have been suggested (Gupta et al. 1996; Mittal et al. 1997). Thus, the fibre can overheat,

fuse, or even burn if the temperature is too high. Still, if the temperature is too low, the reactions are slow and incomplete stabilisation can yield poor carbon fibre properties (Jiménez et al. 2016).

5.1.4.2 Calorimetric studies

The differential scanning calorimetry (DSC) of pristine wool under an atmosphere of nitrogen and air (Figure 5.5a) showed that the raw material is immediately subjected to events with an appreciable heating flux exchange. However, up to 200 °C, these events were not associated with mass loss, leaving aside the loss of water. By contrast, the analysis under air atmosphere barely recorded heating flux until the appearance of an endothermic peak between 215-250 °C (Figure 5.5b). This peak is associated with a thermal event where the sample absorbs heat, typically without mass loss, such as melting the α form crystallites in the intermediate filaments of wool keratin (Cao et al. 1997). However, the shape of the peak suggests more than one endothermic event; for this reason, the peak was deconvoluted (Figure 5.6), resulting in two Gaussian peaks centred at 236 and 255 °C, respectively. The second peak is associated with an event with mass loss and presumable dehydrogenation. At higher temperatures, an exothermic process occurs (sharp increase in the heat flow), likely due to the loss of the secondary structure (i.e., α -helix and β -sheet conformations through hydrogen bonds) of the fibres and the ultimate degradation of the material. Therefore, based on the previous results, and considering that treatments at higher temperatures than 300 °C can lead to a material that did not wholly undergo stabilisation, the temperature range selected to explore the oxidative stabilisation of the wool fibres under air atmosphere is between 200 – 300 °C. This working temperature range is in accordance with previous reports for different materials (Park 2015).



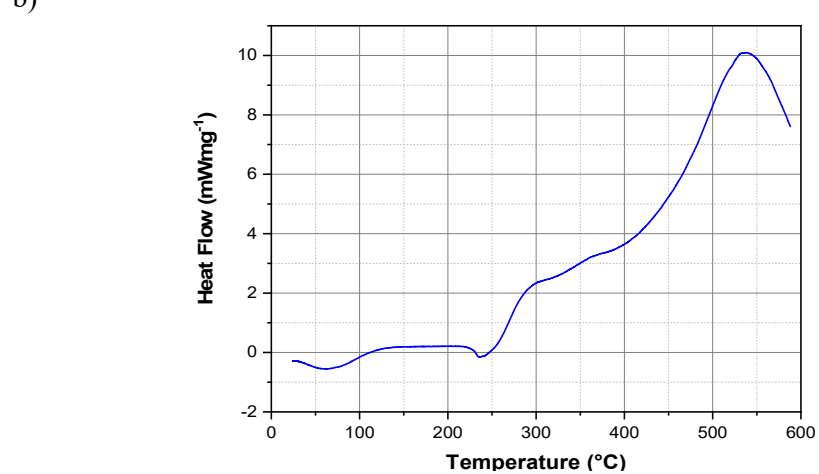


Figure 5.5 Differential Scanning Calorimetry of pristine wool under nitrogen and air atmosphere a), under air atmosphere (full scale) b).

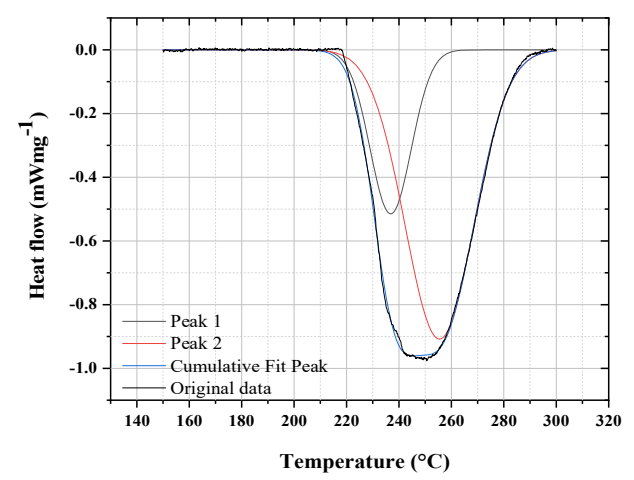


Figure 5.6 Deconvolution of the 220 – 300 °C peak under air atmosphere.

5.2 Stabilisation treatments

The temperature-time conditions tested are listed below (Table 5.2); the samples were labelled as SF-T-t, where T and t stand for temperature and time, respectively. The selected times and temperatures come from the TGA and DSC analysis previously discussed.

Table 5.2 List of stabilisations under air atmosphere tested.

Sample name	Temp.(°C)	Time (min)
SF-200-30	200	30
SF-200-60	200	60
SF-225-30	225	30
SF-225-60	225	60
SF-250-30	250	30
SF-250-60	250	60
SF-275-30	275	30
SF-275-60	275	60
SF-300-30	300	30
SF-300-60	300	60
SF-300-120	300	120

For both experiences, the material yields showed a mass loss that agrees with the thermogravimetric results, the difference in the treatment method notwithstanding. However, the yields recorded for the tubular furnace were larger than those registered for the muffle. This behaviour can be explained based on the difference in the heating rate; the furnace is three times faster than the one used for the muffle.

5.3 Characterisation of the stabilised material

5.3.1 Thermogravimetric studies

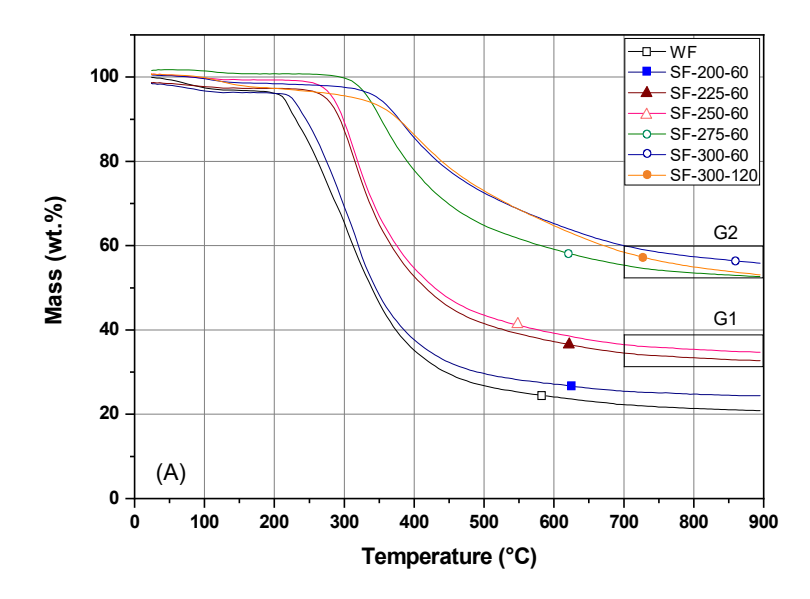
Once the material was submitted to different oxidising conditions, one of the many ways to evaluate whether the material underwent structural changes is to expose the samples to an increase in temperature under an inert atmosphere and record the mass loss (TGA). These SF's thermal profiles in the inert atmosphere were compared with those previously registered for virgin wool (Figure 5.7, a and b). The samples are classified into two groups upon the final weight loss: G1, formed by SF-225-t and SF-250-t, and G2, composed by SF-275-t and SF-300-t. The plots demonstrate that the overall mass loss at 900 °C decreased as the stabilisation temperature increased, following the trend: group G1 > group G2. The total mass loss of the fibres treated at 225 and 250 °C (ca. 32 wt.%) was 1.6 times higher than those stabilised at 275 and 300 °C (ca. 53 wt.%), regardless of the stabilisation time.

The temperature corresponding to the principal mass loss for SF's samples gradually moved towards higher temperatures, indicating that the stabilisation rendered fibres thermally more stable than the pristine one. The sample profile prepared upon stabilisation at 200 °C for 30 and 60 min was similar to that of the WFs, in agreement with the data obtained from the thermal analysis under dynamic conditions (Figure 5.4). These results confirm that oxidative stabilisation does not occur at temperatures equal to or below 200 °C regardless of the heating conditions (i.e., non-isothermal dynamic heating or holding at the selected temperature for a particular dwelling time). On the other hand, the occurrence of slow kinetics stabilisation at the lowest temperatures can be disregarded. The mass loss between 225-300 °C is associated with the rupture of hydrogen-bond peptide helical structures, the cleavage of disulphide bonds and the exothermic oxidation of the wool fibre. Solid-to-liquid phase changes accompany these processes (see calorimetric evidence in Figure 5.6) (Cao et al. 1997).

It should also be noticed that herein obtained yields (36 wt.%) are higher than those reported upon oxidative stabilisation at 160 °C of chemically modified wool (ca. 16-22 wt.%) (Hassan et al. 2015b). Moreover, the yield is also higher than those usually reported for rayon fibres at various oxidative treatments (ca. 20-30 wt.%) (Huang 2009), indicating a more effective oxidative stabilisation. This result might be due to the composition of the pristine wool fibres, richer in di-sulphur bonds located at the cysteine

residues (85 wt.% keratin) (Wojciechowska et al. 1999), compared to cellulosic and synthetic polymeric fibres.







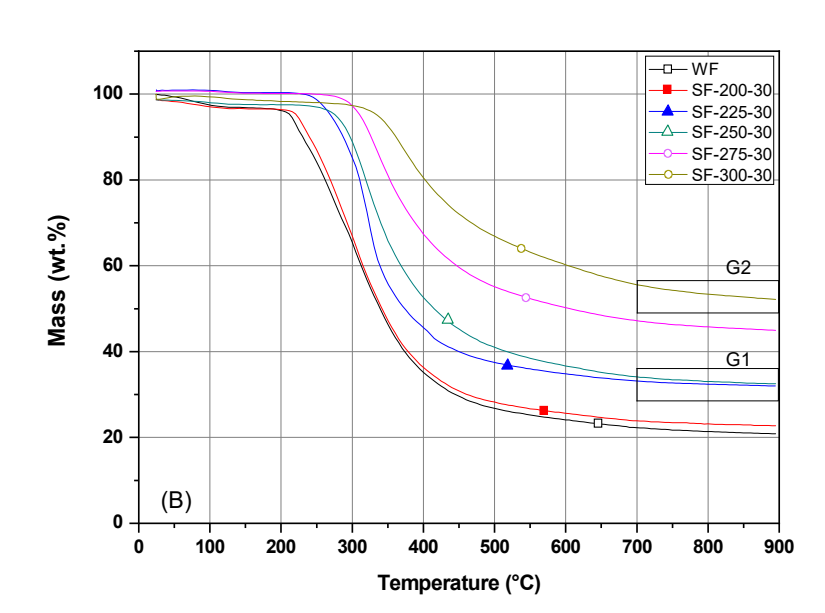


Figure 5.7 Thermogravimetric profile under an inert atmosphere of the wool fibres stabilised in the air at several temperatures for (a) 60 and 120 minutes and (b) 30 minutes.

Regarding the stabilisation time, this parameter did not seem to strongly impact the yields, with similar values (within a 5% difference) for the series treated at 30 and 60 min. Only for the highest temperature (i.e., 300 °C), the reaction rate seems independent of the time framework, with no significant differences in the yields for the samples stabilised at 30, 60, and 120 min.

5.3.2 Elemental content

The elemental composition of all stabilised fibres is compiled below (Table 5.3). The carbon content increased with oxidative stabilisation at the expense of the hydrogen, oxygen, and sulphur decrease. Interestingly, the nitrogen content remained rather constant (Figure 5.8). In contrast, the sulphur content decreased with the oxidation temperature and time, except for the samples treated at 300 °C, which showed similar values for different times. The reduction in the sulphur content is linked to the oxidation of the disulphur bonds of the cysteine residues in the wool, which would decompose into hydrogen sulphide and sulphur dioxide (Savige et al. 1966). The decrease in oxygen and hydrogen contents with the stabilisation temperature is mainly associated with dehydrogenation and dehydration reactions.

Table 5.3 The virgin wool's chemical composition (wt.%, dry-ash free basis) and the samples obtained after oxidative stabilisation at various temperatures and times (average values plus the standard deviation).

Sample	N	C	H	S	0
WF	15.45 ± 0.14	49.03 ± 0.09	6.97 ± 0.15	3.04 ± 0.04	25.52 ± 0.15
SF-200-30	15.09 ± 0.04	46.08 ± 0.16	6.35 ± 0.01	3.77 ± 0.04	25.45 ± 0.42
SF-200-60	15.72 ± 0.06	49.46 ± 0.12	6.67 ± 0.03	2.81 ± 0.04	25.34 ± 0.42
SF-225-30	15.51 ± 0.06	50.29 ± 0.06	6.04 ± 0.17	2.73 ± 0.02	25.12 ± 0.49
SF-225-60	15.48 ± 0.08	51.58 ± 0.10	6.19 ± 0.14	1.94 ± 0.03	24.81 ± 0.35
SF-250-30	15.54 ± 0.04	53.54 ± 0.05	5.71 ± 0.03	2.30 ± 0.01	23.62 ± 0.24
SF-250-60	15.59 ± 0.05	54.79 ± 0.04	5.69 ± 0.05	1.54 ± 0.02	22.03 ± 0.32
SF-275-30	15.12 ± 0.08	54.64 ± 0.02	5.02 ± 0.05	2.06 ± 0.01	21.24 ± 0.67
SF-275-60	15.87 ± 0.09	58.12 ± 0.05	4.91 ± 0.06	1.25 ± 0.03	19.85 ± 0.55
SF-300-30	15.01 ± 0.07	56.73 ± 0.26	4.36 ± 0.07	1.78 ± 0.01	19.73 ± 0.93
SF-300-60	15.83 ± 0.11	60.50 ± 0.13	4.15 ± 0.05	1.15 ± 0.02	18.36 ± 0.83
SF-300-120	15.89 ± 0.06	62.54 ± 0.02	4.09 ± 0.01	1.18 ± 0.01	16.29 ± 0.01

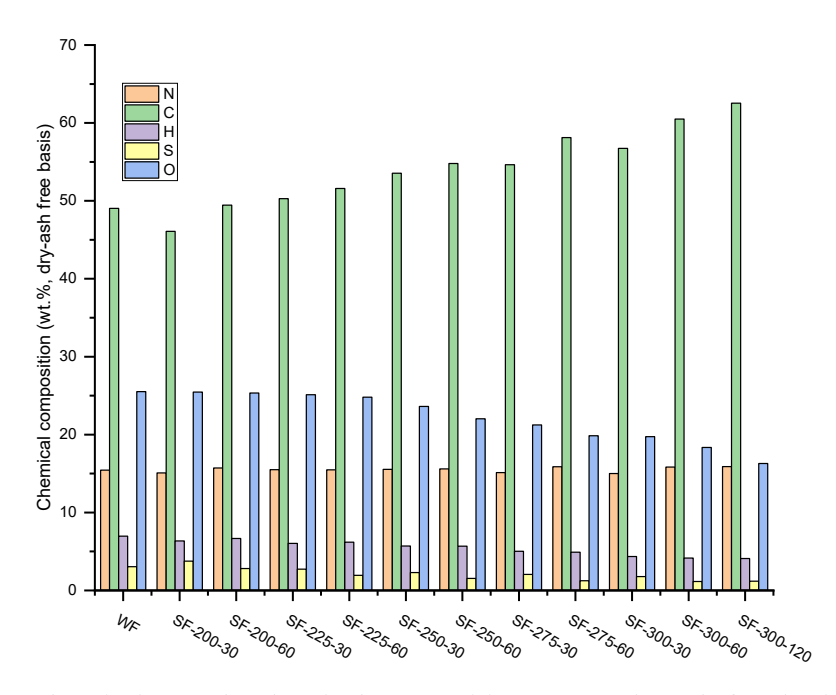


Figure 5.8 The virgin wool's chemical composition (wt.%, dry-ash free basis) and the samples obtained after oxidative stabilisation at various temperatures and times.

5.3.3 pH_{pzc}

Regardless of the treatment received, all the samples presented an acidic nature according to the pH values of zero charge (Table 5.4). The absence of WF and SF-200 series data results from the following technique since the procedure requires contact between the sample and water. WF is hydrophobic, and the SF-200 series kept this feature, which led to these materials avoiding getting wet. For the rest of the series, a pH_{PZC} value decrement is barely recorded with the increase in the treatment time, unmodified by the uncertainty range.

Table 5.4 pH_{PZC} values for stabilised materials (average values plus the standard deviation).

Sample	$pH_{PZC} \pm 0.2$
SF-225-30	4.7
SF-225-60	3.9
SF-250-30	5.3
SF-250-60	4.9
SF-275-30	5.3
SF-275-60	4.9
SF-300-30	5.2
SF-300-60	4.7
SF-300-120	4.1

5.3.4 Fourier transformed infrared spectroscopy

The infrared spectra of the fibres showed significant differences upon the stabilisation (Figure 5.9). The characteristic signal associated with CH groups at 2960 and 2920 cm-1 was observed in all the samples. The band featured at 1111 cm⁻¹, present in all the samples, is assigned to O-C stretching vibrations. The band at ~ 740 cm⁻¹ was set to the presence of esters for the SF-250 series onwards. The broadband between 4000-3000 cm⁻¹ can be interpreted as built by two contributions corresponding to N-H stretching vibration (~ 3300 cm⁻¹) Amide A and O-H stretching (~ 3200 cm⁻¹). In both cases, the frequency registered corresponds to H-bonded groups (Pakkaner et al. 2019). This band is observed for all the samples, regardless of the oxidative stabilisation temperature and time.

On the other hand, the Amide B (Fermi resonance doublet ~ 3100 cm⁻¹) peak, also related to N-H stretching vibrations, was no longer detected for sample SF-250-60 onwards. Amide I features (C=O stretching band ~ 1650 cm⁻¹) were observed in the pristine fibres and up to the series SF-250 at the same frequency. Whereas amide II (out-of-phase combination of the NH in-plane bend and the CN stretching vibration ~ 1500 cm⁻¹) and amide III (in-phase combination of the NH bend and the CN stretching vibration, ~ 1235 cm⁻¹) were not detected for any of the samples stabilised at 300 °C (SF-300 series). Amide IV (C=O-N bending mode ~ 620 cm⁻¹) was detected for all samples (Parker 1971). Thus, even though the signals associated with N-H and C-N (1200-1400 cm⁻¹) bonds are present in all cases, there are significant differences in the group's nature. This agrees with the trend observed for the nitrogen content by elemental analysis (Table 5.1) and confirms that the N-groups are predominantly rearranged during the oxidation.

On the other hand, the lack of Amide I and II groups for the samples stabilised at 300 °C indicates the occurrence of conformational changes in the secondary structure of the fibres, most likely associated with the evolution of hydrogen bonds during dehydration reactions (Parker 1971). A similar trend has been reported for converting amino groups into amide bonds during cross-linking reactions (Chandwani et al. 2016). It is consistent with the high content of amino acids in wool fibres. Such N-moieties rearrangement is supported by the appearance of a peak at 2221 cm⁻¹ for sample SF-275 and onwards series, associated with carbodiimide bond (-N=C=N-). The appearance of this group correlates with the gradual change observed in the 2500-1700 cm-1 range,

indicating the presence of a new group. Carbodiimides are usually formed via isocyanates (-N=C=O) as intermediate sub-products in the oxidation of amines. In the case of proteins, two amino acid residues close to each other in the tertiary structure can form isocyanates, which can undergo into carbodiimides, generating new bonds between protein chains.

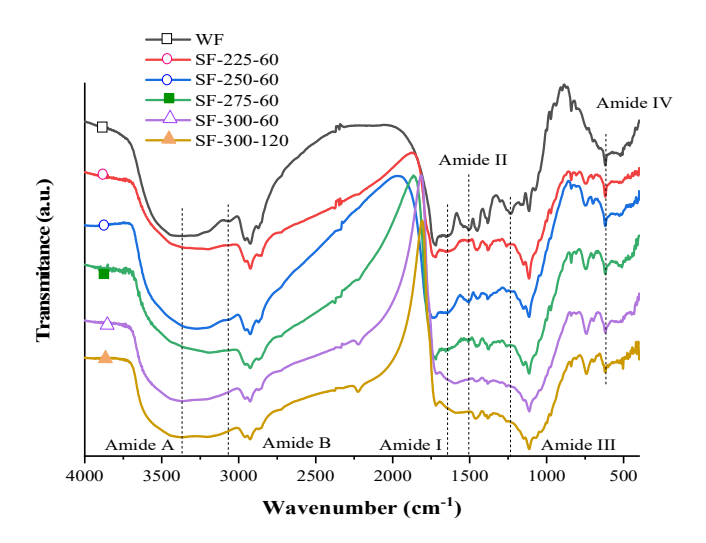


Figure 5.9 Infrared spectra of the pristine wool fibre and the series of samples stabilised at 60 and 120 minutes at various temperatures.

Sulphur-containing groups are challenging to detect by FTIR analysis as they often appear as low-intensity and nearby lying bands. To facilitate the identification of overlapped bands not resolved in the original spectra, we performed a derivative analysis of FTIR data (Puri et al. 1970). As seen in the graphic (Figure 5.10a), the disulphide bonds stretching vibration band at ~522 cm⁻¹ is detected for all samples, although it appears slightly shifted to higher frequencies for the SF-300 series (~524 cm⁻¹). As the wool is oxidised, structural changes could be expected in the cysteine residues. The bands at ca. 1020 and 1040 cm⁻¹ can be assigned to cysteine-sulphonate moieties (Bunte's salt) and cysteic acid, respectively; both were detected for WF with SF-300-60. On the other hand, cysteine monoxide and dioxide, featuring at 1076 and 1121 cm⁻¹, respectively, were observed only for SF-300-60 (Figure 5.10b). These frequencies agree with reported data for plasma treatment of wool fibres (Chandwani et al. 2016), thus confirming the oxidation of sulphur moieties upon the stabilisation in air.

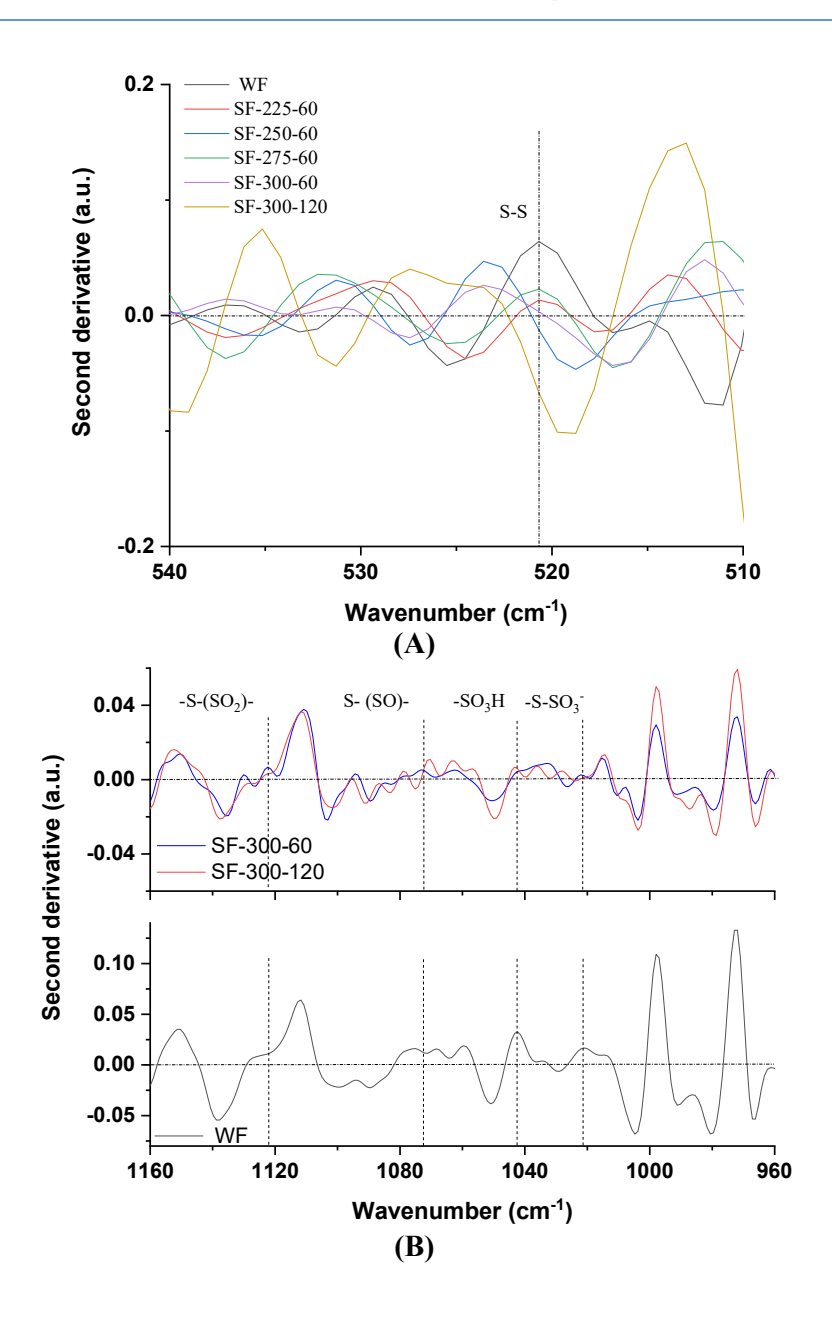


Figure 5.10 The second derivative of the FTIR transmittance spectra of (A) WF and SF-60 and 120-minute series, (B) SF-300 60- and 120-minute samples.

5.3.5 Thermal decomposition coupled with mass spectrometry

Additional characterisation of the changes in the wool fibres upon the oxidative stabilisation was carried out by temperature-programmed desorption coupled with mass spectrometry and the identification of the evolved gases in the samples (Figure 5.11). The graphs show the profiles corresponding to the m/z 2, 18, 28, 44, 46, and 64 of the thermogravimetric profiles recorded in the Ar atmosphere. The evolution of signal m/z 64

(Figure 5.11a) shows a broad emission band in the pristine wool fibres, panning from 200 to 700 °C. The multi-feature profile suggests that all released sulphur is bonded to the carbon surface in various configurations/environments. According to the literature, m/z 64 is assigned to sulphur-carbon complexes in thiol, sulphide, or oxidised forms of carbon (Michell 1988; Puri et al. 1970). This is due to the high reactivity of thiol and sulphide configurations that can be easily oxidised into SO₂-evolving groups upon heating during the TPD assays.

To clarify the different contributions of the profiles, we performed a deconvolution of m/z 64 considering four thermal events (see insets in Figure 5.11) assigned to thiol groups (ca. 180-250 °C), disulphur (ca. 250-350 °C), and oxidised sulphides (ca. 350-500 and 550-700 °C) (Gomis-Berenguer et al. 2016; Terzyk 2003). The first peak between 185 and 250 °C, only observed for WF, is associated with thiol groups belonging to cysteine residues (-SH). Above 200 °C, thiols would be transformed into disulphur bonds (cystine type). The 255 and 377 °C peaks in WF can be associated with thiol groups present in methionine residues and as sulphur from cystine. The peaks at higher temperatures in WF would correspond to the presence of oxidised sulphur groups, such as cystine sulphonate (-SSO₃ -) and cysteic acid (SO₂OH), as evidenced by FTIR (Figure 11b). For the samples stabilised at 250 °C (series SF-250-t), the contribution of disulphur bonds is still observed (250–350 °C), with no evidence of thiol groups. The broad tail in the range 350-600 °C indicates oxidised forms of sulphur in different configurations, most likely esters, cystine monoxide, and cystine dioxide, in agreement with infrared data (Figures 5.9 and 5.10). For the samples stabilised at 300 °C (SF-300-t series), the contribution of unoxidised forms of sulphur can be discarded; for these samples, the prominent peak at ~400 °C suggests oxidised sulphur in various configurations (e.g. cystine monoxide to dioxide).

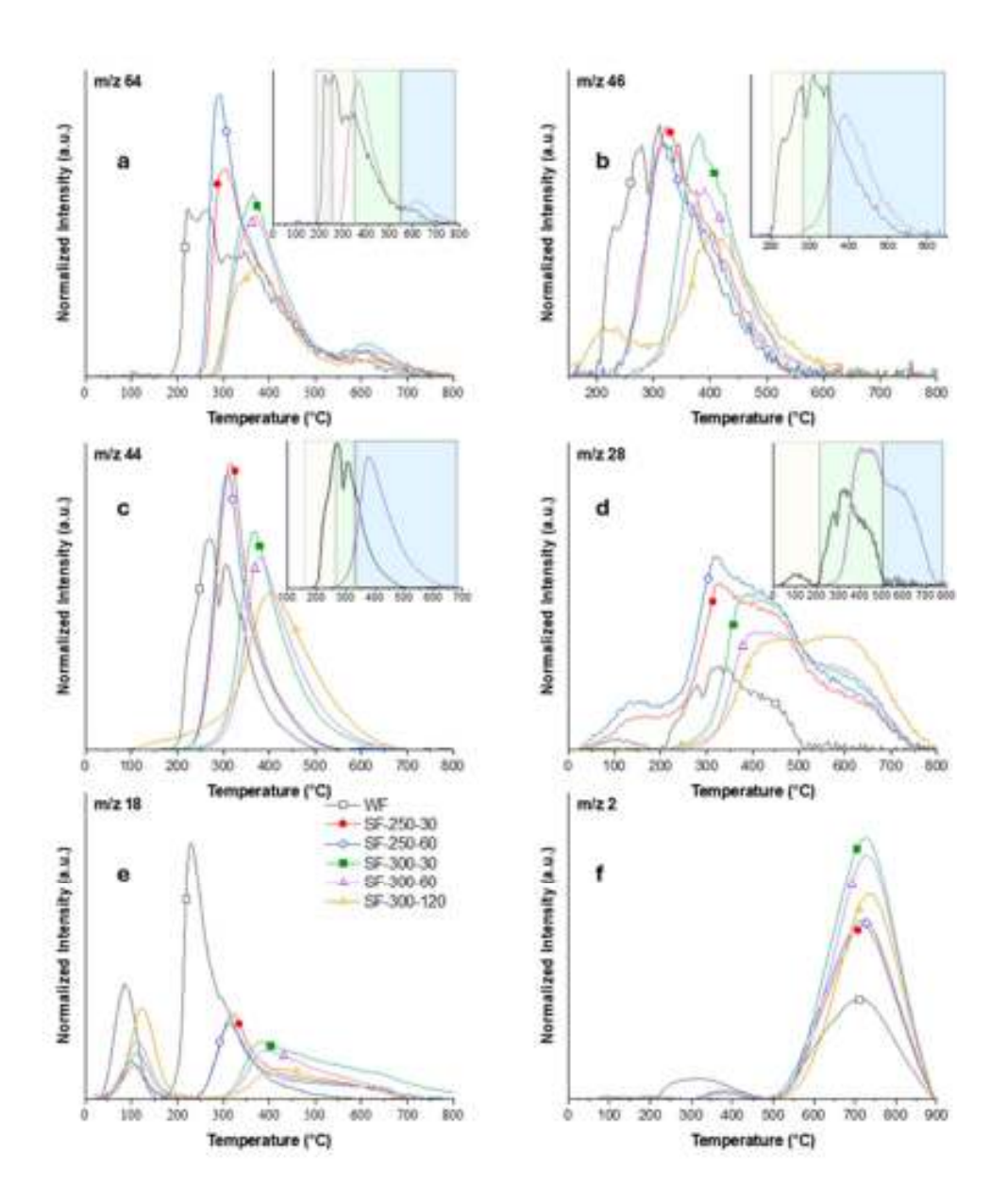


Figure 5.11 TPD-MS profiles of selected m/z for the pristine and stabilised wool fibres. Insets illustrate differentiated emission zones for WF and SF-300-60.

Finally, a small peak centred at 610 °C is visible to all samples, although its contribution increases with the stabilisation temperature. A semi-quantitative analysis inferred from the evolution of the areas of the peaks (Figure 5.11a) shows that the overall m/z 64 signal decreased for the stabilised samples. This agrees with the decrease in sulphur content detected by elemental analysis (Table 5.3).

The m/z 46 signal was assigned to nitrogen moieties decomposing as NO₂; the evolution for the stabilised samples also showed interesting features (Figure 5.11b). Deconvolution of the main peak was carried out considering three regions: 200–300 °C, 300–350 °C, and 350–550 °C. As in the case of m/z 64, pristine wool fibres showed the most significant contribution (Figure 5.11a) in the entire interval. The normalised intensities of the m/z 46 signal did not vary much for the samples, although the profiles shifted towards higher temperatures with the stabilisation temperature. This correlates with the data from elemental analysis (Table 5.3), where the nitrogen content remained relatively unchanged. It suggests that N-containing groups mainly suffer structural/configuration modifications rather than thermal decomposition upon oxidative stabilisation. Considering that peptide bonds are very stable, and the amide groups are present for all samples (Figure 5.9), it may be inferred that the nitrogen in peptide bonds is not affected by the treatment. Therefore, the m/z signal likely comes from residues rather than the main chain. The second region in the SF-250-t series overlaps with that of m/z 64 (ca. 310 °C), suggesting that it may be associated with the evolution of residues containing sulphur (cystine) linked to residues containing amines (e.g. arginine, proline, tryptophan). Furthermore, the shoulder at 390 °C became a peak for the SF-300-t series, implying a greater extent of oxidation. This peak temperature is in accordance with that corresponding to the thermal degradation of carbodiimides, whose presence was evidenced by FTIR. It likely comes from oxidised primary amines (e.g. alanine, glycine, and isoleucine) (Platnieks et al. 2020).

The m/z 44 signal is typically assigned to CO₂ evolving groups (Figure 5.11c); deconvolution shows three zones: 180–290 °C, 290–340 °C, and 340–700 °C. Unlike m/z 64 and 46, the profile of WF did not show the third contribution, indicating that the highest temperature peak is due to products of oxidation of the fibres. The first peak was only featured for WF and could correspond to residues with carboxylic groups (aspartic and glutamic acids). The second and third zones correspond to the emission of carboxylic groups, anhydrides, and lactones (serine residues), also supported by the contribution of the m/z 28 signal. The profile of the total area (Figure 5.12b) shows that the amount of CO₂ evolving groups remains relatively constant for all the samples.

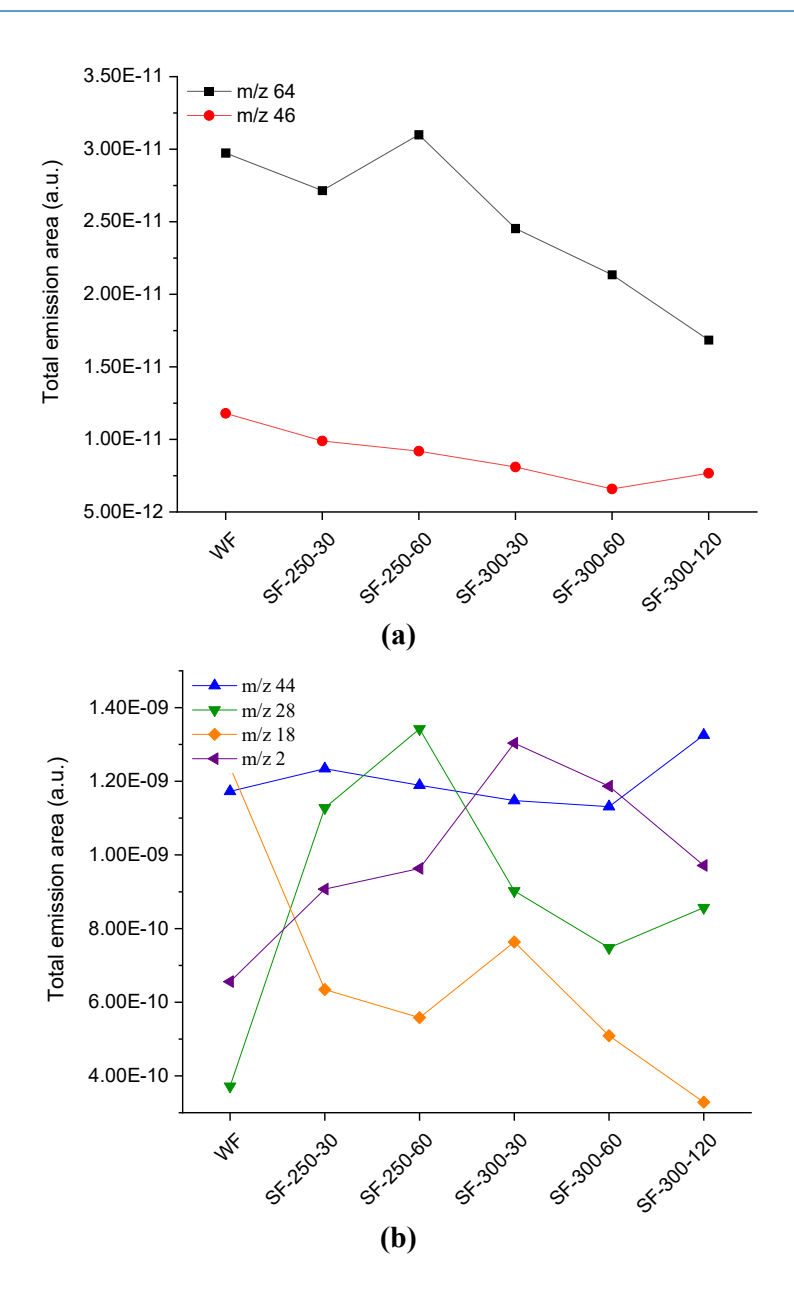


Figure 5.12 The total areas of the profiles correspond to 64 and 46 m/z signals (a), 44, 28, 18, and 2 m/z signals (b) obtained from TPD-MS data.

The m/z 28 signal is assigned to the evolution of CO (Figure 5.11d). Although this signal can also be set to nitrogen, the assignment to carbon monoxide was based on the relative intensities of the mass fragments of the entire mass spectrum compared to the theoretical spectra of pure gases (e.g., N_2 decomposes as m/z 28 and 12, while CO decomposes as m/z 28 and 14). Three main zones can be distinguished: 200–300 °C, 300–500 °C, and 500–800 °C. The signal below 200 °C has no clear origin, although it has

been attributed to the decomposition of vicinal carboxyl groups (Kreuk et al. 2006). Interestingly, the shape of the curves changed with the stabilisation treatments, with peaks featuring at higher temperatures as the stabilisation temperature increased; also, the amount of CO evolved showed a maximum for the series SF-250-t (Figure 5.12b). For these series, the main contribution corresponds to the second peak (300–500 °C), whereas for series SF-300-t, it corresponds to the 500–800 °C zone. The latter can be related to carbonyl groups formed upon oxidation of threonine residues, quinones and ethers.

The release of water, m/z 18 signal (Figure 5.11e), was significant for all the samples, with several peaks in a wide range of temperatures between 100 and 700 °C due to the different dehydration reactions involving adjacent surface groups (e.g., carboxylic, hydroxyl groups) (Figueiredo et al. 1999). This agrees with the fibre's acidic character (average pH values of ca. 4.8 ± 0.2), infrared data, and detected anhydrides in the m/z 28 and 44 profiles at similar temperatures. As the stabilisation time increased, the contribution of m/z 18 evolved in the 400–700 °C range decreased for the SF-300-t series. This could be connected to the lower presence of phenol groups that would be oxidised to quinones (Hotová et al. 2018).

The signal *m/z* 2 assigned to H₂ is linked to the cleavage of C–H and N–H bonds (Figure 11e). In all cases, the signal was recorded above 500 °C, as expected for samples with high volatile matter content. The amounts of evolved CO and CO₂ were quantified (Table 5.5); data showed relatively large quantities of both gases for all the stabilised fibres, regardless of the stabilisation temperature. This indicates that oxidative stabilisation creates O-containing groups with higher thermal stability, as confirmed by the thermogravimetric analysis (Figure 5.7). The ratio of CO/CO₂ increased up to 250 °C, but decreased for the treatments at 300 °C, remaining relatively constant. Since the amount of CO₂ remains practically unchanged, the stabilisation mainly favoured the formation of ethers and carbonyl/quinone groups.

Table 5.5 Quantifies the amounts of CO and CO_2 released by integrating the m/z 28 and 44 peaks in the TPD profiles.

Sample	CO (µmol.mol ⁻¹)	CO ₂ (µmol.mol ⁻¹)	CO/CO ₂
WF	1289	3602	0.36
SF-250-30	2918	3571	0.82
SF-250-60	3654	3532	1.03
SF-300-30	2023	3452	0.59
SF-300-60	1809	3444	0.53
SF-300-120	2061	3726	0.55

The following plots (Figures 5.13 - 5.16) show the evolution of the deconvoluted peaks for selected samples. As discussed above, the most significant peaks have been assigned to the expected functional groups.

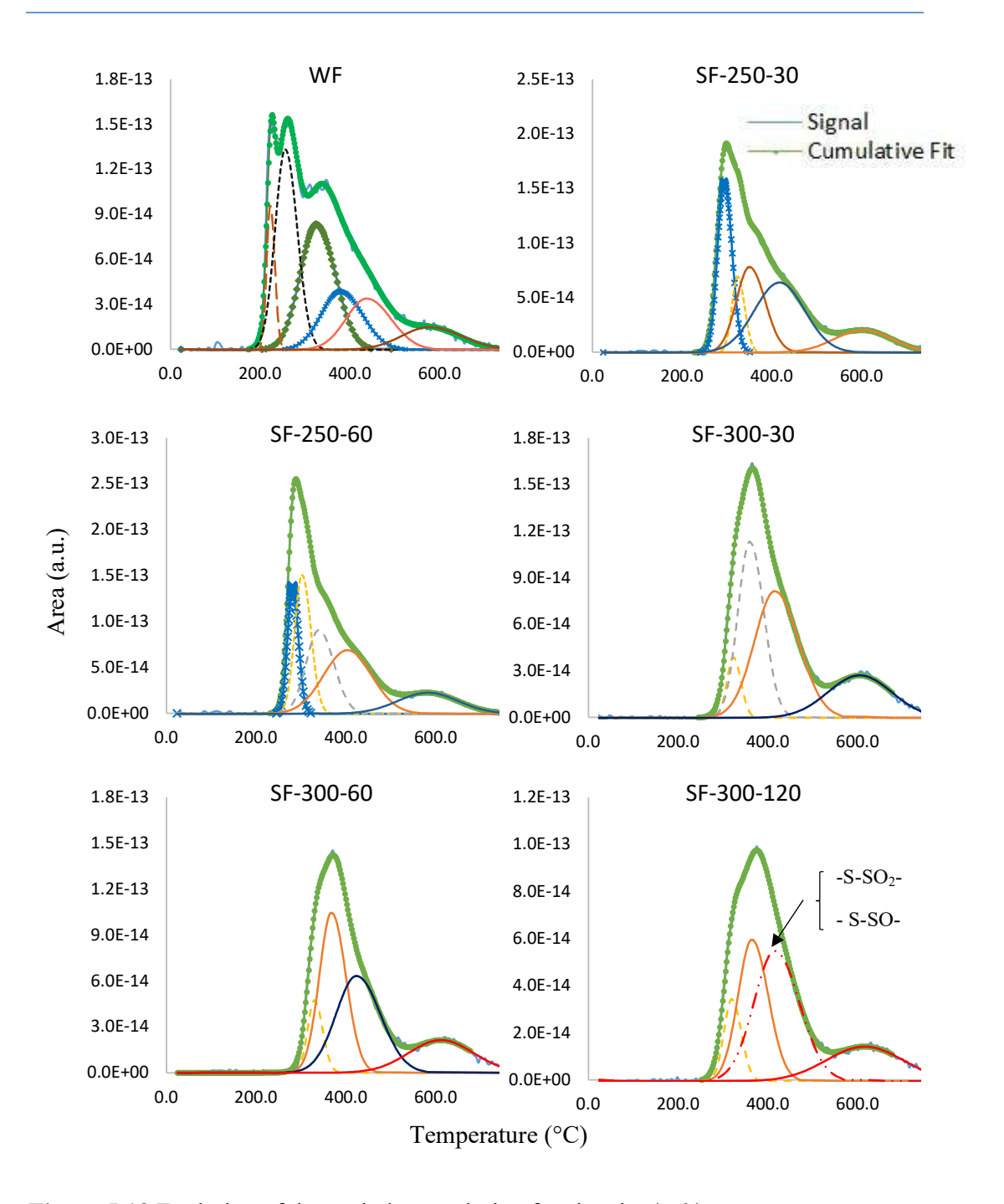


Figure 5.13 Evolution of the peak deconvolution for signal m/z 64.

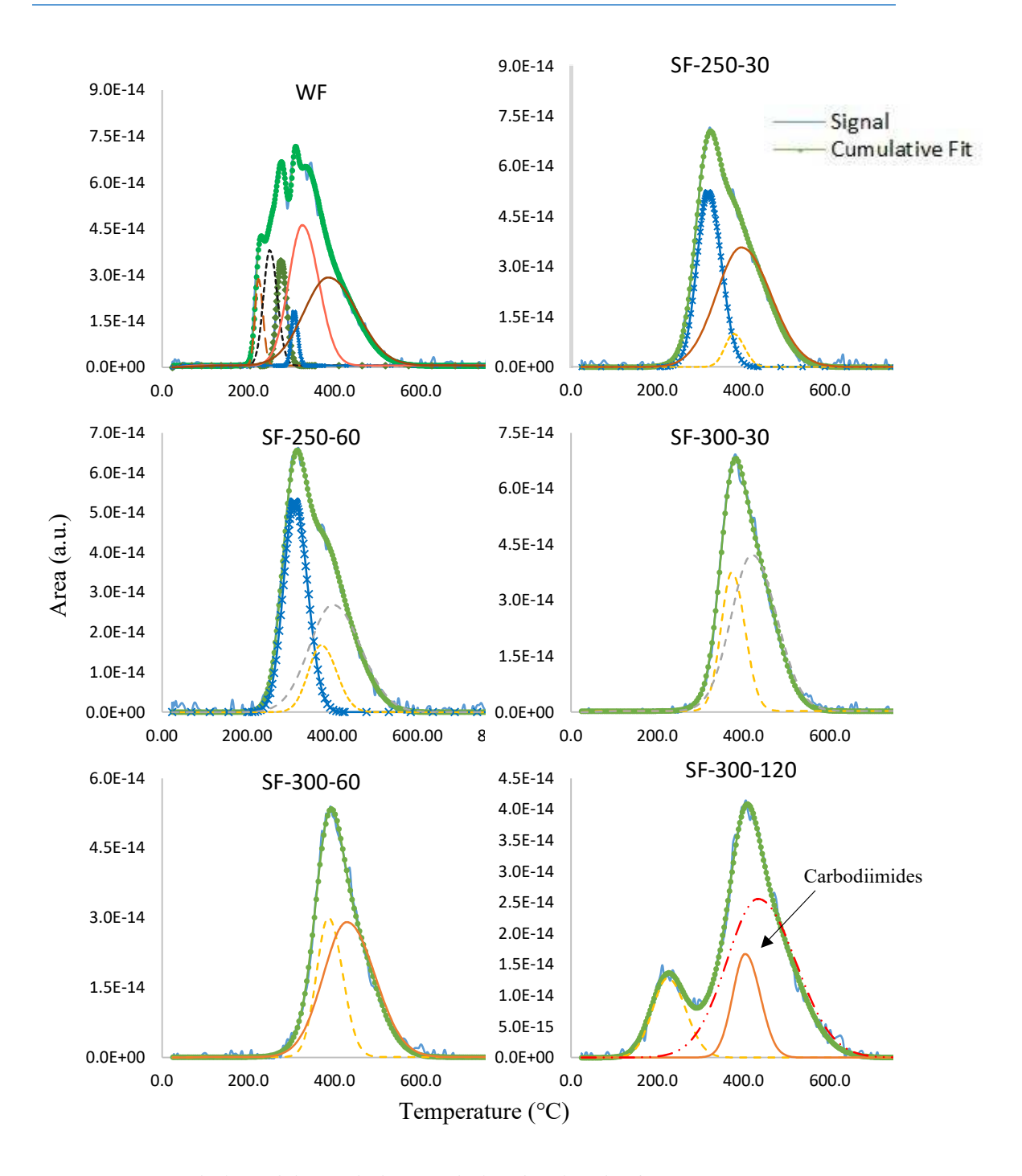


Figure 5.14 Evolution of the peak deconvolution for signal m/z 46.

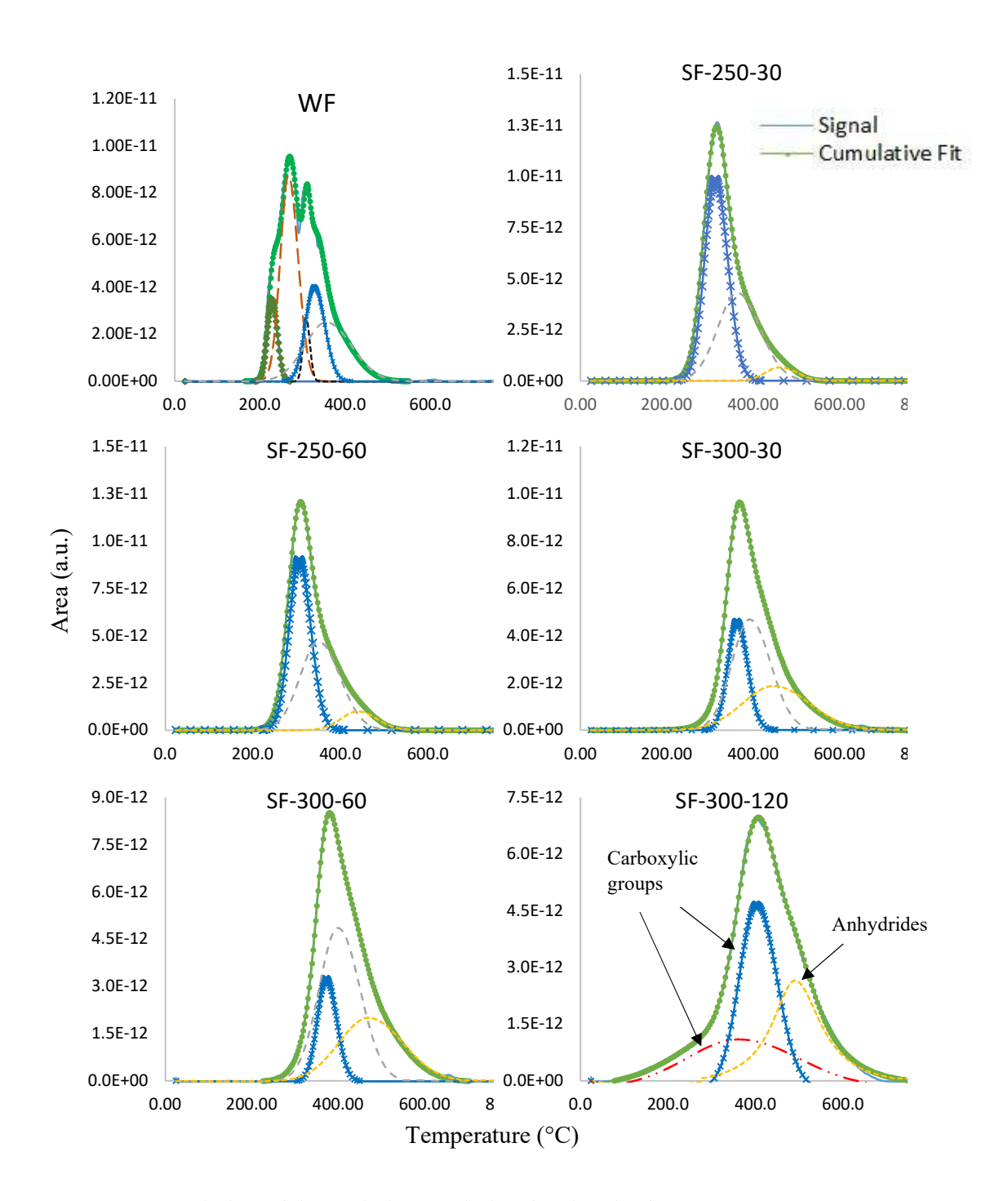


Figure 5.15 Evolution of the peak deconvolution for signal m/z 44.

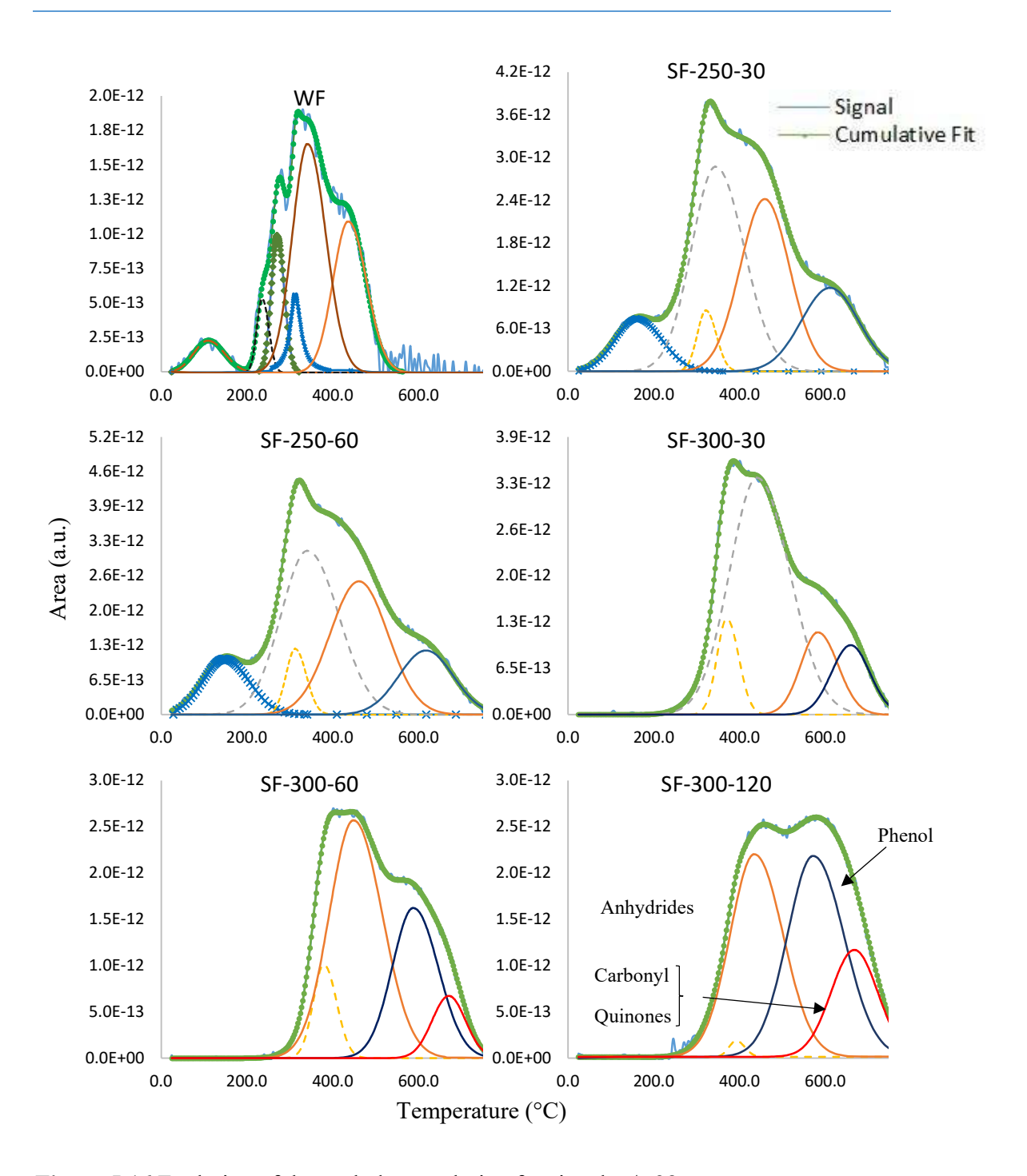


Figure 5.16 Evolution of the peak deconvolution for signal m/z 28.

5.3.6 Raman spectroscopy

The structural changes induced upon stabilisation of the fibres were analysed by Raman spectroscopy (Figure 5.17). It should be mentioned that samples WF and SF 200-225 presented a high fluorescence component that prevented recording the Raman

spectra; therefore, the spectra shown correspond to samples stabilised above 250 °C. The samples' spectra are similar, showing the typical fingerprint of disorganised carbon materials with the characteristic D and G bands (ca. 1350 and 1600 cm⁻¹, respectively) (Dietzek et al. 2010). The former band (Defects) is associated with combining carbon vibrations with sp² and sp³ hybridisation, while the latter band (Graphite) is related to sp² carbon vibrations. The broad profiles of the D and G bands and the absence of second-order spectra indicate the fibres' amorphous character (short-range order). The broadness of the G band also confirmed this observation, with full width at half-maximum (FWHM) values (ca. 89-97) comparable to those reported for stabilised pitch fibres (Kim et al. 2017); the values for the D band are higher due to a significant contribution of defects (Table 5.6). However, analysing the R_a parameter, it can be seen that the G band contribution increased by an average of 7 % for the 300 °C series compared with the 275 series. This tendency can be related to the treatment's temperature, where higher temperatures render more organised materials.

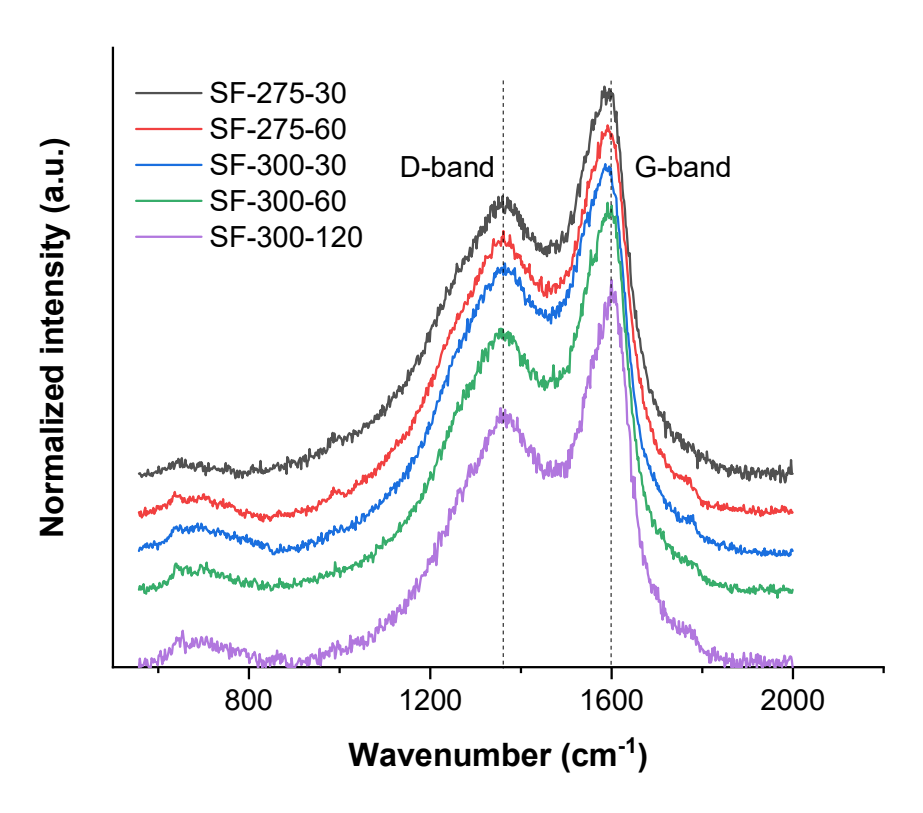


Figure 5.17 Raman spectra of selected stabilised samples; spectra have been shifted for clarity.

Table 5.6 Raman parameters for 275 and 300 series.

D - Band		G - Band				
	Raman shift	FWHM	Raman shift	FWHM	R_a , I_D/I_G	$R_p,I_D/I_G$
	(cm ⁻¹)	(Å)	(cm ⁻¹)	(Å)		
SF-275-30	1345.8	282.2	1600.2	91.0	2.99	1.11
SF-275-60	1348.4	238.8	1601.2	88.9	2.81	1.05
SF-300-30	1355.0	270.7	1596.8	96.5	2.38	1.08
SF-300-60	1355.9	281.0	1602.5	92.2	2.66	1.09
SF-300-120	1358.0	260.9	1608.2	91.0	2.68	1.07

5.3.7 Scanning electronic microscopy

SEM (Figure 5.18) explored the morphology of the fibres upon stabilisation. For the pristine wool fibres, the two distinct zones of the precursor are observed: the inner marrow or cortex and the external cuticle (Wojciechowska et al. 1999). For the stabilised fibres, the characteristic cellular arrangement of the cuticle was still recognisable, although the surface gradually became smoother as the stabilisation temperature increased. While the fibrous morphology was preserved between 200-300 °C, the soft marrow gradually disappeared with temperature. As can be seen for sample SF-300-120, the stabilised fibres become hollow due to the loss of the cortex. The wall thickness of the hollow fibres was ca. $7.0 \pm 0.5 \, \mu m$. Average fibre diameters were barely modified during stabilisation, circa. 26 μm for WF and around $29 \pm 2 \, \mu m$ for sample SF-300-120.

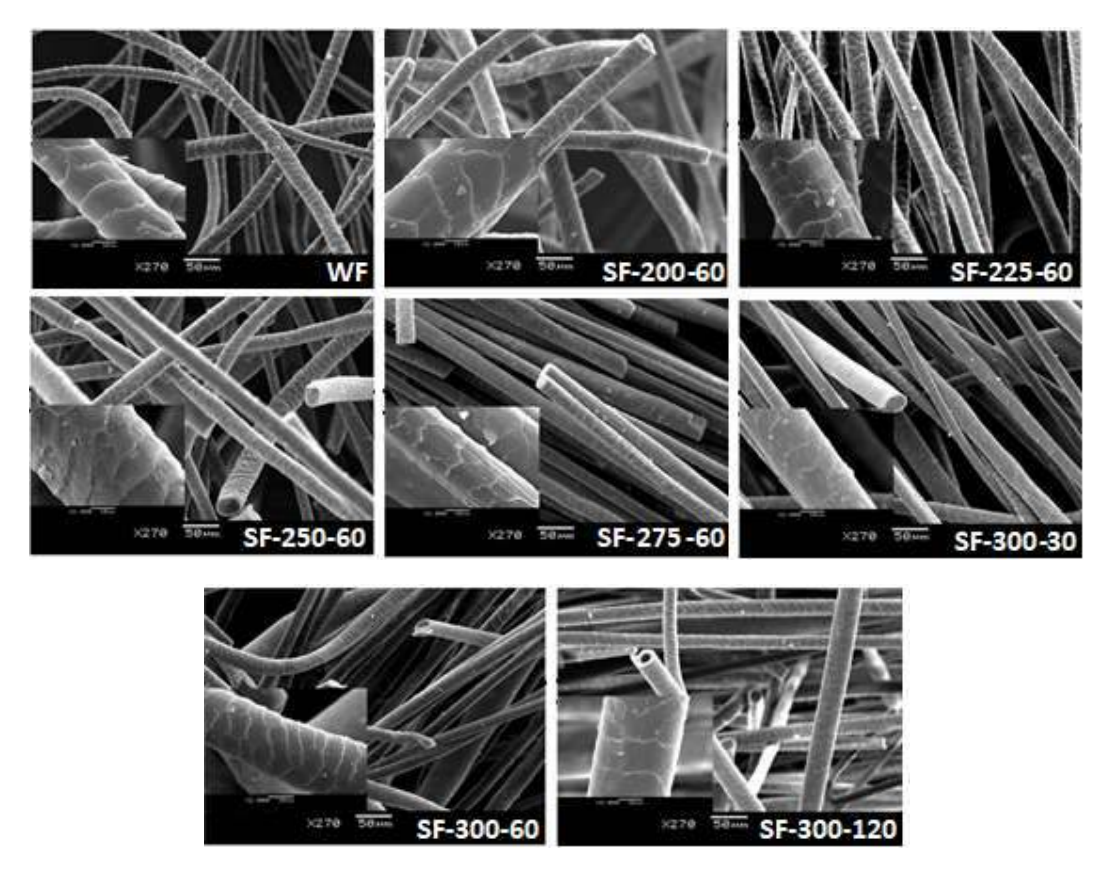


Figure 5.18 SEM images of the pristine (WF) and stabilised (series SF-T-t) wool fibres at various temperatures (magnification of the pictures: x270; magnification of insets: x2000).

At stabilisation temperatures above 400 °C, the fibrous morphology was no longer preserved, as the wool fibres melted (Figure 5.19).

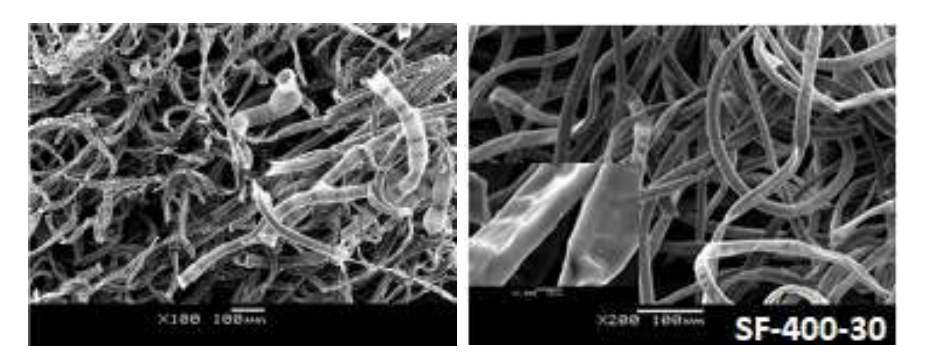


Figure 5.19 SEM image of the stabilised material at 400 °C for 30 minutes, where the fibres collapse can be observed.

5.3.8 X-ray diffraction

The X-ray diffraction (XRD) spectra of WF, SF-250 and upper series (Figure 5.20) show that in the case of the precursor, the typical keratin α -helix and β -sheet diffraction peaks are present (2θ near 10° and 20°) (Wang et al. 2016). The destabilisation of the α -helix at the process's first stages (low times) is observed, evidenced by the disappearance of the peak at $2\theta = 10^{\circ}$. The peaks corresponding to the β -sheet ($2\theta = 20^{\circ}$) were further intensified in the diffraction pattern for higher times and temperatures. These observations indicate cross-linking and loss of the S-S bonds that keep the α -helix conformation and are in accordance with the data results in FTIR, Raman and TG analysis. L_c and L_a values and interlayer d-spacing of the SF (Table 5.7) indicate the presence of non-graphitic carbon. The average interlayer d-spacing for all SF was about 0.4 nm. However, the SF-300-120 sample showed a [002] peak centred at $2\theta = 25.19^{\circ}$, suggesting a structure with a highly organised layer structure (Lavín 2017), possibly because of higher cross-linking. The interlayer d-spacing for this sample was 0.35 nm. A lack of peak definition is observed for all temperatures for the lower residence times. This is consistent with the low reaction rates discussed for FTIR results.

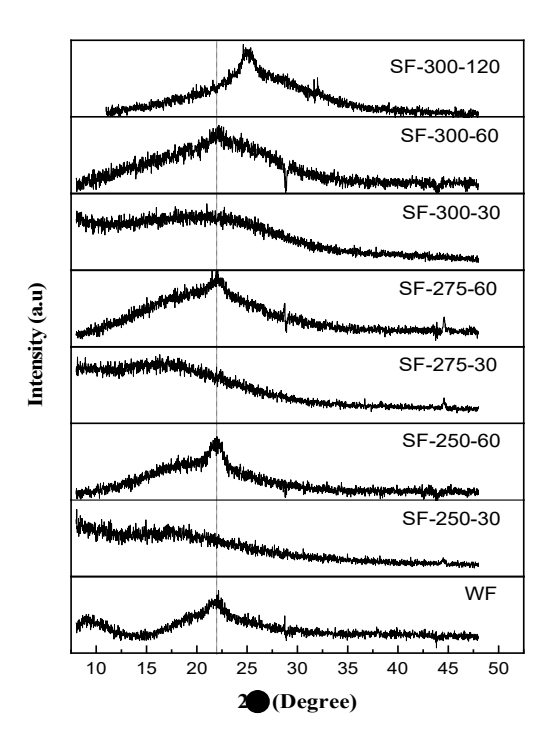


Figure 5.20 XRD spectra of WF, SF-250 and upper series.

Table 5.7 Structure parameters of X-ray diffraction for SF series of selected samples.

Sample	2θ (Deg)	d(002) (nm)	La (nm)	L _c (nm)
SF-250-60	21.87	0.41	3.52	1.72
SF-275-60	21.79	0.41	1.84	0.89
SF-300-60	22.02	0.40	1.32	0.64
SF-300-120	25.19	0.35	2.13	1.04

5.4 Partial conclusions

The oxidative stabilisation of wool fibres in the air between 200-300 °C allowed the obtaining of densified materials with a fibrous morphology and a carbon content of up to 60 wt.%. Above 400 °C, the fibre morphology is lost, and the material becomes fragile, most likely due to the fibres melting. At lower temperatures, the morphology and structural features of the stabilised materials were relatively similar, regardless of the stabilisation conditions. A thorough characterisation of the fibres stabilised up to 300 °C for different times has revealed important changes in the composition due to the thermal evolution of the O-, N- and S- moieties present in the pristine fibres. Overall, the sulphur and oxygen contents decreased with the stabilisation temperature, whereas the nitrogen content remained relatively constant. This indicates different thermal degradation pathways for the surface groups of the wool fibres. The loss of sulphur upon the decomposition and oxidation of sulphur bridges in the pristine fibres leads to different oxidised sulphur complexes, still binding polypeptide chains in most cases. Thiols and disulphur bridged species in the wool fibres (e.g., cysteine, methionine residues) are gradually transformed into oxidised sulphur complexes (e.g., sulphonate, cystine monoxide, and dioxide residues). After stabilisation at 250 °C, thiol groups are no longer observed, but disulphur bonds are still detected.

In contrast, sulphur is predominantly in oxidised complexes for the samples stabilised at 300 °C, with no evidence of thiols and a small contribution of disulphides. The amount of oxygen decreased but remained relatively high in the stabilised fibres due to the forming of new groups (mainly ethers and quinone) during the cross-linking reactions occurring during the oxidative stabilisation. Rather, large quantities of CO₂ and CO were released regardless of the stabilisation temperature due to the decomposition of carboxylic, ethers, and carbonyl groups present or formed upon oxidation of various

residues (e.g., threonine, serine). On the other hand, the rearrangement of N-groups would seem to be associated with the transformation of amides present in the pristine wool fibres into more stable carbodiimide groups. The release of water at various temperatures in the TPD-MS profiles confirmed the occurrence of dehydration reactions involving adjacent surface groups. This would be responsible for the loss of the secondary structure of the fibres. However, the polypeptide bond is unaffected, so the primary structure remains unchanged. This allows for preserving the fibrous morphology of the stabilised materials, which can, therefore, be used as low-cost precursors for preparing carbon fibres upon carbonisation.

Since sulphur-containing groups belonging to oxidised complexes were identified for 300 °C series, and 120-minute treatment SEM images demonstrate the existence of hollow fibres (desirable for adsorption applications), SF-300-120 was the sample selected for further treatment.



"No establezcas alianzas con cuanto hay bajo el cielo.

No busques equilibrio en cuanto hay bajo el cielo.

Confia en tus propios recursos."

El arte de la guerra

Sun Tzu

As mentioned in Chapter IV, two main methods were tested to obtain an activated material that could keep the morphology; one of the main goals of the present work is chemical and physical activation. In this sense, several studies were conducted to establish the best working conditions. This chapter displays the results obtained, focusing the discussion on the textural and chemical properties.

The discussion regarding the results was approached from different angles; thus, here is a quick guide to help understand the chapter structure layout. Sections 6.1 and 6.2 explain the criteria for selecting the temperature of the activations (chemical and physical) based on thermogravimetric reactivity profiles. Section 6.3 discusses the repeatability of the method (subsection 6.3.1), as well as the effect of different technical aspects like the activation method (subsection 6.3.2), the gas flux during physical activation (subsection 6.3.4), and the activation time during physical activation (subsection 6.3.4). Section 6.4 analyses the chemical composition of all the obtained samples. Below are listed all the samples obtained under different techniques and conditions (for techniques, see Chapter IV, section 4.2.3).

Table 6.1 List of the carbonised samples developed for the present work.

Samples	Treatment	Atm./flow (mL min ⁻¹)	Time (min)	Temp. (°C)
ACF-KOH-2503				
ACF-KOH-0104	Chemical	N ₂ / 100	60	600
ACF-KOH-0704				
ACF-0506-30-D				
ACF-0606-30-D				
ACF-0407-30-D				
ACF-0507-30-D	Physical		30	950
ACF-0607-30-D	Tilysical	CO ₂ / 200	30	930
ACF-1107-30-D				
ACF-2107-30-D				
ACF-2807-30-D				
ACF-0908-30-D				

Table 6.1 – continuation List of the activated samples developed for the present work.

Samples	Treatment	Atm./flow (mL min ⁻¹)	Time (min)	Temp. (°C)
ACF-0905-30-CR				
ACF-1005-30-CR				
ACF-1105-30-CR			60	
ACF-1305-60-CR			00	
ACF-1605-60-CR				
ACF-2005-60-CR	Physical	cal CO ₂ / 10		
ACF-0306-120-CR			120	
ACF-0506-120-CR			120	875
ACF-0706-120-CR				
ACF-1304-180-CR			180	
ACF-1504-180-CR				
ACF-2104-180-CR				
ACF-0406-240-CR			240	
ACF-0906-240-CR				
ACF-1506-240-CR				

6.1 Reactivity profiles of the char in CO2 and Ar

The sample stabilised at 300 °C for 120 min (see Chapter IV, section 4.2.2) and was carbonised at two different temperatures (800 and 1000 °C) to obtain chars. Subsequently, to select the activation temperature for the physical activation of those chars, the reactivity profiles were measured under CO₂ and inert atmospheres (Figures 6.1 and 6.2). Data is compared to stabilised carbon before carbonisation (sample SF-300-120). It is important to remark that, under those temperatures, the CF obtained is an isotropic material, shows a random orientation of the crystallites and possesses a modulus as low as 100 GPa combined with low strength (Park 2015).

The profile of the stabilised sample (SF-300-120) under Ar flow (Figure 6.1 black line) shows that the material suffers the loss of volatile matter from 380 to 700 °C (mass loss of ca. 40 wt.%), whereas, at higher temperatures (between 800 to 1000 °C), the mass loss represents ca. 3 wt.%. Both chars behave similarly, which seems reasonable as the main thermal transformations have already occurred at lower temperatures. In sum, the

chars are not expected to display appreciable differences at these chosen working temperatures because the temperature practically does not affect the sample at this stage.

To select the temperature of activation under CO₂ from the reactivity profiles, we must consider that the extent of the activation of reaction (ξ) (Equation 6.1) depends on several parameters like the temperature T (°C), the gas flow \emptyset_{CO2} (mLmin⁻¹), the time of treatment t (min), and the characteristics of the char:

$$\xi = \frac{\Delta n_i}{\nu_i}, \ \xi = f(T, \emptyset_{CO2}, t, char)$$
 Equation 6.1

where Δn_i represents the amount of reacting material in moles, and v_i is related to stoichiometry (Barrow 1961).

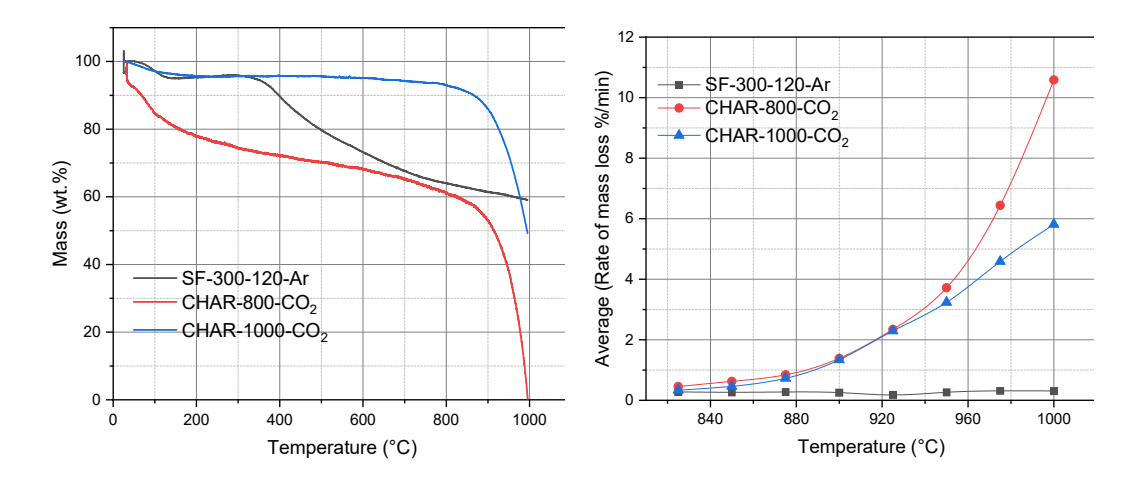
The variation of function 6.1 can be expressed as (Equation 6.2):

$$d\xi = k (t, \emptyset_{CO2}) dT$$
 Equation 6.2

where k is the reaction constant encompassing all the unchanged parameters, while dT is the parameter assessed for each material.

The chars obtained at 800 and 1000°C displayed a different behaviour under a CO₂ flow (Figure 6.1). The rate of the CO₂ reactivity profiles (ξ) increased with temperature from 880 °C (Figure 6.2) compared to the argon profile and followed a similar trend up to 925 °C for both chars. From this temperature onward, the char prepared at 800°C displays a faster reactivity profile than that prepared at 1000°C (Figure 6.2). Therefore, the assumption that the carbonisation treatment does not affect the reaction rate (material - CO₂) is strictly valid up to 925 °C since both plots (char-800-CO₂ and char-1000-CO₂) overlap at this point (Figure 6.2).

The mass loss difference was ca 2 wt.% at 925 °C and ca. 15 wt.% at 950 °C Based on these results, we selected 875 °C as the temperature for the physical activation under chemical reaction control (Chapter IV, section 2.3.1). The residence time varied from 30 minutes up to 4 hours. For diffusion control, we selected 950 °C for a 30-minute treatment. Longer residence times were not further tested since the fibrillar structure of the sample was damaged at those conditions (Chapter VI, figures 6.16 and 6.17).



for SF-300-120 under Ar, and CF obtained at 800 and 1000 °C under CO2.

Figure 6.1. Thermogravimetric analysis Figure 6.2. Reactivity profiles for SF-300-120 under Ar, and CF obtained at 800 and 1000 °C under CO₂.

6.2 Reactivity profiles in KOH

Two samples were tested regarding chemical activation: the pristine WF and the stabilised fibre (SF-300-120) following the same procedure (Chapter IV, section 4.2.3). The sample's reactivity profiles, under an inert atmosphere, before and after impregnation with KOH are shown to discriminate from thermal and impregnant incidence on the sample (Figures 6.3 and 6.4). The profiles of samples WF and WF-KOH (1:1) are rather similar at temperatures above 400°C, but the sample impregnated with KOH shows a mass loss below this temperature due to the reaction with KOH. This behaviour agrees with that reported in the literature (Gillespie et al. 2022; Gousterova et al. 2003; Harris 1935) addressing the hydrolysis of the protein of the wool precursor in the presence of KOH, that attack the disulphide linkages splitting them leading to the destruction of the fibrillar structure. Comparing the pristine (sample WF) and stabilized (SF-300-120) precursors, it can be observed that the thermal stabilisation step at 300°C helps the material to stand the heating in terms of mass loss. For the stabilized sample, the profiles are similar below 500°C, but the rate of mass loss is faster for the sample impregnated with KOH at higher temperatures (Figures 6.3 and 6.4).

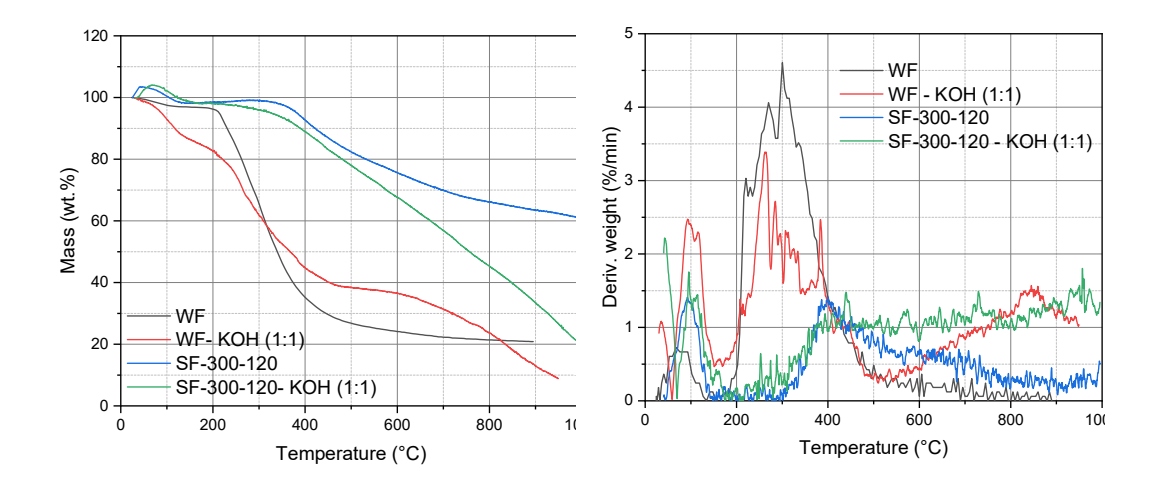


Figure 6.3. Thermogravimetric analysis under Ar atmosphere for the samples impregnated with KOH.

Figure 6.4. DTG analysis under Ar atmosphere for the samples impregnated with KOH.

Note: WF-KOH (1:1) corresponds to the wool fibre impregnated with KOH in a 1:1 mass ratio; SF-300-120-KOH (1:1) corresponds to the stabilised fibre impregnated with KOH in a 1:1 mass ratio.

The activation temperature in KOH was selected according to the DTG recorded data, where the plots demonstrate that there is a threshold temperature (550 °C) after which both samples (impregnated and not impregnated) go separate ways (Figure 6.4). This implies that after 550 °C, the reaction between the chemical agent and the carbon structure occurs (Chapter II, reaction 2.6), discarding temperature effects. Considering all the above, we selected 600 °C as the activation temperature in KOH, expecting that a mild temperature will not strongly impact the fibrillar morphology of the chemically activated material.

6.3 Textural and morphology characterisation

After the activation, the samples were further analysed to discern to which extent the different conditions applied during the activation affected the characteristics of the resulting activated materials and whether the fibre morphology was kept. For the textural characterisation, specific surface area, the volumes of micro and mesopores, nd the pore diameter distribution were evaluated from the gas adsorption data.

6.3.1 Repeatability of the activation methods

To confirm that all the batches obtained by applying a specific activation method are similar, assessing the technique's repeatability* is mandatory. Particularly when natural resources are used as precursors in the preparation of materials, owing to the possible variation in composition and origin of the precursors themselves). One way to carry out this study is to analyse the textural properties of materials prepared in different batches and determine the respective pool data's standard deviation (σ) .

* Repeatability (IUPAC definition): The closeness of agreement between independent results obtained with the same method on identical test material under the same conditions (same operator, same apparatus, same laboratory and after short time intervals). The measure of repeatability is the standard deviation qualified with the term: 'repeatability' as repeatability standard deviation. In some contexts, repeatability may be defined as the value below which the absolute difference between two single test results obtained under the above conditions may be expected to lie with a specified probability (IUPAC 2009).

6.3.1.1 Repeatability of the chemical activation procedure

Three batches of samples were obtained by chemical activation following the same procedure (Chapter IV, section 4.2.3). The figure shows the nitrogen adsorption-desorption isotherms (Figure 6.5), while the table displays the main textural parameters of these samples (Table 6.2). The standard deviation of the textural parameters was calculated (Table 6.2) for batch repeatability. As seen, the standard deviation values of the textural parameters were very low for all of them, accounting for 3-6 % of the values. Low values were obtained for the surface area and micropore volume deviations in particular. Thus, we concluded that the method has good repeatability. All the samples were then mixed and named after ACF-KOH-2604.

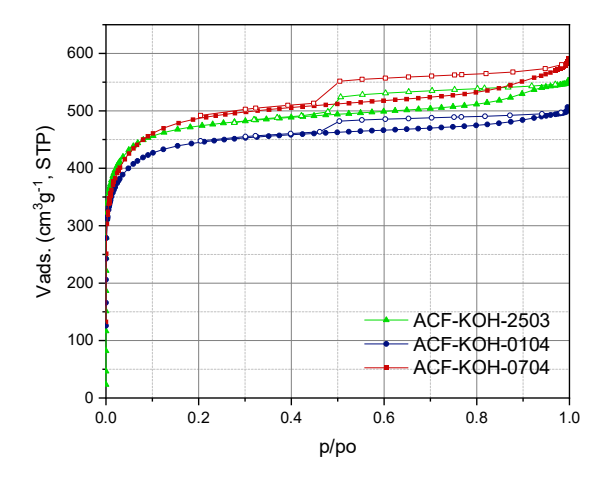


Figure 6.5 N₂ adsorption-desorption isotherms at -196 °C of three batches of chemically activated material.

Table 6.2 Main textural parameters obtained from the nitrogen adsorption-desorption isotherms at -196 °C for the chemically activated samples. Average values and standard deviations ($\sigma = \sqrt{\frac{\sum_{1}^{N}(x_{i}-x)^{2}}{N}}$) have been calculated for the pool of dataset.

			Γ	Dubinin-Radushkevich method			
	SBET	V _{TP} (0.97 p/p0)	W_0, N_2	Eo	Lmicro.	S	Smicro
Sample	m^2g^{-1}	cm ³ g ⁻¹	cm ³ g ⁻¹	kJmol ⁻¹	nm	m^2g^{-1}	m^2g^{-1}
ACF-KOH-2503	1843	0.839	0.713	19.42	1.35	2006	1059
ACF-KOH-0104	1869	0.900	0.678	19.16	1.39	1910	975
ACF-KOH-0704	1727	0.769	0.630	21.06	1.12	1773	1127
Average value	1813	0.836	0.674	19.88	1.29	1896	1054
Standard dev.	62	0.054	0.034	0.84	0.12	96	62

6.3.1.2 Repeatability of the physical activation method controlled by Chemical Reaction

The nitrogen adsorption-desorption isotherms and the main textural parameters of the samples prepared upon physical activation for 240 min under Chemical Reaction control (Chapter IV, section 4.2.3) are shown as follows (Figure 6.6 and Table 6.3). The standard deviation results also confirm the method's reproducibility; however, the values were slightly higher than those of the chemically activated results.

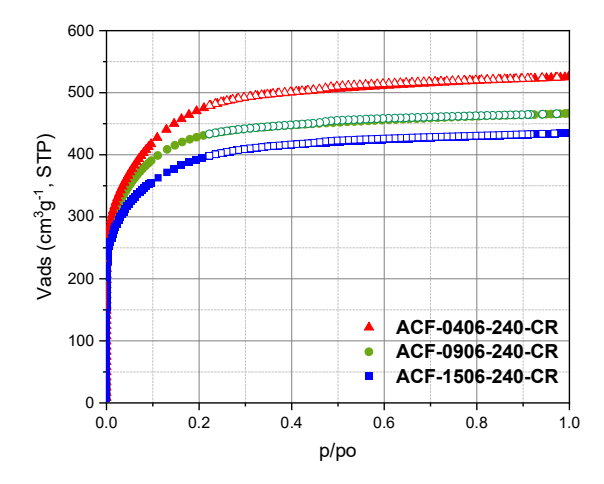


Figure 6.6 N₂ adsorption-desorption isotherms at -196 °C of three batches of physically activated material, all of them under the same working conditions (240 minutes at 950 °C).

Table 6.3 Main textural parameters obtained from the nitrogen adsorption-desorption isotherms at -196 °C for the physically activated samples under chemical reaction control regime (CR). Average values and standard deviations $(\sigma = \sqrt{\frac{\sum_{1}^{N}(x_{i}-x)^{2}}{N}})$ have been calculated for the pool of dataset.

			Γ	ubinin-Rad	lushkevich	method	
	SBET	V _{TP} (0.97 p/p0)	W_0, N_2	$\mathbf{E}_{\mathbf{o}}$	Lmicro.	S	Smicro
Sample	m ² g ⁻	cm ³ g ⁻¹	cm ³ g ⁻¹	kJmol ⁻¹	nm	m^2g^{-1}	m^2g^{-1}
ACF-0406-240-CR	1783	0.811	0.635	17.19	1.86	1787	681
ACF-0906-240-CR	1638	0.720	0.531	20.03	1.24	1495	853
ACF-1506-240-CR	1580	0.672	0.523	18.64	1.49	1473	701
Average value	1667	0.734	0.563	18.62	1.53	1585	745
Standard dev.	85	0.060	0.051	1.2	0.25	143	77

6.3.1.3 Repeatability of physical activation method controlled by Diffusion.

Similarly, three batches of the physical activation method following a diffusion control regime were obtained (Chapter IV, section 4.2.3), and the repeatability was estimated based on the textural parameters (Figure 6.7, Table 6.5). Based on the low standard deviation values, the batch's repeatability was good.

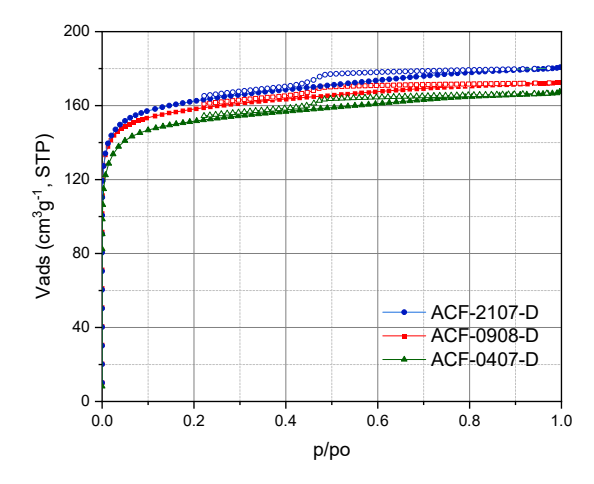


Figure 6.7 N₂ adsorption-desorption at -196 °C of three batches of physically activated material obtained by D control.

Table 6.4 Main textural parameters obtained from the nitrogen adsorption-desorption isotherms at -196 °C for the physically activated samples under diffusion control regime (D). Average values and standard deviations ($\sigma = \sqrt{\frac{\sum_{1}^{N}(x_{i}-x)^{2}}{N}}$) have been calculated for the pool of dataset.

			D	ubinin-Rad	lushkevich	method	
	S _{BET}	$V_{TP (0.97 p/p0)}$	Wo, N ₂	$\mathbf{E}_{\mathbf{o}}$	L _{micro} .	S	S_{micro}
Sample	m^2g^{-1}	cm ³ g ⁻¹	cm ³ g ⁻¹	kJmol ⁻¹	nm	m^2g^{-1}	m^2g^{-1}
ACF-0908-D	624	0.266	0.242	24.30	0.84	682	579
ACF-2107-D	642	0.278	0.249	22.96	0.93	702	534
ACF-0407-D	596	0.257	0.237	21.53	1.07	668	445
Average value	621	0.267	0.243	22.93	0.95	684	519
Standard dev.	19	0.009	0.005	1.13	0.09	14	56

6.3.2 Activation method comparison (Physical vs Chemical)

To assess the difference between both chemical and physical activation, samples ACF-KOH (600°C, 60 min), ACF-60-CR (875°C, 60 min) and ACF-240-CR (875°C, 240 min). According to the IUPAC classification (Thommes et al. 2015), the nitrogen adsorption isotherm of sample ACF-KOH is type Ib with a hysteresis type H4 in the desorption range. This is characteristic of a microporous material with a well-developed mesoporosity. Sample ACF-240-CR also displays a type Ib adsorption isotherm with a wide curve at low relative pressures but a negligible hysteresis loop, indicating wide

micropores and a small volume of mesopores. In contrast, sample ACF-60-CR displays a type Ia isotherm, indicative of predominantly microporous material (Figure 6.7).

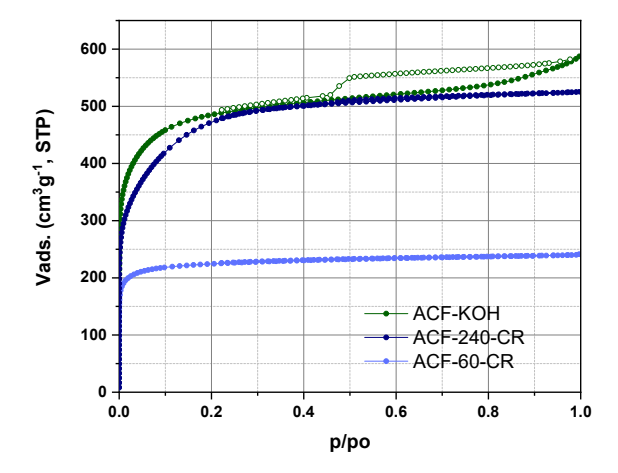


Figure 6.8 Nitrogen adsorption/desorption isotherms at -196C of samples ACF-KOH (600°C, 60 min), ACF-60-CR (875°C, 60 min) and ACF-240-CR (875°C, 240 min).

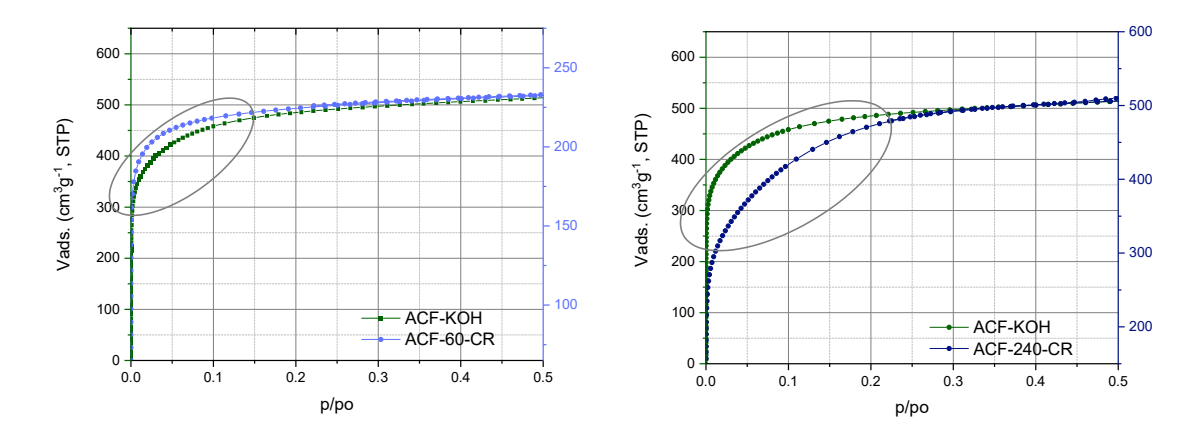


Figure 6.9 Magnification of the low-pressure region of the N₂ adsorption isotherms at -196 region of the N₂ adsorption isotherms at 196 °C of samples ACF-KOH and ACF-60-CR. Note. Isotherms are plotted under different Y axis for clarity.

Figure 6.10 Magnification of the low-pressure °C of samples ACF-KOH and ACF-240-CR.

For all the samples, the gas uptake at low relative pressures is high; this behaviour is distinctive of materials with a considerable contribution of micropores. For the samples obtained under physical activation, the gas uptake at relative pressures above 0.3 is almost constant, owing to the low amount of mesopores (as opposed to the chemically activated sample). This is not a standard characteristic of chemical activation with KOH when working with other precursors.

Comparatively, a remarkable difference in the surface area can be noticed, with a value three times larger for the samples prepared upon chemical activation compared to ACF-60-CR, despite the similar dwelling time of 60 min during the activation (note that neither the activation mechanism nor the temperature is similar). In addition, ACF-KOH also showed a broader knee of the gas adsorption isotherm at low relative pressures, which is attributed to the presence of micropores with wider diameters (Figures 6.9 and 6.10, outline sector). These two main differences can be explained by the nature of the attack of the chemical agent; on the one hand, KOH reacts with the carbon skeleton, breaking the polypeptide chain (evidenced by the absence of fibre morphology) and, therefore, activating at a greater extent despite the mild temperature conditions. Such activation typically leads to a material that no longer displays a fibrillar morphology, as will be discussed later.

On the other hand, samples ACF-KOH and ACF-240-CR have similar surface areas (Table 6.5 and Figure 6.10). Considering only the low relative pressure region, it can be asserted that a long treatment time affects the total area by creating new pores and enlarging the already existing microporous width because a broader curve is recorded for ACF-240-CR in comparison with ACF-60-CR (area signalised in figures 6.9 and 6.10).

The main textural parameters obtained for the samples demonstrate that the micropore volume calculated according to the Dubinin-Radushkevich method significantly contributes to the total pore volume (Table 6.5).

The pore size distributions obtained by application of the 2DNLDFT-HS methods to the nitrogen adsorption data revealed interesting differences among the samples (Figure 6.11). Sample ACF-240-CR sample displayed micropores of smaller sizes than sample ACF-KOH and a lack of mesopores, as discussed above, as seen in the trend of the cumulative pore volume. Hence, despite their similarities in surface area and total pore volume, it is clear that samples ACF-KOH and ACF-240-CR present important differences in the distribution of pore sizes.

Table 6.5 Main textural parameters of selected samples obtained from the N₂ and CO₂ adsorption isotherms analysis at -196 and 0 °C, respectively.

		N ₂ isothe	D	R, CO ₂ @27	3K		
	SBET	V _{TP (0.97 p/p0)}	DR, Wo, N ₂	Wo/	L _{micro} .	Wo, CO ₂	Smicro
Sample	m^2g^{-1}	cm ³ g ⁻¹	cm ³ g ⁻¹	V_{TP}	nm	cm ³ g ⁻¹	m^2g^{-1}
ACF-KOH-2604	1871	0.89	0.725	0.82	0.796	0.600	1507
ACF-0406-240-CR	1783	0.81	0.635	0.78	0.776	0.362	933
ACF-1305-60-CR	891	0.37	0.359	0.97	0.597	0.276	924

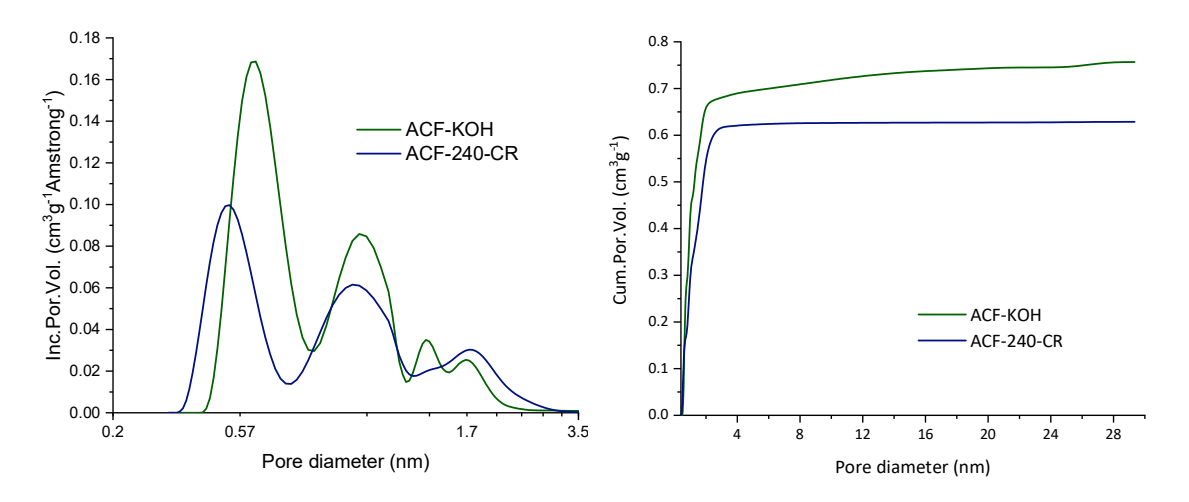


Figure 6.11 Pore size distribution for selected samples obtained from the 2DNLDFT-HS method applied to the N₂ adsorption isotherms at -196 °C; (left) derivative pore volume; (right) cumulative pore volume.

Furthermore, while the physically activated samples kept the desired morphology (even when treated for long times), the chemically activated samples' morphology was modified, with a fibre length shortening (even at lower temperatures and shorter activation times) (Figures 6.12 and 6.13). The surface was more affected for sample ACF-KOH (Figure 6.14), losing the characteristic scale cells and part of the cortex (centre section of the material). This gave rise to shorter hollow fibres or, in some cases, broken fibres at its length.

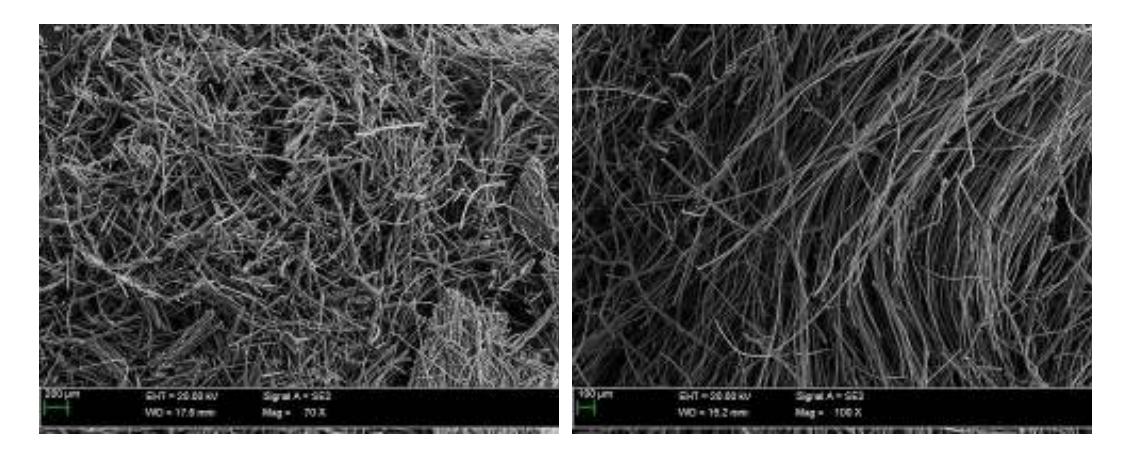


Figure 6.12 SEM image of ACF-KOH, **Figure 6.13** SEM image of ACF-240-CR, 70x. 100x.

On the other hand, the physical treatment did not affect the surface to the same extent as the chemical one (Figure 6.15); however, the loss of the cortex cannot be ruled out since the images were not evident in this aspect. The absence of the hollowness is consistent with a uniform attack of the gas reactant with the material, creating a porous network that does not present different regions visible at SEM.

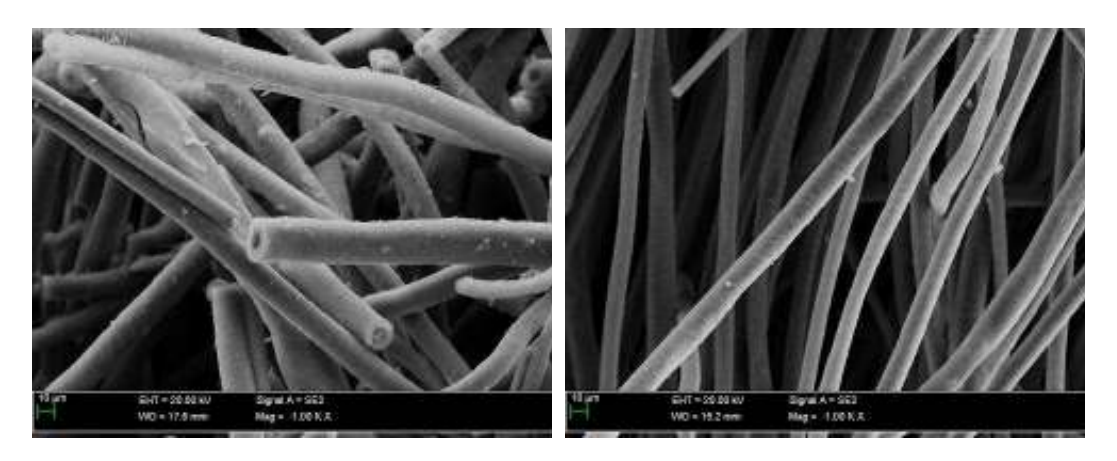


Figure 6.14 SEM image of ACF-KOH, **Figure 6.15** SEM image of ACF-240-CR, 1000x.

As mentioned before, this result was expected since the chemical agent attacks the carbon skeleton and the disulphide linkages, splitting them and eventually destroying the structure. Although the chemical activation fails to achieve one of the primary goals of the present work, which is to keep the fibre morphology to its extent, it cannot be ruled out since the textural analysis proved that the material has interesting features for adsorption applications. Despite the fact that this material is no longer a fibre, the

nomenclature of the sample was kept as "ACF" to avoid ambiguities regarding the nature of the precursor.

On the other hand, treatments under Diffusion control for times longer than 30 minutes render collapsed materials, where the length and the shape are lost. An example is the sample treated for 60 minutes (Figure 6.16), where the extent of structural damage is shown (Figure 6.17).

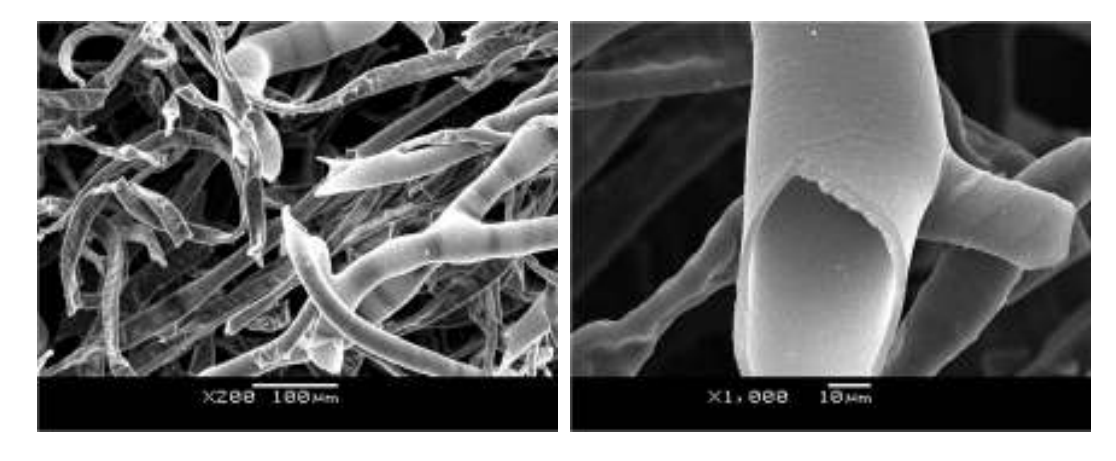


Figure 6.16 SEM image of ACF-60-D, **Figure 6.17** SEM image of ACF-60-D, 200x.

The XRD patterns between 10 - 45° of samples ACF-KOH and ACF-240-CR, determined to investigate the evolution of the crystalline structure of the activated samples, are shown as follows (Figure 6.18). The crystalline parameters calculated from the analysis of the peak centred at 25° confirmed that both are amorphous materials with similar Lc, La and d (002) parameters (Table 6.6). These values are smaller than those reported for polyethylene-based activated carbon fibres (Kang et al., 2023).

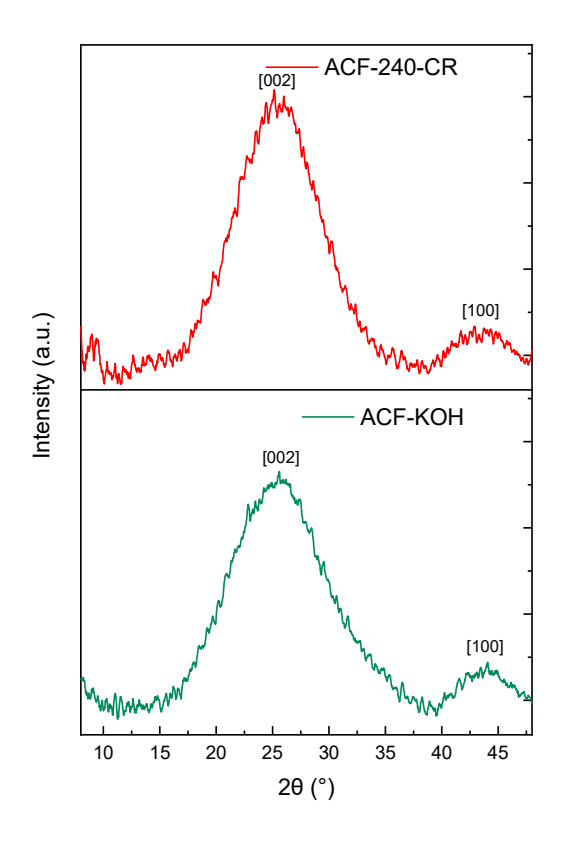


Figure 6.18 XRD patterns of ACF-240-CR and ACF-KOH, where the lack of significant differences between plots is observed.

Table 6.6 Main structural parameters obtained from the XRD pattern analysis for ACF-240-CR and ACF-KOH.

Sample	$L_{c}(nm)$	L _a (nm)	$\mathbf{d}_{[002]}$
ACF-0406-240-CR	0.96	1.96	0.18
ACF-KOH-2604	1.15	2.36	0.18

6.3.3 Control method comparison (Diffusion vs Chemical Reaction)

The literature is unequivocal when it specifies the differences that are expected between samples prepared upon physical activation under *Diffusion (D) or Chemical Reaction (RC)* control regimes (Chapter II, section 2.4.3.1). In this sense, this work aims to discern to which extent the characteristics of the ACF are affected by those differences. For this reason, selected samples were activated for 30 minutes under CO₂, since longer

activation times under the Diffusion control regime rendered materials without fibrillar morphology (Figure 6.18).

The N₂ adsorption-desorption isotherms for samples ACF-2107-D, ACF-0407-D (the date is kept differentiating two batches prepared under the same conditions that were not mixed), and ACF-30-CR are shown (Figure 6.19); data highlight minor differences in the samples' textural parameters. Meanwhile, the ACF's gas adsorption-desorption isotherms activated under CR control belong to type Ib (microporous material with reversible adsorption and a small contribution of mesopores). The ACFs prepared under the D control regime showed type Ib gas adsorption-desorption isotherms displaying a hysteresis loop (type H4) in the desorption range. This latter implies a more significant contribution of mesopores.

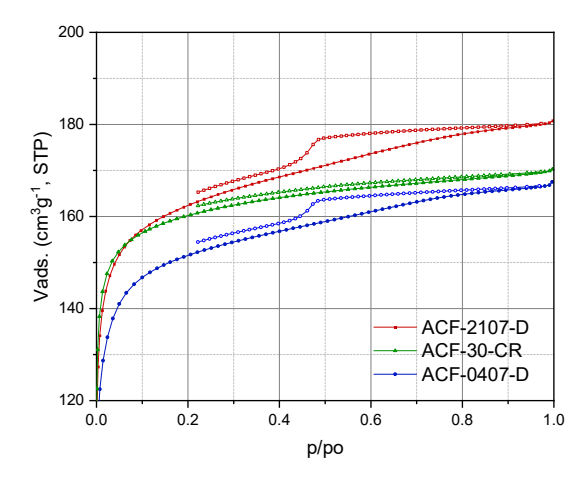


Figure 6.19 N₂ adsorption-desorption isotherm at -196C of selected samples synthesised by physical activation under Diffusion (D) and Chemical Control (CR) conditions.

Table 6.7 The Main textural parameters of selected samples synthesised by physical activation under Diffusion (D) and Chemical Control (CR) conditions were obtained from N₂ and CO₂ adsorption-desorption isotherms at -196 and 0 C, respectively.

		N ₂ isother	DR	, CO ₂ @273	K		
	SBET	V _{TP} (0.97 p/p0)	Wo, N2	Wo/	Lmicro.	Wo, CO ₂	Smicro
Sample	m^2g^{-1}	cm ³ g ⁻¹	cm ³ g ⁻¹	V_{TP}	nm	cm ³ g ⁻¹	m^2g^{-1}
ACF-30-CR	641	0.262	0.250	0.95	0.55	0.242	883
ACF-0407-D	596	0.257	0.237	0.92	0.65	0.251	773
ACF-2107-D	642	0.278	0.249	0.89	0.62	0.246	798

The average micropore diameter calculated from the Stoeckli-Ballerini equation applied to the CO₂ adsorption isotherms demonstrates that ACF-30-CR developed a micropore network with a smaller diameter (ca. 12 % smaller) than sample ACF-2107-D (Table 6.7). On the other hand, the micropores represent ca. 95 % of the total pore volume for sample ACF-30-CR, while they account for ca. 92 and 89 % for the other two samples, in agreement with the N₂ uptake. In addition, the burn-off was reasonably different, standing at 22 % for ACF-30-CR and ca. 33 % for ACF-2107-D and ACF-210407-D.

From the SEM images shown in Figures 6.20 and 6.21, it can be concluded that the morphology of the samples obtained by the D control regime is more damaged than that of sample ACF-CR. Sample ACF-D has brittle fibres (hence of shorter length), while sample ACF-CR has longer fibre lengths for all batches. This behaviour is expected for the former since the D control regime leads to materials that suffer external particle burning (Wigmans 1989). Also, this treatment renders deformed material and hollow tubes (Figures 6.22 and 6.23). For the CR control regime, the images show that the external scale shape is still visible, although to a smaller extent.

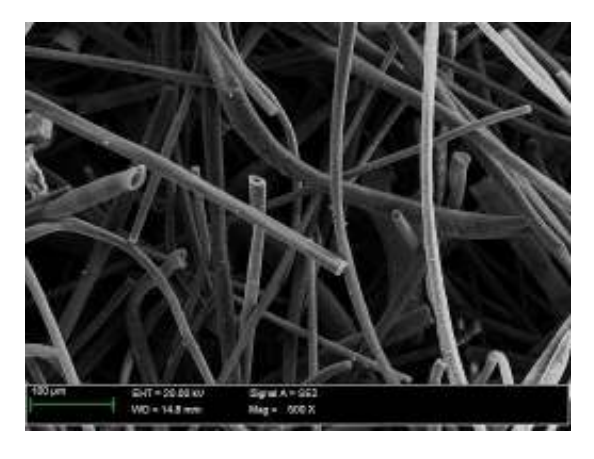


Figure 6.20 SEM image of ACF-30-D sample, 500x.

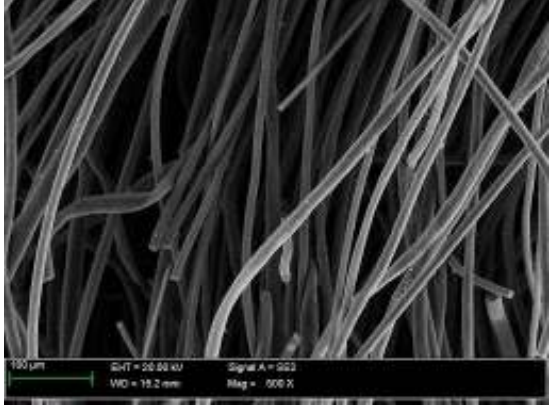
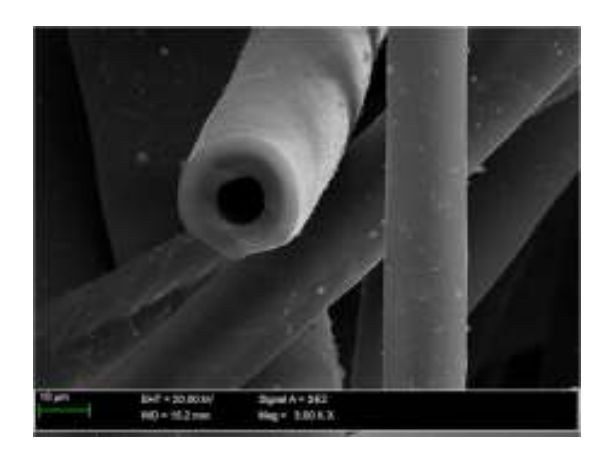


Figure 6.21 SEM image of ACF-30-CR sample, 500x.



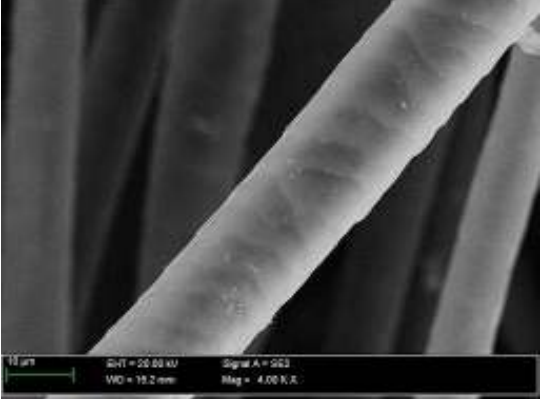


Figure 6.22 SEM image of ACF-30-D sample, 3000x.

Figure 6.23 SEM image of ACF-30-CR sample, 4000x.

The kinetics of each process will be subjected to the activation conditions; the apparent kinetic constant can be calculated from the integrated expression of Equation 2.2 (Chapter II, Equation 2.2), using the tabulated values for reaction order and the correspondent conversion degrees (Table 6.8). The α value is the carbon conversion degree calculated as the mass of reacted carbon vs initial carbon mass (Chapter II, section 2.4.3.1), and n is the reaction order.

Table 6.8 Apparent kinetic constant value as a result of Equation 2.2 integrated expression (n and α: kinetic parameters, see Chapter II, section 2.4.3.1).

Control	n	α	Integrated equation	Kap (min ⁻¹)
CR	1	0 - 0.22	$-In(1-\alpha) = K_{ap}.t$	0.008
D	0.67	0 - 0.44	$-\frac{(1-\alpha)^{1-n}}{1-n} = K_{ap}.t$	0.017

From a heterogeneous reaction's engineering point of view, the apparent kinetic constant can be considered the resistor sums' inverse value (Levenspiel, 2001) (Equation 6.3). Subsequently, it can be concluded that the D control regime faced a minor resistance compared to the CR control one.

$$Kap = \frac{1}{\sum resistances}$$
 Equation 6.3

Note: activation steps that add to the expression of resistance

- Step 1 Diffusion of the gas from the bulk to the surface of the solid
- Step 2 Penetration and diffusion of the gas to the reaction site
- Step 3 Reaction
- Step 4 Diffusion of the gas products throughout the material to the exterior surface
- Step 5 Diffusion of the gas products to the bulk

Therefore, the value reflects that the activation for this method is quicker than CR control because the gas did not diffuse internally, taking place in a superficial activation. The Reynolds number (Equation 6.4) was calculated at the oven centre to discard regime flow effects.

$$Re = \frac{4Q\delta}{\mu\pi D_i}$$
 Equation 6.4

with Q (m³s⁻¹) the gas flow, δ (Kgm⁻³) the density of the gas at the oven centre temperature (Perry et al. 2008) μ (Pa.s) the viscosity of the gas at the oven centre temperature (Perry et al. 2008), and Di (m) the internal diameter of the ceramic tube inside the oven.

Since both method flows are laminar (Table 6.9), the reaction mechanism can be considered independent from the flow regime. However, they have a crucial hydraulic residence time (HRt) difference (Equation 6.5), supporting the idea that for CR control, the gas has much more time to interact with the material, being able to diffuse throughout the fibre.

$$HRt = \frac{V}{O}$$
 Equation 6.5

with V (m³) volume of the ceramic tube.

Table 6.9 Regime flow and hydraulic residence time for both methods.

Method	Re	Flow regime	HRt (min.)
D	5.8E-2	Laminar	27
CR	1.16	Laminar	336

Note: calculation of Reynolds in Annex I.

Summarising, all the previously mentioned results indicate that both methods can be classified depending on the particle behaviour of the reactant (fibres in this work). The

CR control regime kinetics follows the Progressive Conversion Model (PCM) (Figure 6.24) whereas the D control regime follows the Unreacted Core Model (UCM) (Figure 6.25). The PCM model proposes that the reactive gas penetrates and reacts simultaneously throughout the solid particle, barely changing its original section. On the other hand, the UCM model stands for a reaction that takes place on the surface's material, diminishing the initial particle size (Levenspiel, 2001).

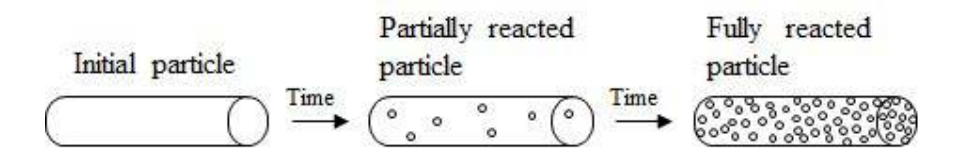


Figure 6.24 Material's behaviour under the PCM kinetic model.

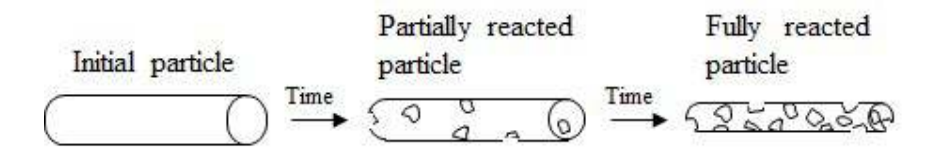


Figure 6.25: The material's behaviour under the UCM kinetic model is based on the model proposed by Levenspiel (Levenspiel, 2001).

Note: Figures 6.24 and 6.25 are schematic representations of how the gas reacts with the material; they do not represent the differences between the size and shape of pores.

6.3.4 Effect of the activation time

One key parameter of physical activation is the time of treatment. It is well known that the longer the residence time, the more affected the final material will be. In this regard, several samples were prepared from 30 to 240 min of exposure to CO₂ under the CR control regime to explore the influence of the activation time. The corresponding gas adsorption-desorption isotherms are shown (Figure 6.26). As seen, the isotherms belong to type I according to the IUPAC classification (Thommes et al. 2015), indicative of microporous materials. In all cases, a significant gas uptake is recorded at low relative pressures, indicating materials with a large fraction of microporosity. The adsorbed volume remained constant above 0.30-0.4 of relative pressures. A trend is observed with the activation time, as the samples that were activated at longer times displayed a marked, wide knee of the isotherm at low relative pressures (Figures 6.27 and 6.28, signalised

sector). This indicates that the activation provokes a widening of the microporosity and larger total pore volumes. As a result, the samples displayed higher surface areas, pore volumes, and higher L values (average micropore size), as seen in the textural values table (Table 6.10).

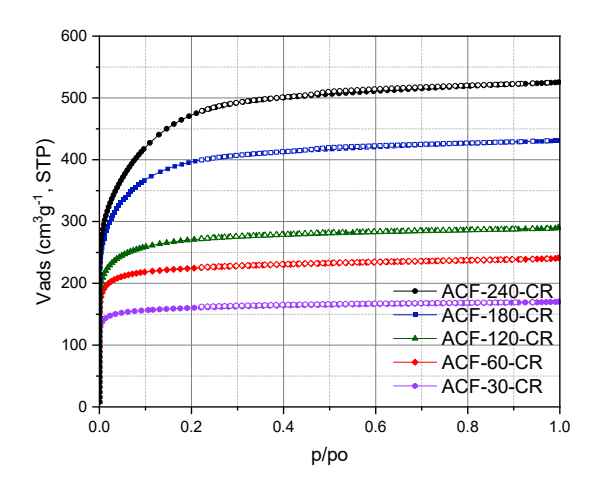


Figure 6.26 N₂ adsorption-desorption isotherms plots for samples obtained by CR control regime at different treatment times.

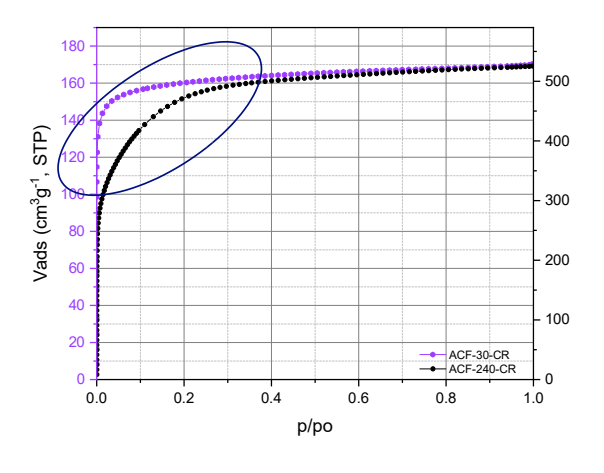


Figure 6.27 Nitrogen adsorption/desorption isotherms at -196 °C of samples (ACF-30-CR and ACF-240-CR) prepared by the physical activation method under CR control regime.

Figure 6.28 Nitrogen adsorption/desorption isotherms at -196 °C of samples (ACF-180-CR and ACF-240-CR) prepared by the physical activation method under CR control regime.

Note. isotherms are plotted in different axes for clarity.

Table 6.10 The main textural parameters of samples synthesised by physical activation under Chemical Control (CR) conditions were obtained from N₂ and CO₂ adsorption-desorption isotherms at -196 and 0 C, respectively.

		N ₂ isother	rm @ 77K		DR	, CO ₂ @27	/3K
Sample	S _{BET} m ² g ⁻¹	V _{TP (0.97 p/p0)} cm ³ g ⁻¹	Wo, N ₂ cm ³ g ⁻¹	Wo/ V _{TP}	L _{micro} .	Wo, CO ₂ cm ³ g ⁻¹	S _{micro} m ² g ⁻¹
ACF-240-CR	1783	0.81	0.63	0.78	0.78	0.36	933
ACF-180-CR	1517	0.67	0.59	0.88	0.70	0.36	1024
ACF-120-CR	1053	0.45	0.41	0.91	0.70	0.36	1013
ACF-60-CR	891	0.37	0.36	0.97	0.60	0.28	924
ACF-30-CR	641	0.26	0.25	0.95	0.55	0.24	883

The recorded values demonstrate a direct linear correlation between the activation time and the textural parameters, showing an increment in all cases except for ratio between the micropore volume and the total pore volume. This agrees with the mechanism since longer residence times favour the gas diffusion throughout the material, creating more pores and enlarging the existing ones. The ratio between the micropore volume and the total pore volume follows a decreasing trend with the activation time (Figure 6.29), indicating that the increase in the total pore volume is more pronounced than that of the micropores. This is in agreement with the enlargement of the size of the micropores with the activation time.

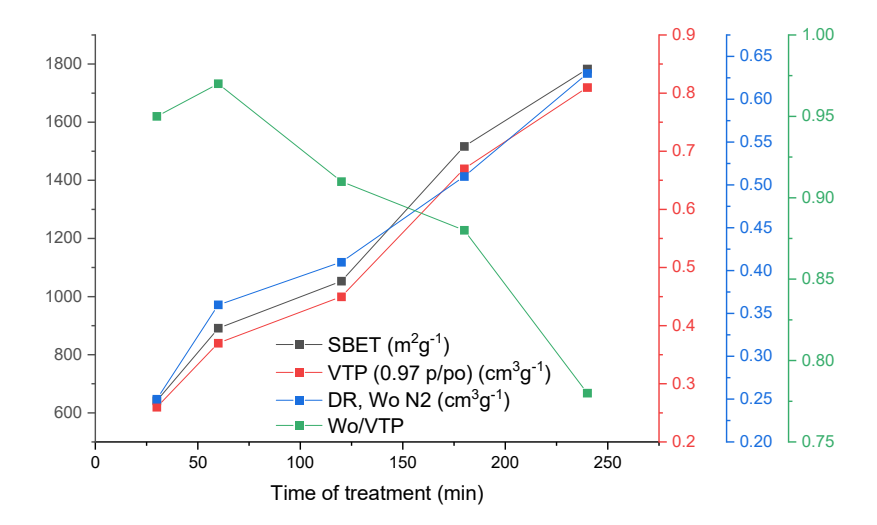


Figure 6.29 Correlation between the textural parameters and the physical activation time under CR control regime. Data are plotted in different axes for clarity.

The correlations between the burn-off and the activation time (Figure 6.30) and the micropore volumes (Figure 6.31) calculated according to Dubinin-Radushkevich confirmed the tendency shown in Figure 6.29 (Belhachemi et al. 2009). Figure 6.31 shows that while the micropore volume increases with the burn-off increment for N₂, it is not the same for CO₂, remaining at around 0.35 cm³g⁻¹ from burn-off values higher than 47 %. This implies that longer activation times enlarge the existing micropores from this threshold value, rather than creating new ones. The maximum capacity for creating new micropores was reached after 120 minutes of treatment.

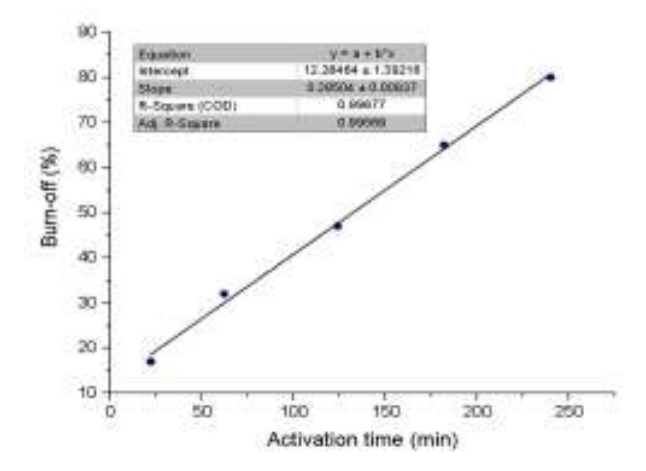


Figure 6.30 Correlation between the burn-off and the activation time for samples treated under CR control regime (the inset shows the fitting parameters).

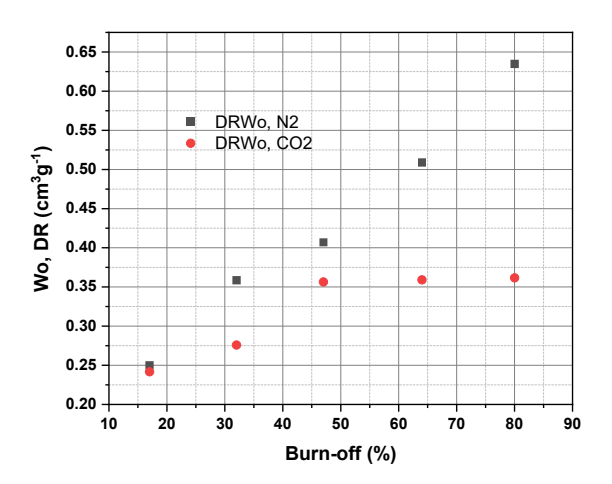


Figure 6.31 Correlation between the burn-off and the micropore volumes for samples treated under CR control regime.

On the other hand, regarding the mesopore volume calculated as $V_{TP\ (0.97\ p/po)}$ - Wo, N_2 (Figure 6.32) complements the behaviour previously seen in Figure 6.30. A significant increment can be seen from 47 to 65 % of burn-off standing for 180 and 240 minutes of treatment.

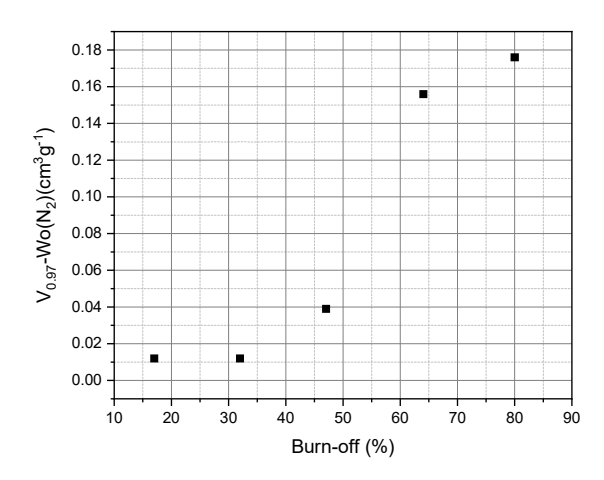


Figure 6.32 Correlation between the burn-off and the mesopore volume for samples treated under CR control regime.

The materials activated under CR control regime did not change its structure, as evidenced by XRD patterns (Table 6.11 and Figure 6.33).

Table 6.11 Crystalline parameters obtained from XRD patterns of samples ACF-120-CR and ACF-240-CR.

Sample	L _c (nm)	$L_a\left(nm\right)$	d [002]	
ACF-240-CR	0.96	1.96	0.18	_
ACF-120-CR	0.99	2.03	0.18	

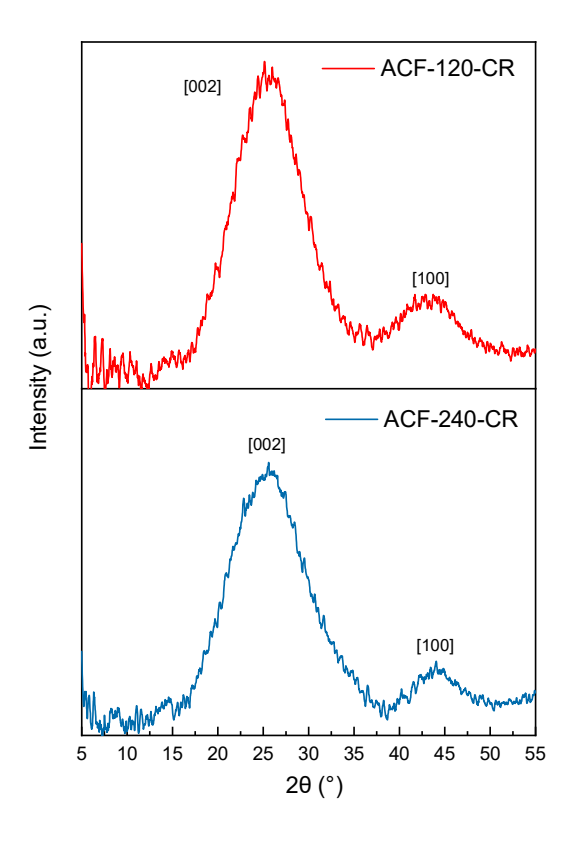


Figure 6.33 XRD patterns of samples ACF-120-CR and ACF-240-CR.

6.4 Chemical characterisation

The chemical composition of the activated carbon fibres was investigated by several techniques, such as elemental composition, pH of the point of zero charge, potentiometric titration and infrared spectroscopy.

6.4.1 Elemental composition

The elemental analysis of the activated carbon fibres was determined and compared with that of the precursor WF for a better understanding of the chemical transformation during activation (Table 6.12). As a general rule, the carbon content increased with the activation time at the expense of the rest of the heteroatoms (Figure 6.34). It is interesting to remark that the nitrogen content was relatively high, even after long activation times; this is attributed to the high nitrogen content in the precursor.

Table 6.12 Elemental analysis on a dry-ash free basis (wt.%) of the wool precursor (WF) and the ACFs obtained by different methods (average values and standard deviations are presented).

Sample	N	C	Н	S	0
WF	15.45 ± 0.14	49.03 ± 0.09	6.97 ± 0.15	3.04 ± 0.04	25.52 ± 0.15
ACF-KOH	9.29 ± 0.08	76.93 ± 0.12	3.64 ± 0.06	$\textbf{0.21} \pm 0.02$	5.89 ± 0.13
ACF-30-D	4.25 ± 0.07	86.23 ± 0.12	2.24 ± 0.05	$\textbf{1.98} \pm 0.01$	5.29 ± 0.10
ACF-30-CR	5.09 ± 0.08	85.04 ± 0.10	1.60 ± 0.06	$\textbf{1.93} \pm 0.02$	4.48 ± 0.11
ACF-60-CR	4.01 ± 0.06	87.01 ± 0.11	1.37 ± 0.07	$\textbf{1.94} \pm 0.02$	4.36 ± 0.11
ACF-120-CR	3.05 ± 0.05	89.01 ± 0.13	1.16 ± 0.08	$\textbf{1.89} \pm 0.01$	3.43 ± 0.09
ACF-180-CR	2.76 ± 0.08	89.31 ± 0.11	1.14 ± 0.06	$\textbf{1.87} \pm 0.03$	3.13 ± 0.11
ACF-240-CR	2.65 ± 0.05	90.15 ± 0.12	1.13 ± 0.06	$\textbf{1.87} \pm 0.03$	3.06 ± 0.12

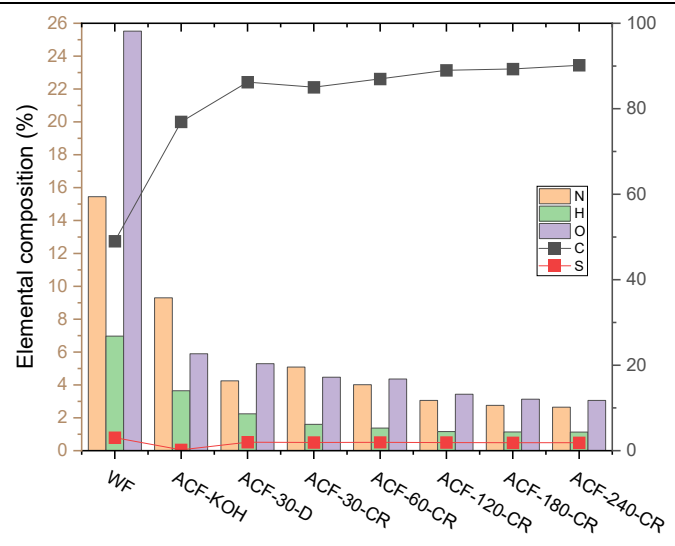


Figure 6.34 The virgin wool's chemical composition (wt.%, dry-ash free basis) and the ACFs obtained by different methods (chemical, physical-D, and physical-CR).

It is interesting to highlight that the EDS analysis of the samples rendered much higher nitrogen content (ca. 20 %) for all the samples. This difference with the elemental composition is attributed to the fact that EDS is a surface technique, whereas elemental analysis is a bulk technique. This only indicated that the N-moieties would mainly be located on the material's surface.

6.4.2 Surface charge

The surface charge was assessed by determining the pH value at the point of zero charge (Table 6.13). The results obtained show that the pH value for zero charge of the ACF is alkaline for all the samples. This implies that when used in solutions with pH

below the pH of the point of zero charge, the ACF's surface will be positively charged. While, at a higher solution pH, the surface of the ACF will be negatively charged.

Table 6.13 pH_{pzc} measures average values for ACFs obtained by physical and chemical activation (average values plus standard deviation).

Sample	pH _{pzc} (+/- 0.01)
ACF-KOH	8.31
ACF-30-D	7.90
ACF-30-CR	7.82
ACF-60-CR	7.92
ACF-120-CR	8.01
ACF-180-CR	8.16
ACF-240-CR	8.18

These values indicate basic groups at the edges of the condensed, polyaromatic sheets constituting the ACF structure. These heteroatoms are oxygen and nitrogen-containing functional groups and delocalised π -electrons of the polyaromatic sheets of the basal planes. Groups like chromene, pyrone-type, diketone, or quinone may be responsible for the basicity of activated carbons. In addition, the presence of nitrogen-containing functional groups could also contribute to the material's basicity (Newcombe et al. 2006).

6.4.3 Protons exchange capacity in aqueous solution

The ACFs were titrated to assess the presence of proton exchange groups on the material's surface (Chapter IV, section 4.3.10). The procedure proved to be not suitable for fibrous materials, with poor reproducibility, most likely since ACFs are lightweight and tend to wrap around the electrode, hindering the proton exchange with the electrolyte (Figure 6.35). However, explaining the sample's proton exchange capacity is useful. The net charge concentration values recorded are positive; this implies that the exchanged protons are retained on the material's surface. The material's surface retained the protons added to the medium, and once the titration started, the charge was exchanged. This behaviour confirmed that the ACFs do not possess functional groups with the ability to exchange protons.

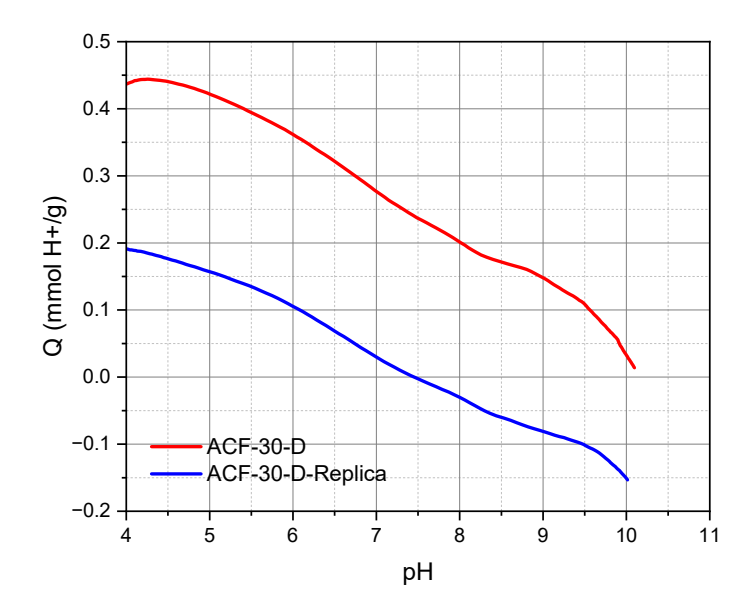


Figure 6.35 Charge exchange during a potentiometric titration with NaOH 0.1 M for the sample ACF-300-D and its replica.

6.4.4 Functional groups

The following figure portrays the FTIR spectra for all the different ACFs (6.36). As can be seen, there are no remarkable differences among the physically activated samples. The bands at 544 cm⁻¹ correspond with the S – S bond stretching vibration, while the peak at around 1025 cm⁻¹ is assigned to the stretching vibration of the S = O bonds. The signal at 790 cm⁻¹ is assigned to the stretching vibration of the C – H bond present in pyridine and pyrrole structures. Between 1200 – 1025 cm⁻¹, the band is assigned to the C – N stretching bond and the band at 1535 – 1522 cm⁻¹ is attributed to C = N bond in pyridine (this band is usually seen in the range 1660 – 1480 cm⁻¹). The 990 – 1011 cm⁻¹ band is assigned to C-H bending and ring puckering from arenes structures, with C=C stretching in rings and C=C asymmetric stretch contributions associated with the signals at 1500 and 1910 cm⁻¹, respectively. The presence of ethers or lactones functional groups is confirmed by the signal at 1186 cm⁻¹ corresponding to the C-O bond stretching. These results are in accordance with the pH_{PZC} results since all the ACFs are basic.

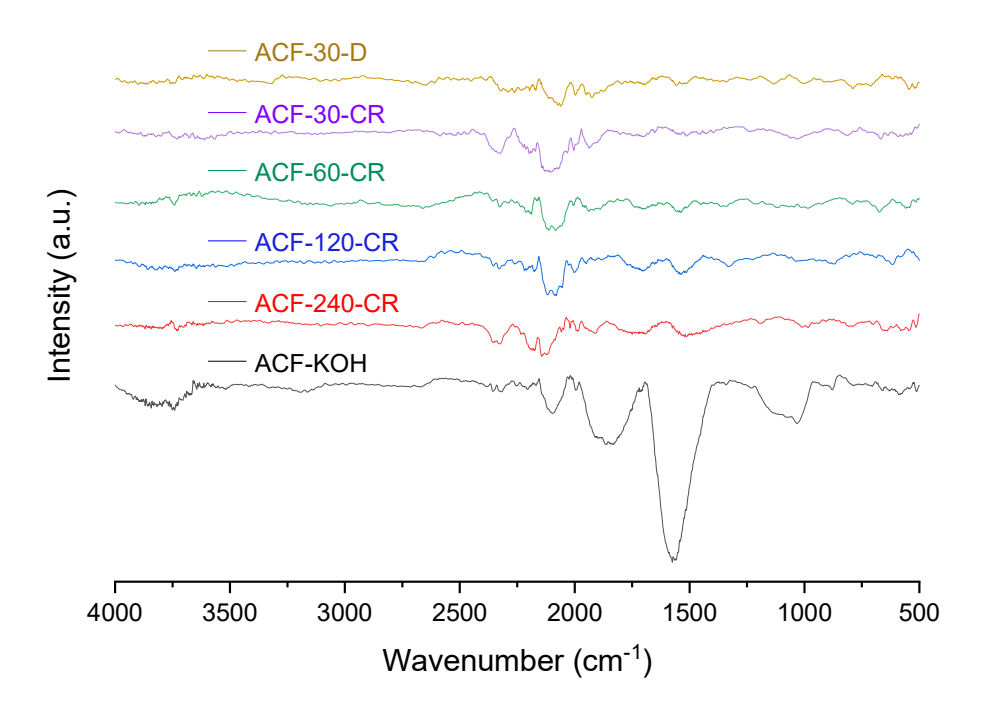


Figure 6.36 FTIR spectra for all the different activation methods followed in this work (separate spectra in Annex I).

On the other hand, the ACF-KOH sample showed a distinctive band located at ca. 1558 cm⁻¹ (double peak) assigned to C=C bending in a tri-substituted arene structure. The most important feature in ACF-KOH sample is the absence signals assigned to sulphur-containing groups, in concordance with the elemental analysis (see Figure 6.12) and the discussion about the short-length fibres by SEM. Compared with the stabilised samples (Chapter V, Figure 5.9), it is noticeable that the characteristic amide signals are absent.

According to the collected data, we propose two possible structures for the ACF (Figure 6.37) prepared by physical and chemical activation.

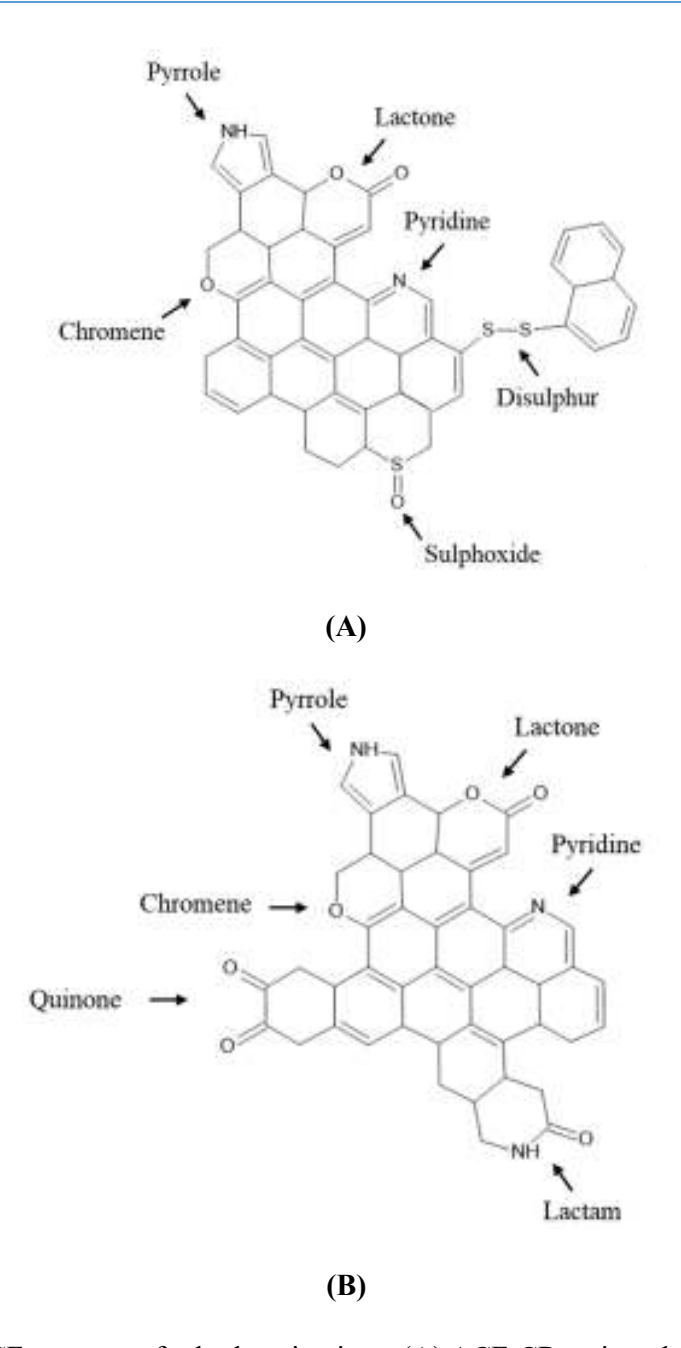


Figure 6.37 ACF structures for both activations, (A) ACF-CR series where the disulphur bridge that sustains the morphology can be seen, and (B) ACF-KOH.

6.5 Partial conclusions

Regarding the textural features, both activation methods led to materials with specific surface areas near 1900 m²g⁻¹ and predominantly microporosity. However, the chemical activation failed to maintain the fibrillar morphology, rendering very short-

length and weak fibres. In contrast, the physical activation preserved the morphology of the fibres while allowing a well-developed porosity.

For the physical activation method, the activation time and the gas flow proved to be essential for preparing a material with the desired characteristics. A low flow of CO₂ gas during the activation (CR control regime) allows for better control of the extent of the activation, affecting the precursor's structure and morphology to a lesser degree. On the other hand, higher flows of CO₂ during the activation (D control regime) give rise to materials less uniformly activated, having mainly undergone external activation. This type of mechanism renders a more brittle material. Therefore, the fibres are shorter than those obtained under the CR control regime. However, the hollow tubes obtained by physical activation under the D control regime could be expected to show better performance in adsorption from liquid phase applications, as an interconnectivity improvement should be expected.

The activation time was also demonstrated to be of great importance when selecting the material features. Longer times translated into larger specific surface areas and wider microporous widths. This last characteristic makes this material a fit for the type of application utilised in the present work.

Finally, the activation conditions may have significant changes in the nitrogen and sulphur contents, which have significant consequences, such as the material's integrity. As an example, ACF-KOH displayed the highest nitrogen content, almost no presence of sulphur and this material lost its fibre morphology; thus, it may be concluded that sulphur is strongly responsible for the structural integrity of the fibres. This is supported by the results obtained for the ACF-CR series, where the sulphur content is appreciable, but the nitrogen content is much lower than that of ACF-KOH. Nevertheless, ACF-30-D escapes this tendency; although its sulphur content is similar to that presented for ACF-CR series, the morphology difference is remarkable. For this reason, it can be concluded that both the sulphur content and the CO₂ flux are vital for the fibre's structural integrity. Higher CO₂ fluxes can maintain the required sulphur content but provoke the burning of the fibre, leading to its rupture. Regarding composition, the activated carbon fibres showed a basic surface nature, with few to no proton exchange groups on their surface.

In summary, the method that best suits these characteristics is physical activation under a CR control regime for three hours onward to obtain ACF with fibrillar morphology, large specific surface areas, and wide micropore diameters.



"In forty hours, I shall be in battle, with little information, and on the spur of the moment will have to make most momentous decisions, but I believe that one's spirit enlarges with responsibility and that, with God's help, I shall make them and make them right."

War as I knew it

George S. Patton, Jr.

7.1 Adsorption in aqueous solution

Studies regarding pollutant adsorption onto an adsorbent material imply the assessment of the kinetic and thermodynamic behaviour of the process to identify which model best fits the studied adsorption. Once all the information is gathered, an adsorption mechanism that contemplates all these aspects can be proposed. In this regard, the present chapter displays the results obtained for the adsorption of three pharmaceutical compounds on activated carbon fibres from monocomponent aqueous solutions. In this sense, various operating parameters were selected with the aim of understanding the forces that command the adsorption of those pollutants on ACF. The characteristics of the selected ACFs were already discussed in Chapter VI, and the results were gauged against their textural and chemical characteristics.

The analysis was carried out using techniques already described (Chapter IV). The linear optimisation technique was applied using the Origin software to assess the model that best fits the experimental results. The statistics include the adjusted coefficient of determination (adj-R²), reduced chi-square test or mean squared weighted deviation (MSWD, χ^2), and residual sum of squares (RSS). The best-fitting model criteria, in all cases, was selected through the highest value of adj-R² but the lowest value of χ^2 and RSS. The RSS is the sum of the squared differences between the observed values and the predicted values by the regression model, and it is a critical measure to assess the quality of the regression analysis.

7.2 Kinetic studies

The kinetic studies for the adsorption of the pharmaceutical compounds were performed as described (Chapter IV, section 4.4.1); the ambient temperature conditions were 22 °C for all cases.

7.2.1 SMX adsorption kinetics

The concentration decay curves (Figure 7.1) show the kinetic profiles of the adsorption of sulfamethoxazole (SMX) on the studied chemically (ACF-KOH) and physically activated samples (ACF-120-CR, ACF-60-CR and ACF-30-D). As seen, the equilibrium times were very different for the studied samples, varying from 120 min for ACF-KOH to 2880 (48 hours) for the physically activated samples. This difference can

be related to the porosity of the samples, particularly their differences in micro/mesoporosity. The two samples that showed the fastest kinetic were those with wider micropores (Figure 7.2), higher surface areas (Chapter IV, section 6.2.2) and higher volumes of mesopores. Considering the fraction of micropore volume, calculated by DR, the series of samples can be divided into two main groups: the first one involving ACF-KOH and ACF-240 with ca. 80 % contribution of microporosity, and a second one with contributions from 91 % onward. Thus, it is clear that the samples with a higher contribution of mesopores presented faster kinetics, which helps the adsorbate reach the adsorption site by shortening the time but does not collaborate as an adsorption site itself. The uptake efficiency, calculated as follows (Equation 7.1), explains this last observation:

Uptake efficiency =
$$\left(\frac{C_o - C_{eq}}{C_o}\right) * 100$$
 Equation 7.1

where C_o and Ceq (mmolL-1) are the initial and the equilibrium concentrations, respectively.

The uptake for ACF-120-CR, ACF-60-CR and ACF-30-D series decreased by the total surface area (Figure 7.3), but their equilibrium increased by a factor of more than twenty times when compared with ACF-KOH and ACF-240-CR (Figure 7.1). On the other hand, ACF-KOH and ACF-240-CR showed similar adsorption uptakes at the equilibrium. Considering these factors, it could be assumed that the pollutant has the same accessibility to the adsorption site in both materials, with differences in their morphology notwithstanding since ACF-KOH is a very short and hollow fibre (at a superficial view, looks like a powder although the SEM images confirmed its fibrosity). At the same time, ACF-240-CR is a long, dense fibre (not hollow) (Chapter VI, section 6.2.2).

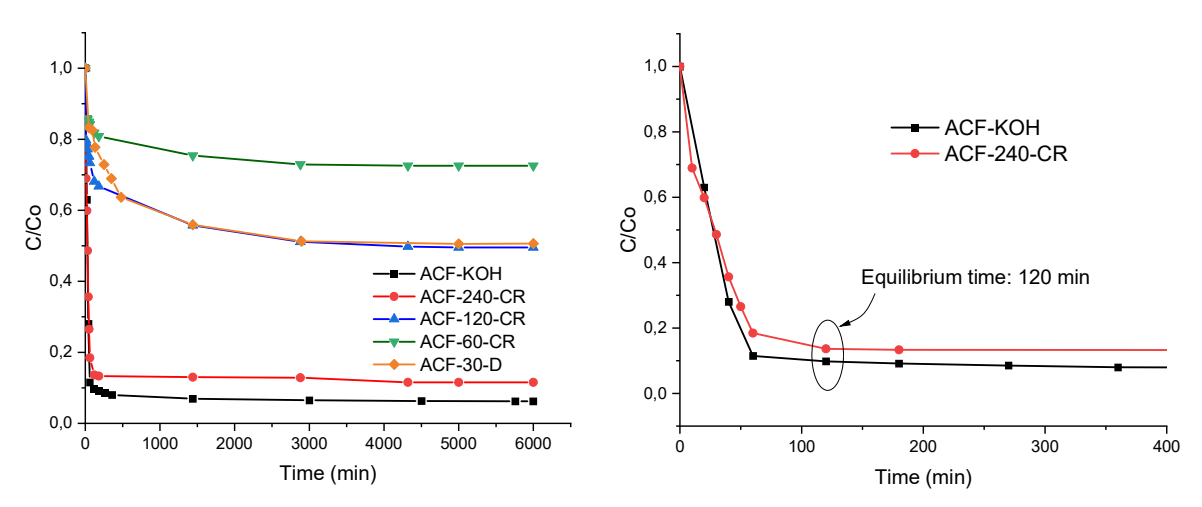


Figure 7.1 Concentration decay curve of SMX as a function of time for ACF samples from the different activation methods (chemical and physical under D and CR regimes).

Figure 7.2 Concentration decay curve of SMX as a function of time for samples with similar textural features (see Chapter VI, section 6.2.2).

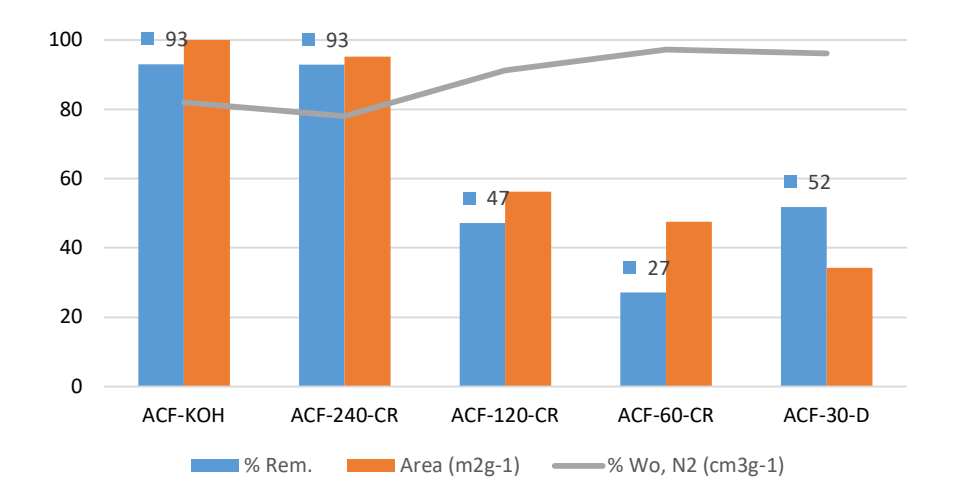


Figure 7.3 Comparison between the absolute removal of SMX (percentage), the normalised specific surface area and the micropore volume (percentage), for selected samples obtained under physical -CR, D control regimes- and chemical activation.

The remaining samples from the series displayed longer equilibrium times (Figure 7.4). These materials have narrow micropores and smaller specific surface areas than the previous ones (Chapter VI, sections 6.2.3 and 6.2.4). However, it is interesting to note that the amount adsorbed at the equilibrium time for ACF-30-D is similar to that of sample ACF-120-CR despite its smaller microporous volume and specific surface area (Figure

7.4). This result can also be related to the sample's morphology (i.e., brittle and short fibres) since both samples displayed hollow fibres, which would improve the accessibility. Also, this is the only example where the uptake of SMX did not follow the linear trend with the normalised specific area; the uptake was higher than the expected one according to the surface area.

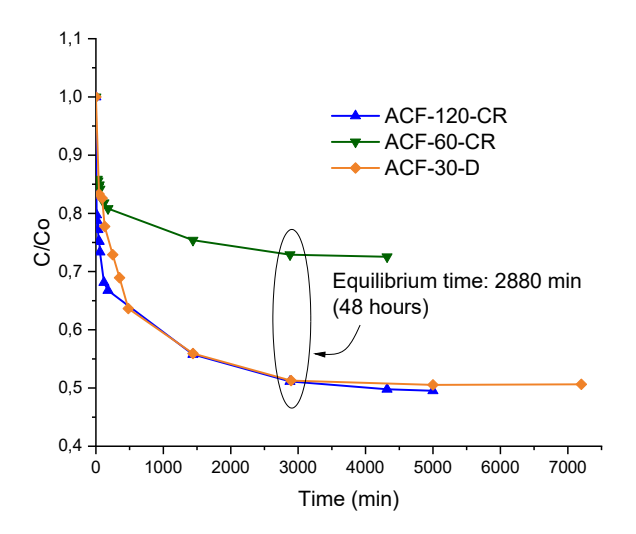


Figure 7.4 Concentration decay curve of SMX as a function of time for the physically activated samples. The similar equilibrium time of the samples is marked.

The experimental results were fitted to three kinetic models; as explained before, the criteria followed to assess the best fit were the highest adj-R2 and the lowest values for $\chi 2$ and RSS (Table 7.1). The results showed that ACF-KOH and ACF-240-CR fit the PSO model (concentration-dependent LDF model), with the mass transfer coefficient increasing with concentration. This is typical of systems displaying a Langmuir isotherm (Brandani 2021). The mass transfer coefficient goes to zero at equilibrium, and the equilibrium concentration is assumed to be constant and equal to the final value.

It is interesting to point out that the adsorption kinetics for samples with the longest equilibrium times (120 and 60 CR samples and ACF-30-D) depend on the diffusion phenomenon. This behaviour may be attributed to the textural characteristics of these samples: strictly microporous materials. SMX is a relatively bulky and planar compound with a certain angle in its structure (see Section IV, Figure 4.11). Those two factors may be responsible for the diffusion resistance phenomenon becoming the step that governs the kinetics. The calculated kinetic constant values agree with the trends of

the equilibrium times, as the fastest process has one order bigger constants than those with longer equilibrium times.

On the other hand, the predominant forces involved in the adsorption process are both electrostatic and dispersive in nature. At the pH of the working solutions, the ACF surface is positively charged (pH_{ZPC} circa 8 in all cases), favouring the adsorption of anionic species through favourable electrostatic interactions. At the same time, SMX exists predominantly in its anionic form (working solution pH > p_{Ka2}) in the solution in contact with the ACFs due to the deprotonation of the secondary amine group (Figure 7.5). This change in the solution's pH favours the adsorbate-adsorbent electrostatic attraction. The dispersive π - π interactions between the aromatic rings of SMX (the isoxazole and aniline aromatic rings, which provide high electron density) and the π electron density of the ACF are also expected to occur and thus cannot be ruled out.

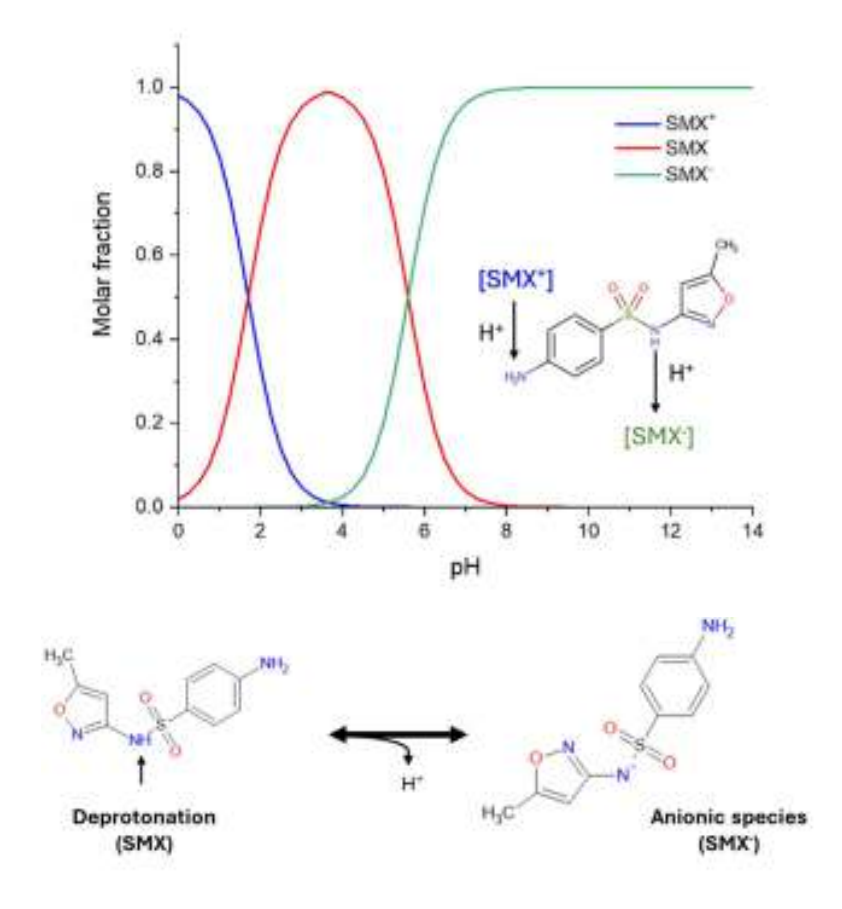


Figure 7.5 Speciation diagram of SMX in aqueous solution and the deprotonation equilibrium due to pH changes.

Table 7.1 Kinetic fitting comparison for SMX (1.0 mmolL-1) adsorption onto ACF obtained under chemical and physical activation (D and CR methods) and different times for CR control.

	Units	ACF-KOH	ACF-240-CR	ACF-120-CR	ACF-60-CR	ACF-30-D
PFO model						
k_1	min ⁻¹	0.0017	0.0008	0.0015	0.0012	0.0018
adj-R ²		0.9253	0.6801	0.9440	0.9856	0.9886
X^2		0.0632	0.0956	0.0239	0.0083	0.0020
RSS		0.2526	0.3467	0.1569	0.0543	0.0087
PSO model						
k_2	g mmol ⁻¹ min ⁻¹	0.1672	0.1679	0.0391	0.0731	0.0098
adj-R ²		0.9999	0.9999	0.9990	0.9991	0.9975
X^2		0.2935	0.1218	354	2930	10073
RSS		0.1897	0.2473	2296	6121	37130
Diffusion model						
k_3	mmolg ⁻¹ min ^{-1/2}	0.0025	0.0020	0.0051	0.0039	0.0124
adj-R ²		0.6722	0.5705	0.8587	0.9508	0.9756
X^2		0.0003	0.0003	0.0018	0.0001	0.0002
RSS		0.0025	0.0012	0.0118	0.0009	0.0011

The 0.4 mmolL⁻¹ concentration solution fitted a PSO model in all cases. This means that at low concentrations, the presence of mesopores does not affect the process. Therefore, in this case, at least for microporous samples, the initial concentration affects the model (see Annex I).

7.2.2 MNZ adsorption kinetics

MNZ has a less complex structure and a smaller size (topological polar surface area: 83.9 A² against 107 A² for SMX); therefore, shorter equilibrium times are expected. The pKa value of MNZ is 2.62, indicating that at pH above this value, the molecule is predominantly in its neutral form. The kinetic studies of the samples showed equilibrium times of ca. 45 minutes for all samples except for ca. 30 minutes for sample ACF-240-CR (Figure 7.6).

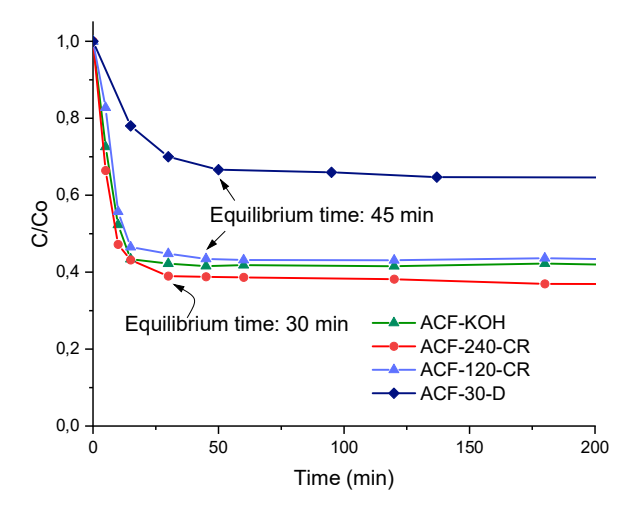


Figure 7.6 Concentration decay curve of MNZ as a function of time for ACF samples from the different activation methods (chemical and physical under D and CR regimes).

The rate constants of MNZ adsorption were bigger than those recorded for SMX adsorption (Table 7.2). Also, the amount adsorbed was smaller than that of SMX in all cases. It should be noted that, although the ACF surface is slightly positively charged at the working pH (with pHzc values of approximately 8), this is not expected to affect the kinetic adsorption rate, as the MNZ is neutral under these conditions (Figure 7.7).

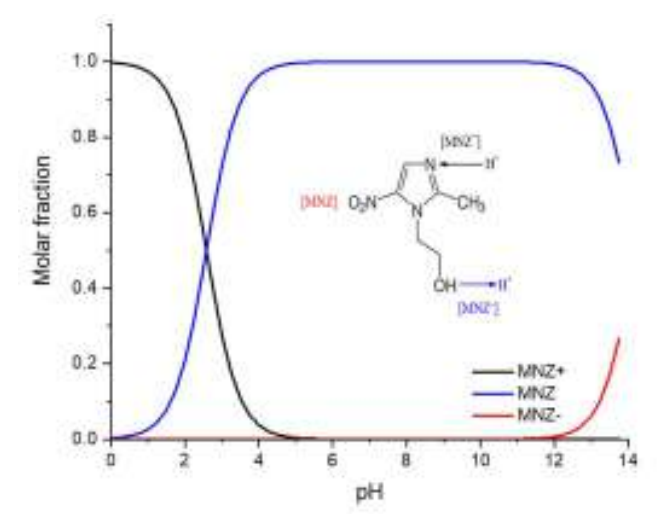


Figure 7.7 Speciation diagram of MNZ in aqueous solution and the species present depending on the medium pH.

The smaller uptake of MNZ, compared with SMX, can be attributed to its composition. The nitro group in MNZ is an electron-withdrawing moiety that decreases the electron density of the imidazole ring (Figure 7.8), thus leading to smaller π - π interactions with the carbon fibres. In addition, MNZ is not planar, which is expected to hinder (or slow down) the accessibility to the pores.

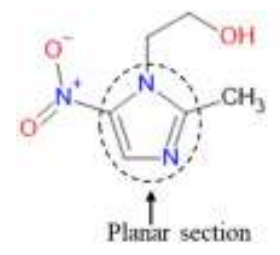


Figure 7.8 MNZ's molecule, the dashed circle englobes the structure's planar section.

As in the case of SMX, the experimental data was fitted to three kinetic models, using adj-R2, χ^2 and RSS as fitting criteria (Table 7.2). Except for sample ACF-30-D, all the kinetic curves fitted to the PSO model. The presence of mesopores and the material's morphology do not seem to affect the rate since ACF-KOH and ACF-120-CR displayed similar equilibrium times and kinetic parameters. This contrasts with the previous case about the removal of SMX, where a two-order magnitude difference was observed and was explained in terms of their different textural features and fibre morphology.

In all cases, the kinetic constant values are larger than those recorded for SMX adsorption. Therefore, the adsorption reaction is faster than that recorded for SMX. Since electrostatic attraction was ruled out (see above discussion about speciation diagram), this can only be explained by the molecule's size compared with SMX, leading to less movement resistance.

For ACF-30-D adsorption kinetic, considering only the adj-R² value, the result leads to categorising the process as a PSO model. However, the values of χ^2 and RSS suggest that PFO or Diffusional models could be applied. The difference between the χ^2 and RSS values in those models differ in two and three orders, suggesting a better fitting to the Diffusional model. The latter renders a smaller kinetic constant value and smaller calculated uptake than the rest of the samples (Table 7.2, Figure 7.9). Since all the samples have similar surface chemistry, the porosity must explain this behaviour. This ACF is strictly a microporous material, accounting for more than 96 % microporous volume. This

would indicate that the accessibility to these small micropores is somehow restricted; this could eventually explain the model followed by the experimental data despite being a hollow fibre.

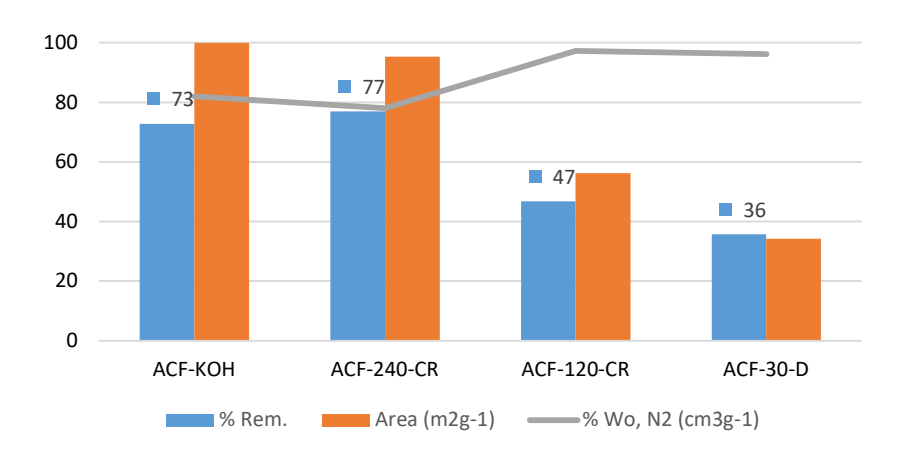


Figure 7.9 Comparison between the absolute removal of MNZ (percentage), the normalised specific surface area and the micropore volume (percentage), for selected samples obtained under physical -CR, D control regimes- and chemical activation.

Table 7.2 Kinetic fitting comparison for MNZ adsorption onto ACF obtained under CR and D method, chemical and physical activation, and different times for CR control.

	Units	ACF-KOH	ACF-240-CR	ACF-120-CR	ACF-30-D
PFO model					
k_1	min ⁻¹	0.0478	0.1601	0.1402	0.0257
adj-R ²		0.7369	0.7515	0.6520	0.8828
X^2		3.23	2.59	2.66	0.3004
RSS		20.73	7.76	7.98	1.0401
PSO model					
k_2	g mmol ⁻¹ min ⁻¹	0.4583	0.2754	0.2252	0.2449
adj-R ²		0.9975	0.9868	0.9589	0.9994
X^2		15.85	2.96	24.95	18.47
RSS		98.02	8.88	99.80	73.89
Diffusion model					
\mathbf{k}_3	mmolg ⁻¹ min ^{-1/2}	0.0725	0.0951	0.0951	0.0124
adj-R ²		0.4444	0.5410	0.5410	0.6372

X^2	 0.0243	0.0210	0.0210	0.0031
RSS	 0.0972	0.0630	0.0630	0.0092

An interesting question is, what would happen if only the first adsorption minutes were fitted? Would the model remain the same or change to another one? The data was considered only for the first 15 minutes to answer those questions. In almost all cases, the adsorption kinetic fits the diffusion model (Table 7.3), except for ACF-30-D, where the kinetic model remains unchanged. Note that we could not perform a similar analysis to SMX because the first data point was recorded at sixty minutes (slower kinetic).

This behaviour implies that adsorption is a complex process that evolves with time. In the early stages, at least for MNZ, the diffusion phenomena have a significant weight in the mechanism and are governed by the mass transfer's Fick law. This law states that in a system with a gradient concentration, a mass current will be spontaneously established in the decreasing direction. The transfer of molecules can be diffusive (without external forces, like stirring involved) or convective (with external forces involved). In the current case, the stirring helps the external adsorbate transfer from the bulk to the ACF surface. Nonetheless, once on the surface, the adsorbate needs to reach the adsorption site inside the porous network; at this point, the stirring is unuseful and the diffusive forces command. Once the concentration gradient diminishes, meaning the inside network is full of adsorbate, the rules change, and the PSO model is mainly responsible for the adsorption kinetics.

Regarding the experiences with the 0.4 mmolL-1 concentration solution, the process fitted PSO in all cases (considering all the data intervals). For this type of adsorbate, the concentration affected only the ACF-30-D. This microporous material is very brittle, and its morphology does not help the adsorption kinetics, which is ruled by the molecule diffusion inside the porous network.

Table 7.3 Kinetic fitting comparison, for the first 15 minutes of the process, for MNZ adsorption onto ACF obtained under the CR and D methods, chemical and physical activation, and different times for CR control.

	Units	АСҒ-КОН	ACF-240-CR	ACF-120-CR	ACF-30-D
PFO model					
k_1	min ⁻¹	0.4196	0.4018	0.4744	0.0333
adj-R ²		0.8578	0.8704	0.8761	0.7205
X^2		0.6652	1.2941	0.9334	0.0980
RSS		0.6652	1.2941	0.9334	0.0980
PSO model					
k_2	g mmol ⁻¹ min ⁻¹	0.1219	0.1432	0.0832	0.2270
adj-R ²		0.9395	0.9751	0.8400	0.9693
X^2		0.2807	0.2118	11.65	18.96
RSS		0.2807	0.2118	11.65	18.96
Diffusion					
model					
\mathbf{k}_3	mmolg ⁻¹ min ^{-1/2}	0.3162	0.2876	0.3292	0.0308
adj-R ²		0.9657	0.9625	0.9292	0.7277
X^2		0.0026	0.0018	0.0053	0.0026
RSS		0.0026	0.0018	0.0053	0.0026

7.2.3 AMP adsorption kinetics

The adsorption of AMP was tested only for sample ACF-30-D, and the results were compared to those obtained for SMX and MNZ. Even though the adsorption of this compound was not further tested in the binary mixtures, it is interesting to describe its kinetic behaviour. From an acid-base point of view, AMP is a weak acid with a pKa of 9.4 (Figure 7.10). The working solution pH (6.5) and the ACF pH_{PZC} ensure the surface of the carbon adsorbent is positively charged while AMP remains neutral; hence, the contribution of favourable electrostatic interactions is ruled out as the primary adsorption mechanism. Hence, π - π dispersive interactions between the aromatic structure of the ACFs and AMP molecules are the main driving force for adsorption.

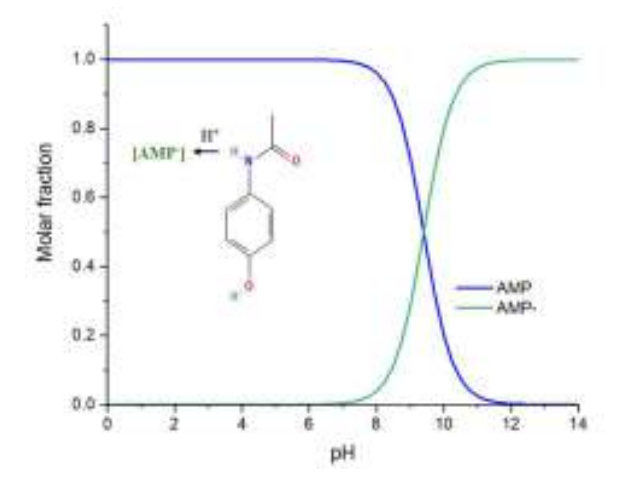


Figure 7.10 Speciation diagram for AMP in aqueous solution the species present depending on the medium pH.

Interestingly, while the equilibrium time and the kinetic constants for the adsorption of SMX and AMP on sample ACF-30-D are similar, the uptakes are rather different. At the working solution pH, SMX is a negatively charged compound (where favourable electrostatic interactions apply on the positively charged surface of the carbon fibres, as discussed above), while AMP is neutral. On the other hand, there is a remarkable difference in the removal capacity: 52 % for SMX and 96% for AMP, which can be attributed to the differences in the adsorption mechanism, the structure of the adsorbates, and their size. In this sense, the charged compounds are more stable in a polar medium like water, explaining the removal capacity difference.

The equilibrium time for AMP was reached at 2880 minutes (Figure 7.11), similar to that recorded for the adsorption of SMX (Figure 7.4). The kinetic data was well-fitted to the Diffusion model, with a smaller kinetic constant value than that for MNZ. As in the previous compounds, the kinetic change in the dilute solution (0.4 mmolL⁻¹) where its behaviour fits a PSO model. Another important aspect is that the adsorption of MNZ displayed the smallest equilibrium time and the biggest kinetic constant (Table 7.5). MNZ is similar to AMP in terms of size and both are in neutral forms in the operating conditions. The adsorption efficiency of MNZ decayed to 36 %; hence it is clear that the affinity of ACF-30-D for MNZ is smaller than for AMP; this could be explained by the presence of the nitro group in the structure of MNZ, as discussed above.

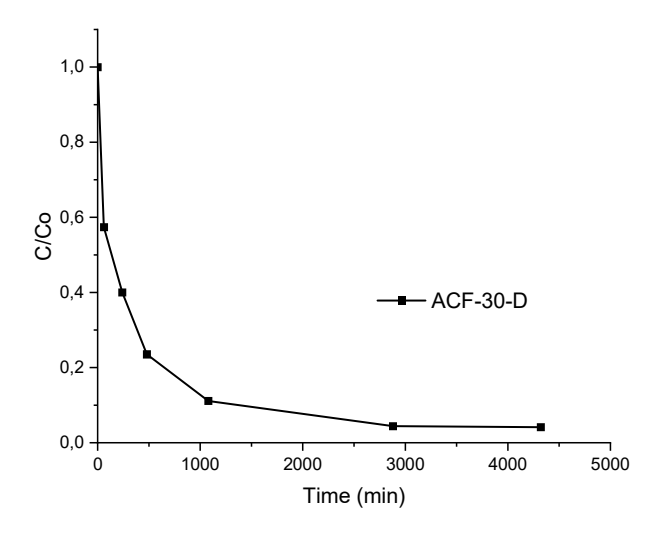


Figure 7.11 AMP normalised decay concentration curve as a function of time for ACF-30-D sample.

Table 7.4 Kinetic fitting for AMP adsorption onto ACF-30-D.

	Units	ACF-30-D
PFO model		
k_1	min ⁻¹	0.0019
adj-R ²		0.9978
X^2		0.0079
RSS		0.0397
PSO model		
k_2	g mmol ⁻¹ min ⁻¹	0.0012
adj-R ²		0.9997
X^2		15.29
RSS		91.77
Diffusion model		
\mathbf{k}_3	mmolg ⁻¹ min ^{-1/2}	0.0180
adj-R ²		0.9931
X^2		0.0060
RSS		0.0180

Table 7.5 Kinetic features comparison among SMX, MNZ and AMP adsorbates for the same adsorbent ACF-30-D.

Adsorbate	Kinetic constant	Equilibrium time	Surface charge
	(mmolg ⁻¹ min ^{-1/2})	(min)	Adsorbate/ACF
SMX	0.0124	2880	-/+
MNZ	0.0308	45	Neutral / +
AMP	0.0180	2880	Neutral / +

7.3 Equilibrium adsorption

An important aspect of adsorption analysis is the study of thermodynamics. In this sense, the isotherm adsorption experiments were carried out on at least a pool of three batches with a difference of no more than 15 % among points. The potentiometric titration already proved the material's particularity (Chapter VI, section 6.4.3); thus, based on these data, a certain dispersion degree is expected to reinforce the 15 % tolerance decision.

The experimental data was fitted to three models: Langmuir, Freundlich, and Elovich for each pollutant (Chapter III, section 3.2). The results were discussed in terms of the characteristics (textural and chemical) of the ACFs. For the assessment of the best thermodynamic model fitting, the same criteria described for the kinetic studies were applied (Chapter VII, section 7.1).

7.3.1 SMX adsorption thermodynamics

The SMX adsorption isotherms were carried out from solutions with initial concentrations from 0.1 to 1.0 mmolL⁻¹. The general adsorption trend (Figures 7.12 and 7.13) shows that the adsorption capacity goes along with the specific surface area and, in the case of the physically activated samples, with the activation time. This behaviour is observed for the CR series, where the uptake increases with the activation time. The initial curvature in the equilibrium adsorption isotherms indicates a gradual filling of the active sites, being characteristic of asymptotic L-type behaviour according to Giles' classification (Giles et al. 1960; Giles et al. 1974). This is characteristic of systems

without strong competition from the solvent. The adsorbed molecules are most likely in a flat orientation, indicating that the aromatic rings in the SMX structure adsorb parallel to the graphitic planes of the ACF.

One of the most remarkable features of the plot is the behaviour of samples ACF-KOH, ACF-240-CR, and ACF-30 for both D and CR control regimes. While the first two samples have similar kinetic behaviour and similar textural characteristics (see Chapter VI, table 6.5), the concentration at the equilibrium for the first points showed a difference that can not be ignored; such difference becomes smaller at higher equilibrium concentrations in solution (Figure 7.13). Something similar occurred for samples ACF-30-CR and ACF-30-D - submitted to similar activation temperature and time but different gas flux-, with equilibrium concentrations differing in one order (Figure 7.14). On the other hand, for the ACF-CR series (Figure 7.12), the isotherms recorded the expected behaviour, increasing the uptake of SMX by the apparent surface area increment.

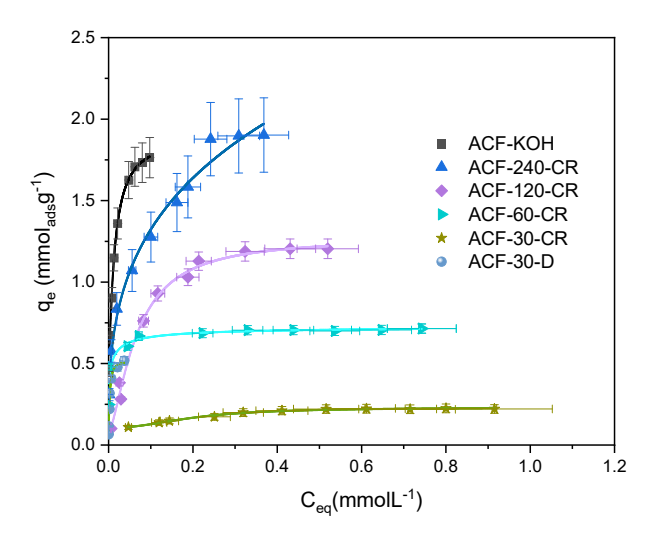


Figure 7.12 SMX adsorption isotherms for ACF samples from the different activation methods (chemical and physical under D and CR regimes).

Note: The trend lines were calculated using a growth/sigmoidal function with a Hill model, applying the Levenberg—Marquardt iteration algorithm using Origin Pro and fitting data in Annex I.

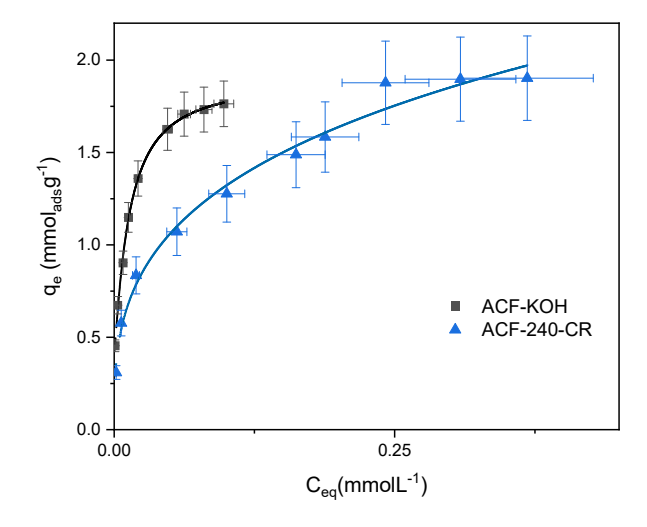


Figure 7.13 SMX adsorption isotherms for ACF-KOH and ACF-240-CR samples.

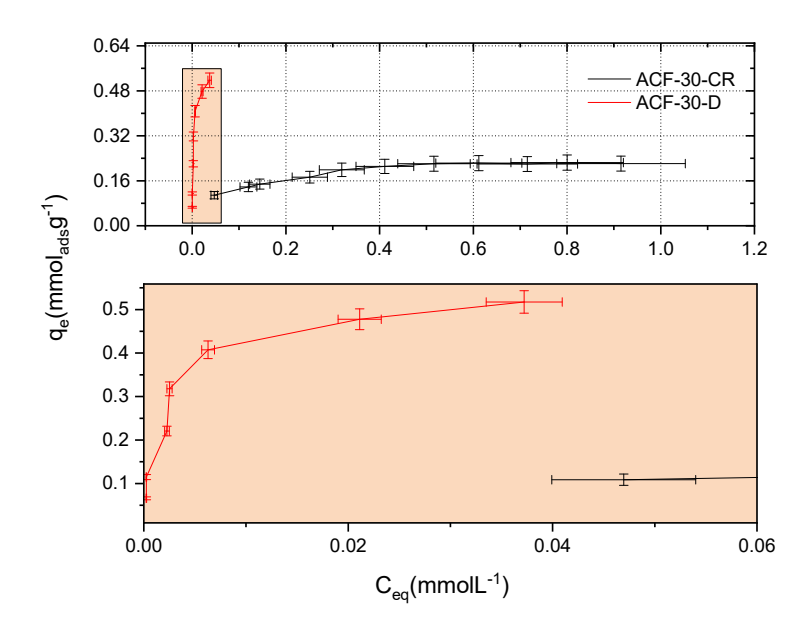


Figure 7.14 Isotherms comparison between samples activated under CR and D regimes for 30 minutes.

Regarding the adsorption models, in all cases, the equilibrium adsorption isotherms fitted well to the Langmuir adsorption model (Table 7.6). The features considered to analyse the proper fit were the same as explained (Chapter VII, section 7.1). Considering the Langmuir constant values, an interesting difference can be observed among samples, for example, ACF-KOH and ACF-240-CR, where the former is more than five times bigger than ACF-240-CR, indicating a more favourable affinity adsorbent-adsorbate in the pores of sample ACF-KOH.

Table 7.6 Isotherms fitting comparison for SMX adsorption onto ACF obtained under chemical and physical activation (D and CR methods) and different times for CR control.

	ACF-KOH	ACF-240-CR	ACF-120-CR	ACF-60-CR	ACF-30-CR	ACF-30-D
Langmuir						
K_L (Lmmol ⁻¹)	157	29.3	13.0	189	12.6	499
$q_{max.}$ (mmolg ⁻¹)	1.87	2.03	1.42	0.71	0.25	0.54
adj-R ²	0.9972	0.9765	0.9884	0.9998	0.9962	0.9964
X^2	1.05E-6	9.95E-5	1.85E-4	3.29E-5	0.0054	2.44E-6
RSS	7.38E-6	7.96E-4	0.0015	2.96E-4	0.0487	1.22E-5
Freundlich						
K_F (mmolL ⁻¹) ⁻ⁿ	1.50	1.40	0.52	1.29	4.04	0.45
n	0.005	0.059	0.463	0.090	0.259	0.376
adj-R ²	-0.1411	0.0031	0.7931	0.9756	0.9496	0.8755
X^2	0.0551	0.0976	0.1121	0.0023	0.0031	0.0755
RSS	0.3855	0.7804	0.8964	0.0206	0.0276	0.3776
Elovich						
$K_E \left(\text{Lg}^{-1} \right)$	2772	528.8	28.81	1.55E8	194.6	4205
$q_{max.}$ (mmolg ⁻¹)	0.44	0.48	0.69	0.05	0.062	0.150
adj-R ²	0.9673	0.9451	0.7854	0.9727	0.9140	0.8525
X^2	0.0431	0.0804	0.0975	0.2817	0.0409	0.2305
RSS	0.3014	0.6436	0.7803	2.5351	0.3687	1.1526

To gauge the incidence of the adsorbent textural features onto the adsorption capacity, the study was divided into three main characteristics: micropore volume (N_2 and CO_2 gas adsorption data), micropore area (N_2 and CO_2 gas adsorption data) and apparent specific surface area (S_{BET} , N_2 adsorption data).

Analysing the microporous plots (Figure 7.15), the adsorption capacity obtained from the Langmuir model showed a general trend that goes conjointly with N₂ microporosity volume (calculated by DR) and is less dependent on CO₂ volume. This suggests that the presence of wide micropores (seen by N₂ adsorption isotherms at 77 K) is important for the adsorption of SMX. In comparison, some of the narrow micropores (seen by CO₂ adsorption isotherms at 273 K) may not be accessible for this molecule.

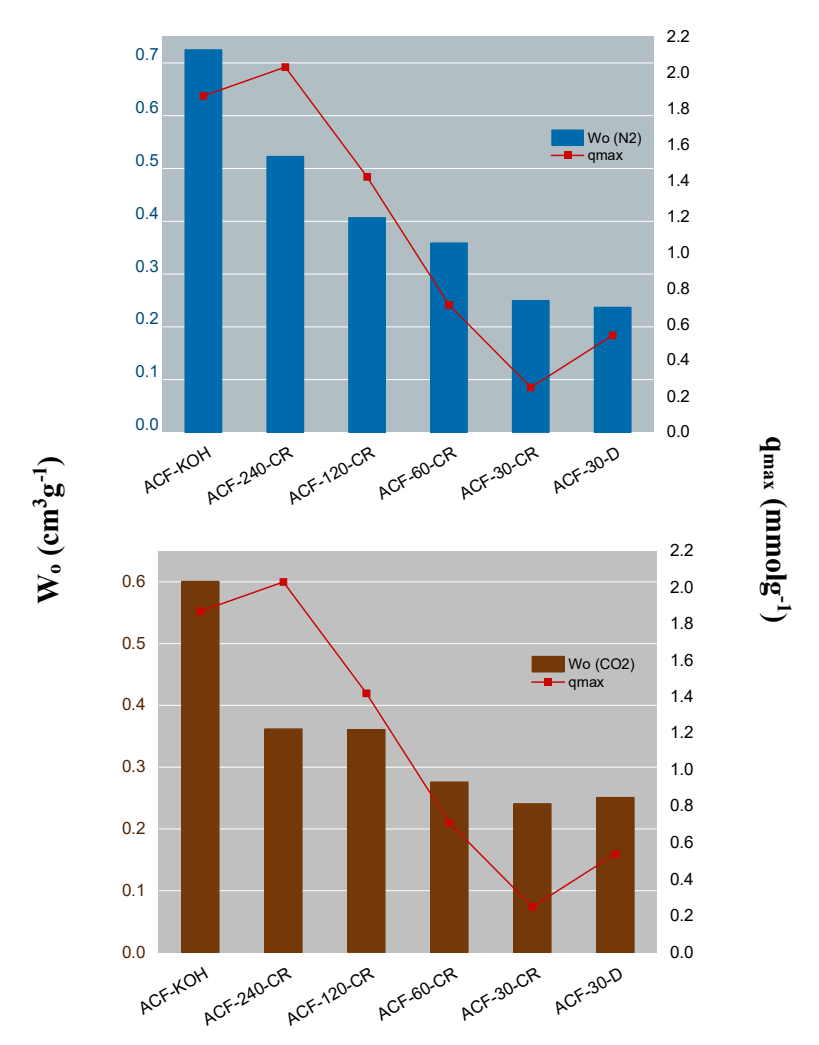


Figure 7.15 Comparison of SMX adsorption capacities against the microporous volume calculated by DR (for all the samples obtained under different conditions).

On the other hand, no clear correlation was found with micropore areas (calculated by DR) (Figure 7.16), but it also goes conjointly with SBET (Figure 7.17). This can be analysed considering only the contribution of microporous presence, despite the mesopore's importance for the kinetic process. This assertion can be proved by considering the recorded uptakes for each case. For example, for samples ACF-KOH and ACF-240-CR with similar apparent specific surface areas and around 20 % of mesopores contribution, the average uptakes were around 1.95 mmolg⁻¹. Compared with sample ACF-120-CR, with no mesopore contribution and an area representing 60 % of the previous samples, the uptake was 70 % of the former. These figures proved that the mesopore presence does not affect the adsorption capacity of the samples.

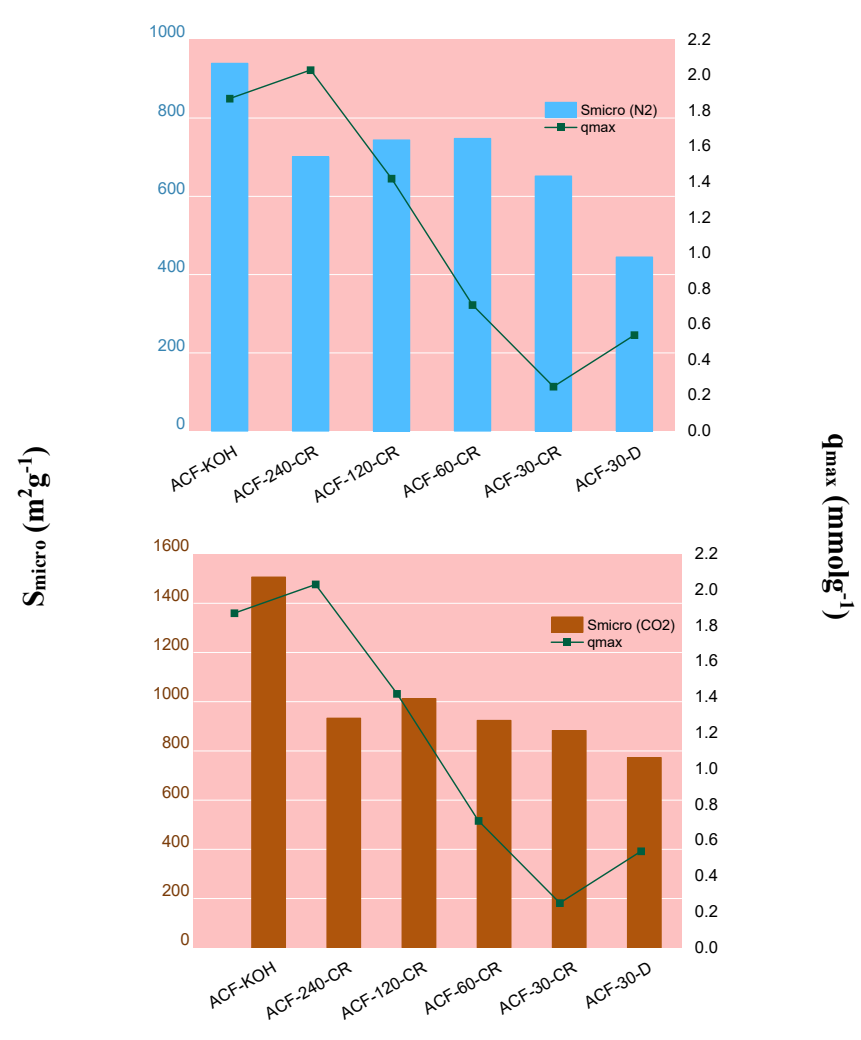


Figure 7.16 Comparison of SMX adsorption capacities against the microporous areas (calculated by DR for all the samples obtained under different conditions).

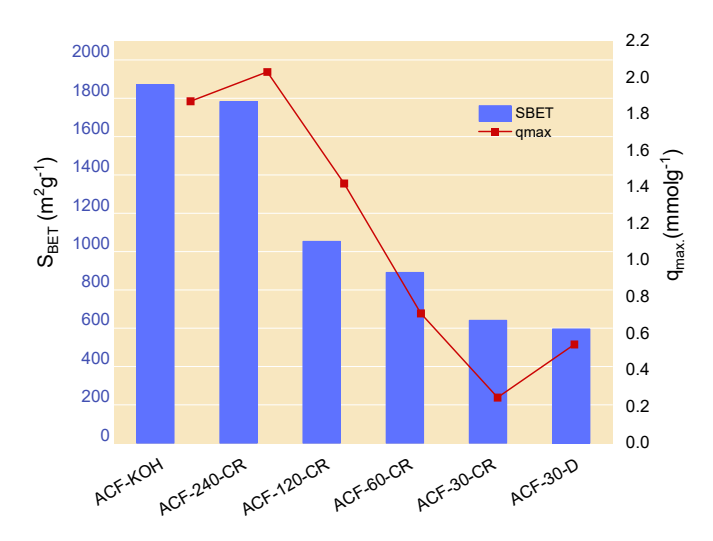


Figure 7.17 Comparison of SMX adsorption capacities against the S_{BET} values for all the samples obtained under different conditions.

Considering all the facts mentioned, it can be asserted that the adsorption takes place in the microporosity of the adsorbents but from a certain microporous width onward. The small micropores and the mesopores are not participating. An esteric problem can explain the former; the drug is bigger than the available pore (Figure 7.18).

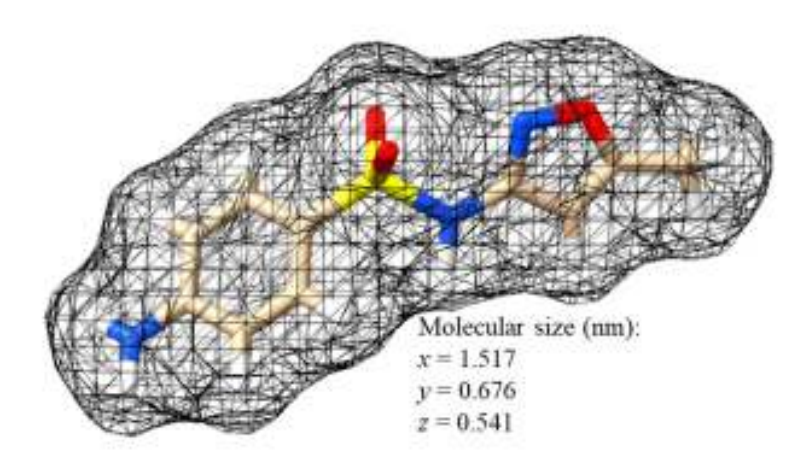


Figure 7.18 SMX spatial structure and size (Serna-Carrizales et al. 2023).

From a thermodynamic perspective, adsorbing the pharmaceutical compound in a micropore is beneficial because it falls into a more significant energy well than that provided by a mesopore, owing to the better confinement in pores of dimensions close to those of the adsorbed molecule.

A more precise analysis of the effect of the pore size can be performed by correlating the uptake at a specific equilibrium concentration with the cumulative pore (Figures 7.19 a, b, c and d) illustrating the correlation between the adsorption capacity of SMX and selected ranges of pores of sizes between 0.7 and 3.0 nm as determined by the analysis of the nitrogen adsorption isotherms of the materials using the 2D-NLDFT-HS method (Jagiello and Olivier 2013). The obtained fitting values (Table 7.7) indicate that there is no clear correlation between the amount of SMX adsorbed and the volume of micropores smaller than 0.7 nm. On the other hand, large coefficients of determination are observed for the correlation between the uptake and the volume of pores of sizes between 0.7 and 2.0 nm and, to a minor extent, with mesopores. The contour plot (Figure 7.20) provides a more comprehensive view of the dependence between the determination coefficient for the uptake of SMX at specific equilibrium concentrations (ranging from 0.025 to 0.2 mmol L⁻¹) and the pore sizes from 0.36 to 3.0 nm. As shown, high coefficients of determination (i.e., strong dependence between the adsorption capacity of SMX and the pore volumes) were obtained for pores larger than 1.5 nm at equilibrium concentrations above 0.075 mmol L⁻¹. This suggests that the adsorption of SMX would primarily occur within that specific pore size range.

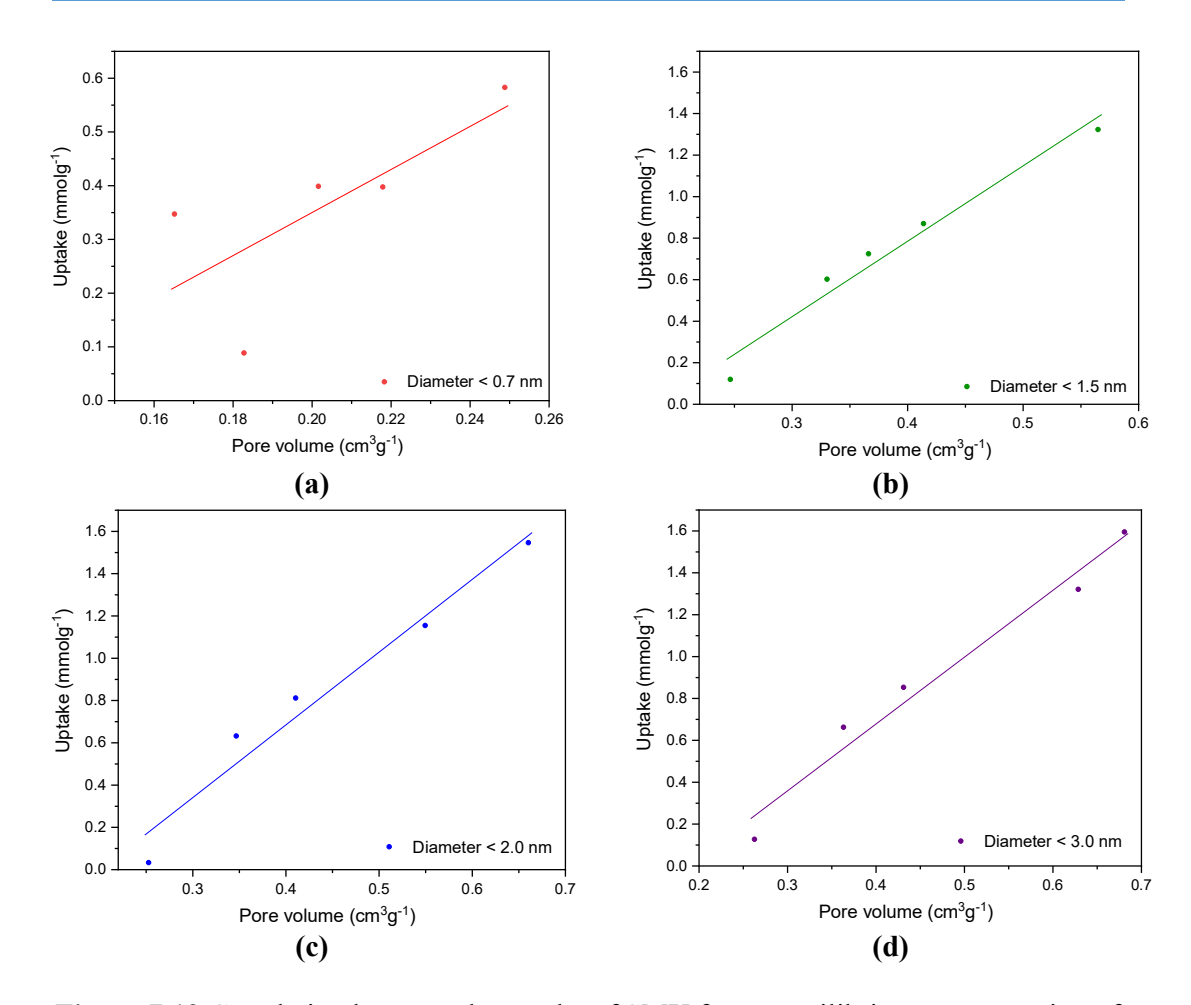


Figure 7.19 Correlation between the uptake of SMX for an equilibrium concentration of 0.1 mmolL⁻¹ as a function of the size of the pores: (a) up to 0.7 nm, (b) up to 1.5 nm, (c) up to 2.0 nm, and (d) up to 3.0 nm. Pore volumes were evaluated from the nitrogen adsorption isotherms at 77K of the ACF using the 2D-NLDFT-HS method.

Table 7.7 Fitting parameters for the SMX uptake at an equilibrium concentration of 0.1 mmolL⁻¹ as a function of the pore size distribution for pores of selected ranges.

Pore Size Range	0.7 nm	1.5 nm	2.0 nm	3.0 nm
adj-R ²	0.5295	0.9666	0.9765	0.9723
RSS	0.0594	0.3593	0.0560	0.0002

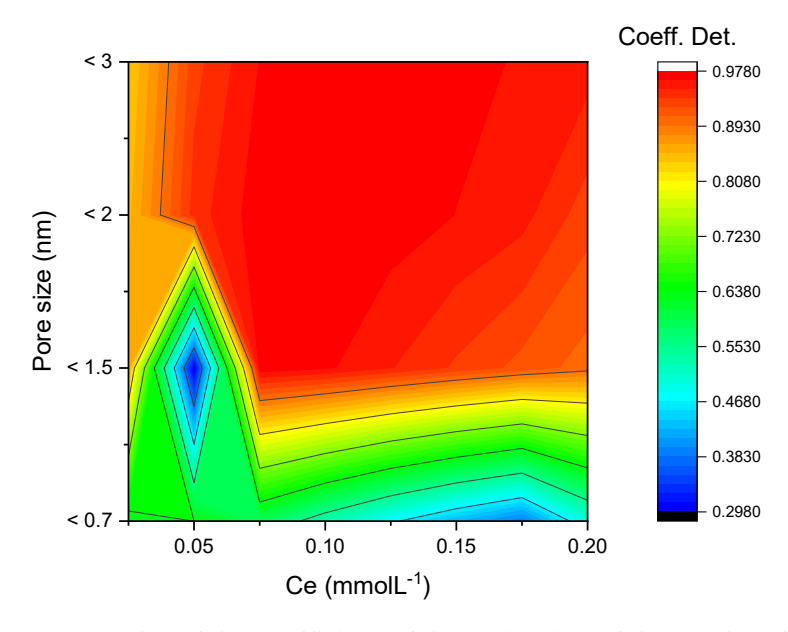


Figure 7.20 Contour plot of the coefficient of determination of the uptake of SMX at various equilibrium concentrations and pore sizes.

Now, let us consider the chemistry perspective. The ACFs used in this study have nitrogen and sulfur. Thus, the question to be clarified is: why is the presence of these heteroatoms significant? In this sense, many studies demonstrate that incorporating heteroatoms, such as nitrogen, sulphur, phosphorus, and boron, may significantly impact the adsorption performance (Krstic et al., 2022; Wei et al. 2023). Nitrogen, in particular, has a high electronegativity (3.04); therefore, its presence provides a variety of functional groups and defect sites and can impact the surface charge distribution depending on the nature of those N-moieties. Sulphur has a higher atomic radius than carbon and nitrogen and an electronegativity (2.58) similar to that of carbon (2.55). It is generally present in the form of rather bulky S-groups and not inserted in the aromatic carbon matrix; its presence slightly changes the electronic structure of the carbon material but also affects the reactivity and/or accessibility to the pores.

Comparing samples ACF-KOH and ACF-240-CR, both present similar textural features (already discussed) but distinctly different nitrogen and sulphur content (9.29 and 0.21 for ACF-KOH; 2.65 and 1.87 for ACF-240-CR), thus a likely incidence of those heteroatoms should be considered. Regarding the equilibrium adsorption isotherms (Figure 7.12), the uptake is bigger for ACF-KOH at low equilibrium concentrations; however, after a certain point, the uptake of ACF-240-CR surpasses the former. In fact,

according to the Langmuir model, the largest adsorption capacity is set for this last (Table 7.6). The ratios between nitrogen and sulphur content for ACF-KOH/ACF-240-CR are 3.5 and 0.11, respectively. Based on this, one may infer that the presence of S-containing moieties is important for the adsorption because ACF-240-CR displayed the highest adsorption capacity at high SMX concentrations. However, this hypothesis is risky because the Langmuir constant (K_L, Table 7.6) fitted from the equilibrium adsorption isotherms was higher for sample ACF-KOH, indicating more energetically favourable adsorption in this adsorbent. For the series of adsorbents prepared upon the CR regime, analysing the impact of nitrogen and sulphur-containing surface groups is not evident since they are materials with different specific surface areas and textural features.

Due to the material's nature, it is only possible to assess its adsorption performance with nitrogen and sulphur and compare it with the obtained samples. Consequently, the available results could be more conclusive. However, a future XPS study could be interesting (in fact, it is planned for the near future) to assess the corresponding percentages of nitrogen present in the Pyridine and Pyrrole structures and the sulphur-containing groups. Those results could help determine if the presence of those heteroatoms affected the adsorption performance.

The pH is another parameter to consider since both the adsorbent surface and the SMX molecules' charge are susceptible to changes in pH. The initial solution pH was sensitive to the concentration of SMX in the absence of the adsorbent, as seen in Figure 7.21. Under these conditions, SMX is predominantly deprotonated, as indicated by its speciation diagram (see Figure 7.7). This deprotonated form releases protons into the surrounding medium, thereby accounting for the observed decrease in pH. The trend aligns with the initial concentration: a higher quantity dissolved results in a greater decrease in pH.

The solution pH was also measured after equilibrium was achieved in contact with the ACF adsorbents. An average pH increase of two points was consistently obtained for all the samples. This is illustrated in Figure 7.21 for samples ACD-KOH and ACF-240-CR; this pattern is typical for a compound with the ability to donate and receive protons, such as SMX. Interestingly, a rise in the pH following the adsorption was observed, showing the contribution of the adsorbent's surface to the modifications of the pH.

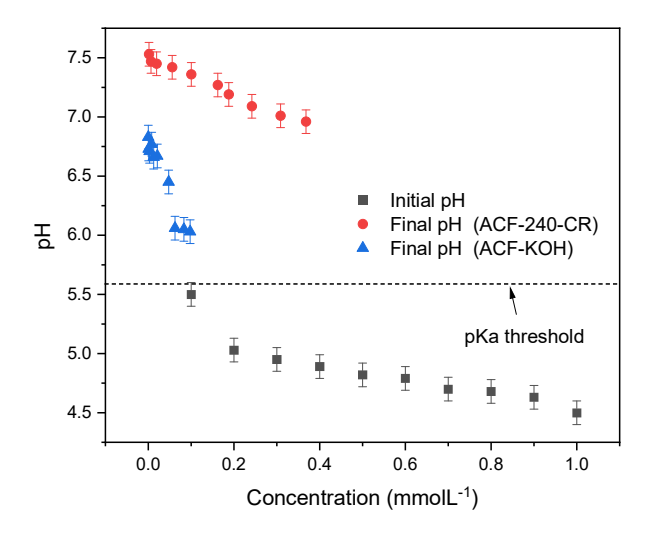


Figure 7.21 Evolution of the solution pH at different concentrations of SMX before (squares) and after the adsorption on samples ACF-KOH (triangles) and ACF-240-CR (circles). 20 mg of adsorbent have been used for all the adsorption assays.

The removal efficiency was sensitive to the concentration in solution, except for ACF-KOH, which remained relatively constant (Figure 7.22). The rest of the samples have a fibrous morphology. The removal efficiency is directly affected by the initial concentration for this type of material and compound. Thus, we could assume that for this kind of compound, as the concentration increases, certain interactions among molecules are established that interfere with the movement along the fibres. We can eliminate the possibility of pH interference as the ACF consistently carries a positively charged surface, given that the operating pH values fall below the material's pH_{PZC}. Additionally, potentiometric titrations (see Chapter VI, section 6.4.3) reveal that the ACF does not feature proton exchange functional groups.

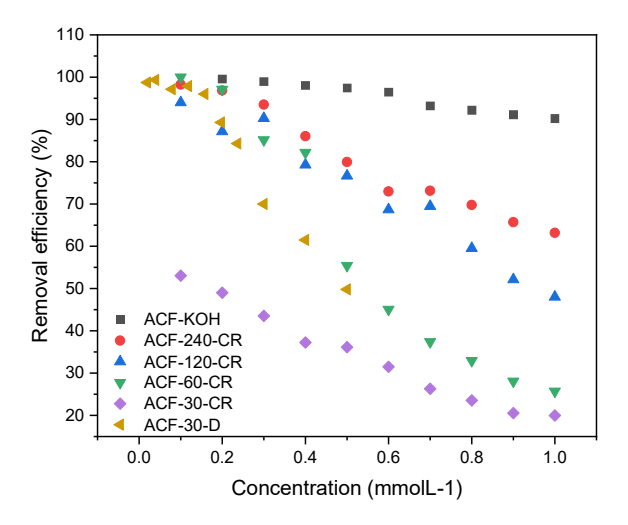
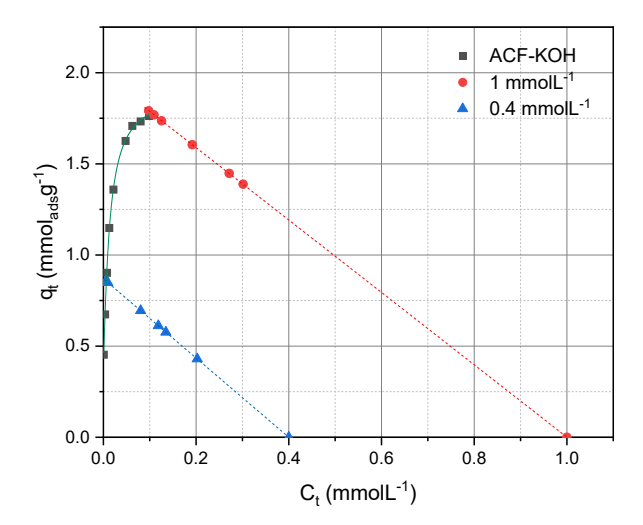


Figure 7.22 SMX removal efficiency evolution for all the samples obtained under different activation conditions vs the initial SMX concentration (20 mg of adsorbent per analysis).

The operating lines of both datasets were plotted to assess the concordance between the kinetic and equilibrium adsorption data. The next figure (Figure 7.23) shows examples of the operating lines of selected ACFs prepared upon chemical and physical activation. The operating lines (from kinetic data) must cross the path of the equilibrium adsorption isotherms at the time designed as equilibrium (Hirschler et al.1955; Mckay 1984). This behaviour can clearly be seen in the samples plotted.



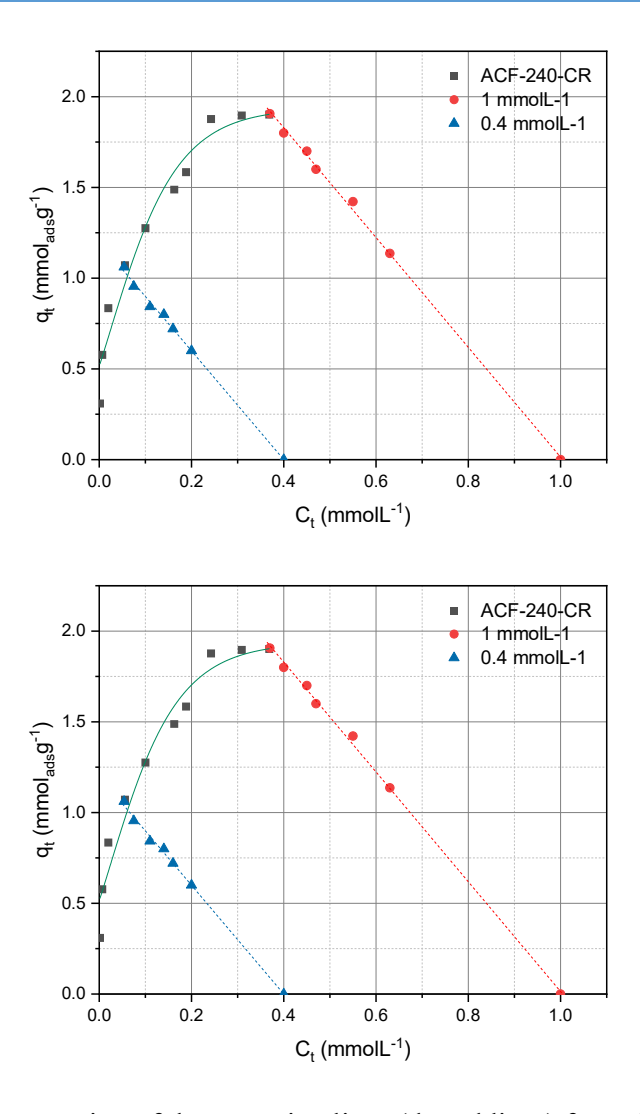


Figure 7.23 Representation of the operating lines (dotted lines) from the kinetic data on the equilibrium adsorption isotherms for samples ACF-KOH, ACF-240-CR, and ACF-60-CR, for the adsorption of SMX.

7.3.2 MNZ adsorption thermodynamics

MNZ equilibrium adsorption isotherms were carried out from solutions with initial concentrations from 0.1 up to 1.0 mmolL-1. The general adsorption trend (Figure 7.24) shows three main groups, ACF-KOH and ACF-240-CR with higher MNZ uptake; ACF-120-CR and ACF-60-CR, and finally, the ACF-30 samples (both CR and D control regimes). Comparatively, the adsorption rate of MNZ is faster than that of SMX, which could be expected because of its smaller size. Despite this, the quantities adsorbed for the first group are smaller than those recorded for SMX. On the contrary, the second group

registers a detriment for ACF-120-CR but a small increment for ACF-60-CR. Moreover, in the third group, the behaviours are reversed compared to those recorded for the adsorption of SMX.

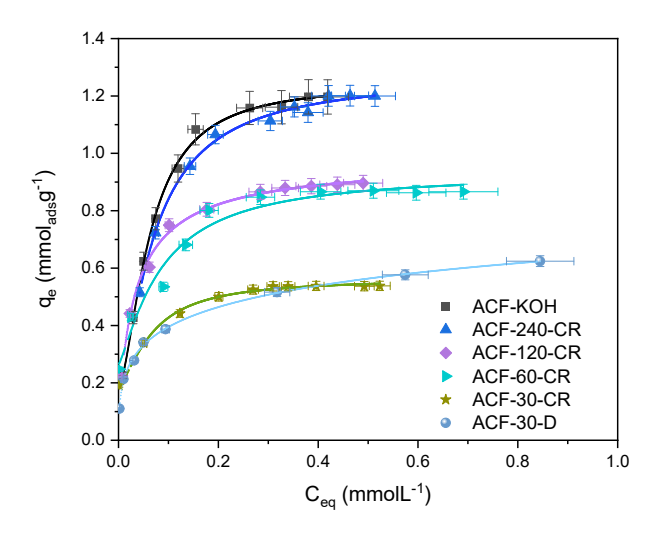


Figure 7.24 MNZ adsorption isotherms for samples prepared upon different activation methods (chemical and physical under D and CR regimes).

Note: The trend lines were calculated using a growth/sigmoidal function with a Hill model, applying the Levenberg-Marquardt iteration algorithm using Origin Pro and fitting data in Annex I.

Considering that the molecule remains neutral during adsorption due to its p_{Ka} , the predominant interactions are π - π bonds. Nevertheless, the electron density over the imidazole ring is affected by the presence of the nitro group, disfavouring the adsorption. In addition, as mentioned before, MNZ is planar only in the imidazole ring, meaning that its interaction area is smaller than that of SMX (Figure 7.25). Therefore, accessibility to narrow and tortuous pores is impeded, as the structure requires a correct angle to interact with the adsorbent. Those two characteristics lead to smaller uptakes than expected for a smaller molecule compared to SMX.

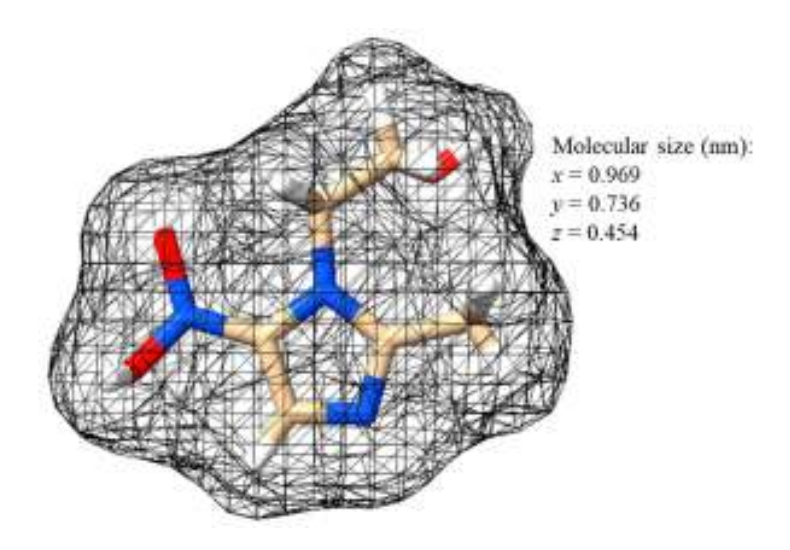


Figure 7.25 MNZ spatial structure and size (Serna-Carrizales et al. 2023).

In all cases, the recorded data fitted the Langmuir adsorption model, and the results denoted the same pattern shown by the plots, which are divided into three main groups. There are two opposite general trends: where the Langmuir equilibrium constant increases, the adsorption capacity decreases (Table 7.8). In this context, it is important to consider that while the K_L value is linked to the interaction energy between the adsorbate and adsorbent, q_{max} is associated with the material's volume. As a result, they are independent of each other. On the other hand, Langmuir is a model initially formulated for the adsorption of gases, focusing solely on the interaction between the adsorbate and the adsorbent within a monolayer of coverage. However, when it comes to adsorption in the liquid phase, the scenario is considerably more intricate, requiring consideration of up to five distinct interactions: adsorbate-adsorbent, adsorbate-solvent, adsorbate-adsorbate, adsorbate-solvent and solvent-solvent, and possibly the presence of other forces if the adsorbate form micelles or aggregates (Giles et al. 1974), adding complexity to the study of this type of system.

Furthermore, ACF-30-D is outside the trend; the equilibrium constant value is between ACF-240-CR and ACF-120-CR, although its adsorption capacity is between ACF-60-CR and ACF-30-CR. Considering the morphological differences between those samples, it could be assumed that the off-trend ACF-30-D is a direct result of the structural characteristics of the adsorbent and not a change in the adsorbate molecule's behaviour. However, what is striking is that the MNZ adsorption capacity for samples ACF-60-R, ACF-30-CR and ACF-30-D is higher than that recorded for SMX,

respectively. These three adsorbents are characterised by a low contribution of mesopores (Tables 6.7 and 6.10) and rather similar contents of heteroatoms (Table 6.15).

From the chemical point of view, ACF-240 and ACF-120 have a low nitrogen content and similar sulphur contents as ACF-60-R, ACF-30-CR and ACF-30-D, whereas sample ACF-KOH displayed 3.5 times more nitrogen content than most of the samples but hardly any sulphur. Considering all this, the difference in the elemental content of nitrogen and sulphur cannot explain the adsorption capacity results because there is no clear trend.

Table 7.8: Fitting parameters for different adsorption models of the experimental equilibrium adsorption data for MNZ on a series of ACF obtained under chemical and physical activation (D and CR control regimes) and varying activation times for the CR control regimes.

	ACF-KOH	ACF-240-CR	ACF-120-CR	ACF-60-CR	ACF-30-CR	ACF-30-D
Langmuir						
K_L (Lmmol ⁻¹)	18.7	15.7	36.0	33.7	48.6	25.5
$q_{max.}$ (mmolg ⁻¹)	1.36	1.36	0.95	0.91	0.56	0.63
adj-R ²	0.9977	0.9987	0.9996	0.9953	0.9970	0.9936
X^2	3.28E-5	2.25E-5	1.49E-5	3.47E-4	2.99E-4	0.0016
RSS	2.63E-4	1.80E-4	1.19E-4	0.0028	0.0024	0.0095
Freundlich						
K_F (mmolL ⁻¹) ⁻ⁿ	2.04	1.60	1.25	1.01	0.63	0.70
n	0.43	0.32	0.30	0.215	0.182	0.276
adj-R ²	0.9333	0.9201	0.9151	0.9604	0.9784	0.9781
X^2	0.0205	0.0062	0.0171	0.0069	0.0024	0.0074
RSS	0.1644	0.0498	0.1367	0.0558	0.0193	0.0444
Elovich						
$K_E \left(\mathrm{Lg}^{\text{-1}} \right)$	79.73	118.9	455.5	2731	12247	969
$q_{max.}$ (mmolg ⁻¹)	0.51	0.42	0.24	0.16	0.08	0.12
adj-R ²	0.9009	0.8963	0.9310	0.8775	0.9310	0.9891
X^2	0.0520	0.0348	0.0689	0.2779	0.1521	0.0247
RSS	0.4164	0.2787	0.5516	2.2231	1.2169	0.1485

MNZ is consistently maintained in ist neutral form throughout the adsorption, since the operating pH remains above its pKA value with minimal fluctuations during the adsorption experiments (Figure 7.26). As already mentioned, this result discards the presence of the electrostatic interactions, leaving the π - π interaction, hydrogen bonds and Van der Waal forces acting as predominant adsorption forces.

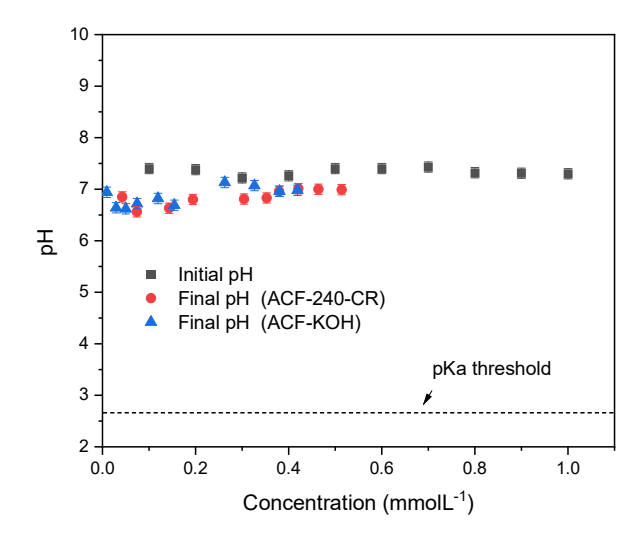


Figure 7.26 Evolution of the solution pH at different MNZ concentrations before (squares, initial concentration) and after the adsorption for samples ACF-KOH (triangles) and ACF-240-CR (circles). 20 mg of adsorbent were used in all cases.

On the other hand, the recovery efficiency exhibited an intriguing pattern, with the exception of samples ACF-60-CR and ACF-30-D, as the remaining samples maintained a relatively consistent efficiency from a concentration of 0.7 mmolL⁻¹ onwards (Figure 7.27). Considering the chemistry and textural features, there is no clear explanation for why this behaviour changes, except for the loss of materials' integrity during the experiment for samples ACF-30-D and ACF-60-CR, which would lead to enhanced accessibility. The mesoporosity of the samples does not seem to impact significantly the efficiency of MNZ adsorption. This is highlighted by the notable difference in the volume of mesopores of samples ACF-KOH and ACF-240-CR (both with ca. 20 % mesopore volume) compared to sample ACF-120-CR (with a low mesopore contribution). The three samples showed similar MNZ uptakes.

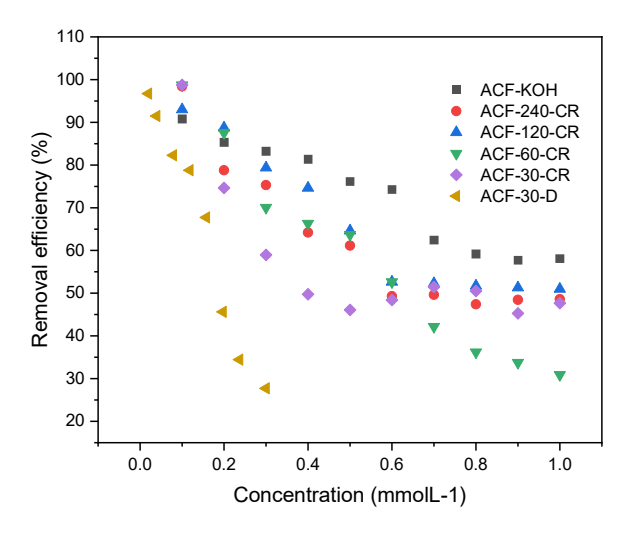


Figure 7.27 MNZ removal efficiency evolution for all the samples obtained under different activation conditions vs the initial MNZ concentration (20 mg of adsorbent per analysis).

The maximum adsorption capacity calculated by fitting the experimental data to the Langmuir equation (q_{max}) showed a clear correlation with the micropore volumes of the adsorbents determined from gas adsorption data (Figure 7.28). Samples ACF-240-CR and ACF-120-CR display ca. 78 % and 91 % (Tables 6.5 and 6.10) contribution of micropores. The MNZ uptake of ACF-120-CR is 69 %, higher than that of sample ACF-240-CR despite its lower contribution of micropores to the total pore volume.

The micropore surface area evaluated from the DR formulism from the N_2 and CO_2 adsorption isotherms does not directly correlate with the adsorption capacity (Figure 7.29). For instance, samples ACF-120-CR and ACF-60-CR exhibit large micropore surface areas but display moderate MNZ adsorption capacities.

The apparent specific surface area (S_{BET}) trend is similar to that of the micropore volume (Figure 7.30). This similarity is expected, considering that the micropores are the main contributors to the specific surface area.

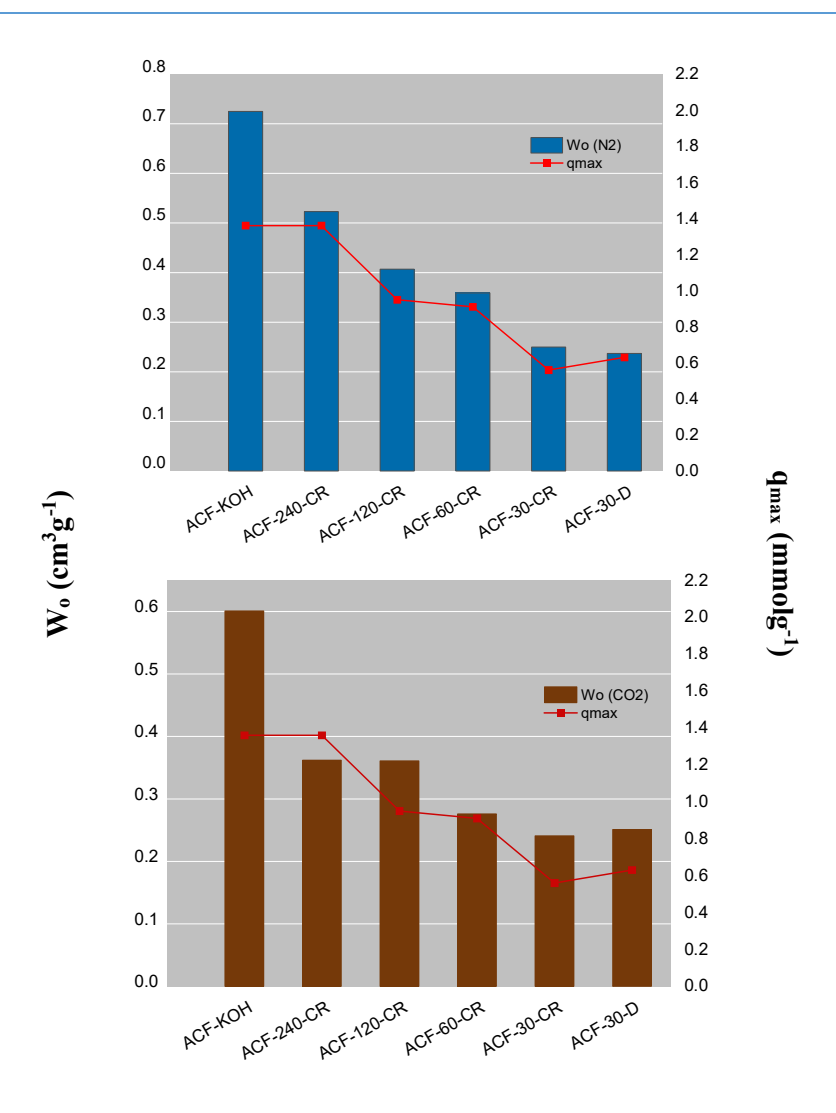


Figure 7.28 Correlation between the MNZ adsorption capacities and the micropore volumes, calculated by the DR formulism applied to N₂ and CO₂ adsorption isotherms.

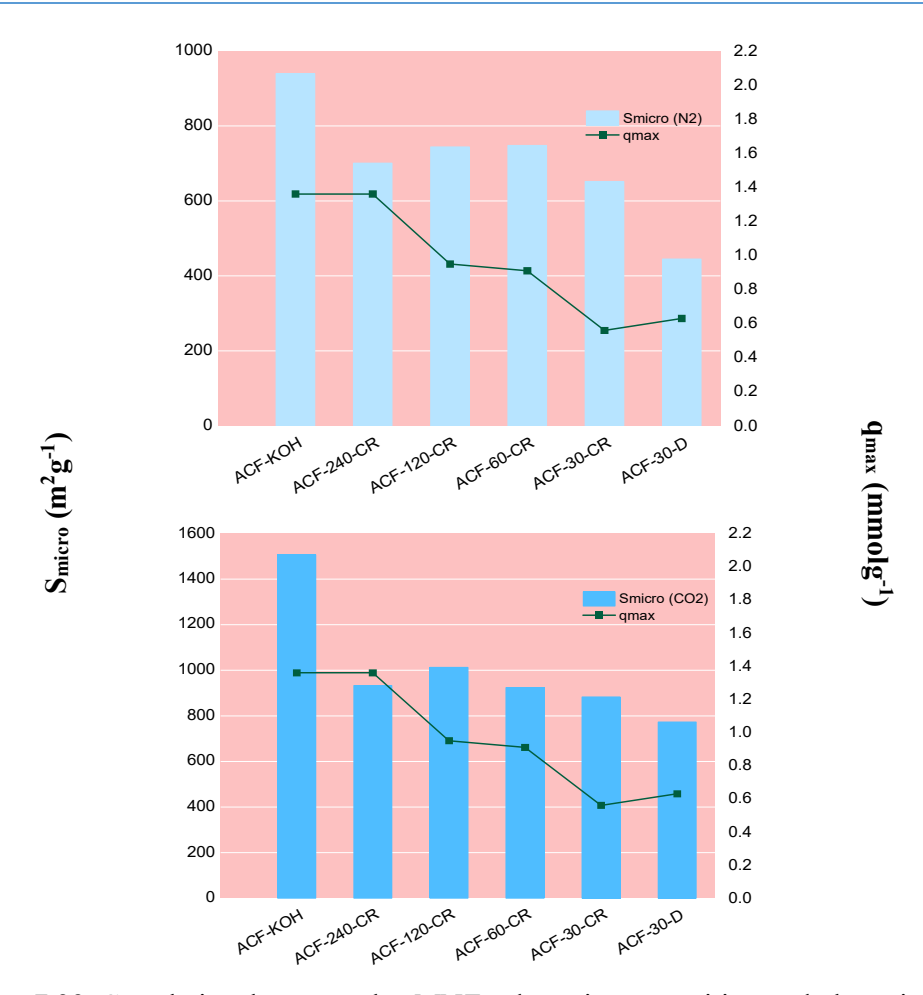


Figure 7.29 Correlation between the MNZ adsorption capacities and the micropore surface area calculated by the DR formulism applied to N₂ and CO₂ adsorption isotherms.

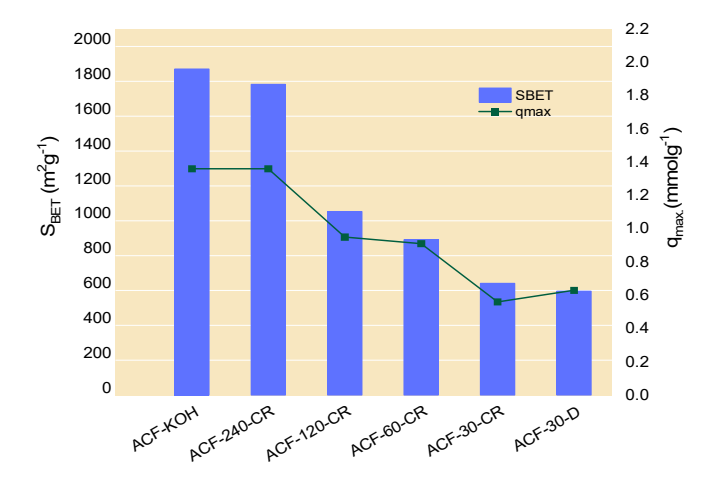


Figure 7.30 Correlation between the MNZ adsorption capacities and the specific surface area (S_{BET}) calculated by the BET equation from the N_2 adsorption isotherms.

In this scenario, when comparing the uptake at an equilibrium concentration of 0.1 mmol L⁻¹ with the pore volume (Figures 7.31 a, b, c and d), clear correlations are observed for pores diameters of 1.5 nm and 2.0 nm (being more pronounced in the former). The fitting values (Table 7.9) confirm that there is no clear correlation between the MNZ quantity adsorbed and the volume of pores smaller than 0.7 nm. Given its size and, more notably, its shape, this outcome is to be expected. As previously mentioned, MNZ is planar only in the imidazole ring, resulting in a smaller interaction area compared to SMX. To better clarify this dependence between the MNZ uptake at specific equilibrium concentrations and the pore sizes, contour maps with the determination coefficients were created (Figure 7.32). Obtained representations confirm the strongest correlation between the pores with diameters larger than 1.5 nm for equilibrium concentrations of 0.1 mmolL⁻¹ onwards, suggesting that adsorption primarily occurs within that specific pore size range.

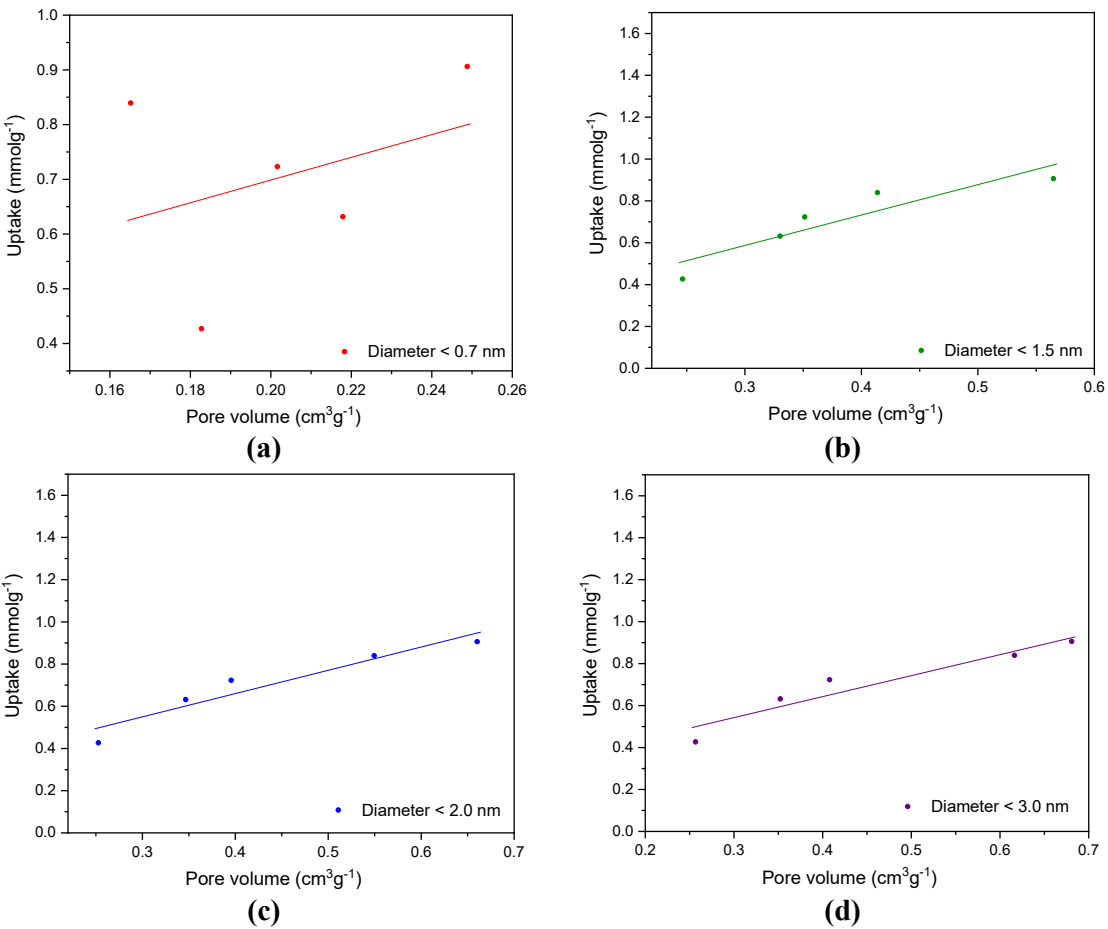


Figure 7.31 MNZ uptake for equilibrium concentrations of 0.1 mmolL⁻¹ as a function of the volume of pores below (a) 0.7 nm, (b) 1.5 nm, (c) 2.0 nm, and (d) 3.0 nm.

Table 7.9 Fitting parameters for the MNZ uptake for Ceq 0.1 mmolL⁻¹ as a function of the volume of pores plots for 0.7, 1.5, 2.0 and 3.0 nm.

	0.7 nm	1.5 nm	2.0 nm	3.0 nm
\mathbb{R}^2	0.1266	0.8414	0.9124	0.9115
RSS	0.1236	0.0224	0.0124	0.0125

The contour displays (Figure 7.32) for the uptake of MNZ differs from that shown for SMX (Figure 7.20), where the maximum determination coefficients were obtained for pores between 1.5-3 nm regardless of the equilibrium concentration. Conversely, for MNZ, low determination coefficients are obtained for low equilibrium concentrations in solution.

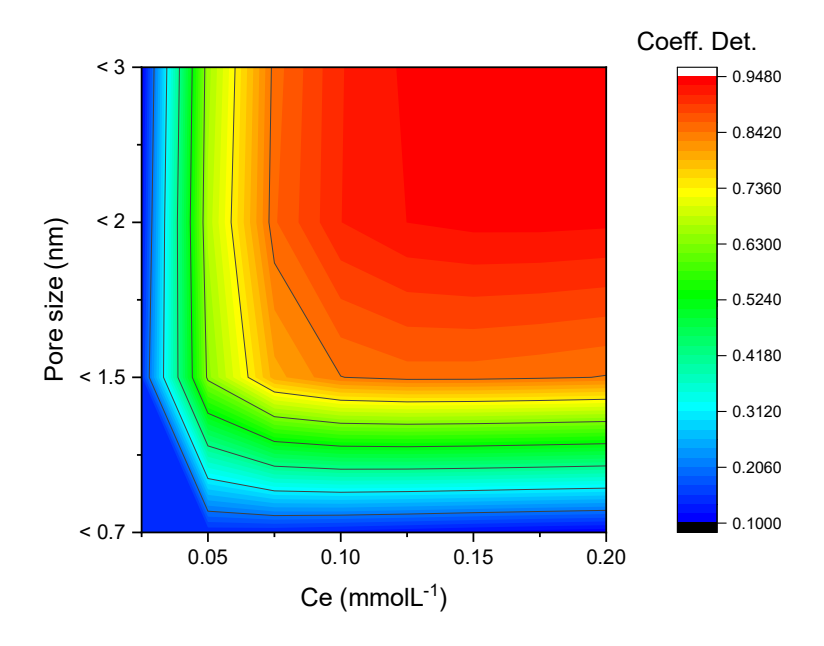


Figure 7.32 Contour plot of the coefficient of determination of the uptake of MNZ at various equilibrium concentrations and pore sizes.

The next plot (Figure 7.33) shows the kinetic operating lines of MNZ at two different initial concentrations compared to the equilibrium adsorption data. The lines cross paths at the equilibrium concentration in all cases, demonstrating that the isotherms were recorded under similar kinetic conditions.

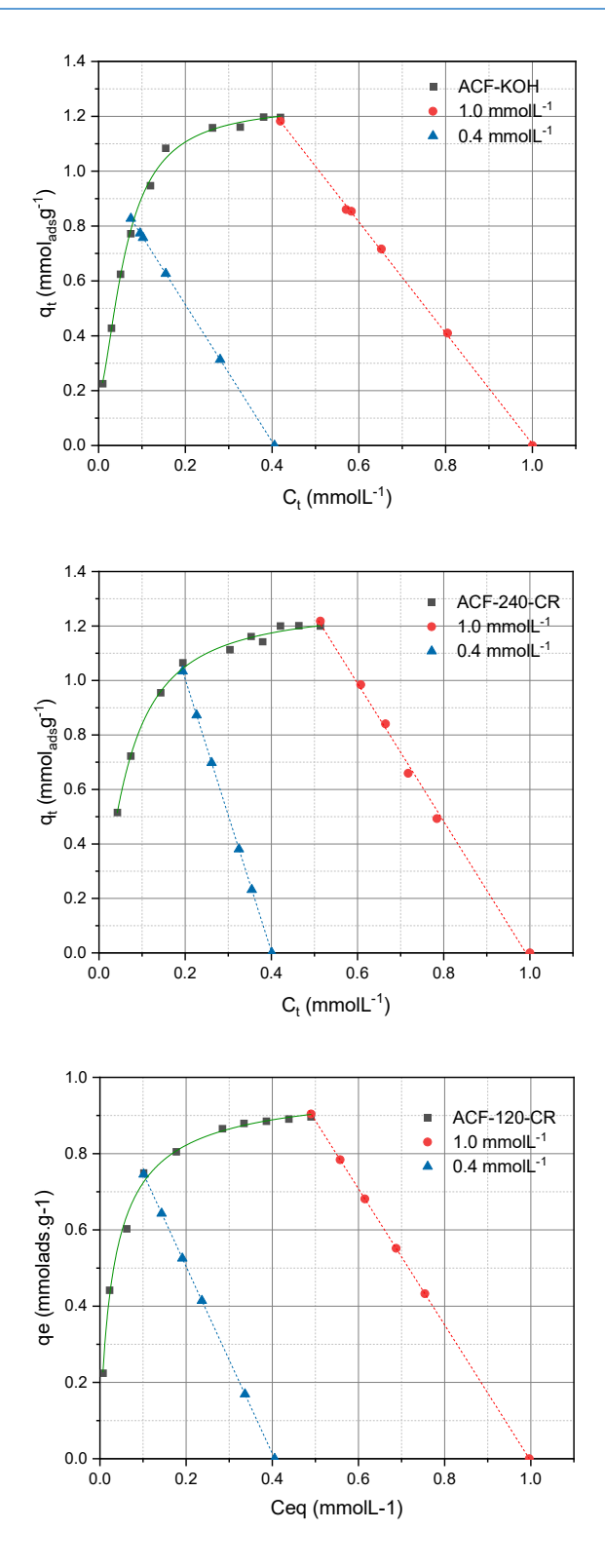


Figure 7.33 Representation of the operating lines (dotted lines) from the kinetic data on the equilibrium adsorption isotherms for samples ACF-KOH, ACF-240-CR, and ACF-120-CR, for the adsorption of MNZ.

7.3.3 AMP adsorption thermodynamics

The AMP molecule is the smallest of the three tested with a pKa = 9.4; therefore, as already mentioned, the molecule remains neutral during the experience. For experimental reasons, the selected initial concentrations for this drug ranged between 1 and 11.5 mmolL⁻¹. The equilibrium adsorption isotherm of AMP shows a similar profile to those reported for MNZ and SMX on sample ACF-30-D (Figure 7.34), with the exception that the trend line was calculated using a growth/sigmoidal function with a logistic model applying the Levenberg – Marquardt iteration algorithm by using Origin Pro. The AMP uptake was larger than that recorded for SMX and MNZ for this adsorbent.

The adsorption fitted a Langmuir model by reported works (Sajid et al. 2022). The feature that captures the attention is the Langmuir maximum adsorption capacity since it is more than three times bigger than SMX and more than five times MNZ (Table 7.10). There is more than one factor that favours the uptake. For example, this material, ACF-30-D, is a very short hollow fibre, which improves the interconnectivity, making it easier to reach the adsorption site. In addition, this molecule is smaller than the previous one and has a more straightforward structure. However, it contains a benzenic ring, allowing the π - π interactions; in addition, OH and NH groups that can establish H-bonds with the adsorbent.

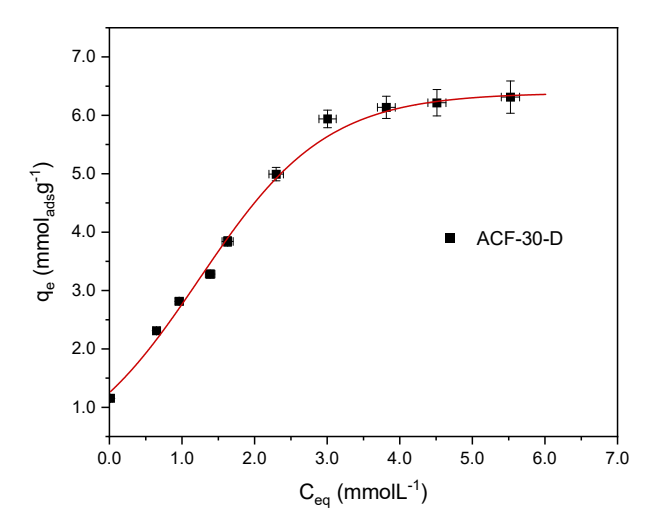


Figure 7.34 AMP adsorption isotherms for ACF-30-D, fitting data in Annex I.

Table 7.10 Isotherms fitting comparison for SMX adsorption onto ACF obtained under physical activation under Diffusion control.

Sample ACF-30D	Sam	nle	A(TF-	30	D
----------------	-----	-----	----	-----	----	---

Langmı	Langmuir Freundlic		lich Elov		h
K_L (Lmmol ⁻¹)	0.79	K_F (mmolL ⁻¹) ⁻ⁿ	3.53	K_E (Lg ⁻¹)	4205
$q_{max.}$ (mmolg ⁻¹)	7.78	n	0.311	$q_{max.}$ (mmolg ⁻¹)	0.150
adj-R²	0.9144	adj-R ²	0.8926	adj-R²	0.5558
X^2	0.0049	X^2	0.03317	X^2	0.6253
RSS	0.0395	RSS	0.2654	RSS	5.0027

The pH remained rather constant during the adsorption experiences, as depicted in Figure 7.35. This behaviour is expected during adsorption as the deprotonation of AMP is established at a higher pH than that used in our operating conditions.

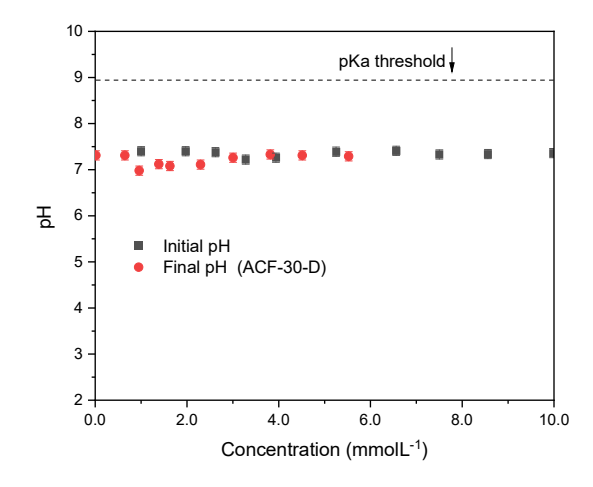


Figure 7.35 Evolution of the solution pH at different pharmaceutical compound concentrations before (black squares, initial concentration) and after the adsorption for sample ACF-60-D (red circles) (20 mg of adsorbent per analysis).

7.4 Ionic strength studies

The ionic strength (IS) plays a significant role in adsorption processes as it can alter the solvent structure, thereby impacting the interactions between the adsorbate and the adsorbent. In the case of polar solvents like water and for molecules such as SMX and

MNZ, the occurrence of other charged species can influence the adsorption. To investigate this effect, the equilibrium uptake was evaluated at two concentrations (0.5 and 0.8 mmol L¹) in the presence of an ionic salt (see Chapter IV, section 4.4.5). The results are shown in Figure 7.36 for sample ACF-KOH as an example (all the series of samples followed a similar behaviour). As seen, the presence of NaCl in the solution decreased the uptake of MNZ, although the effect was less remarkable than in the case of SMX (for which the adsorption was almost depleted). NaCl is a structure-making salt consisting of small ions that increase the cohesive energy in water due to their strong interactions with water dipoles (Endo et al. 2012). For the case of MNZ and SMX, the presence of NaCl is expected to increase the cohesive energy between these molecules and their respective solvation spheres. This phenomenon stabilises the molecule in the solution; this effect is known as salting-in.

For MNZ, the uptake decreases in the presence of the salt, and this effect can be directly correlated to the salt concentration (Figure 7.36). In the case of SMX, a strong salting-in effect is observed, which may be attributed to the charged structure of this molecule in solution (compared to MNZ, which is mainly in its neutral form). Thus, from a thermodynamic point of view, it is more favourable for SMX to stay in the bulk solution, which results in a sharp decrease in adsorption.

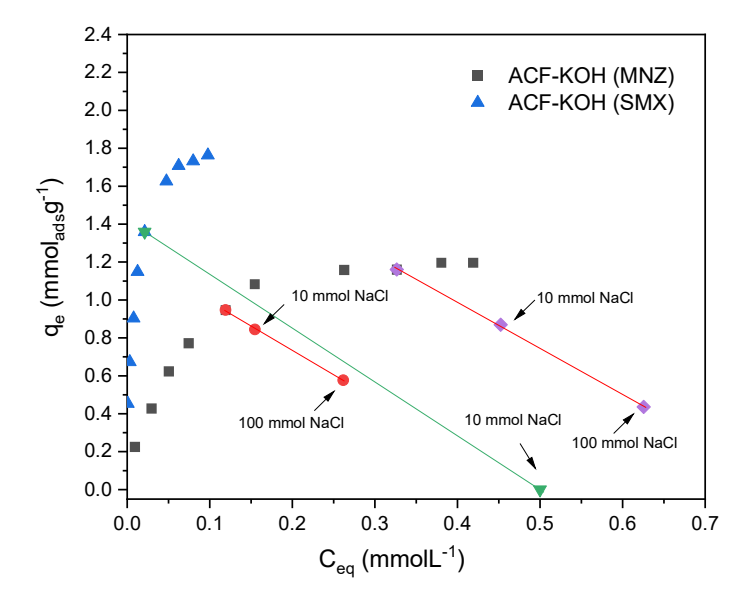


Figure 7.36 Equilibrium adsorption isotherms of SMX and MNZ on sample ACF-KOH, showing the response in solutions with varied ionic strength: NaCl 10 and 100 mmol.

AMP's adsorption exhibits similar characteristics to MNZ's. Both molecules remained neutral during the adsorption process and displayed the same response in the presence of charged ions in the solution (Figure 7.37). Hence, a similar analysis to the one conducted for MNZ would be appropriate for the adsorption of AMP in solutions of increasing ionic strength.

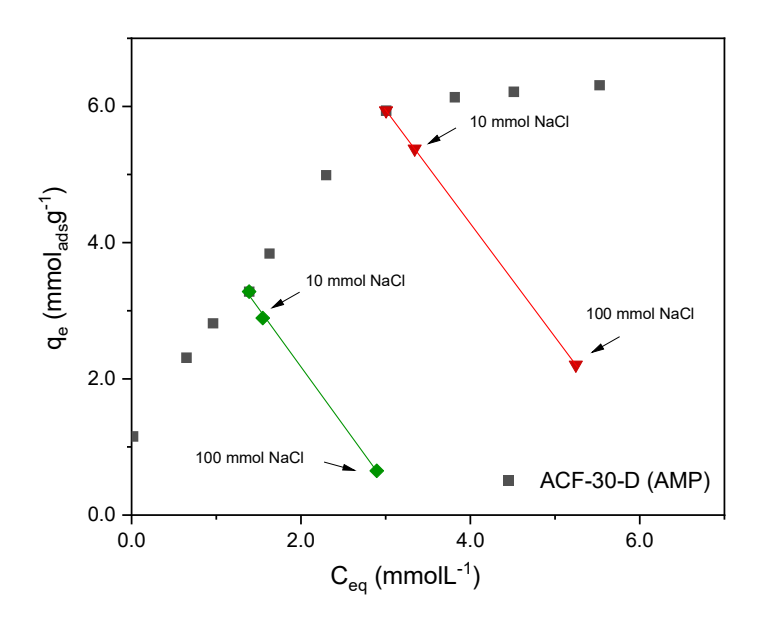


Figure 7.37 Equilibrium adsorption isotherms of AMP in sample ACF-30-D, showing the response in solutions with varied ionic strength: NaCl 10 and 100 mmol.

7.5 pH variation studies

Another important characteristic to consider is the impact of pH changes on the adsorption process. According to current national regulations in Uruguay, effluent discharges are permitted within a pH range of 5.5 to 9.5. This pH's value range could potentially influence the adsorption process. To investigate this, two concentrations from the isotherm were selected for testing (the same as those used to analyse the ionic strength), with the pH adjusted by adding NaOH 0.1 M. The amounts added were on the order of μ L, ensuring that the ionic strength of the solution was not affected.

The influence of pH on the process was examined within the range of 5 to 10. As depicted in Figures 7.38 and 7.39, variations in pH notably affected the adsorption of SMX, whereas the adsorption of MNZ and AMP remained relatively unaffected. As discussed above, the solution pH is largely affected by the concentration of SMX in the solution (Figure 7.21) due to the release of protons into the medium. However, the final

pH remains rather neutral when the carbon adsorbents are added to the solution due to the interaction of the ACFs in the aqueous medium. When the solution pH is increased by adding hydroxide anions, the uptake of SMX decreases. This behaviour was recorded for all the samples, regardless of their porosity and/or composition differences. This may indicate the importance of the electrostatic interactions in the adsorption mechanism for this compound. Some hydroxide anions will react with the protons in the solution, thereby reducing the amount of protons available for the molecule to undergo adsorption.

On the other hand, the adsorption of MNZ and AMP remained largely unaffected by the pH. Figures 7.26 and 7.35 depict the effect of the solution pH on the retention of SMX and MNZ. Therefore, the adsorption of both compounds is independent of the pH of the solution.

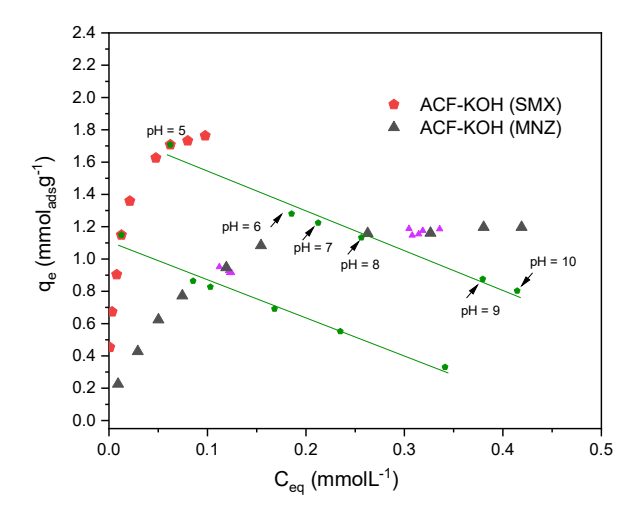


Figure 7.38 SMX and MNZ effect of the solution's pH on the adsorption capacity (for clarity reasons, the pH values were marked for one experience, while the others follow the same criteria).

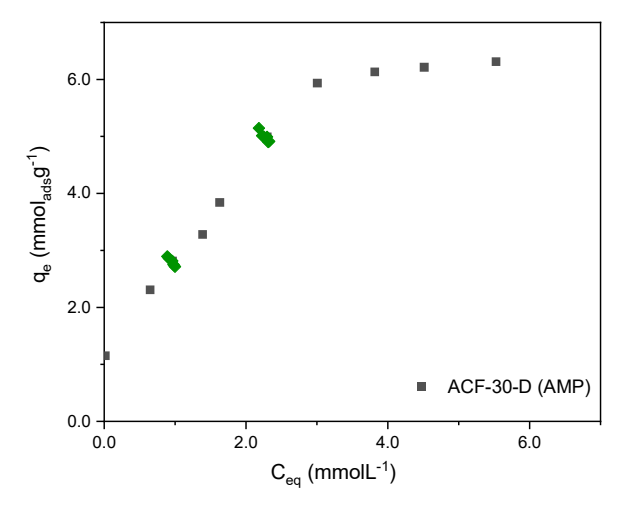


Figure 7.39 The effect of the solution's pH on the AMP's adsorption capacity.

7.6 Partial conclusions

The adsorption rate and equilibrium uptake of MNZ, SMX and AMP were investigated in the series of ACFs prepared by physical and chemical activation. All the compounds tested followed a Langmuir thermodynamic model at equilibrium conditions, indicating that the adsorbent possesses a uniform distribution of adsorption sites regarding its energy. The adsorption kinetics varied significantly depending on the morphology and textural characteristics of the material. Both Diffusion and PSO were found to govern the adsorption process, with intraparticle diffusion playing an important role in the initial stages of adsorption. ACFs with a relatively small specific surface area are effective adsorbents for the studied compounds, facilitating easy access for the compound molecules to the adsorption sites. In all cases, the initial concentration affected the adsorption kinetics. Specifically, diffusional phenomena dominate the adsorption kinetics at higher concentrations.

Depending on the nature of the pharmaceutical compound, electrostatic and/or dispersive interactions may be dominant, and the influence of the solution pH and ionic strength may be relevant. While the uptake of MNZ and AMP is independent of the solution pH, this was not the case for SMX, which showed a drastic decrease in the adsorption capacity with the pH increment. The retention of SMX was also significantly hindered by the presence of ions, whereas AMP and MNZ show reduced adsorption with increasing pH, although to a lesser extent. The roles of nitrogen and sulphur groups on the ACFs could not be resolved based on the recorded data. Further studies are required

to discriminate the contribution of different functional groups in the graphitic matrix (pyrrole, pyridine). These findings suggest a complex adsorption behaviour in real effluents containing a mix of compounds due to their differing responses to environmental conditions. This underscores the importance of studying binary compound mixtures (Chapter VIII). Implementing this approach as a tertiary treatment in the final stage of a WTP could yield successful results.

This adsorption process involves a combination of several interactions. A reversible and rapid process involving weak forces like Van Der Waals is established between the ACF and the drugs in solution (Figures 7.40 – 7.42). Hydrogen bonding between H from OH (for MNZ and AMP), N from the adsorbent, H from NH₂ (for SMX) and N from the adsorbent. Also, a certain degree of electrostatic attraction between the ACF surface and the deprotonated SMX cannot be discarded. Lone electron pairs from C and O at the ACF surface are delocalised to the SMX and AMP aromatic rings. They allow the connection between the compounds and the surface atoms, so the drugs are deposited on it. Finally, the π electrons from benzene rings present in the ACF interact with the π electrons present in the drugs molecules (SMX, MNZ and AMP) via π - π coupling.

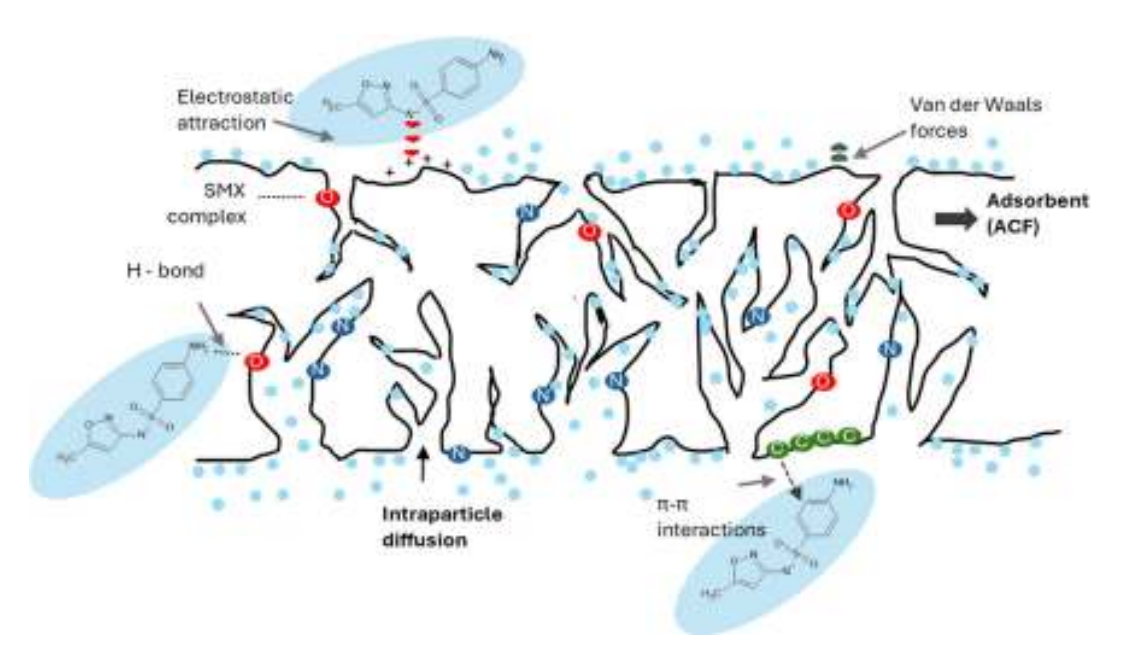


Figure 7.40 Schematic representation of the mechanisms involved in the SMX adsorption.

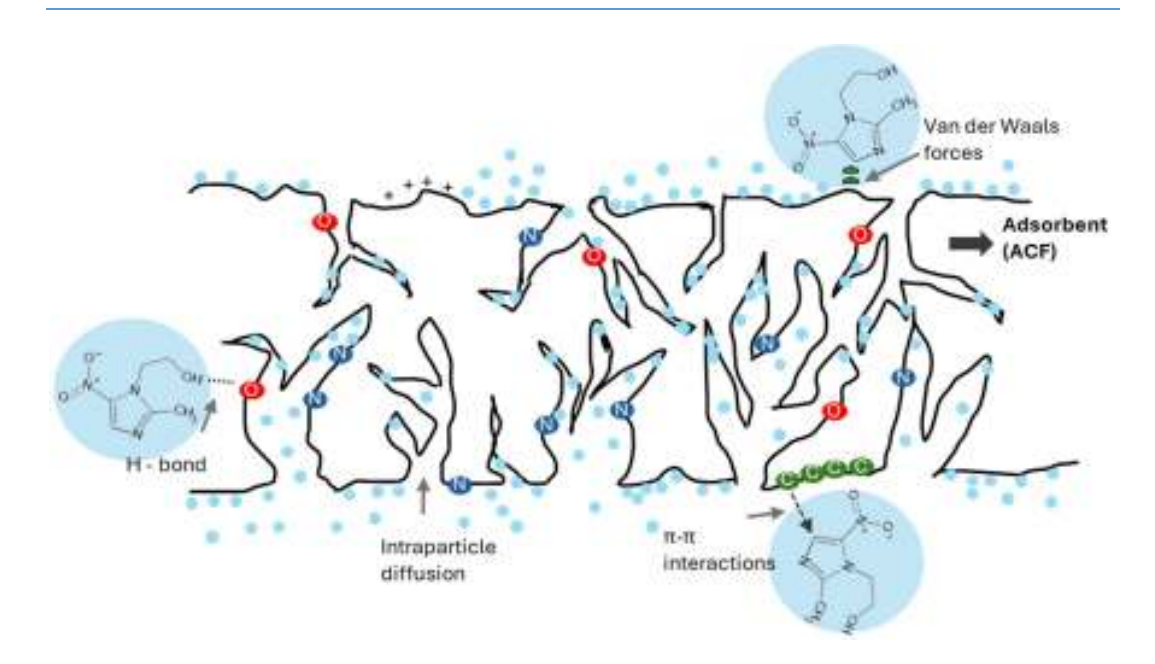


Figure 7.41 Schematic representation of the mechanisms involved in the MNZ adsorption.

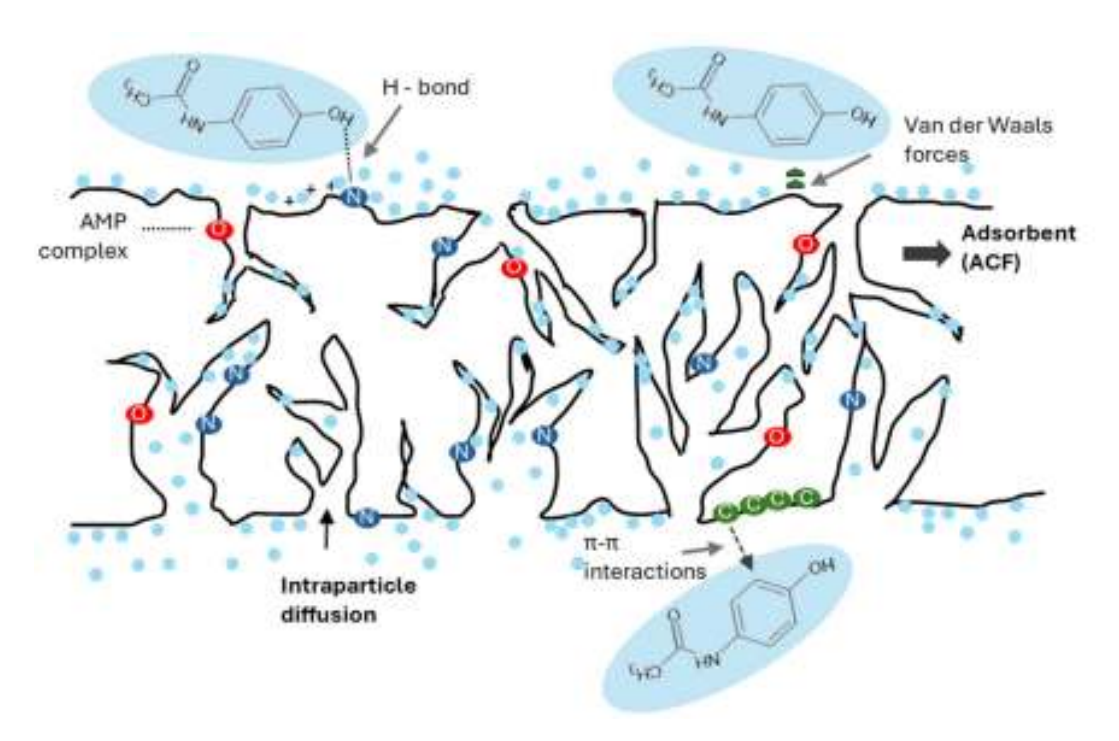


Figure 7.42 Schematic representation of the mechanisms involved in AMP adsorption.



"La mente científica tiene estas cosas. Vea usted, si no, a don Alberto Einstein. Tanto inventar prodigios y el primero al que encuentran aplicación práctica es la bomba atómica, y encima sin su permiso."

La sombra del viento

Carlos Ruiz Zafón

8.1 Adsorption in complex mixtures

While valuable, research conducted in monocomponent mixtures serves as an initial exploration into the governing principles of adsorption. However, to truly understand the behaviour of a specific component during adsorption, it is crucial to explore competitive effects when various pollutants are present in the medium. This comparative approach can offer valuable perspectives on the extended interactions and outcomes within the adsorption process, enhancing our understanding.

The competitive adsorption capacity of MNZ and SMX in mixtures was evaluated over samples AC-KOH, ACF-240-CR, ACF-120-CR and ACF-30-D. Their characteristics were previously detailed in Chapter VI, and their responses to adsorption in a single-component situation in Chapter VII. These experiments were conducted under identical conditions to those used for single-component solutions, ensuring a fair comparison. Subsequently, the data were rigorously analysed using several models that account for introducing a secondary pollutant in the system. This further enhances the reliability of our results.

For the comparative multi-component models, the percentage deviation (% D) between what the model predicts and the experimental data recorded was calculated according to the following expression (Equation 8.1) known as the Average Relative Error (ARE):

$$\%D = \left[\frac{1}{n} * \sum_{i=1}^{n} \left| \frac{q_{exp} - q_{pred}}{q_{exp}} \right| \right] * 100$$
 Equation 8.1

It should be noted that % D can acquire negative values, suggesting that the predicted values exceed those obtained through experimentation. This discrepancy may occur when the model fails to account for all phenomena during the adsorption process, resulting in predicted adsorption capacities higher than those observed in the experiment. This outcome is likely to be observed repeatedly when employing different competition models.

8.2 Adsorption experiences (1:1, molar ratio)

The initial experiments were designed for a 1:1 molar mixture of SMX and MNZ. The concentrations employed mirrored those utilised for the mono-component adsorption assays. In each case, the uptake of both pollutants from the binary mixtures was compared with the data recorded for the single-component solutions.

The following figure shows the uptake of SMX and MNZ for sample ACF-KOH in the 1:1 molar binary mixture and the single-component solutions at various initial concentrations (Figure 8.1). The uptake of MNZ by ACF-KOH is notably influenced by the presence of SMX in the medium. Interestingly, the uptake of SMX is impacted at lower initial concentrations, whereas at higher concentrations, its adsorption remains relatively unaffected (Figure 8.1, concentrations 0.8 and 0.9 mmolL⁻¹). The pH values observed during the experiment align with those documented for the adsorption of SMX in a monocomponent setup, showing almost the same behaviour (Figure 8.2). Thus, the same considerations were applied (see Chapter VII, section 7.3.1), wherein SMX released its proton to the medium for subsequent recovery through adsorption. As the observed variations closely resemble those found in the single SMX experiments, it can be inferred that the presence of MNZ does not impact the pH values. As a result, the pH is unlikely to affect the behaviour of SMX significantly. However, pH values differ remarkably from those recorded for monocomponent MNZ solutions after adsorption (Chapter VII, Figure 7.26). The molecule remained neutral according to its speciation diagram (Chapter VII, Figure 7.7); however, the pH evolution caused by the presence of SMX can influence the adsorption behaviour of MNZ. What is remarkable is that not only does the adsorption of MNZ decrease in a binary configuration, but for higher concentrations, MNZ is displaced by SMX (Figure 8.1, light blue bars). If we translate those figures to the pH evolution, it can be noted that for higher concentrations, the final pH reached values circa 6.8, where the presence of the anionic species of SMX reached 96 % according to its speciation diagram (Chapter VII, figure 7.5). This molecule configuration favours the adsorption of SMX against MNZ and, therefore, explains the latter's displacement.

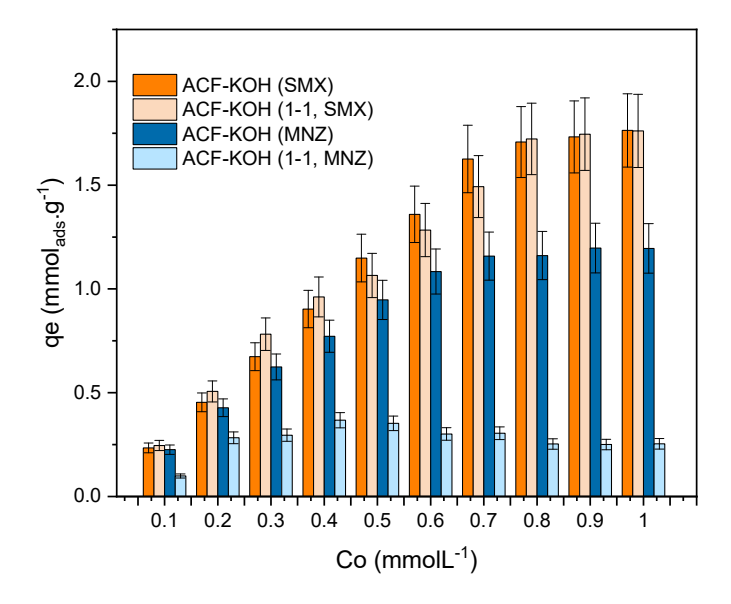


Figure 8.1 Comparative uptakes of SMX and MNZ in monocomponent solutions and equimolar (1:1) binary mixtures for sample ACF-KOH at various initial concentrations.

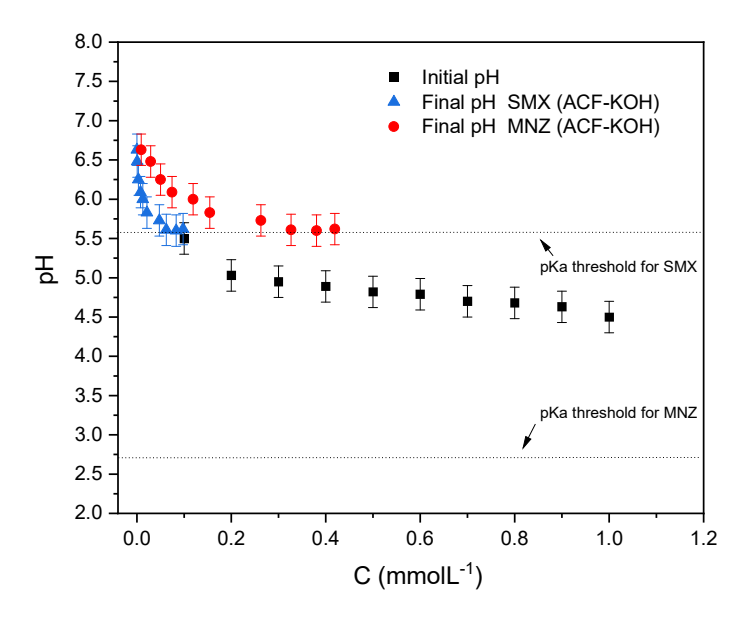


Figure 8.2 Evolution of the solution pH at different concentrations of the equimolar (1:1) binary mixture before (black squares) and after (blue triangles and red dots) reaching the adsorption equilibrium on sample ACF-KOH. 20 mg of adsorbent have been used for all the adsorption assays.

As discussed in previous chapters, samples ACF-240-CR and ACF-KOH display numerous similarities but present distinct morphologies. Whereas the former is fibrous, the latter resembles more of a granular material. The next figure shows the uptake of SMX

and MNZ for sample ACF-240-CR in the 1:1 molar binary mixture and the single component solutions at various initial concentrations (Figure 8.3). The overall trend observed for the uptake of both pollutants in the binary mixture in sample CF-240-CR closely mirrors that of sample ACF-KOH, different morphologies notwithstanding. However, there are slight variations concerning the uptake of SMX that decrease consistently regardless of the initial concentration. Nevertheless, this decrease in the uptake of SMX in the binary mixtures is less pronounced than the fall in the uptake of MNZ. The displacement of MNZ by SMX at high concentrations is recurrent. However, the evolution of the solution pH before and after the adsorption on sample ACF-240-CR (Figure 8.4) differs from that reported for sample ACF-KOH (Figure 8.2).

Although the overall trend is the same, higher pH values were obtained after the adsorption (ca. 6.5-7.5). Between pH 6.5-7.5, SMX is predominantly anionic (88 and 98 %, respectively), while MNZ retains its neutral molecular state. This suggests that the significant drop in the uptake of SMX for sample ACF-240-CR in the binary mixtures when compared with KOH may be linked to the morphology. This is not the case for sample ACF-KOH (where SMX uptake is less impacted).

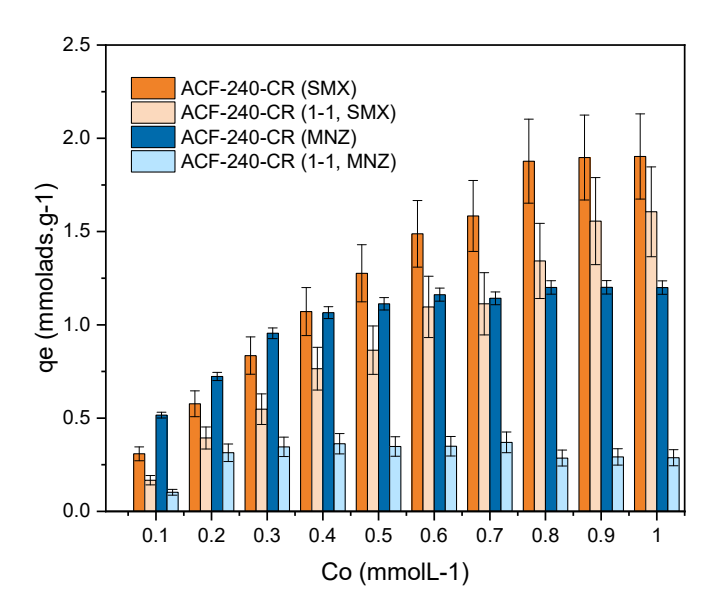


Figure 8.3 Comparative uptakes of SMX and MNZ in monocomponent solutions and equimolar (1:1) binary mixtures for sample ACF-240-CR at various initial concentrations.

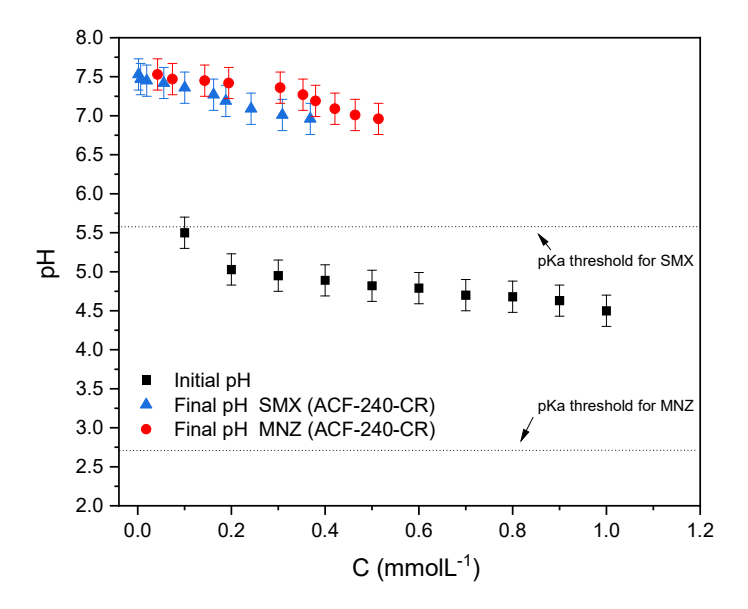


Figure 8.4 Evolution of the solution pH at different concentrations of the equimolar (1:1) binary mixture before (black squares) and after (blue triangles and red dots) reaching the adsorption equilibrium on sample ACF-240-CR. 20 mg of adsorbent have been used for all the adsorption assays.

For the case of sample ACF-120-CR, the uptake of both pollutants from binary solutions does not exhibit a clear trend but instead displays a random behaviour (Figure 8.5). It is important to note that the porosity of this material is characterised by a significant contribution of micropores, as opposed to the samples ACF-KOH and ACF-240-CR (both samples with 20 % mesopore volume). In general, the uptake of MNZ was more affected by the presence of SMX in the medium (still a sharp decrease in the uptake compared to monocomponent solutions).

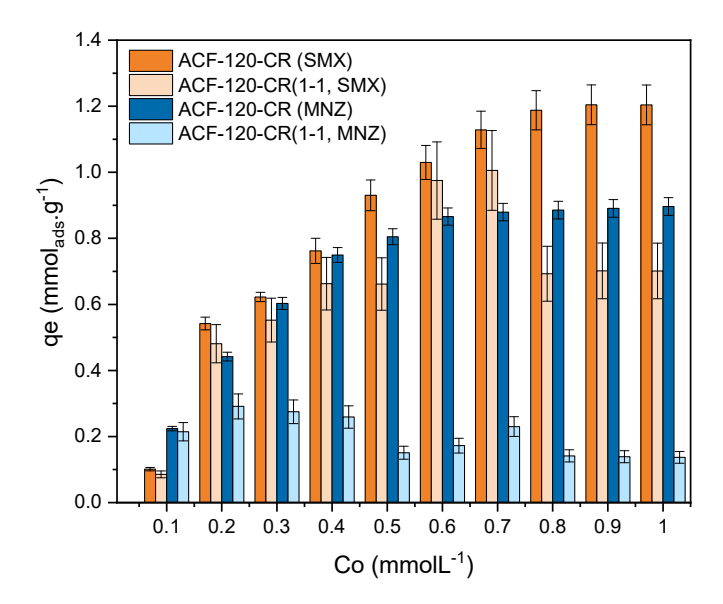


Figure 8.5 Comparative uptakes of SMX and MNZ in monocomponent solutions and equimolar (1:1) binary mixtures for sample ACF-120-CR at various initial concentrations.

The pH evolution before and after adsorption mirrors the trend observed for sample ACF-KOH, with high concentrations only restoring one pH point after adsorption, transitioning from 4.5 to 5.5 without recomposing the values registered for pure water, circa 6.5 (Figure 8.6). It should be noted the difference is in the final pH when the adsorption takes place from the monocomponent solution compared to the binary mixture. This can be explained by the higher concentration of SMX in the solution.

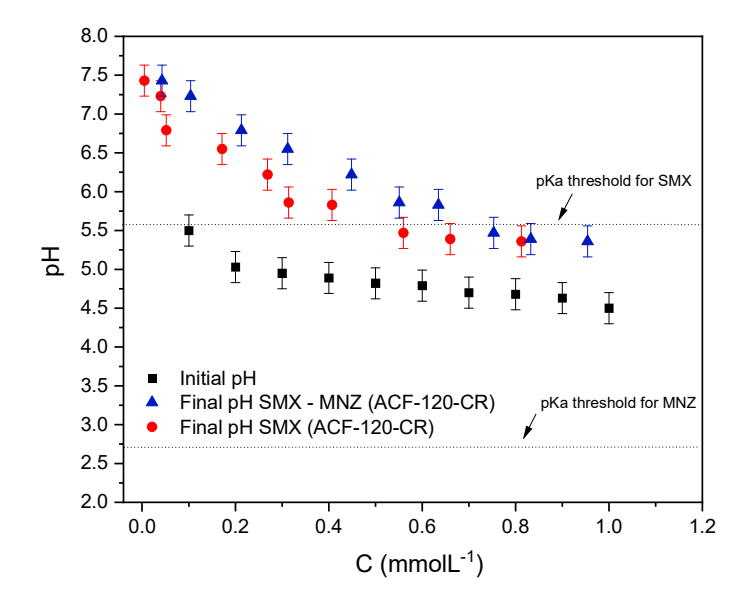


Figure 8.6 Evolution of the solution pH at different concentrations of the equimolar (1:1) binary mixture before (red dots) and after the adsorption on sample ACF-120-CR (triangles). 20 mg of adsorbent has been used for all the adsorption assays.

A different scenario emerges for sample ACF-30-D, where the adsorption of both compounds is significantly affected (Figure 8.7). Indeed, a sharp fall in the uptakes of MZN and SMX was observed from the binary mixtures. It also displayed a distinct morphology composed of hollow (see Chapter VI, Figure 6.22). The pH evolution aligns with the expected trend, showing an increase only in dilute solutions, where the small initial concentration of SMX and the quantity adsorbed help the system increase the pH value.

From a chemical perspective, sample ACF-30-D is similar to samples ACF-240-CR and ACF-120-CR (see Chapter VI, section 6.4). Thus, this factor cannot account for this different behaviour in the uptakes from the binary solution. However, regarding morphological features, it should be recalled that sample ACF-30-D was synthesized under a D regime; thus, it is more brittle than those obtained under the CR regime. Hence, it appears that adsorption is not favoured in hollow fibres.

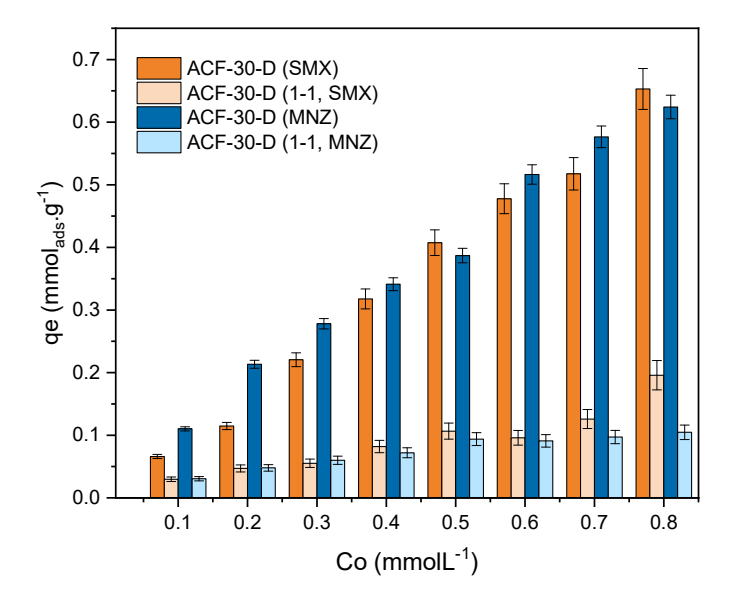


Figure 8.7 Comparative uptakes of SMX and MNZ in monocomponent solutions and equimolar (1:1) binary mixtures for sample ACF-30-D at various initial concentrations.

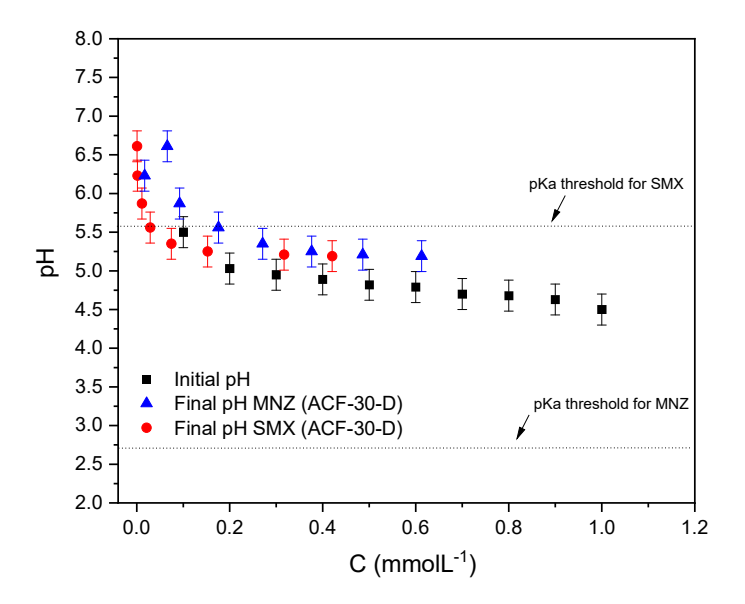


Figure 8.8 Evolution of the solution pH at different concentrations of the equimolar (1:1) binary mixture before (red dots) and after the adsorption on sample ACF-30-D (triangles). 20 mg of adsorbent has been used for all the adsorption assays.

After adsorption, these data were plotted in a three-dimensional graphic to give a general view of the equilibrium concentration and the respective adsorption capacities (Figures 8.9 and 8.10). From these representations, it can be seen how the uptake of SMX follows a general trend, where the quantity adsorbed increases with the increment of the

SMX initial concentration, leading to higher equilibrium concentrations (Figure 8.9). Furthermore, the adsorption capacities reach values between 88% and 98 % (for initial concentrations of 0.8, 0.9 and 1.0 mmolL⁻¹) compared to those recorded for a single-component solution for the ACF-KOH adsorbent (Figure 8.1). ACF-240-CR follows a similar trend. However, the adsorption capacities are smaller, accounting for circa 84 % (for the same initial concentrations) compared to the adsorption in a single component. On the contrary, the uptake of MNZ decreases dramatically (only 24 % of the value recorded in a single-component situation), and the adsorption goes to a detriment as the initial concentration increases (Figure 8.10).

Without further analysis, it is patent that the adsorption of MNZ is the most affected by the presence of the second pollutant. On the other hand, although the SMX adsorption data reflects an inevitable interference by the presence of MNZ, it does not show the extent of MNZ adsorption.

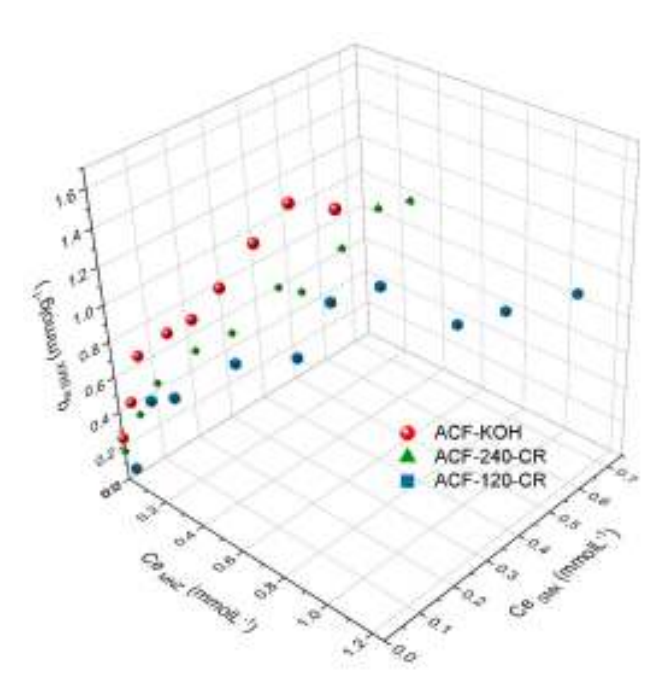


Figure 8.9 Evolution of the uptake of SMX in an equimolar (1:1) binary mixture for different adsorbents with the corresponding equilibrium concentrations of both pollutants.

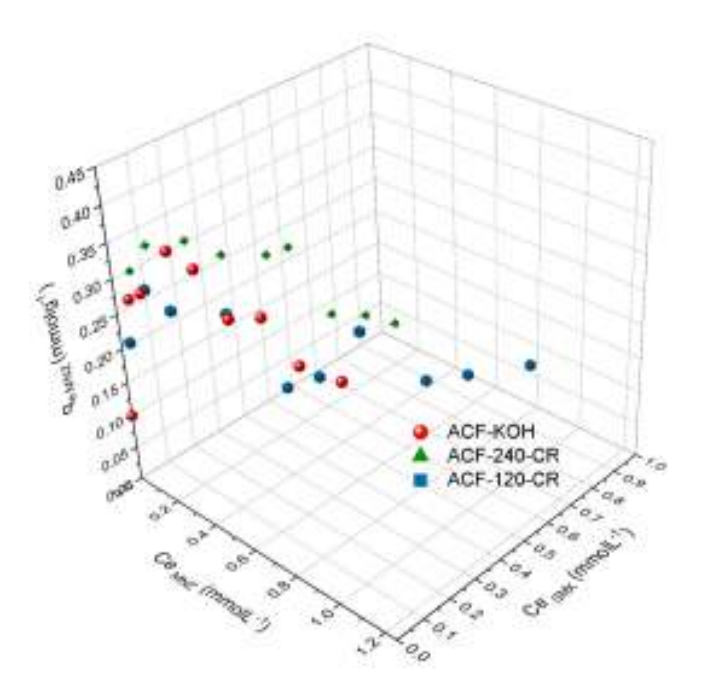


Figure 8.10 Evolution of the uptake of MNZ in an equimolar (1:1) binary mixture for different adsorbents with the corresponding equilibrium concentrations of both pollutants.

When analysing the pore size distribution, some remarkable differences among samples can be noted (Figure 8.11). For instance, between 0.7 and 2.0 nm, the accumulated pore volume for ACF-30-D is almost negligible compared with the rest of the samples. However, the differences in the uptake of both compounds can not be solely due to the corresponding pore volume. For example, while the total pore volume of sample ACF-120-CR is twice as much as ACF-30-D, the uptake of SMX is ten times bigger for the former (Figure 8.12). This behaviour is kept regardless of the initial concentration of both compounds. On the contrary, the uptake of MNZ does not show the same behaviour, pairing the trend with that recorded for the pore volume.

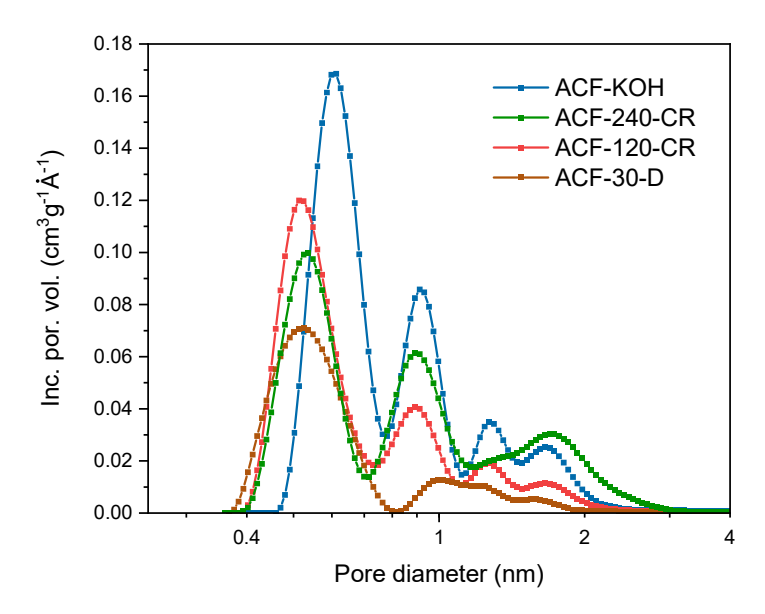


Figure 8.11 Pore size distribution for samples utilised for binary adsorption experiences, obtained from the 2D-NLDFT-HS method applied to the N_2 adsorption isotherms at -196 °C.

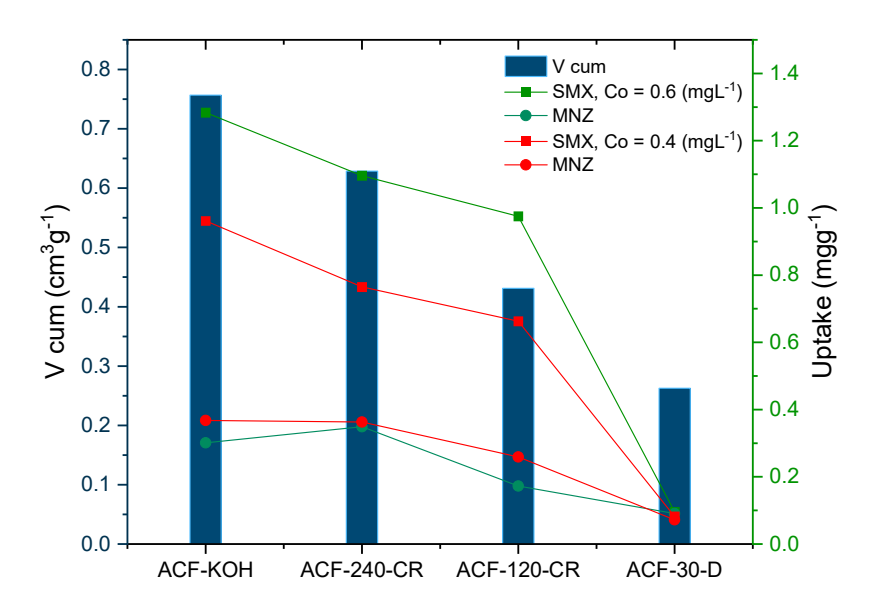


Figure 8.12 Correlation between the cumulative total pore volume and the uptake of SMX and MNZ in binary solutions (1:1 molar ratio, initial concentrations of 0.4 and 0.6 mgL⁻¹).

Since there is a remarkable difference in pore size distribution among samples, it is interesting to try to locate where the adsorption mainly occurs. Therefore, we plot the contour map of the uptake for both compounds (Figures 8.13 and 8.14). Independent of

the differences between plots, the region that covers 0.7 up to 2.0 nm is where the adsorption is most likely to happen. However, since there is no direct relationship between volume and uptake (shown by the correspondent plot, Figure 8.12), it can be assumed that the micropore volume is not the only parameter affecting the process. Comparing ACF-30-D with the rest of the samples, we must remember that this adsorbent material was subjected to a higher CO₂ flux, rendering it more brittle and most likely affecting its surface. This could explain why, despite the difference in pore volume recorded for ACF-120-CR and ACF-30-D, the uptake of SMX is much more affected for the latter.

The uptake of MNZ is located in an area restricted to pores between 0.7 and 1.5 nm (up to 2.0 nm, but its coefficient of determination decreases from 1.5 onwards) and for equilibrium concentrations from 0.125 mmolL⁻¹ (Figure 8.14). For SMX, the pore volume region is more extended, and the equilibrium concentrations involve the entire range (Figure 8.13). Therefore, the uptake of SMX is favoured compared to MNZ, which explains the sharp decline in MNZ uptake in the presence of SMX.

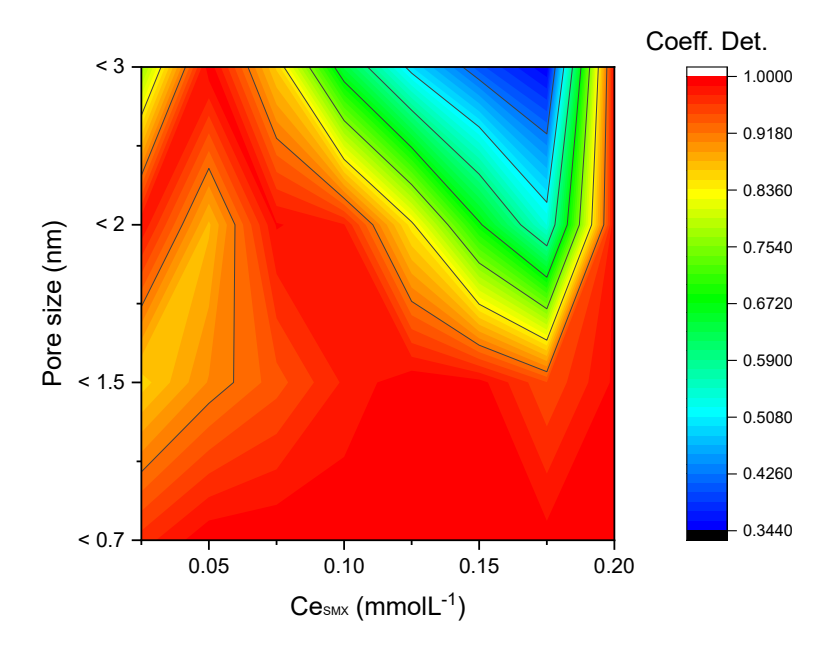


Figure 8.13 Contour plot of coefficient of determination for the dependence of the uptake of SMX in binary mixtures at various equilibrium concentrations and pore sizes.

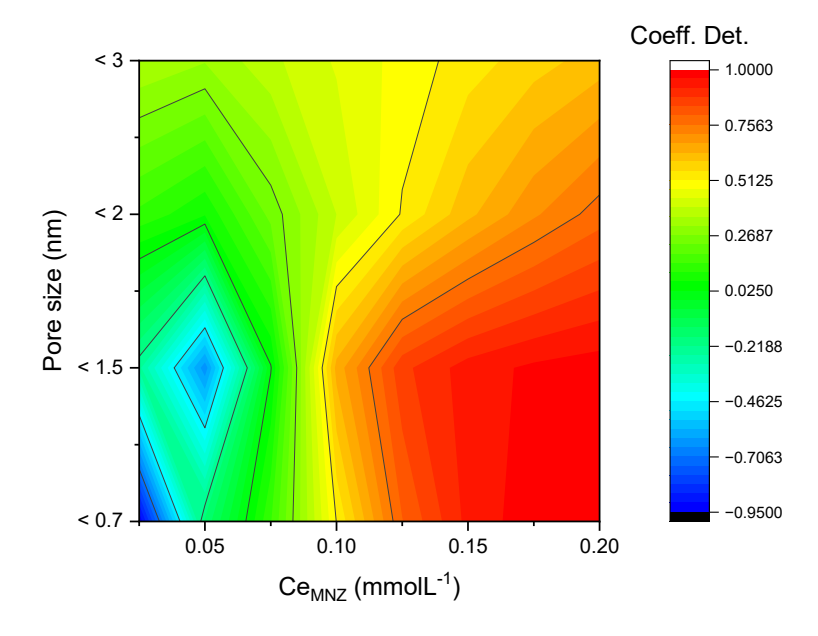


Figure 8.14 Contour plot of the coefficient of determination for the dependence of the uptake of MNZ in binary mixtures at various equilibrium concentrations and pore sizes.

8.3 Competition models

Since the differences in the competitive adsorption behaviour in the studied samples cannot be explained in terms of the material's surface chemistry, the discussion should focus on the adsorbent-adsorbate and adsorbate-adsorbate interactions. Hence, various theoretical models were used to determine the nature of the competition for the adsorption sites (or the lack thereof), and the results were compared with the experimental data. From the plethora of models described in the literature to analyse multi-component adsorption from solution, in this study, we opted for Langmuir-based models since the adsorption in single-component solutions consistently conformed to the Langmuir model.

8.3.1 Model for Non-competitive adsorption systems (NC)

This model assumes unspecific selectivity for the adsorption site in a multicomponent system. For a binary mixture, this implies independent adsorption sites for each adsorbate and no interference between them (see Chapter III, section 3.3.1). To assess if the competitive adsorption behaviour from the binary mixtures follows this model, the experimental molar uptake data is plotted against the predicted molar uptake data (Chapter III, equation 3.5). The deviation from the bisector line in the graphical representation is a tool to assess the model's correctness. Therefore, if the model assumption is correct, the experimental and predicted uptakes should be equal, and thus, the plot data would be located on top of the bisector line. Both axes should be scaled equally for the plot to make sense.

The following plot shows distinctive differences between the model predictions and the experimental data for all the samples (Figure 8.15). Differences are slightly less pronounced from sample ACF-30-D, yet the model largely overestimates the experimental uptakes for both compounds. This result indicates that the premises of this model are not correct. The adsorption sites for each pollutant are not independent (i.e., both compounds would be adsorbed in the same sites) and/or interactions between adsorbates would be applied.

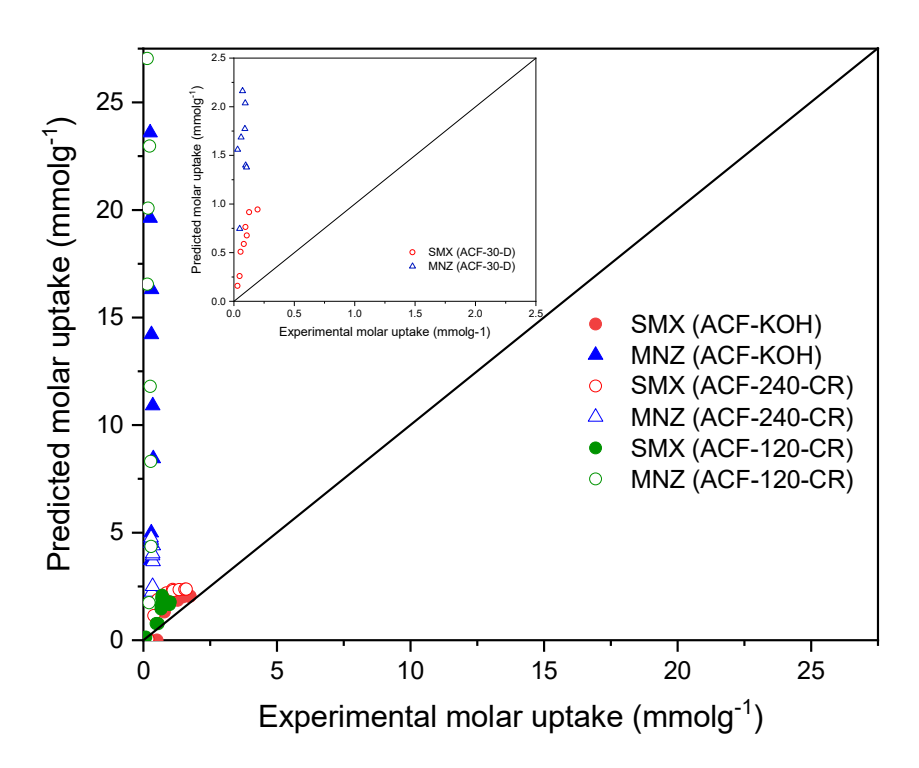


Figure 8.15 Comparison between the experimental and the predicted molar uptakes by the NC adsorption model for the adsorption of MNZ and SMX from equimolar (1:1) binary solutions for ACF-KOH and ACF-240-CR and ACF-120-CR samples, ACF-30-D sample (inset).

The following table shows the study systems' percentage deviation (% D) values (Table 8.1). As seen, more significant deviations were obtained for MNZ, which is

consistent with the fact that the uptake of this compound decreased more remarkably than that of SMX.

Table 8.1 Percentage deviation (% D) between the predicted and the experimental uptakes of SMX and MNZ in equimolar (1:1) binary mixtures.

ACF	Adsorbate	% Deviation
ACF-KOH .	SMX	-14.8
	MNZ	-3860.7
ACF-240-CR	SMX	-103.6
	MNZ	-819.2
ACF-120-CR	SMX	-94.5
7101 120 CK	MNZ	-9123.2
ACF-30-D	SMX	-571.7
	MNZ	-2320.2

8.3.2 Langmuir Multicomponent Model (LM)

This model was applied to the binary mixtures' experimental data, considering both expressions for similar (LM-s) and different (LM-d) adsorption capacities in single component solutions (Chapter III, equations 3.6 and 3.7). Chapter III explains that the LM model assumes that the adsorbate competition depends exclusively on the concentration ratio. Therefore, it can be applied to predict the adsorptive capacity of a given material in a multi-component system using the single-component parameters. The comparative plot of the experimental and predicted adsorption capacities for sample ACF-KOH reveals less dispersion than the previous (NC) model (Figure 8.16). This suggests that the occurrence of adsorbate-adsorbate interactions is important to understanding the competitive adsorption behaviour of these compounds and thus cannot be disregarded (as in the NC model). Still, the uptakes of MNZ and SMX are slightly overestimated. For both compounds, the uptakes predicted by the LM-s model are less accurate (higher deviation from the bisection line) than those predicted by the LM-d model.

Sample ACF-240-CR (Figure 8.16) showed a similar behaviour (better prediction for the **LM** model compared to **NC**); however, in this case, the uptake predicted for SMX is lower than that predicted for ACF-KOH, despite the similar experimental uptakes for

both samples. The **LM-s** model overestimates the uptakes of MNZ, while SMX's are underestimated for high adsorption capacities. The **LM-d** model is more precise for estimating MNZ uptakes (values are closer to the bisection line), but SMXs are overestimated over a larger range.

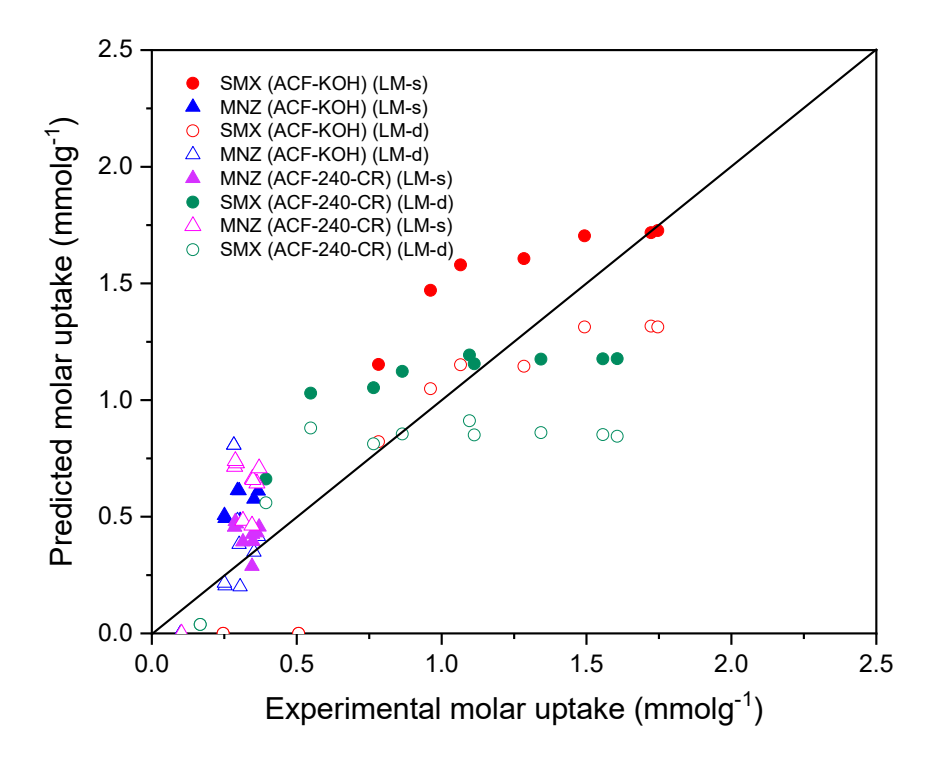


Figure 8.16 Comparison between the experimental and the predicted molar uptakes by the Langmuir Multicomponent adsorption model for the adsorption of MNZ and SMX from equimolar (1:1) binary mixtures for ACF-KOH and ACF-240-CR samples.

The comparative plot of the experimental and predicted adsorption capacities for sample ACF-120-CR showed that regardless of the model applied (LM-s or LM-d), the predicted values for MNZ are higher than the experimental ones (Figure 8.17). For SMX, the trend is the opposite (predictions underestimate the uptakes). In all cases, the data deviates (upper for MNZ and lower for SMX) from the bisector line, indicating that the interference impacting the competitive adsorption process cannot be solely attributed to concentration effects.

In the case of sample ACF-30-D (Figure 8.17), both predicted uptakes for SMX and MNZ are largely overestimated. The interpretation remains consistent with the previous

samples: the concentration of the components involved impacts the adsorption process, but it is not the sole phenomenon to be considered.

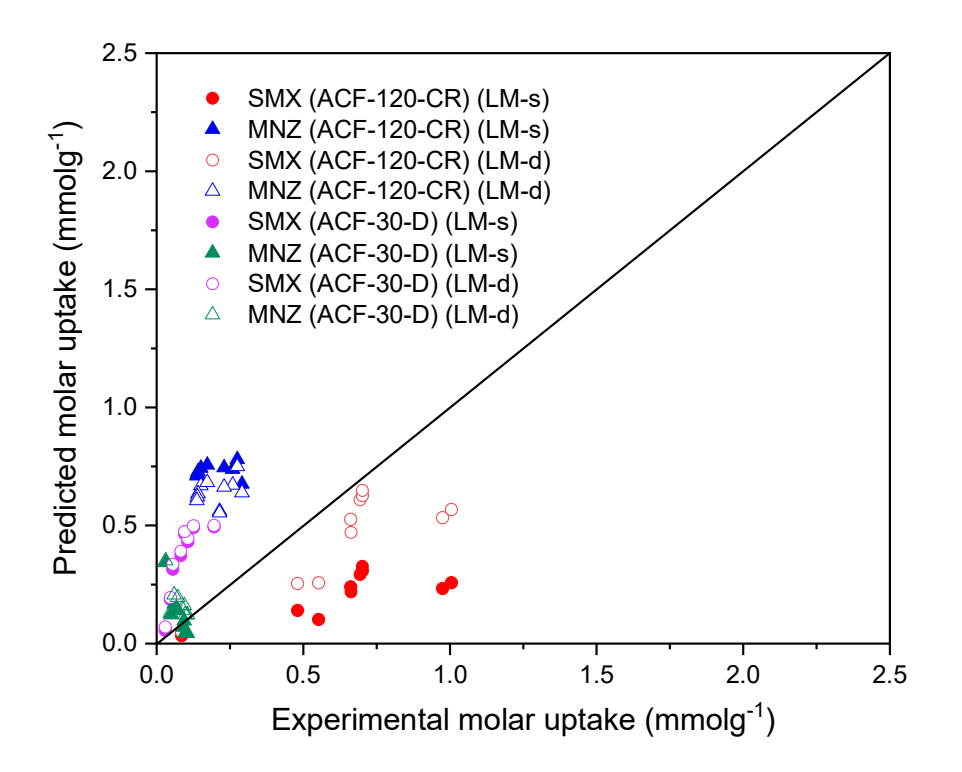


Figure 8.17 Comparison between the experimental and the predicted molar uptakes by the Langmuir Multicomponent adsorption model for the adsorption of MNZ and SMX from equimolar (1:1) binary mixtures for ACF-120-CR and ACF-30-D samples.

The percentage deviation between the model's predictions and the recorded experimental data is notably lower for the **LM** models than for the **NC** one described above, suggesting that these models' assumptions are closer to reality (Table 8.2).

Table 8.2 Percentage deviation between the experimental and the predicted molar uptakes of MNZ and SMX from equimolar (1:1) binary mixtures using the LM models for similar (s) and different (d) adsorption capacities.

ACF	Adsorbate	% Deviation	% Deviation
		LM-s	LM-d
ACF-KOH	SMX	1.5	27.7
	MNZ	-75.8	-13.5
ACF-240-CR	SMX	9.1	-12.2
	MNZ	-63.5	-10.6
ACF-120-CR	SMX	60.9	30.5
1101 120 011	MNZ	-244.8	-213.2
ACF-30-D	SMX	-312.3	-292.9
1101 30 B	MNZ	-165.7	-226.4

8.3.3 Modified Langmuir Multicomponent Model with discount factor δ (MLM δ)

The particularity of this model (Chapter III, equation 3.8) is that it considers the exclusion effect based on pore size, introducing a discount factor δ . For a binary mixture of compounds with different molecular sizes, only a fraction of pores are accessible to the larger compounds. This parameter is accounted for in the discount factor.

Considering that SMX is bigger than MNZ (see Chapter VII, sections 7.3.1 and 7.3.2), the adsorption (and any competitive effects) is expected to be conditioned by the differences in the accessibility to the pores of the adsorbents. The graphical representation of the experimental and predicted uptakes of MNZ and SMX with the **MLMô** model for the studied samples shows important differences depending on the samples (Figure 8.18). For ACF-KOH, the uptake of MNZ is rather well predicted, but this model largely underestimates that of SMX. In contrast, for sample ACF-240-CR, both SMX and MNZ predicted uptakes to be higher than the experimental ones (overestimated). A similar situation is obtained from the predicted uptakes of MNZ on sample ACD-120-CR (higher than the experimental one, Figure 8.18 inset). For sample ACD-30-D, the sample with

the lowest uptake for both compounds (Figure 8.18, inset), the predicted uptakes are still largely overestimated.

To understand the discrepancy between the predicted and the experimental uptakes with the $MLM\delta$ model in the rest of the samples, one must take into account the differences in porosity. Besides the size, the conformational structure of the molecules also should be considered to unravel the inaccuracy of the $MLM\delta$ model; while SMX has a coplanar structure, MNZ has a small sector that can be regarded as planar. Thus, the orientation of the molecule can have a significant effect on the adsorption.

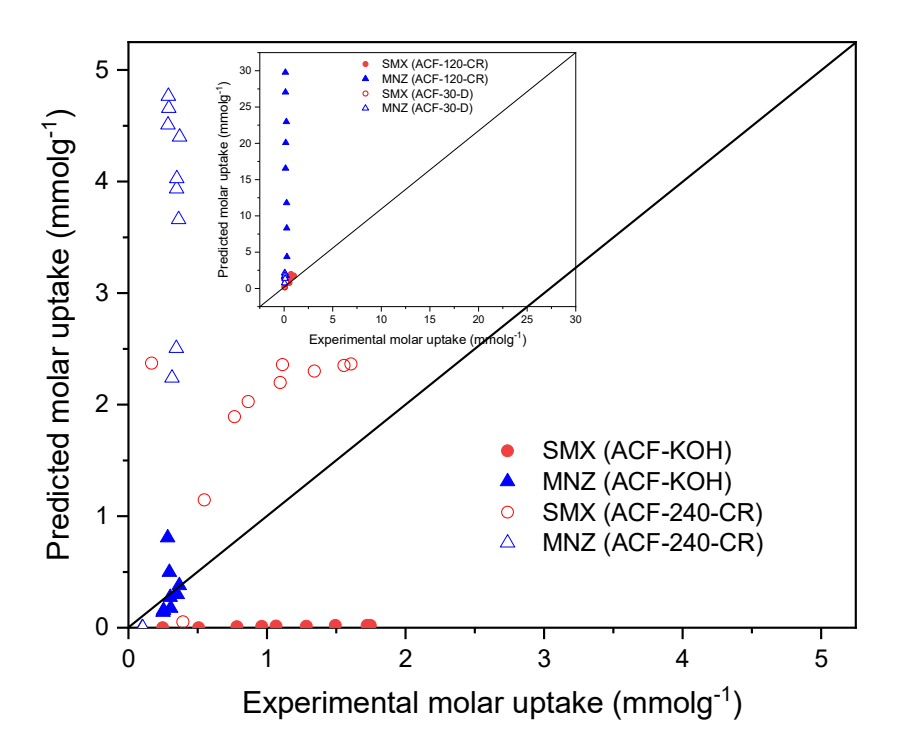


Figure 8.18 Comparison between the experimental and the predicted molar uptakes by the (MLMδ) adsorption model for the adsorption of MNZ and SMX from equimolar (1:1) binary mixtures for ACF-KOH and ACF-240-CR samples, ACF-120-CR and ACF-30-D (inset).

Table 8.3 Percentage deviation between the predicted adsorption capacity and the experimental data for the adsorption of SMX and MNZ from equimolar (1:1) binary mixtures using the (MLM δ) adsorption model.

ACF	Adsorbate	% Deviation
ACF-KOH -	SMX	99.0
	MNZ	-0.76
ACF-240-CR	SMX	90.7
	MNZ	5.74
ACF-120-CR	SMX	137.9
1101-120-CK	MNZ	-98.1
ACF-30-D	SMX	94.3
	MNZ	-394.9

8.3.4 Extended Langmuir Multicomponent Model (ELM)

This model (Chapter III, equation 3.9) assumes uniform pore size distribution of the adsorbent, thus leading to the competition of the adsorbates for the same adsorption sites (of equal energy). However, except for ACF-30-D (Figure 8.19), the **ELM** model application proved to be inadequate for the rest of the adsorbents, leading to incoherent equilibrium constant values ($K_L < 0$). This indicates that the assumption of a homogenous pore size distribution on those ACF samples cannot be sustained, which agrees with the characterisation of these materials (Chapter VI).

On the other hand, the application of the **ELM** model for sample ACF-30-D shows a random data distribution without a clear trend (Figure 8.19). As a general rule, the predicted uptakes of MNZ and SMX were underestimated (Table 8.4). This contrasts with the textural characterisation of this sample, dominated by a narrow distribution of pores in the micropore range. The discussion in Chapter VII about the nature of the pores that effectively participate in the adsorption demonstrates that the adsorption takes place at a specific pore width range. This discards the pore's width uniformity of this sample.

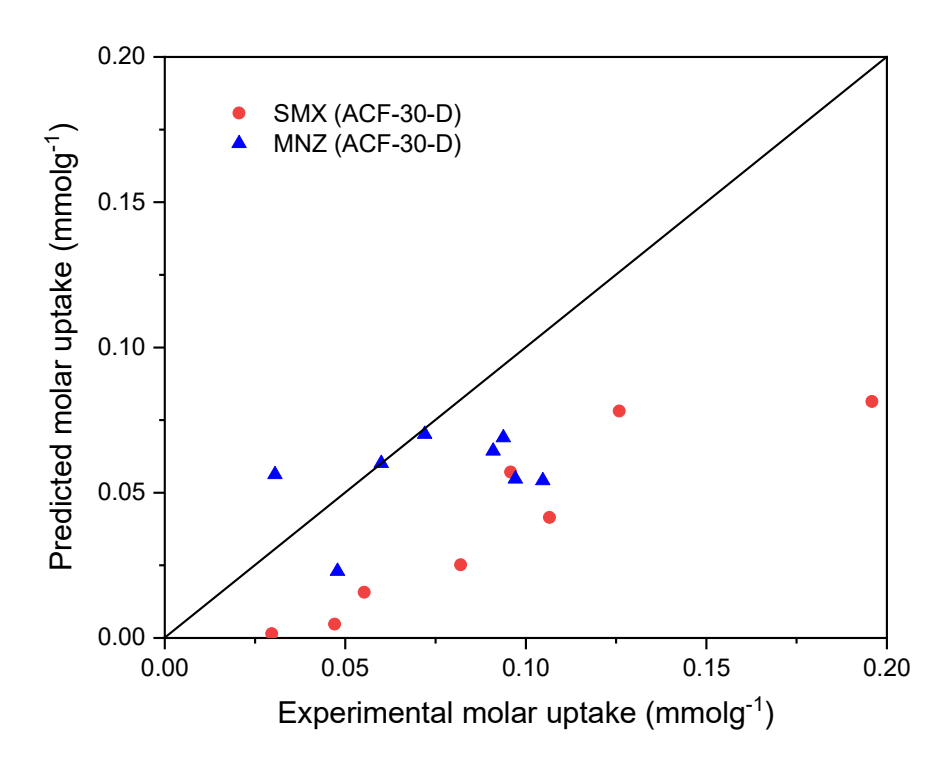


Figure 8.19 Comparison between the experimental and the predicted molar uptakes by the ELM adsorption model for the adsorption of MNZ and SMX from equimolar (1:1) binary mixtures for sample ACF-30-D.

Table 8.4 Percentage deviation between the predicted adsorption capacity and the experimental data for the adsorption of SMX and MNZ in equimolar (1:1) binary mixtures onto ACF-30-D adsorbent for (ELM) adsorption model (1:1 molar ratio).

ACF	Adsorbate	% Deviation
ACF-30-D	SMX	65.4
	MNZ	14.7

8.3.5 Modified Langmuir Multicomponent Model with Interaction Factor (\eta) (MLM $\!\eta)$

This model (Chapter III, equations 3.10 and 3.11) introduces an interaction factor $(\eta_i, \eta_j, \eta_{ij}, \eta_{ji})$ that considers the interaction effect between the adsorbate and the adsorbant and the interaction between adsorbates. This factor quantifies competition; the higher the values, the lower the surface's affinity for the adsorbate (Table 8.5). The parameters were

determined by iterating the objective function, where the parameters considered for each component contemplated the interaction component – surface and component 1 – component 2. The function was programmed in Origin using the Levenberg-Marquardt optimisation algorithm that minimises the least squares function.

The values of the interaction parameter $\eta_{i,j}$ representing the interaction between adsorbates or the influence of compound "i" on the compound "j" adsorption- are compiled (Table 8.5). The interaction established by this model involves several factors, including the hydration sphere, molecular sizes, ionic radii and the respective diffusivities (Acharya et al. 2023). The corresponding comparison between the experimental and predicted uptakes using these correction factors is shown in the following plot (Figure 8.20). In the case of sample ACF-KOH, the predicted uptake for SMX reveals a contribution of self-interaction ($\eta_{SMX, SMX}$ 4.03) to be considered in the adsorption process, albeit to a limited degree. The interaction parameter $\eta_{SMX, MNZ}$ was much higher (ca. 2.65 x10²³), evidencing that the presence of the MNZ substantially impacts the adsorption of SMX. Therefore, it can be inferred that the surface's affinity for SMX decreases due to the presence of the MNZ, and consequently, the uptakes of SMX are reduced.

Table 8.5 Interaction factors for each component depending on the ACF.

		η SMX,	η MNZ,	η MNZ,	η SMX,
Sample	Adsorbate	SMX	SMX	MNZ	MNZ
ACF-KOH	SMX	4.03			2.65E23
ACI-KOII	MNZ		2.43	5.11	
ACF-240-CR	SMX	4.65			1.05E22
ACI -240-CK	MNZ		6.58E-5	2.45E-4	
ACF-120-CR	SMX	0.24			1.29
11C1 -120-CR	MNZ		8.40E-2	1.21	
ACF-30-D	SMX	6.09E-3			2.13E21
	MNZ		106.32	28.44	

An opposite trend is shown for the ACF-30-D sample (Table 8.5), where the presence of MNZ less affects the uptake of SMX than the presence of SMX itself. This is the only sample where the uptake of SMX was deeply affected (Figure 8.7), with similar quantities adsorbed for both components. As stated before, this can only be accounted for by considering accessibility restrictions of SMX to the pores, which would be enhanced in the presence of MNZ.

When considering the interaction factors in MNZ adsorption, it is particularly intriguing that, except ACF-30-D, factors $\eta_{MNZ,\,MNZ}$ are higher than factors $\eta_{MNZ,\,SMX}$. This indicates that the adsorption is more influenced by the presence of MNZ itself $(\eta_{MNZ,\,MNZ})$ than by the proximity of SMX in the medium $(\eta_{MNZ,\,SMX})$ (Table 8.5). This means that the affinity of MNZ for the ACF adsorbents is less favourable than the interactions between MNZ molecules and between MNZ and SMX.

Furthermore, except for ACF-30-D (Figure 8.20 inset), the initial concentrations are somewhat independent (Figure 8.20). All data points related to the uptake are clustered within a specific plot region, regardless of the initial concentration.

On the other hand, it can be observed that in all the cases, the MLMη model adjusts better than the previous models. The best predictions of the MLMη model were obtained for SMX uptakes on samples ACF-KOH and ACF-240-CR. For MNZ, predicted uptakes were independent of the adsorption conditions regarding respective concentrations. We could assume that this predicament lies in the morphological and electrical aspects of the molecule. Despite variations in initial concentration, the uptakes exhibit similar quantities and reach a saturation point. However, upon closer examination of the uptakes versus initial concentration plots (Figures 8.1 and 8.3), the possibility of displacement of adsorbed MNZ molecules by SMX cannot be overlooked. The experimental uptake trends support this assumption. SMX adsorption increased at higher concentrations, whereas MNZ adsorption decreased and remained relatively stable across the concentration range.

The overall trend in the adsorption of SMX for samples ACF-120-CR and ACF-30-D shows some deviations compared to ACF-KOH and ACF-240-CR (Figures 8.20). The trend for MNZ exhibits significant differences, with data points distributed over a broader range than those for ACF-KOH and ACF-240-CR. Here, the main difference

among samples is the micropore contribution to the overall porosity. Samples ACF-KOH and ACF-240-CR account for ca. 20 % of mesoporosity, while samples ACF-120-CR and ACF-30-D are strictly microporous materials. The accessibility is expected to be more restricted in the micropores; thus, this affects the diffusion throughout the pores network, and the second compound's incidence is more evident.

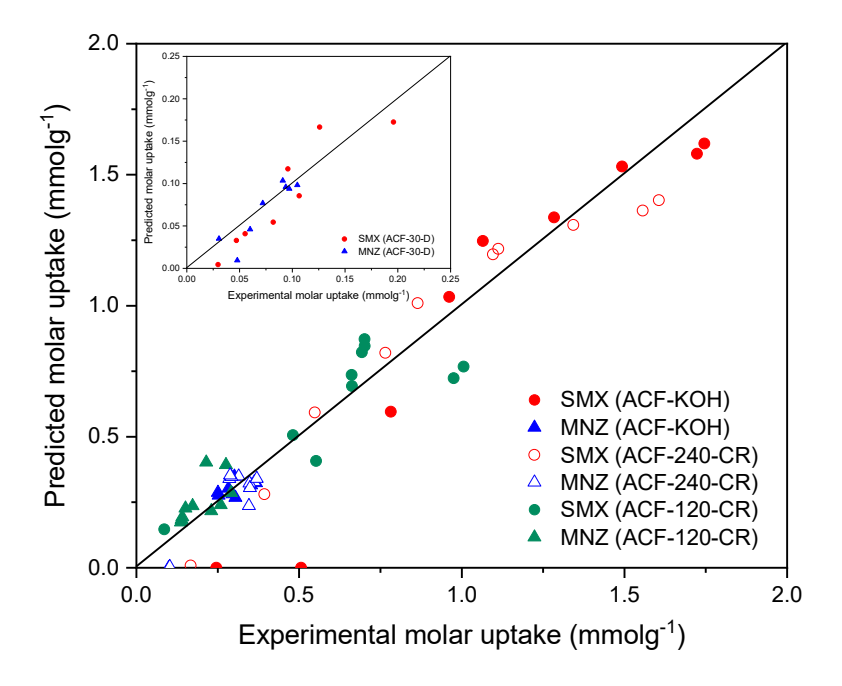


Figure 8.20 Comparison between the experimental and the predicted molar uptakes by the MLMη adsorption model for the adsorption of MNZ and SMX from equimolar (1:1) binary mixtures for ACF-KOH, ACF-240-CR and ACF-120-CR samples, ACF-30-D sample (inset).

Further analysis, calculating the deviation percentage between the experimental and predicted data, confirms the model's best fit (Table 8.6). As explained before, this model introduces several factors that influence the adsorption, which explains why it has a better fit than the previous models.

Table 8.6 Percentage deviation between the experimental and the predicted molar uptake by the (MLM η 0 adsorption model of MNZ and SMX from equimolar (1:1) binary mixtures for the studied samples.

Adsorbate	% Deviation
SMX	23.1
MNZ	10.3
SMX	10.0
MNZ	9.4
SMX	-7.9
MNZ	-29.9
SMX	18.9
MNZ	9.5
	SMX MNZ SMX MNZ SMX MNZ SMX MNZ

8.4 Comparison among models

When comparing the deviation percentages between the experimental data and the predicted values for the respective uptakes, the MLM η model (Table 8.7) best aligns with the experimental results. This outcome is not surprising, as the MLM η model is the only one that considers the adsorbent's respective morphologies, hydration spheres, and surface features of the adsorbent.

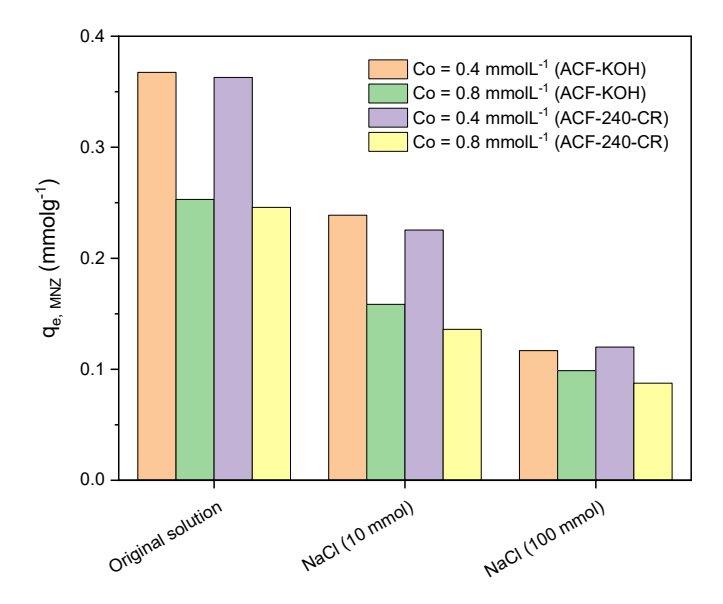
On the other hand, the remaining models, which are derived from the Langmuir model for gas adsorption, only consider the interaction between the adsorbent and the adsorbate, the presence of a monolayer, and crucially, do not account for the hydration sphere (Acharya et al., 2023). These previous models lack considerations for adsorption in the liquid phase. However, they are commonly used and are beneficial for adsorbing metal ions, where the molecule is viewed as a charged sphere. Introducing respective molecule morphologies adds complexity to the adsorption process, as the shapes of the components are less regular than expected from a sphere. This aspect enhances the interaction factor, making the MLM η model the most accurate and applicable choice.

Table 8.7 Comparison of the respective percentage Deviation (%D) for each model applied to the adsorption data obtained from the binary mixtures.

ACF	Adsorbate	NC	LM-s	LM-d	MLMδ	MLMη
ACF-KOH	SMX	-14.8	1.5	27.7	99.0	23.1
ACI-KOII	MNZ	-3860.7	-75.8	-13.5	-0.76	10.3
ACF-240-CR	SMX	-103.6	9.1	-12.2	90.7	10.0
ACI-240-CK	MNZ	-819.2	-63.5	-10.6	5.74	9.4
ACF-120-CR	SMX	-94.5	60.9	30.5	137.9	-7.9
7101 120 CR	MNZ	-9123.2	-244.8	-213.2	-98.1	-29.9
ACF-30-D	SMX	-571.7	-312.3	-292.9	94.3	18.9
	MNZ	-2320.2	-165.7	-226.4	-394.9	9.5

8.5 Ionic strength studies

The IS was found to play a crucial role in adsorption in monocomponent solutions (see Chapter VII). The next plot shows the uptake decay of SMX and MNZ at varied ionic strengths (Figure 8.21). As expected, the trends observed from the binary mixture follow a similar trend; the presence of an ionic salt also impedes the adsorption of SMX in mixtures. For MNZ, the ionic strength also diminished the uptake in the binary mixtures. Here, we can consider two factors contributing to the interference: the presence of the SMX and the increase in IS, which have a similar effect in reducing the amount of MNZ adsorbed.



8.21 Evolution of the SMX and MNZ uptake in the presence of various concentrations of sodium chloride.

8.6 pH variation studies

The working medium's pH value has already been proven to affect the uptake of SMX in monocomponent solutions (Chapter VII, section 7.5) by decreasing the adsorption capacity as the pH increases. In contrast, the adsorption of MNZ is practically unaffected.

As shown in the following plots (Figures 8.22 and 8.23), the response remains relatively the same for binary mixtures, discarding the detriment in the uptakes generated by the competence (Figures 8.22 and 8.23). The uptake of both compounds displayed the same behaviour as in monocomponent solutions. Thus, the pH variation does not alter the medium, provoking new interactions, at least in the range tested (5.5 - 9.5).

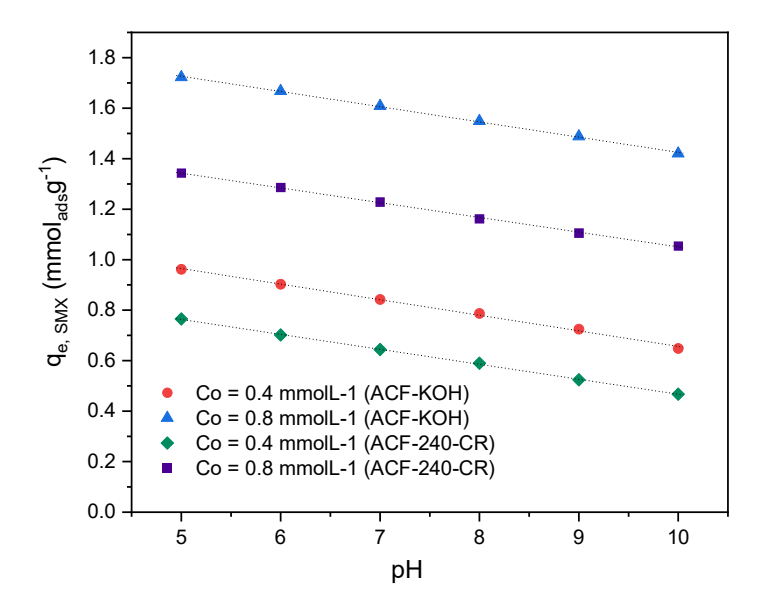


Figure 8.22 Evolution of the SMX adsorption capacity with the solution pH variation in equimolar (1:1) binary mixtures at different initial concentrations.

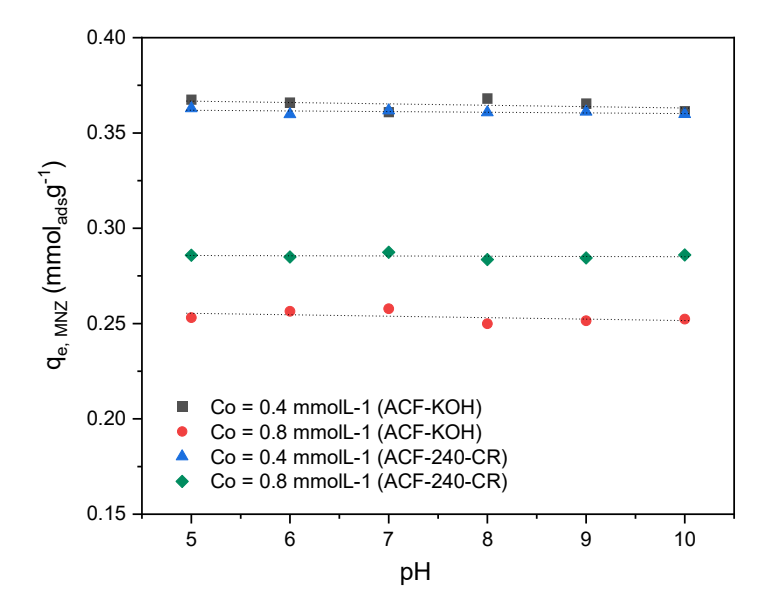


Figure 8.23 Evolution of the MNZ adsorption capacity with the solution pH variation in equimolar (1:1) binary mixtures at different initial concentrations.

8.7 Competition under other molar ratios

Various scenarios were tested by altering the molar ratio of the components to investigate the concentration effect on the overall adsorption process. The ACF-30-D adsorbent was chosen for this analysis to streamline the experimentation process. The different working scenarios were compared at one fixed concentration (ca. 0.2 mmolL⁻¹) for each compound and compared with the adsorption from monocomponent solutions (Figures 8.24 and 8.25).

Notably, the presence of MNZ appears to enhance the adsorption of SMX from the mixture at a ratio of 1:1.5 (SMX:MNZ) and beyond (Figure 8.25). Even some mixtures showed adsorption capacities bigger than those recorded for the single-component solution; this indicates that a certain synergy is established that improves the uptake of SMX. Thermodynamically, the adsorption of SMX is more favourable under these conditions than in a monocomponent configuration.

However, the adsorption of MNZ under similar conditions has proved to be affected by the presence of SMX, decreasing the uptake for the former and leading to smaller adsorption capacities (Figure 8.25). Thus, the system works by increasing the adsorption capacity towards SMX in favour of a decrease in the uptake of MNZ.

To further analyse the results and try to elucidate the forces involved in the adsorption process, the same models were applied to binary mixtures as to 1:1 binary mixtures.

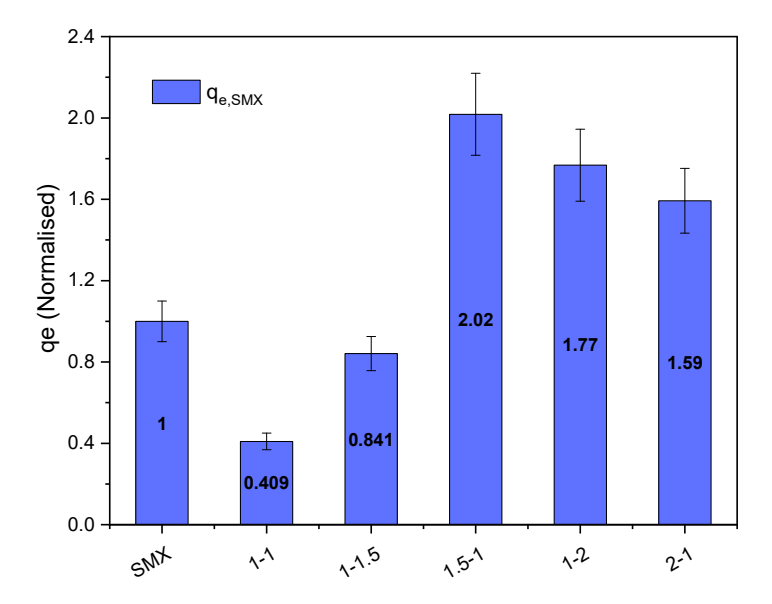


Figure 8.24 Comparison of the SMX adsorption capacity onto sample ACF-30-D under different conditions: monocomponent solution and binary mixtures SMX:MNZ at various molar ratios. Uptakes are normalised towards the adsorption capacity in the monocomponent solution.

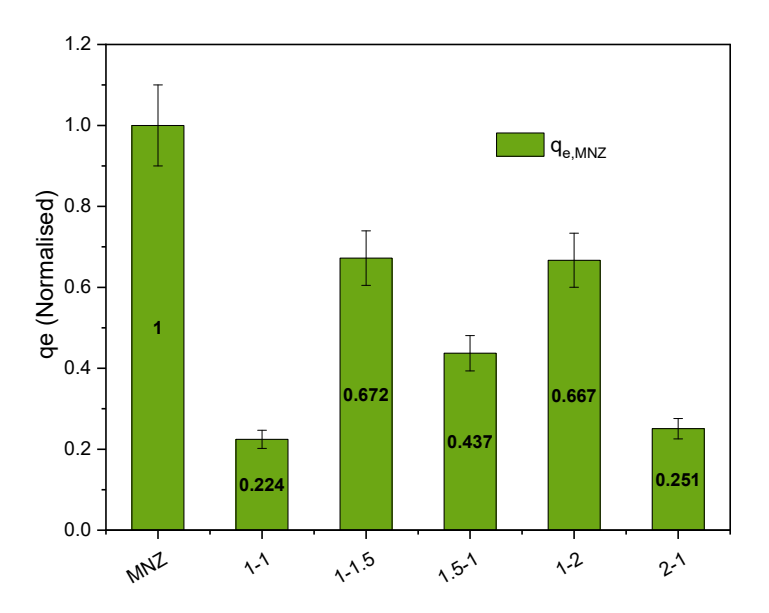


Figure 8.25 Comparison of the MNZ adsorption capacity onto sample ACF-30-D under different conditions: monocomponent solution and binary mixtures SMX:MNZ at various molar ratios. Uptakes are normalised towards the adsorption capacity in the monocomponent solution.

8.7.1 Competition under 1:1.5 (SMX:MNZ) molar ratio conditions

The next plots compare the predicted and experimental uptakes for SMX and MNZ on sample ACF-30-D using different theoretical models (Figures 8.26 and 8.26 inset). It can be noted that the best-fitted model was $MLM\eta$. This result is further supported by the percentage deviation values compiled (Table 8.8).

Despite the good fitting, it should be noted that the predicted uptakes for SMX with model MLM η are slightly higher than the experimental ones; this points out the contribution of some interactions affecting the adsorption that the model is not considering. On the contrary, it seems to work well to predict the uptake of MNZ, with the small deviation percentages (ca. 1.4).

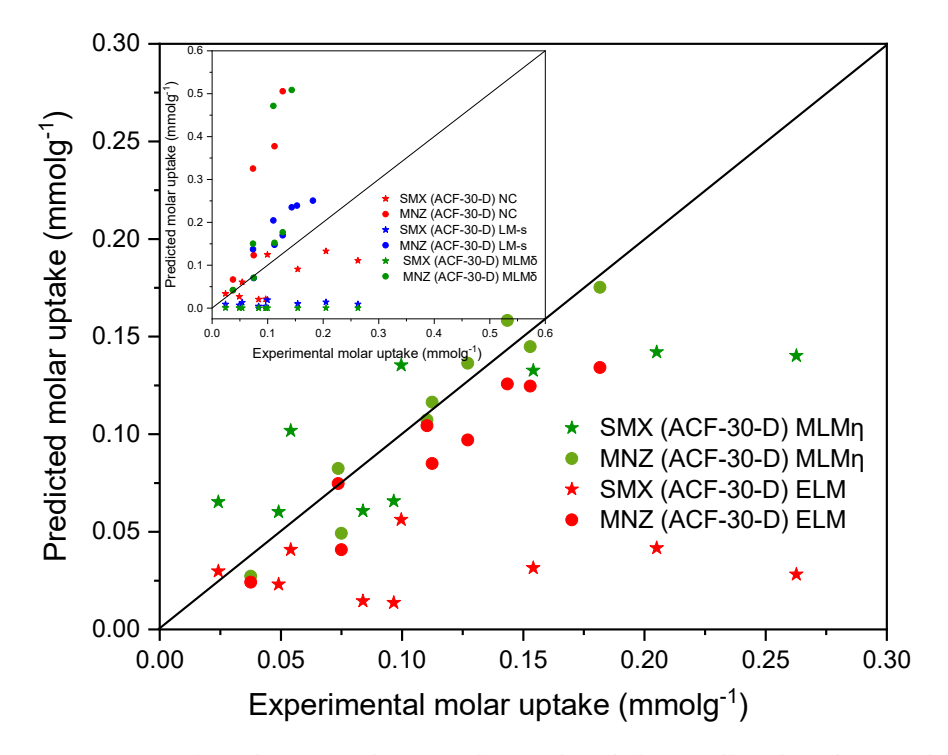


Figure 8.26 Comparison between the experimental and the predicted molar uptakes by the ELM and MLMη adsorption models, NC, LM-s, and MLMδ inset, for the adsorption of MNZ and SMX from binary solutions (1:1.5 SMX:MNZ molar ratio) for ACF-30-D sample.

Table 8.8 Comparison of the respective (%) Deviation for each model applied to the adsorption data obtained under binary conditions for solutions (1:1.5 SMX:MNZ molar ratio) for ACF-30-D sample.

Model	Adsorbate	% Deviation
NC	SMX	28.6
NC	MNZ	-147.1
LM-s	SMX	86.6
1711-2	MNZ	-44.4
LM-d	SMX	106.3
LIVI-U	MNZ	-49.6
ΜΙΜδ	SMX	77.2
IVILIVIO	MNZ	-85.3
ELM	SMX	64.4
LLIVI	MNZ	23.7
MLMη	SMX	-18.4
141171411	MNZ	1.4

8.7.2 Competition under 1.5:1 (SMX:MNZ) molar ratio conditions

In this case, again, for the overall adsorption, the best-fit model was MLM η (Figures 8.27 and 8.27 inset). However, considering only the adsorption of SMX, it can be seen that the predicted capacities are overestimated and that the NC model adjusts better in this case, suggesting that there is little contribution of competitive effects for the overall uptake of SMX in the presence of MNZ at a molar ratio SMX:MNZ of 1.5:1 (Table 8.9). This result follows the comparative plot (Figure 8.24), where the uptake of SMX is higher than that from the monocomponent solution. It also confirms that there is no competition for the adsorption of SMX in the presence of MNZ at this molar ratio.

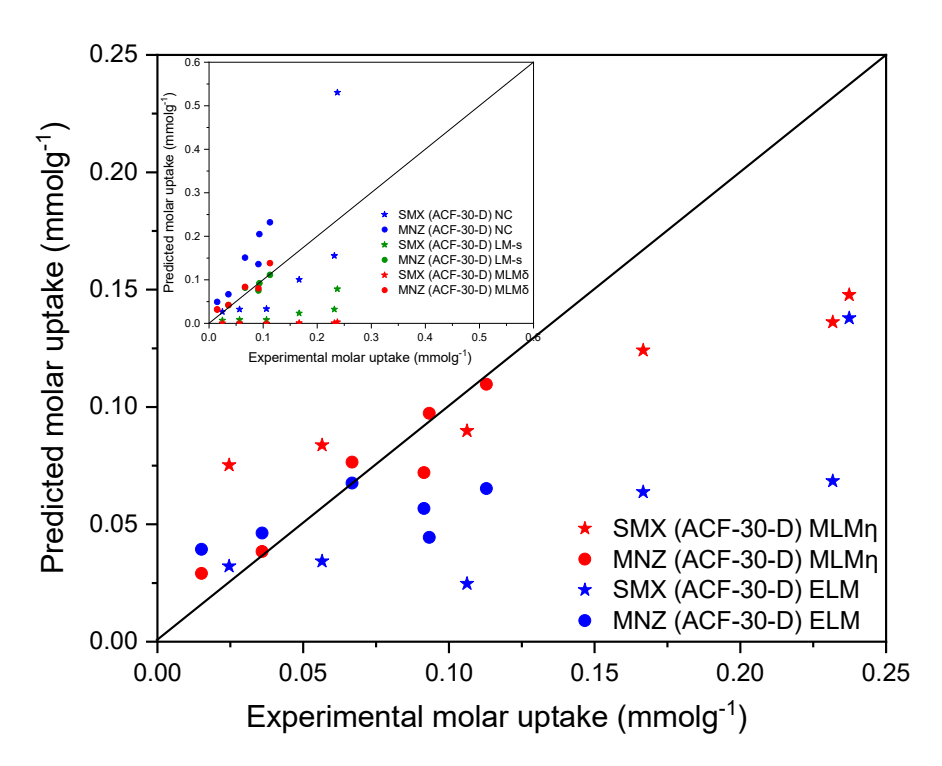


Figure 8.27 Comparison between the experimental and the predicted molar uptakes by the ELM and MLM η adsorption models, NC, LM-s, and MLM δ inset, for the adsorption of MNZ and SMX from binary solutions (1.5:1 SMX:MNZ molar ratio) for ACF-30-D sample.

Table 8.9 Comparison of the respective percentage Deviation (%) for each model applied to the adsorption data obtained for a binary mixture (1.5:1 SMX:MNZ molar ratio) for sample ACF-30-D.

Model	Adsorbate	% Deviation
NC	SMX	8.5
NC	MNZ	-118.8
LM-s	SMX	81.0
LIVI-S	MNZ	-21.6
LM-d	SMX	86.9
LIVI-U	MNZ	-35.3
ΜLΜδ	SMX	98.8
IVILIVIO	MNZ	-13.0
ELM	SMX	43.3
LLIVI	MNZ	-9.6
MLMη	SMX	-14.9
	MNZ	-10.5

8.7.3 Competition under 1:2 (SMX:MNZ) molar ratio conditions

In these working conditions, the mixture has double the concentration of MNZ (1:2). While for **ELM** and **MLMη** models, the data dispersion is appreciable (Figure 8.28), for the rest of the models, a certain trend can be observed (Figure 8.29). For the **MLMδ** and **ML-s** models, the predicted SMX uptakes are close to zero.

Like in the previous cases, the model that best fits the experimental data is **MLMη**. However, the predicted uptakes were overestimated compared to the experimental ones. The percentage deviation for SMX adsorption is similar to the one recorded for a 1:5-1 mixture, but in this situation, the %D for the **NC** model is considerably bigger (Tables 8.9 and 8.10). Thus, it could be inferred that the adsorption of SMX under this situation is affected by the presence of MNZ.

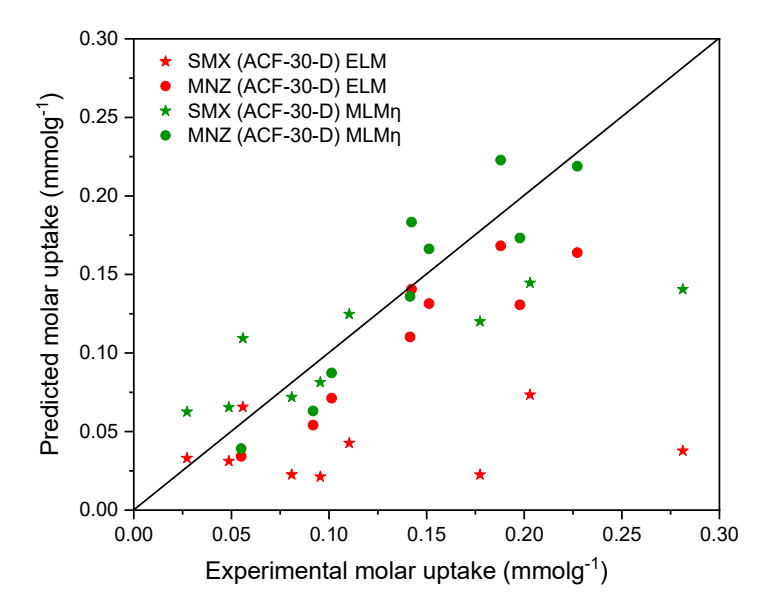


Figure 8.28 Comparison between the experimental and the predicted molar uptakes by the ELM and MLMη adsorption models for the adsorption of MNZ and SMX from binary solutions (1:2 SMX:MNZ molar ratio) for ACF-30-D sample.

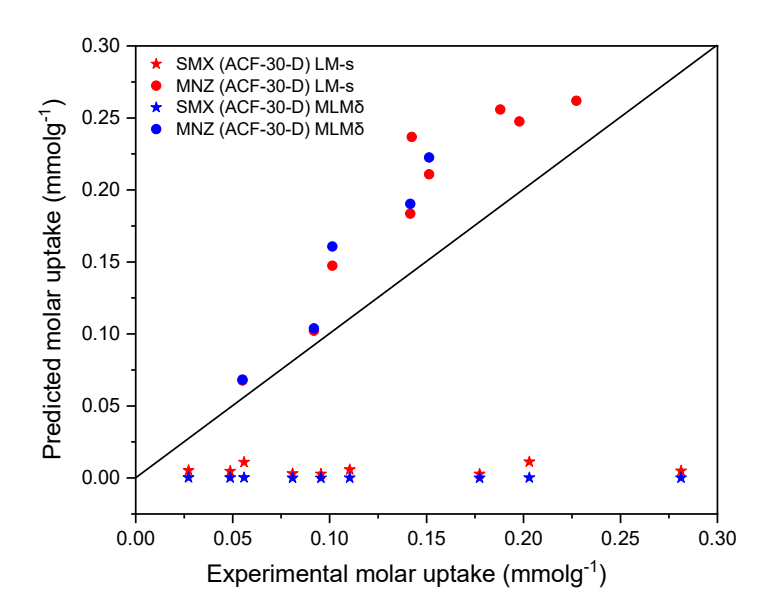


Figure 8.29 Comparison between the experimental and the predicted molar uptakes by the LM-s, and MLMδ adsorption models for the adsorption of MNZ and SMX from binary solutions (1:2 SMX:MNZ molar ratio) for ACF-30-D sample.

Table 8.10 Comparison of the respective (%) Deviation for each model applied to the adsorption data obtained under binary conditions for solutions (1:2 SMX:MNZ molar ratio) for ACF-30-D sample.

Model	Adsorbate	% Deviation
NC	SMX	54.4
NC	MNZ	-686.0
LM-s	SMX	92.3
	MNZ	-32.4
LM-d	SMX	107.9
	MNZ	-34.87
ΜLΜδ	SMX	99.7
	MNZ	-53.0
ELM	SMX	56.7
	MNZ	25.1
MLMη	SMX	-15.0
	MNZ	4.1

8.7.4 Competition under 2:1 (SMX:MNZ) molar ratio conditions

In this case, where the mixture has double the concentration of SMX, the plots have a certain resemblance (Figures 8.30 and 8.31) to those obtained for the 1:2 mixture (Figures 8.28 and 8.29). While the data dispersion is significant for the **MLM** δ and **MLM** η models (Figure 8.30), the other models exhibit a distinct trend (Figure 8.31). Here, the predicted values for the adsorption of SMX are also close to zero.

An interesting point to note is that the percentage deviation value for the adsorption of MNZ is the highest among all the mixtures (Table 8.11). This indicates that the experimentally determined quantity adsorbed was much bigger than the value predicted by the model. There is no direct explanation for this result, except that the model fails to assess the adsorption of MNZ under these working conditions.

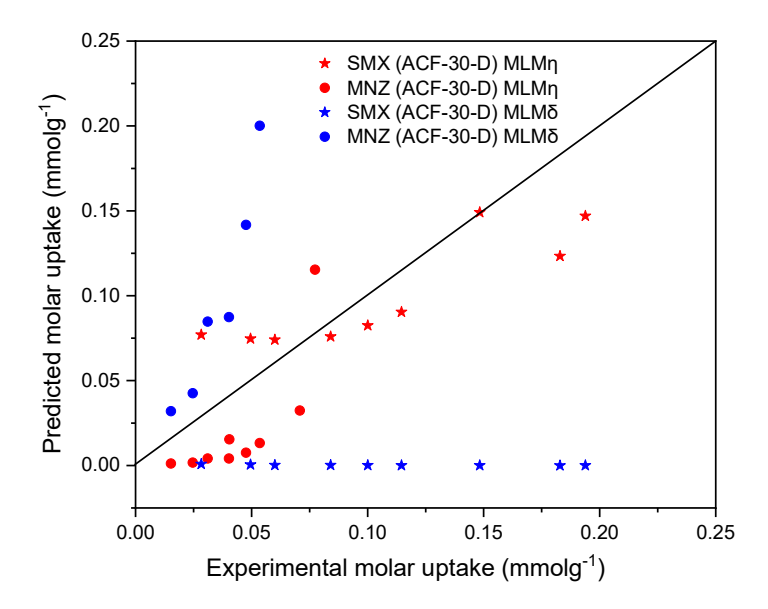


Figure 8.30 Comparison between the experimental and the predicted molar uptakes by the MLM η and MLM δ adsorption models for the adsorption of MNZ and SMX from binary solutions (2:1 SMX:MNZ molar ratio) for ACF-30-D sample.

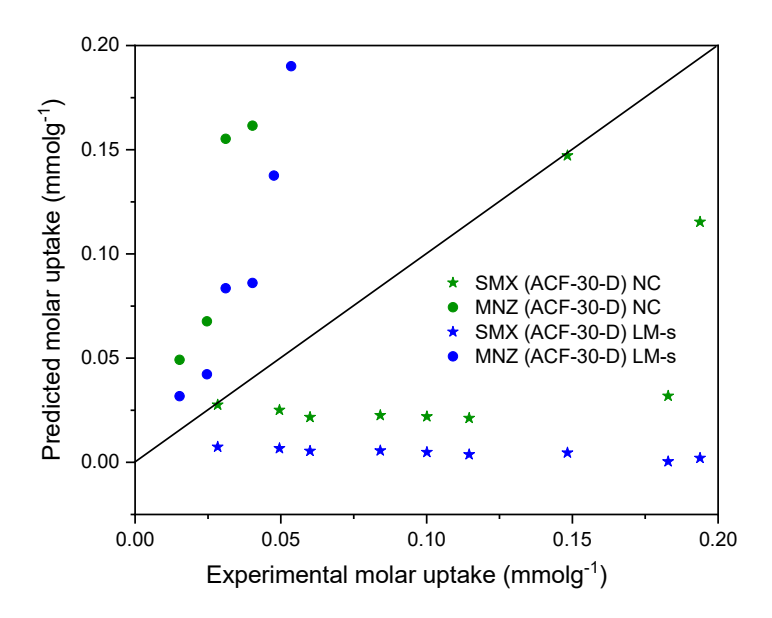


Figure 8.31 Comparison between the experimental and the predicted molar uptakes by the NC and LM-s adsorption models for the adsorption of MNZ and SMX from binary solutions (2:1 SMX:MNZ molar ratio) for ACF-30-D sample.

Table 8.11 Comparison of the percentage Deviation (%) for each model applied to the adsorption data obtained under binary solutions (1:2 SMX:MNZ molar ratio) for sample ACF-30-D.

Model	Adsorbate	% Deviation
NC	SMX	52.5
	MNZ	-283.3
LM-s	SMX	92.4
	MNZ	-224.8
LM-d	SMX	110.2
	MNZ	-229.2
ΜLΜδ	SMX	77.2
	MNZ	-145.0
MLMη	SMX	-15.7
	MNZ	65.4

8.8 Comparison among binary mixtures for the MLMn model

Since all the molar ratios fit the same model, it could be interesting to analyse how each case's corresponding percentage deviation values (%D) vary (Figure 8.32).

It is notorious that the $MLM\eta$ model can be considered more adequate for the adsorption of SMX, where the percentage deviation values remain relatively constant for all the binary mixtures, except for the 1:1 molar ratio (ca. -15 %). The predicted values SMX are always larger than those derived from the experimental data, except for the 1:1 molar ratio. This suggests that the model fails to consider all the phenomena involved at high molar ratios, which experimentally lead to large uptakes. The SMX uptake exceeds the expectations based on the results obtained from a single-component solution (Figure 8.24). This means that the presence of MNZ favours the uptake of SMX.

Regarding MNZ, except for the 1.5:1 molar ratio mixtures, the predicted values are consistently lower than the experimental values in all cases. The dispersion of the deviation percentage for MNZ is larger than that of SMX. Except for the 2:1 molar ratio mixture, where the %D is around 65%, the remaining mixtures took values in the range

of -10 and 10 %; thus, the predicted values are near the experimental data. Unlike SMX, the model forecasts lower uptake values in this scenario, whereas the experimental data shows larger values in nearly all cases. In addition, the observed uptake is lower than the result obtained from a single-component solution (Figure 8.25). Therefore, as a general rule, it can be concluded that the presence of SMX decreases the adsorption of MNZ in all cases.

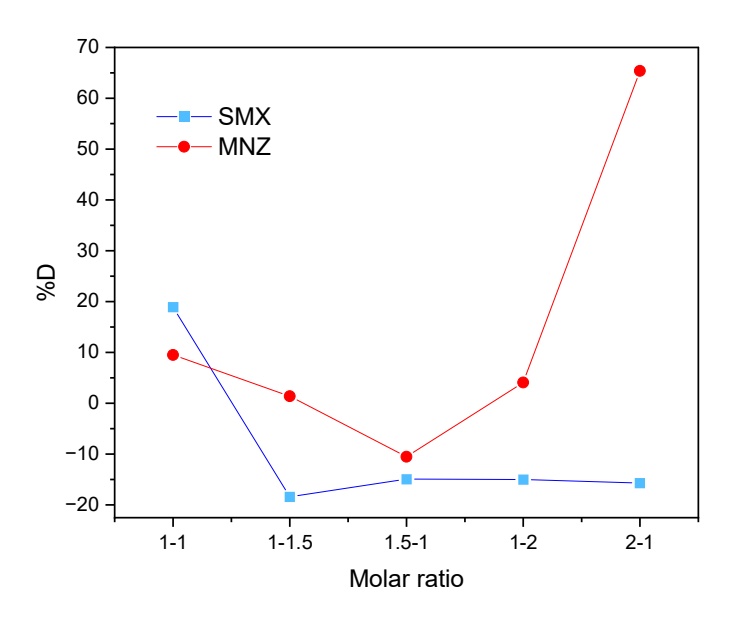


Figure 8.32 %D between the experimental adsorption uptake and the model's prediction for every working condition when using ACF-30-D as adsorbent.

The interaction factor follows a certain trend (Table 8.12) where the minor values are for the adsorption of SMX interacting with itself ($\eta_{SMX-SMX}$ ca. 0.06). corroborating the higher affinity of the adsorbent for this molecule, this is in agreement with the experimental result. This is also consistent with the extremely high value of the factor SMX-MNZ ($\eta_{SMX-MNZ}$ between 10E18 and 10E24). In contrast, since larger values mean a lower affinity of the adsorbent surface for the molecule, it can be seen that this holds for MNZ adsorption and agrees with the recorded uptake values.

Table 8.12 Interaction factors for each component depending on the molar ratio (SMX:MNZ) for the ACF-30-D adsorbent.

		η SMX,	η MNZ,	η MNZ,	η SMX,
Mixture	Adsorbate	SMX,	SMX	MNZ	MNZ
1 – 1	SMX	6.09E-3			2.13E21
	MNZ		106.32	28.44	
1.5 – 1	SMX	0.057			5.75E18
	MNZ		1.29	1.12	
1 – 1.5	SMX	0.097			4.11E24
	MNZ		0.14	1.15	
2 – 1	SMX	0.056			8.86E18
	MNZ		1.41E-3	0.76	
1 – 2	SMX	0.068			6.96E22
	MNZ		0.28	1.75	

8.9 Partial conclusions

Competitive effects have been observed for the uptake of SMX and MNZ from binary solutions at varied molar ratios for the different ACF samples investigated. As a general rule, the uptake of MNZ is greatly diminished regardless of the carbon adsorbent in the presence of SMX, whereas for the latter, the effect is much less pronounced.

For samples ACF-KOH and ACF-240-CR and in the case of binary mixtures with a 1:1 molar ratio, the uptakes of both compounds together lead to larger adsorption capacities than the ones showed for SMX from single-component solutions. This behaviour is attributed to the large mesopore fraction of these materials (Figures 8.1 and 8.3). For the rest of the ACF samples, the adsorption of both compounds is lower than the one recorded for the SMX single-component solution. This is attributed to the restricted accessibility of the pollutants in samples with a significant contribution of micropores.

For binary mixtures with molar ratios different from 1:1, the uptake of SMX is larger than that recorded in single-component solutions. This could be explained by the fact that the presence of MNZ provokes somehow a destabilisation of SMX in solution (SMX is a charged molecule) that would increase the uptake. On the other hand, the uptake of MNZ largely decreases in the presence of SMX. This decrease is more notorious when the molar ratios are higher for SMX (i.e., 1.5:1 and 2:1 SMX:MNZ).

In all cases, the experimental adsorption capacities of the binary mixtures are better represented by the **MLM** η model. This is reasonable since it is the only model that considers interactions of varied nature: adsorbate-adsorbent and adsorbate-adsorbate (including crossed adsorbate-adsorbate). In this sense, the η values obtained are in accordance with the experimental data. In this case, the adsorbent exhibits a greater affinity for the SMX molecule in the presence of MNZ compared to MNZ itself under identical conditions, regardless of the molar ratio.

The mechanisms involved in the adsorption process are expected to be the same as those presented for single solution configuration (see Chapter VII, section 7.6).



"La universidad no debe ser un templo aislado del pueblo, sino una institución al servicio de la nación, formando ciudadanos conscientes y comprometidos."

La universidad y el pueblo

Luis Alberto de Herrera

The next section summarises the most relevant conclusions of the present PhD thesis, related to synthesising and optimising activated carbon fibres prepared from a protein-based natural precursor and further analysing their performance as adsorbents of pharmaceutical compounds in monocomponent and binary solutions.

9.1 Overall conclusions

- Meticulous oxidative stabilisation studies on natural wool fibres demonstrated that the composition and morphology of carbon fibres could be modulated upon the time and temperature of the oxidation. The best material was achieved by exposing the WF under a 100 mLmin⁻¹ air flow at 300 °C for 2 hours, rendering hollow fibres. Under those conditions, the sulphur content (crucial for the morphology integrity) decreases but remains in the structure material predominantly in oxidised complexes, with no evidence of thiols and a small contribution of disulphides. The amount of oxygen decreased but remained relatively high in the stabilised fibres due to the forming of new groups (mainly ethers and quinone) during the cross-linking reactions occurring during the oxidative stabilisation. On the other hand, the rearrangement of N-groups would seem to be associated with the transformation of amides present in the pristine wool fibres into more stable carbodiimide groups. The polypeptide bond is unaffected, so the primary structure remains unchanged. This allows for preserving the fibrous morphology of the stabilised materials, which can, therefore, be used as low-cost precursors for preparing carbon fibres upon carbonisation.
- The activation method proved to be essential to preserving the fibrous morphology. The chemical activation allowed the achievement of materials with specific surface areas near 1900 m²g⁻¹ and more than 80 % micropores; however, it failed to maintain the fibrillar morphology, rendering very short-length and weak fibres. In contrast, the physical activation preserved the fibres' morphology and allowed a well-developed porosity.
- The flow of CO₂ in the physical activation proved essential for preparing a fibrous material. A low flow of CO₂ gas during the activation (CR control regime) allows for better control of the extent of the activation, affecting the precursor's structure and morphology to a lesser degree. On the other hand, high flows of CO₂ during the activation (D control regime) favoured the external activation of the materials. This type of

mechanism renders a more brittle material. Therefore, the fibres are shorter than those obtained under the CR control regime.

- The activation time was also demonstrated to be important, with long times favouring large specific surface areas and wide micropores.
- Regarding the chemical composition of the ACF, the activation conditions significantly changed the nitrogen and sulphur contents, which have significant consequences for the material's integrity. The chemically activated sample (ACF-KOH) displayed the highest nitrogen content and a negligible contribution of sulphur. The lack of fibre morphology on this material suggests that sulphur plays an important role in the structural integrity of the fibres, compared to nitrogen content. This is supported by the results obtained for the ACF-CR series, where the sulphur content is appreciable, but the nitrogen content is much lower than that of ACF-KOH.
- All the synthesised activated carbon fibres showed a basic surface nature.
- Regarding the adsorption experiments in monocomponent solutions, all the samples presented good adsorption capacities towards the studied pollutants. In all cases, the adsorption followed a Langmuir thermodynamic model, indicating that the adsorbent possesses a uniform distribution of adsorption sites regarding its energy. The adsorption kinetics varied significantly depending on the morphology and textural characteristics of the material. Both diffusion and PSO were found to govern the adsorption process, with intraparticle diffusion playing an important role in the initial stages of adsorption. ACFs with a relatively small contribution of mesopores are effective adsorbents for the studied compounds, facilitating access towards the adsorption sites. In all cases, the initial concentration of the pollutants in the solution affected the adsorption kinetics. Specifically, diffusional phenomena dominate the adsorption kinetics at high initial concentrations.
- While the uptake of MNZ and AMP is independent of the solution pH, this was not the case for SMX, which showed a drastic decrease in the adsorption capacity with the pH increment. The retention capacity of SMX was also significantly hindered by the ionic strength, this effect being much less pronounced for AMP and MNZ.

- The mechanisms involved in the adsorption process account for a combination of interactions. A reversible and rapid process involving weak forces like Van Der Waals is established between the ACF and the compounds in solution. Hydrogen bonding between the moieties of the pollutants (ca. hydroxyl groups for MNZ and AMP and amino groups for SMX) and the surface groups of the adsorbent. Electrostatic interactions may also occur between the ACF surface and the deprotonated form of SMX. Finally, dispersive interactions occur between the π electrons from aromatic sp² carbons in the ACF and the benzene ring of the studied pollutants via π - π coupling.
- Regarding the adsorption trends in the binary solutions, as a general rule, the uptake of MNZ is greatly diminished in the presence of SMX, regardless of the carbon adsorbent. On the other hand, the decrease in the uptake of SMX in the presence of MNZ is much less pronounced. For binary mixtures with a 1:1 molar ratio SMX:MNZ, the uptakes of both compounds together lead to larger adsorption capacities than the ones shown for SMX from single-component solutions for samples with a large fraction of mesopores (ACF-KOH and ACF-240-CR). For the rest of the ACF samples, the adsorption of both compounds is lower than the one recorded for the SMX single-component solution, which is attributed to the competitive adsorption in the micropores (similar adsorption sites).
- The pH and the ionic strength effects behave similarly for binary mixtures to those in monocomponent solutions.
- For binary mixtures with molar ratios different from 1:1, the uptake of SMX is more significant than that recorded in single-component solutions. This is attributed to the fact that the presence of MNZ somehow provokes a destabilisation of SMX in the solution, favouring the adsorption. The uptake of MNZ is largely decreased in the presence of SMX. This decrease is more notorious when the molar ratios are higher for SMX (i.e., 1.5:1 and 2:1 SMX/MNZ).
- In all cases, the experimental adsorption capacities of the binary mixtures are better represented by the MLM η model. This is reasonable since it is the only model that considers interactions of varied nature: adsorbate-adsorbate and adsorbate-adsorbate (including crossed adsorbate-adsorbate). In this sense, the η values obtained are following the experimental data.

- In all cases, the adsorbent exhibits a greater affinity for the SMX molecule in the presence of MNZ than MNZ itself under identical conditions, regardless of the molar ratio.
- The mechanisms involved in the adsorption process are expected to be the same as those presented for the single solution configuration.

9.2 Perspectives

Current research is focused on advancing the understanding of continuous adsorption processes using ACFs. Studies are being carried out under single-component and binary mixture systems to simulate real-world conditions better and evaluate competitive adsorption effects. These investigations aim to optimise operational parameters and improve the performance of ACFs in dynamic systems. In parallel, efforts are being directed toward regenerating and reusing ACFs through thermal treatment methods. These approaches are critical for assessing the economic and environmental feasibility of the adsorbents in long-term applications. Additionally, establishing the service life of ACFs under repeated adsorption-desorption cycles has become a key objective, as it provides essential data for predicting material stability and durability. Overall, these research directions are crucial for scaling up the application of ACFs in continuous-flow systems for water and air purification.

Building upon the knowledge acquired with ACFs, new studies are now exploring using fibres of different natures and compositions, such as bio-based or synthetic precursors, to broaden the range of functional properties and adsorption capacities. These investigations aim to tailor the structural and surface characteristics of novel fibres to specific applications, thereby enhancing their potential for targeted pollutant removal in continuous systems.



"En un lugar de la Mancha, de cuyo nombre no quiero acordarme, no ha mucho tiempo que vivía un hidalgo de los de lanza en astillero, adarga antigua, rocín flaco y galgo corredor."

Don Quijote de la Mancha

Miguel de Cervantes Saavedra

- Acharya, Amrutha, Gautham Jeppu, Chikmagalur Raju Girish, and Balakrishna Prabhu. 2023. "Development of a Multicomponent Adsorption Isotherm Equation and Its Validation by Modeling." *Langmuir* 39 (49): 17862–78. https://doi.org/10.1021/acs.langmuir.3c02496.
- "Advanced Materials / Activated Carbon Market." Accessed June 22, 2024 https://www.fortunebusinessinsights.com/activated-carbon-market-102175.
- Aksu, Zümriye. 2005. "Application of Biosorption for the Removal of Organic Pollutants: A Review." *Process Biochemistry* 40 (3–4): 997–1026. https://doi.org/10.1016/j.procbio.2004.04.008.
- Al-Asheh, S., F. Banat, R. Al-Omari, and Z. Duvnjak. 2000. "Predictions of Binary Sorption Isotherms for the Sorption of Heavy Metals by Pine Bark Using Single Isotherm Data." *Chemosphere* 41 (5): 659–65. https://doi.org/10.1016/S0045-46535(99)00497-X.-
- Ania, C. O., B. Cabal, J. B. Parra, and J. J. Pis. 2007. "Importance of the Hydrophobic Character of Activated Carbons on the Removal of Naphthalene from the Aqueous Phase." *Adsorption Science and Technology* 25 (3–4): 155–67. https://doi.org/10.1260/026361707782398164.
- Ania, C. O., J. A. Menéndez, J. B. Parra, and J. J. Pis. 2004. "Microwave-Induced Regeneration of Activated Carbons Polluted with Phenol. A Comparison with Conventional Thermal Regeneration." *Carbon* 42 (7): 1383–87. https://doi.org/10.1016/j.carbon.2004.01.010.
- Ania, Conchi, and Encarnación Raymundo-Piñero. 2019. "Nanoporous Carbons with Tuned Porosity Nanoporous Materials for Gas Storage." In *Nanoporous Materials for Gas Storage*, edited by Katsumi Kaneko and Francisco Rodríguez-Reinoso, 91–135. Singapore: Springer Nature Singapore.
- Aniagor, Chukwunonso O., A. Hashem, Nahla M. Badawy, and A.A. Aly. 2023. "Verification of the Optimal Kinetics Behaviour during the Methyl Blue Dye Adsorption onto Quaternized Starch Derivative." *Hybrid Advances* 3 (August):100047. https://doi.org/10.1016/j.hybadv.2023.100047.
- Apiratikul, Ronbanchob, and Prasert Pavasant. 2006. "Sorption Isotherm Model for Binary Component Sorption of Copper, Cadmium, and Lead Ions Using Dried Green Macroalga, Caulerpa Lentillifera." *Chemical Engineering Journal* 119 (2–3): 135–45. https://doi.org/10.1016/j.cej.2006.02.010.

- B. Halling-Sorensen j, S. Nors Nielsen, P. F. Lanzky, F. Ingerslev, H.C. Holten Liitzhofl and S.E. Jorgensen. 1998. "Occurrence, Fate and Effects of Pharmaceutical Substances in the Environment- A Review." *Chemospher* 36 (2): 357–93. https://doi.org/10.1016/S0045-6535(97)00354-8.
- Baek, Jin, Hyung Shik Shin, Dong Chul Chung, and Byung Joo Kim. 2017. "Studies on the Correlation between Nanostructure and Pore Development of Polymeric Precursor-Based Activated Hard Carbons: II. Transmission Electron Microscopy and Raman Spectroscopy Studies." *Journal of Industrial and Engineering Chemistry* 54:324–31. https://doi.org/10.1016/j.jiec.2017.06.007.
- Bandekar, Jagdeesh. 1992. "Amide Modes and Protein Conformation." *Biochimica et Biophysica Acta (BBA)/Protein Structure and Molecular* 1120 (2): 123–43. https://doi.org/10.1016/0167-4838(92)90261-B.
- Bandosz, T. J., and C. O. Ania. 2006a. "Chapter 4 Surface Chemistry of Activated Carbons and Its Characterization." *Interface Science and Technology* 7 (C): 159–229. https://doi.org/10.1016/S1573-4285(06)80013-X.
- Bandosz, T.J., and C.O. Ania. 2006b. *Activated Carbon Surfaces in Environmental Remediation. Interface Science and Technology*. Vol. 7. https://doi.org/10.1016/S1573-4285(06)80013-X.
- Bansal, RC, JB Donnet, and F Stoeckli. 1988. Active Carbon. New York: Marcel Dekker.
- Bansal, Roop Chand, and Meenakshi Goyal. 2005. *Activated Carbon Adsorption*. Edited by Roop Chand Bansal and Meenakshi Goyal. 1st. Ed. Boca Raton: Taylor & Francis Group.
- Barth, Andreas. 2007. "Infrared Spectroscopy of Proteins." *Biochimica et Biophysica Acta Bioenergetics* 1767 (9): 1073–1101. https://doi.org/10.1016/j.bbabio.2007.06.004.
- Belhachemi, Meriem, Rachel V.R.A. Rios, Fatima Addoun, Joaquín Silvestre-Albero, Antonio Sepúlveda-Escribano, and Francisco Rodríguez-Reinoso. 2009. "Preparation of Activated Carbon from Date Pits: Effect of the Activation Agent and Liquid Phase Oxidation." *Journal of Analytical and Applied Pyrolysis* 86 (1): 168–72. https://doi.org/10.1016/j.jaap.2009.05.004.

- Bernal, Valentina, Liliana Giraldo, and Juan Carlos Moreno-Piraján. 2020. "Thermodynamic Analysis of Acetaminophen and Salicylic Acid Adsorption onto Granular Activated Carbon: Importance of Chemical Surface and Effect of Ionic Strength." *Thermochimica Acta* 683. https://doi.org/10.1016/j.tca.2019.178467.
- Borukati, Sandhya Rani, B. Durga Prasad, and A. Ramesh. 2019. "Development and Charecterization of Natural Fiber /Carbon Fiber Reinforced Hybrid Composite Material." *Materials Today: Proceedings* 18:5394–99. https://doi.org/10.1016/j.matpr.2019.07.567.
- Bottom, Rod. 2008. "Thermogravimetric Analysis." *Principles and Applications of Thermal Analysis*, 87–118. https://doi.org/10.1002/9780470697702.ch3.
- Bragg, W.H., and W.L. Bragg. 1913. "The Reflection of X-Rays by Crystals." *Proceedings of the Royal Society of London. Series A, Containing Papers of a Mathematical and Physical Character* 88 (605): 428–38. https://doi.org/10.1098/rspa.1913.0040.
- Bralower, Timothy, and David Bice. n.d. "Distribution of Water on the Earth's Surface." The Pennsylvania State University. Accessed October 7, 2024. https://www.e-education.psu.edu/earth103/node/701#:~:text=The%20distribution%20of%20water%20 on,lakes%2C%20rivers%2C%20and%20swamps.
- Brandani, Stefano. 2021. "Kinetics of Liquid Phase Batch Adsorption Experiments." *Adsorption* 27 (3): 353–68. https://doi.org/10.1007/s10450-020-00258-9.
- Brasquet, C., and P. Le Cloirec. 1997. "Adsorption onto Activated Carbon Fibers: Application to Water and Air Treatments." *Carbon* 35 (9): 1307–13. https://doi.org/10.1016/S0008-6223(97)00079-1.
- Broda, Jan, Stanisława Przybyło, Katarzyna Kobiela-Mendrek, Dorota Biniaś, Monika Rom, Joanna Grzybowska-Pietras, and Ryszard Laszczak. 2016. "Biodegradation of Sheep Wool Geotextiles." *International Biodeterioration and Biodegradation* 115:31–38. https://doi.org/10.1016/j.ibiod.2016.07.012.
- Brunauer, Stephen, P. H. Emmett, and Edward Teller. 1938. "Adsorption of Gases in Multimolecular Layers." *Journal of the American Chemical Society* 60 (2): 309–19. https://doi.org/10.1021/ja01269a023.

- Burchell, T. D., C. I. Contescu, and N. C. Gallego. 2017. *Activated Carbon Fibers for Gas Storage*. *Activated Carbon Fiber and Textiles*. Elsevier Ltd. https://doi.org/10.1016/B978-0-08-100660-3.00012-2.
- Bury, Naomi A., Kathryn A. Mumford, and Geoffrey W. Stevens. 2021. "The Electro-Fenton Regeneration of Granular Activated Carbons: Degradation of Organic Contaminants and the Relationship to the Carbon Surface." *Journal of Hazardous Materials* 416 (January): 125792. https://doi.org/10.1016/j.jhazmat.2021.125792.
- Campinas, Margarida, Rui M.C. Viegas, Catarina Silva, Helena Lucas, and Maria João Rosa. 2021. "Operational Performance and Cost Analysis of PAC/Ceramic MF for Drinking Water Production: Exploring Treatment Capacity as a New Indicator for Performance Assessment and Optimization." *Separation and Purification Technology* 255 (July 2020): 117443. https://doi.org/10.1016/j.seppur.2020.117443.
- Cao, Jinan, Kyohei Joko, and John R. Cook. 1997. "DSC Studies of the Melting Behavior of α-Form Crystallites in Wool Keratin." *Textile Research Journal* 67 (2): 117–23. https://doi.org/10.1177/004051759706700207.
- Chandwani, Nisha, Purvi Dave, Vishal Jain, S. K. Nema, and S. Mukherjee. 2016. "Experimental Study To Improve Anti- Felting Characteristics of Merino Wool Fiber By Atmosphere Pressure Air Plasma." Gandhinagar. https://doi.org/10.13140/RG.2.1.2818.7281.
- Chang, E. E., Jan Chi Wan, Hyunook Kim, Chung Huei Liang, Yung Dun Dai, and Pen Chi Chiang. 2015. "Adsorption of Selected Pharmaceutical Compounds onto Activated Carbon in Dilute Aqueous Solutions Exemplified by Acetaminophen, Diclofenac, and Sulfamethoxazole." *Scientific World Journal* 2015. https://doi.org/10.1155/2015/186501.
- Chen, W., X. Liu, R. L. He, T. Lin, Q. F. Zeng, and X. G. Wang. 2013. "Activated Carbon Powders from Wool Fibers." *Powder Technology* 234:76–83. https://doi.org/10.1016/j.powtec.2012.09.026.
- Chihara, Kazuyuki, Kanji Oomori, Takao Oono, and Yosuke Mochizuki. 1997. "Supercritical CO2 Regeneration of Activated Carbon Loaded with Organic Adsorbates." *Water Science and Technology* 35 (7): 261–68. https://doi.org/10.1016/S0273-1223(97)00139-X.

- COD 2022/0344. 2022. "Proposal for a Directive of the European Parliament and of the Council Amending Directive 2000/60/EC Establishing a Framework for Community Action in the Field of Water Policy, Directive 2006/118/EC on the Protection of Groundwater against Pollution and d." Vol. 0344. https://environment.ec.europa.eu/system/files/2022-10/Proposal for a Directive amending the Water Framework Directive%2C the Groundwater Directive and the Environmental Quality Standards Directive.pdf.
- Comerton, Anna M., Robert C. Andrews, and David M. Bagley. 2009. "Practical Overview of Analytical Methods for Endocrine-Disrupting Compounds, Pharmaceuticals and Personal Care Products in Water and Wastewater." *Philosophical Transactions of the Royal Society A: Mathematical, Physical and Engineering Sciences* 367 (1904): 3923–39. https://doi.org/10.1098/rsta.2009.0111.
- Conte, Giuseppe, Sara Stelitano, Alfonso Policicchio, Francesco Demetrio Minuto, Victor Lazzaroli, Francesco Galiano, and Raffaele G. Agostino. 2020. "Assessment of Activated Carbon Fibers from Commercial Kevlar® as Nanostructured Material for Gas Storage: Effect of Activation Procedure and Adsorption of CO2 and CH4." *Journal of Analytical and Applied Pyrolysis* 152 (October): 104974. https://doi.org/10.1016/j.jaap.2020.104974.
- Contescu, Cristian, Jacek Jagiełło, and James A. Schwarz. 1993. "Heterogeneity of Proton Binding Sites at the Oxide/Solution Interface." *Langmuir* 9 (7): 1754–65. https://doi.org/10.1021/la00031a024.
- Couto, Carolina F., Lisete C. Lange, and Miriam C.S. Amaral. 2019. "Occurrence, Fate and Removal of Pharmaceutically Active Compounds (PhACs) in Water and Wastewater Treatment Plants—A Review." *Journal of Water Process Engineering*. Elsevier Ltd. https://doi.org/10.1016/j.jwpe.2019.100927.
- Cristóvão, M. B., J. Bernardo, A. Bento-Silva, M. Ressureição, M. R. Bronze, J. G. Crespo, and V. J. Pereira. 2022. "Treatment of Anticancer Drugs in a Real Wastewater Effluent Using Nanofiltration: A Pilot Scale Study." *Separation and Purification Technology* 288 (January). https://doi.org/10.1016/j.seppur.2022.120565.

- CSIRO. 2015. "The Chemical & Physical Structure of Merino Wool," Accessed March 17, 2020. https://csiropedia.csiro.au/wp-content/uploads/2015/01/6229343.pdf.
- Dai, Jiangdong, Sujun Tian, Yinhua Jiang, Zhongshuai Chang, Atian Xie, Ruilong Zhang, and Yongsheng Yan. 2018. "Facile Synthesis of Porous Carbon Sheets from Potassium Acetate via In-Situ Template and Self-Activation for Highly Efficient Chloramphenicol Removal." *Journal of Alloys and Compounds* 732:222–32. https://doi.org/10.1016/j.jallcom.2017.10.237.
- Dai, Pengcheng, Shuo Zhang, Haijun Liu, Liting Yan, Xin Gu, Liangjun Li, Dandan Liu, and Xuebo Zhao. 2020. "Cotton Fabrics-Derived Flexible Nitrogen-Doped Activated Carbon Cloth for High-Performance Supercapacitors in Organic Electrolyte." *Electrochimica Acta* 354:136717. https://doi.org/10.1016/j.electacta.2020.136717.
- Dalton, Stephen, Frank Heatley, and Peter M Budd. 1999. "Thermal Stabilization of Polyacrylonitrile Fibres" 40 (August 1998): 5531–43.
- Danish, Mohammed, and Tanweer Ahmad. 2018. "A Review on Utilization of Wood Biomass as a Sustainable Precursor for Activated Carbon Production and Application." *Renewable and Sustainable Energy Reviews* 87 (April 2017): 1–21. https://doi.org/10.1016/j.rser.2018.02.003.
- Decision 2020/1161/EU. 2020. "Commission Implementing Decision (EU) 2020/1161." Off.

 J. Eur. Union 257 (March 2015): 32–35. https://eur-lex.europa.eu/legal-content/EN/TXT/?uri=uriserv:OJ.L_.2020.257.01.0032.01.ENG&toc=OJ:L:2020:257:TOC.
- Decreto Nro. 253/979. 1979. "Código de Aguas de 15/12/1978." 1979. www.impo.com.uy/bases/decretos/253-1979.
- Decreto Nro.205/017. 2017. *Plan Nacional de Aguas*. http://www.mvotma.gub.uy/ciudadania/item/10008231-propuesta-del-plan-nacional-deaguas.html.
- Decreto Nro.222/019. 2019. Plan Nacional Ambiental Para El Desarrollo Sostenible.
- Dietzek, Benjamin, Dana Cialla, Michael Schmitt, and and Jürgen Popp. 2010. *Introduction to the Fundamentals of Raman Spectroscopy Benjamin. Confocal Raman Microscopy*.

- Dutta, Soumi, Bramha Gupta, Suneel Kumar Srivastava, and Ashok Kumar Gupta. 2021. "Recent Advances on the Removal of Dyes from Wastewater Using Various Adsorbents: A Critical Review." *Materials Advances*. Royal Society of Chemistry. https://doi.org/10.1039/d1ma00354b.
- Elvira, M. 2009. "DE QUÉ ESTÁ HECHA LA LANA Y PRINCIPALES CARACTERÍSTICAS TEXTILES Volver a: Producción Ovina de Lana." *INTA (Instituto Nacional de Tecnología Agropecuaria)* 1:4. www.produccion-animal.com.ar.
- Endo, Satoshi, Andrea Pfennigsdorff, and Kai Uwe Goss. 2012. "Salting-out Effect in Aqueous NaCl Solutions: Trends with Size and Polarity of Solute Molecules." *Environmental Science and Technology* 46 (3): 1496–1503. https://doi.org/10.1021/es203183z.
- Evans, R., and P. Tarazona. 1984. "Theory of Condensation in Narrow Capillaries." *Physical Review Letters* 52 (7): 557–60. https://doi.org/10.1103/PhysRevLett.52.557.
- Evgenidou, Eleni N., Ioannis K. Konstantinou, and Dimitra A. Lambropoulou. 2015. "Occurrence and Removal of Transformation Products of PPCPs and Illicit Drugs in Wastewaters: A Review." *Science of the Total Environment* 505:905–26. https://doi.org/10.1016/j.scitotenv.2014.10.021.
- Ewen, Margaret, Marjolein Zweekhorst, Barbara Regeer, and Richard Laing. 2017. "Baseline Assessment of WHO's Target for Both Availability and Affordability of Essential Medicines to Treat Non-Communicable Diseases." *PLoS ONE* 12 (2): 1–13. https://doi.org/10.1371/journal.pone.0171284.
- Ferrari, AC, and J Robertson. 1969. "Thermische Klärschlammbehandlung." *Schweizerische Zeitschrift Für Hydrologie* 31 (2): 632–45. https://doi.org/10.1007/BF02543692.
- Ferrari, Andrea C., and Denis M. Basko. 2013. "Raman Spectroscopy as a Versatile Tool for Studying the Properties of Graphene." *Nature Nanotechnology* 8 (4): 235–46. https://doi.org/10.1038/nnano.2013.46.
- Figini-Albisetti, Alessandro, Leticia F. Velasco, José B. Parra, and Conchi O. Ania. 2010. "Effect of Outgassing Temperature on the Performance of Porous Materials." *Applied Surface Science* 256 (17): 5182–86. https://doi.org/10.1016/j.apsusc.2009.12.090.

- Figueiredo, J. L., M. F.R. Pereira, M. M.A. Freitas, and J. J.M. Órfão. 1999. "Modification of the Surface Chemistry of Activated Carbons." *Carbon* 37 (9): 1379–89. https://doi.org/10.1016/S0008-6223(98)00333-9.
- Fitzer, E., K. H. Köchling, H. P. Boehm, and H. Marsh. 1995. "Recommended Terminology for the Description of Carbon as a Solid." *Pure and Applied Chemistry* 67 (3): 473–506. https://doi.org/10.1351/pac199567030473.
- Franklin, R. 1951. "Crystallite Growth in Graphitizing and Non-Graphitizing Carbons." Proceedings of the Royal Society of London. Series A. Mathematical and Physical Sciences 209 (1097): 196–218. https://doi.org/10.1098/rspa.1951.0197.
- Freundlich, H. 1926. "Colloid and Capillary Chemistry". Methuen, London.
- Gao, Yuan, Qinyan Yue, Baoyu Gao, and Aimin Li. 2020. "Insight into Activated Carbon from Different Kinds of Chemical Activating Agents: A Review." *Science of the Total Environment* 746:141094. https://doi.org/10.1016/j.scitotenv.2020.141094.
- Garcia-Ivars, Jorge, Lucia Martella, Manuele Massella, Carlos Carbonell-Alcaina, Maria Isabel Alcaina-Miranda, and Maria Isabel Iborra-Clar. 2017. "Nanofiltration as Tertiary Treatment Method for Removing Trace Pharmaceutically Active Compounds in Wastewater from Wastewater Treatment Plants." *Water Research* 125:360–73. https://doi.org/10.1016/j.watres.2017.08.070.
- García-Zubiri, Iñigo X., Gustavo González-Gaitano, and José Ramón Isasi. 2009. "Sorption Models in Cyclodextrin Polymers: Langmuir, Freundlich, and a Dual-Mode Approach."

 Journal of Colloid and Interface Science 337 (1): 11–18.

 https://doi.org/10.1016/j.jcis.2009.04.071.
- Garke, G., R. Hartmann, N. Papamichael, W. D. Deckwer, and F. B. Anspach. 1999. "The Influence of Protein Size on Adsorption Kinetics and Equilibria in Ion-Exchange Chromatography." Separation Science and Technology 34 (13): 2521–38. https://doi.org/10.1081/SS-100100788.
- Giles, Charles, David Smith, and Alan Huitson. 1974. "A General Treatment and Classification of the Solute Adsorption Isotherm I. Theoretical." *Journal of Colloid and Interface Science*, 47 (3): 755–65.

- Giles, H, TH Macewan, SN Nakhwa, and D Smith. 1960. "Solution Adsorption Isotherms, and Its Use in Diagnosis of Adsorption Mechanisms and in Measurement of Specific Surface Areas of Solids." *Journal of Chemical Society*, 3973–93.
- Gillespie, Gary D., Oyinlola Dada, and Kevin P. McDonnell. 2022. "The Potential for Hydrolysed Sheep Wool as a Sustainable Source of Fertiliser for Irish Agriculture." *Sustainability (Switzerland)* 14 (1): 1–12. https://doi.org/10.3390/su14010365.
- Gomis-Berenguer, Alicia, Raquel García-González, Ana S. Mestre, and Conchi O. Ania. 2017. "Designing Micro- and Mesoporous Carbon Networks by Chemical Activation of Organic Resins." *Adsorption* 23 (2–3): 303–12. https://doi.org/10.1007/s10450-016-9851-4.
- Gomis-Berenguer, Alicia, Mykola Seredych, Jesus Iniesta, Joao C. Lima, Teresa J. Bandosz, and Conchi O. Ania. 2016. "Sulfur-Mediated Photochemical Energy Harvesting in Nanoporous Carbons." *Carbon* 104:253–59. https://doi.org/10.1016/j.carbon.2016.02.058.
- Gousterova, A., M. Nustorova, I. Goshev, P. Christov, D. Braikova, K. Tishinov, T. Haertlé, and P. Nedkov. 2003. "Alkaline Hydrolysate of Waste Sheep Wool Aimed as Fertilizer." Biotechnology and Biotechnological Equipment 17 (2): 140–45. https://doi.org/10.1080/13102818.2003.10817072.
- Guillot, A., and F. Stoeckli. 2001. "Reference Isotherm for High Pressure Adsorption of CO2 by Carbons at 273 K." *Carbon* 39 (13): 2059–64. https://doi.org/10.1016/S0008-6223(01)00022-7.
- Guo, Junjie, James R. Morris, Yungok Ihm, Cristian I. Contescu, Nidia C. Gallego, Gerd Duscher, Stephen J. Pennycook, and Matthew F. Chisholm. 2012. "Topological Defects: Origin of Nanopores and Enhanced Adsorption Performance in Nanoporous Carbon." Small 8 (21): 3283–88. https://doi.org/10.1002/smll.201200894.
- Gupta, A, and I.R. Harrison. 1996. "New Aspects in the Oxidative Stabilization of Pan-based Carbon fibers." *Carbon* 34 (11): 1427–45. https://doi.org/10.1016/S0008-6223(96)00094-2.
- Hamdaoui, Oualid, and Emmanuel Naffrechoux. 2007. "Modeling of Adsorption Isotherms of Phenol and Chlorophenols onto Granular Activated Carbon. Part I. Two-Parameter

- Models and Equations Allowing Determination of Thermodynamic Parameters." *Journal of Hazardous Materials* 147 (1–2): 381–94. https://doi.org/10.1016/j.jhazmat.2007.01.021.
- Harris, M. 1935. "Effect of Alkalies on Wool." *Journal of Research of the National Bureau of Standards* 15 (1): 63. https://doi.org/10.6028/jres.015.048.
- Hassan, Mohammad M., Linda Schiermeister, and Mark P. Staiger. 2015. "Sustainable Production of Carbon Fiber: Effect of Cross-Linking in Wool Fiber on Carbon Yields and Morphologies of Derived Carbon Fiber." *ACS Sustainable Chemistry and Engineering* 3 (11): 2660–68. https://doi.org/10.1021/acssuschemeng.5b00994.
- Hassan, Mohammad Mahbubul, Linda Schiermeister, and Mark Peter Staiger. 2015. "Thermal, Chemical and Morphological Properties of Carbon Fibres Derived from Chemically Pre-Treated Wool Fibres." *RSC Advances* 5 (68): 55353–62. https://doi.org/10.1039/c5ra10649d.
- Haul, R. 1969. "Adsorption, Surface Area and Porosity." *Zeitschrift Für Physikalische Chemie*. https://doi.org/10.1524/zpch.1969.63.1_4.220.
- Heek, K. H., and H.-J. Mühlen. 1991. *Chemical Kinetics of Carbon and Char Gasification*. Fundamental Issues in Control of Carbon Gasification Reactivity. https://doi.org/10.1007/978-94-011-3310-4_1.
- Hijnen, W. A.M., G. M.H. Suylen, J. A. Bahlman, A. Brouwer-Hanzens, and G. J. Medema. 2010. "GAC Adsorption Filters as Barriers for Viruses, Bacteria and Protozoan (Oo)Cysts in Water Treatment." *Water Research* 44 (4): 1224–34. https://doi.org/10.1016/j.watres.2009.10.011.
- Hirschler, Alfred, and Thomas Mertes. 1955. "Liquid-Phase Adsorption Studies Related to the Arosorb Process." *Industrial and Engineering Chemistry* 47 (2): 193–201.
- Horng, Richard S., and I. Chin Tseng. 2008. "Regeneration of Granular Activated Carbon Saturated with Acetone and Isopropyl Alcohol via a Recirculation Process under H2O2/UV Oxidation." *Journal of Hazardous Materials* 154 (1–3): 366–72. https://doi.org/10.1016/j.jhazmat.2007.10.033.

- Hotová, Gabriela, Václav Slovák, Olívia S.G.P. Soares, José L. Figueiredo, and Manuel F.R. Pereira. 2018. "Oxygen Surface Groups Analysis of Carbonaceous Samples Pyrolysed at Low Temperature." *Carbon* 134:255–63. https://doi.org/10.1016/j.carbon.2018.03.067.
- Hsiao, Chia Yu, Ching Hung, Eilhann Kwon, Chao Wei Huang, Chih Feng Huang, and Kun Yi Andrew Lin. 2021. "Electrospun Nanoscale Iron Oxide-Decorated Carbon Fiber as an Efficient Heterogeneous Catalyst for Activating Percarbonate to Degrade Azorubin S in Water." *Journal of Water Process Engineering* 40 (October 2020): 101838. https://doi.org/10.1016/j.jwpe.2020.101838.
- Huang, Jung Jie, Yu Lee Hsueh, and Yu Xuan Zhang. 2018. "Silver Nanowire Doped Active Carbon Thin Film Electrode by Ultrasonic Spray Coating for High Performance Supercapacitor." *Surface and Coatings Technology* 350:788–94. https://doi.org/10.1016/j.surfcoat.2018.04.053.
- Huang, Xiaosong. 2009. "Fabrication and Properties of Carbon Fibers." *Materials* 2 (4): 2369–2403. https://doi.org/10.3390/ma2042369.
- Irving Langmuir. 1918. "The Adsorption of Gases on Plane Surfaces of Glass, Mica and Platinum."
- IUPAC. 2009. *Compendium of Chemical Terminology*. *Gold Book*. 2nd. Oxford: Blackwell Scientific Publications. https://doi.org/10.1351/goldbook.
- Ivanova, Nadezhda, Viliana Gugleva, Mirena Dobreva, Ivaylo Pehlivanov, Stefan Stefanov, and Velichka Andonova. 2016. *A Study of the Porosity of Activated Carbons Using the Scanning Electron Microscope*. Edited by Viacheslav Kazmiruk. *Intech*. 1st ed. Rijeka: Intech.
- Jagiello, Jacek, and James P. Olivier. 2013a. "2D-NLDFT Adsorption Models for Carbon Slit-Shaped Pores with Surface Energetical Heterogeneity and Geometrical Corrugation." *Carbon* 55 (2): 70–80. https://doi.org/10.1016/j.carbon.2012.12.011.
- ———. 2013b. "Carbon Slit Pore Model Incorporating Surface Energetical Heterogeneity and Geometrical Corrugation." *Adsorption* 19 (2–4): 777–83. https://doi.org/10.1007/s10450-013-9517-4.

- Jagtoyen, Marit, and Frank Derbyshire. 1993. "Some Considerations of the Origins of Porosity in Carbons from Chemically Activated Wood." *Carbon* 31 (7): 1185–92. https://doi.org/10.1016/0008-6223(93)90071-H.
- ——. 1998. "Activated Carbons from Yellow Poplar and White Oak by H3PO4 Activation." *Carbon* 36 (7–8): 1085–97. https://doi.org/10.1016/S0008-6223(98)00082-7.
- Jain, J. S., and V. L. Snoeyink. 1973. "Adsorption from Bisolute Systems on Active Carbon."
 Journal of the Water Pollution Control Federation 45 (12): 2463–79.
- Jareteg, Adam, Dario Maggiolo, Henrik Thunman, Srdjan Sasic, and Henrik Ström. 2021. "Investigation of Steam Regeneration Strategies for Industrial-Scale Temperature-Swing Adsorption of Benzene on Activated Carbon." *Chemical Engineering and Processing - Process Intensification* 167 (June): 108546. https://doi.org/10.1016/j.cep.2021.108546.
- Jiménez, V., P. Sánchez, and A. Romero. 2016. "Materials for Activated Carbon Fiber Synthesis." Activated Carbon Fiber and Textiles, 21–38. https://doi.org/10.1016/B978-0-08-100660-3.00002-X.
- Jo, Hyejun, Shahbaz Raza, Adeel Farooq, Jungman Kim, and Tatsuya Unno. 2021. "Fish Farm Effluents as a Source of Antibiotic Resistance Gene Dissemination on Jeju Island, South Korea." *Environmental Pollution* 276:116764. https://doi.org/10.1016/j.envpol.2021.116764.
- Jones, Leslie, and George Rogers. 2009. "2 . Structure and Composition of Wool." Woolwise Australian Wool Education Trust. 2009. https://www.woolwise.com/wp-content/uploads/2017/07/Wool-472-572-08-T-02.pdf.
- Kang, Seong Hyun, Hye Min Lee, Kwan Woo Kim, and Byung Joo Kim. 2023. "Preparation and Characterization of Polyethylene-Based Activated Carbon Fibers Stabilized at Low Temperatures." *Journal of Industrial and Engineering Chemistry* 121:401–8. https://doi.org/10.1016/j.jiec.2023.01.042.
- Khan, Abrar, Raja Arumugam Senthil, Junqing Pan, Sedahmed Osman, Yanzhi Sun, and Xin Shu. 2020. "A New Biomass Derived Rod-like Porous Carbon from Tea-Waste as Inexpensive and Sustainable Energy Material for Advanced Supercapacitor Application." *Electrochimica Acta* 335:135588. https://doi.org/10.1016/j.electacta.2019.135588.

- Kim, Chansik, Sueng Il Lee, Suhyun Hwang, Myoungsu Cho, Han Seung Kim, and Soo Hong Noh. 2014. "Removal of Geosmin and 2-Methylisoboneol (2-MIB) by Membrane System Combined with Powdered Activated Carbon (PAC) for Drinking Water Treatment."

 **Journal of Water Process Engineering 4 (C): 91–98. https://doi.org/10.1016/j.jwpe.2014.09.006.
- Kim, Jung Dam, Jae-Seung Roh, and Myung-Soo Kim. 2017. "Effect of Carbonization Temperature on Crystalline Structure and Properties of Isotropic Pitch-Based Carbon Fiber." *Carbon Letters* 21:51–60. https://doi.org/10.5714/cl.2017.21.051.
- Kim, Ki Yong, Okon Dominic Ekpe, Heon Jun Lee, and Jeong Eun Oh. 2020. "Perfluoroalkyl Substances and Pharmaceuticals Removal in Full-Scale Drinking Water Treatment Plants." *Journal of Hazardous Materials* 400 (December). https://doi.org/10.1016/j.jhazmat.2020.123235.
- Kim, Min Jeong, Seung Wan Choi, Hyunwook Kim, Sungyong Mun, and Ki Bong Lee. 2020. "Simple Synthesis of Spent Coffee Ground-Based Microporous Carbons Using K2CO3 as an Activation Agent and Their Application to CO2 Capture." *Chemical Engineering Journal* 397 (May): 125404. https://doi.org/10.1016/j.cej.2020.125404.
- Knight, Diane S., and William B. White. 1989. "Characterization of Diamond Films by Raman Spectroscopy." *Journal of Materials Research* 4 (2): 385–93. https://doi.org/10.1557/JMR.1989.0385.
- Ko, Tse-Hao -H. 1991. "Influence of Continuous Stabilization on the Physical Properties and Microstructure of PAN-based Carbon Fibers." *Journal of Applied Polymer Science* 42 (7): 1949–57. https://doi.org/10.1002/app.1991.070420719.
- Kolb, D. M. 2002. "An Atomistic View of Electrochemistry." *Surface Science* 500 (1–3): 722–40. https://doi.org/10.1016/S0039-6028(01)01583-7.
- Kreuk, Merle K. de, and Mark C. M. van Loosdrecht. 2006. "Formation of Aerobic Granules with Domestic Sewage." *Journal of Environmental Engineering* 132 (6): 694–97. https://doi.org/10.1061/(ASCE)0733-9372(2006)132.
- Kwiatkowski, Mirosław, and Elzbieta Broniek. 2013. "Application of the LBET Class Adsorption Models to the Analysis of Microporous Structure of the Active Carbons Produced from Biomass by Chemical Activation with the Use of Potassium Carbonate."

- Colloids and Surfaces A: Physicochemical and Engineering Aspects 427:47–52. https://doi.org/10.1016/j.colsurfa.2013.03.002.
- Kyriakopoulos, Grigorios, Danae Doulia, and Adamadia Hourdakis. 2006. "Effect of Ionic Strength and PH on the Adsorption of Selected Herbicides on Amberlite." *International Journal of Environmental Analytical Chemistry* 86 (3–4): 207–14. https://doi.org/10.1080/03067310500247678.
- La Casa-Lillo, M. A. De, J. Alcañiz-Monge, E. Raymundo-Piñero, D. Cazorla-Amorós, and A. Linares-Solano. 1998. "Molecular Sieve Properties of General-Purpose Carbon Fibres." *Carbon* 36 (9): 1353–60. https://doi.org/10.1016/S0008-6223(98)00120-1.
- Larasati, Amanda, Geoffrey D. Fowler, and Nigel J.D. Graham. 2022. "Extending Granular Activated Carbon (GAC) Bed Life: A Column Study of in-Situ Chemical Regeneration of Pesticide Loaded Activated Carbon for Water Treatment." *Chemosphere* 286 (P3): 131888. https://doi.org/10.1016/j.chemosphere.2021.131888.
- Lastoskie, Christian, Keith E. Gubbins, and Nicholas Quirke. 1993. "Pore Size Distribution Analysis of Microporous Carbons: A Density Functional Theory Approach." *Journal of Physical Chemistry* 97 (18): 4786–96. https://doi.org/10.1021/j100120a035.
- Lavín López, María del Prado. 2017. "Definición y optimización de la Síntesis de Nanomateriales Basados en Grafeno." PhD, Castilla La Mancha: Universidad de Castilla La Mancha.
- Lee, Ji Hae, Chang Soon Choi, Il Hong Bae, Jin Kyu Choi, Young Ho Park, and Miyoung Park. 2018. "A Novel, Topical, Nonsteroidal, TRPV1 Antagonist, PAC-14028 Cream Improves Skin Barrier Function and Exerts Anti-Inflammatory Action through Modulating Epidermal Differentiation Markers and Suppressing Th2 Cytokines in Atopic Dermatitis." *Journal of Dermatological Science* 91 (2): 184–94. https://doi.org/10.1016/j.jdermsci.2018.04.017.
- Lennard-Jones, J. E. 1932. "Processes of Adsorption and Diffusion on Solid Surfaces." Transactions of the Faraday Society 28:333–59. https://doi.org/10.1039/tf9322800333.
- Lever, Trevor, Peter Haines, Jean Rouquerol, Edward L. Charsley, Paul Van Eckeren, and Donald J. Burlett. 2014. "ICTAC Nomenclature of Thermal Analysis (IUPAC

- Recommendations 2014)." *Pure and Applied Chemistry* 86 (4): 545–53. https://doi.org/10.1515/pac-2012-0609.
- Leyva-Ramos, R., L. A. Bernal-Jacome, R. M. Guerrero-Coronado, and L. Fuentes-Rubio. 2001. "Competitive Adsorption of Cd(II) and Zn(II) from Aqueous Solution onto Activated Carbon." *Separation Science and Technology* 36 (16): 3673–87. https://doi.org/10.1081/SS-100108355.
- Li, Kunlin, Chi Wang, Ping Ning, Kai Li, Xin Sun, Xin Song, and Yi Mei. 2020. "Surface Characterization of Metal Oxides-Supported Activated Carbon Fiber Catalysts for Simultaneous Catalytic Hydrolysis of Carbonyl Sulfide and Carbon Disulfide." *Journal of Environmental Sciences (China)* 96:44–54. https://doi.org/10.1016/j.jes.2020.03.019.
- Li, Yue, Hongwen Li, Caiyun Jin, Zigeng Wang, Ji Hao, Yaqiang Li, and Jianglin Liu. 2021. "Multi-Scale Investigation and Mechanism Analysis on Young's Modulus of C-S-H Modified by Multi-Walled Carbon Nanotubes." *Construction and Building Materials* 308 (August). https://doi.org/10.1016/j.conbuildmat.2021.125079.
- Lillo-Ródenas, M. A., J. Juan-Juan, D. Cazorla-Amorós, and A. Linares-Solano. 2004. "About Reactions Occurring during Chemical Activation with Hydroxides." *Carbon* 42 (7): 1371–75. https://doi.org/10.1016/j.carbon.2004.01.008.
- Linares-Solano, Angel, and Diego Cazorla-Amorós. 2008. "Adsorption on Activated Carbon Fibers." *Adsorption by Carbons*, no. iii, 431–54. https://doi.org/10.1016/B978-008044464-2.50021-3.
- Lotay, S. S., and P. T. Speakman. 1977. "Three-Chain Merokeratin from Wool May Be a Fragment of the Microfibril Component Macromolecule." *Nature* 265 (5591): 274–76. https://doi.org/10.1038/265274a0.
- Lozano-Castelló, D., J. M. Calo, D. Cazorla-Amorós, and A. Linares-Solano. 2007. "Carbon Activation with KOH as Explored by Temperature Programmed Techniques, and the Effects of Hydrogen." *Carbon* 45 (13): 2529–36. https://doi.org/10.1016/j.carbon.2007.08.021.
- M. J. Mufioz-Guillena, M. J. Illiin-G6mez, J. M. Martin-Martinez, A. Linares-Solano, C. Salinas-Martinez de Lecea. 1992. "Activated Carbons from Spanish Coals." *Energy & Fuels* 6 (i): 9–15.

- Ma, Zheng Wei, Kai Ning Zhang, Zhi Jin Zou, and Qiu Feng Lü. 2021. "High Specific Area Activated Carbon Derived from Chitosan Hydrogel Coated Tea Saponin: One-Step Preparation and Efficient Removal of Methylene Blue." *Journal of Environmental Chemical Engineering* 9 (3). https://doi.org/10.1016/j.jece.2021.105251.
- Mackay, D. M., and P. V. Roberts. 1982. "The Dependence of Char and Carbon Yield on Lignocellulosic Precursor Composition." *Carbon* 20 (2): 87–94. https://doi.org/10.1016/0008-6223(82)90412-2.
- Márquez, P., A. Benítez, J. Hidalgo-Carrillo, F. J. Urbano, Caballero, J. A. Siles, and M. A. Martín. 2021. "Simple and Eco-Friendly Thermal Regeneration of Granular Activated Carbon from the Odour Control System of a Full-Scale WWTP: Study of the Process in Oxidizing Atmosphere." Separation and Purification Technology 255 (September 2020). https://doi.org/10.1016/j.seppur.2020.117782.
- Marsh, H., and F. Rodríguez-Reinoso. 2006. "Activation Processes (Chemical)." In *Activated Carbon*, edited by Harry Marsh and Franciso Rodríguez-Reinoso, 322–65. Elsevier Science Ltd.

 https://www.sciencedirect.com/science/article/abs/pii/B9780080444635500200.
- Marsh Harry, and Rodríguez-Reinoso Francisco. 2006. "Activated Carbon (Origins)." In , edited by Marsh Harry and Rodríguez-Reinoso Francisco, First Edition, 1:13–86. https://doi.org/Marsh, H., & Rodríguez-Reinoso, F. (2006). Activated Carbon (Origins). Activated Carbon, 13–86. doi:10.1016/b978-008044463-5/50016-9.
- Marsh, Harry, and Francisco Rodríguez-Reinoso. 2006a. "Introduction to the Scope of the Text." *Activated Carbon*, 1–12. https://doi.org/10.1016/b978-008044463-5/50015-7.
- ——. 2006b. *Porosity in Carbons: Modeling*. Edited by Francisco Rodríguez-Reinoso Harry Marsh. *Activated Carbon*. Oxford: Elsevier Science Ltd. https://doi.org/10.1016/b978-008044463-5/50017-0.
- Masood, Zafar, Amir Ikhlaq, Osama Shaheen Rizvi, Hafiz Abdul Aziz, Mohsin Kazmi, and Fei Qi. 2023. "A Novel Hybrid Treatment for Pharmaceutical Wastewater Implying Electroflocculation, Catalytic Ozonation with Ni-Co Zeolite 5A° Catalyst Followed by Ceramic Membrane Filtration." *Journal of Water Process Engineering* 51 (November 2022). https://doi.org/10.1016/j.jwpe.2022.103423.

- Mckay, Gordon. 1984. "The Adsorption of Basic Dye onto Silica from Aqueous Solution-Solid Diffusion Model." *Chemical Engineering Science* 39 (1): 129–38.
- Menéndez-Díaz, J. A., and I. Martín-Gullón. 2006. "Chapter 1 Types of Carbon Adsorbents and Their Production." *Interface Science and Technology* 7 (C): 1–47. https://doi.org/10.1016/S1573-4285(06)80010-4.
- Mercosur. 2010. *Acuerdo Sobre Acuífero Guarani*. https://www.parlamentomercosur.org/innovaportal/v/14499/1/parlasur/propuesta-dedeclaracion-pretende-la-ratificacion-del-acuerdo-sobre-el-acuifero-guarani.html.
- Mestre, A. S., J. Pires, J. M.F. Nogueira, and A. P. Carvalho. 2007. "Activated Carbons for the Adsorption of Ibuprofen." *Carbon* 45 (10): 1979–88. https://doi.org/10.1016/j.carbon.2007.06.005.
- Mestre, Ana S., Fabian Hesse, Cristina Freire, Conchi O. Ania, and Ana P. Carvalho. 2019. "Chemically Activated High Grade Nanoporous Carbons from Low Density Renewable Biomass (Agave Sisalana) for the Removal of Pharmaceuticals." *Journal of Colloid and Interface Science* 536:681–93. https://doi.org/10.1016/j.jcis.2018.10.081.
- Michell, Anthony J. 1988. "Second Derivative F.t.-i.r. Spectra of Celluloses I and II and Related Mono- and Oligo-Saccharides." *Carbohydrate Research* 173 (2): 185–95. https://doi.org/10.1016/S0008-6215(00)90814-0.
- Millington, K. R., and J. A. Rippon. 2017. *Wool as a High-Performance Fiber*. Edited by Gajanan Bhat and In Woodhead Publishing Series in Textiles. *Structure and Properties of High-Performance Fibers*. First. Woodhead Publishing. https://doi.org/10.1016/B978-0-08-100550-7.00014-0.
- Mittal, J., O. P. Bahl, and R. B. Mathur. 1997. "Single Step Carbonization and Graphitization of Highly Stabilized PAN Fibers." *Carbon* 35 (8): 1196–97. https://doi.org/10.1016/S0008-6223(97)84653-2.
- Molina-Sabio, M., and F. Rodríguez-Reinoso. 2004. "Role of Chemical Activation in the Development of Carbon Porosity." In *Colloids and Surfaces A: Physicochemical and Engineering Aspects*, 241:15–25. Elsevier. https://doi.org/10.1016/j.colsurfa.2004.04.007.

- Montes-Morán, Miguel A., J. Angel Menéndez, Enrique Fuente, and Dimas Suárez. 1998. "Contribution of the Basal Planes to Carbon Basicity: An Ab Initio Study of the H3O+-π Interaction in Cluster Models." *Journal of Physical Chemistry B* 102 (29): 5595–5601. https://doi.org/10.1021/jp972656t.
- Müssig, Jürg, Holger Fischer, Nina Graupner, and Axel Drieling. 2010. Testing Methods for Measuring Physical and Mechanical Fibre Properties (Plant and Animal Fibres). Industrial Applications of Natural Fibres: Structure, Properties and Technical Applications. https://doi.org/10.1002/9780470660324.ch13.
- Newcombe, G, D Dixon, and D R U Knappe. 2006. "Interface Science in Drinking Water Treatment Chapter 9: Surface Chemistry Effects in Activated Carbon Adsorption of Industrial Pollutants." https://doi.org/10.1016/S1573-4285(06)80078-5 Get rights and content.
- Noh, Joong S., and James A. Schwarz. 1989. "Estimation of the Point of Zero Charge of Simple Oxides by Mass Titration." *Journal of Colloid And Interface Science* 130 (1): 157–64. https://doi.org/10.1016/0021-9797(89)90086-6.
- Oladejo, Jumoke, Kaiqi Shi, Yipei Chen, Xiang Luo, Yang Gang, and Tao Wu. 2020. "Closing the Active Carbon Cycle: Regeneration of Spent Activated Carbon from a Wastewater Treatment Facility for Resource Optimization." *Chemical Engineering and Processing Process Intensification* 150 (November 2019): 107878. https://doi.org/10.1016/j.cep.2020.107878.
- Paiva, M. C., P. Kotasthane, D. D. Edie, and A. A. Ogale. 2003. "UV Stabilization Route for Melt-Processible PAN-Based Carbon Fibers." Carbon 41 (7): 1399–1409. https://doi.org/10.1016/S0008-6223(03)00041-1.
- Pakkaner, Efecan, Damla Yalçın, Berk Uysal, and Ayben Top. 2019. "Self-Assembly Behavior of the Keratose Proteins Extracted from Oxidized Ovis Aries Wool Fibers." *International Journal of Biological Macromolecules* 125:1008–15. https://doi.org/10.1016/j.ijbiomac.2018.12.129.
- Papageorgiou, S. K., F. K. Katsaros, E. P. Kouvelos, and N. K. Kanellopoulos. 2009. "Prediction of Binary Adsorption Isotherms of Cu2+, Cd2+ and Pb2+ on Calcium

- Alginate Beads from Single Adsorption Data." *Journal of Hazardous Materials* 162 (2–3): 1347–54. https://doi.org/10.1016/j.jhazmat.2008.06.022.
- Park, Soo Jin, and Yu Sin Jang. 2003. "Preparation and Characterization of Activated Carbon Fibers Supported with Silver Metal for Antibacterial Behavior." *Journal of Colloid and Interface Science* 261 (2): 238–43. https://doi.org/10.1016/S0021-9797(03)00083-3.
- Park, Soo-Jin. 2015. Springer Series in Materials Science 210 Carbon Fibers. Springer. Vol. 210. https://doi.org/10.1007/978-94-017-9478-7.
- Parker, Frank S. 1971. "Proteins and Polypeptides." In *Applications of Infrared Spectroscopy in Biochemistry, Biology, and Medicine*, edited by Frank S. Parker, 1st. Edition, 1–612. New York: Plenum Press.
- Parra, J. B., J. J. Pis, J. C. De Sousa, Jesús A. Pajares, and R. C. Bansal. 1996. "Effect of Coal Preoxidation on the Development of Microporosity in Activated Carbons." *Carbon* 34 (6): 783–87. https://doi.org/10.1016/0008-6223(96)00030-9.
- Pereira, Diogo, María V. Gil, Valdemar I. Esteves, Nuno J.O. Silva, Marta Otero, and Vânia Calisto. 2023. "Ex-Situ Magnetic Activated Carbon for the Adsorption of Three Pharmaceuticals with Distinct Physicochemical Properties from Real Wastewater."

 Journal of Hazardous Materials 443 (April 2022). https://doi.org/10.1016/j.jhazmat.2022.130258.
- Pina, A. C., N. Tancredi, M. Baldan, J. S. Marcuzzo, and A. Amaya. 2018. "CO₂ Capture and Biomethane Obtention Using Activated Carbon Filter of Animal Origin." *MRS Advances* 3 (61): 3589–3600. https://doi.org/10.1557/adv.2018.588.
- Pina, A.C., Alejandro Amaya, Jossano Marcuzzo, Aline Rodrigues, Mauricio Baldan, Nestor Tancredi, and Andrés Cuña. 2018. "Supercapacitor Electrode Based on Activated Carbon Wool Felt." *C* 4 (2): 24. https://doi.org/10.3390/c4020024.
- Platnieks, Oskars, Sergejs Gaidukovs, Anda Barkane, Gerda Gaidukova, Liga Grase, Vijay Kumar Thakur, Inese Filipova, Velta Fridrihsone, Marite Skute, and Marianna Laka. 2020. "Highly Loaded Cellulose/Poly (Butylene Succinate) Sustainable Composites for Woody-like Advanced Materials Application." *Molecules* 25 (1). https://doi.org/10.3390/molecules25010121.

- Przepiórski, J. 2006. "Chapter 9 Activated Carbon Filters and Their Industrial Applications." Interface Science and Technology 7 (C): 421–74. https://doi.org/10.1016/S1573-4285(06)80018-9.
- Puri, R A I, and R A M Singh Hazra. 1970. "Carbon-Sulphur Surface Complexes On Charcoal." Carbon 9: 123 134.
- Qian, Mancai, Meijiao Xu, Shuqing Zhou, Jianniao Tian, Tayirjan Taylor Isimjan, Zhongfeng Shi, and Xiulin Yang. 2020. "Template Synthesis of Two-Dimensional Ternary Nickel-Cobalt-Nitrogen Co-Doped Porous Carbon Film: Promoting the Conductivity and More Active Sites for Oxygen Reduction." *Journal of Colloid and Interface Science* 564:276–85. https://doi.org/10.1016/j.jcis.2019.12.089.
- Qiu, Hui, Lu Lv, Bing Cai Pan, Qing Jian Zhang, Wei Ming Zhang, and Quan Xing Zhang. 2009. "Critical Review in Adsorption Kinetic Models." *Journal of Zhejiang University: Science A* 10 (5): 716–24. https://doi.org/10.1631/jzus.A0820524.
- Radovic, Ljubisa R., and Bradley Bockrath. 2005. "On the Chemical Nature of Graphene Edges: Origin of Stability and Potential for Magnetism in Carbon Materials." *Journal of the American Chemical Society* 127 (16): 5917–27. https://doi.org/10.1021/ja050124h.
- Reporte Exportaciones. 2023. "Uruguay: Exportaciones Del Rubro Ovino Período: Enero a Diciembre de 2022." *Boletín de Exportaciones*. Montevideo. https://www.sul.org.uy/mercados.
- Rezende, J. C.T. De, V. H.S. Ramos, A. S. Silva, C. P. Santos, H. A. Oliveira, and E. De Jesus. 2019. "Assessment of Sulfamethoxazole Adsorption Capacity on Pirangi Clay from the State of Sergipe, Brazil, Modified by Heating and Addition of Organic Cation." *Ceramica* 65 (376): 626–34. https://doi.org/10.1590/0366-69132019653762774.
- Robinson, T., G. Mc Mullan, R. Marchant, and P. Nigam. 2001. "Remediation of Dyes in Textile e?Uent: A Critical Review on Current Treatment Technologies with a Proposed Alternative." *Bioresource Technology* 77:247–55.
- Rodriguez-Reinoso, F., A. Linares-Solano, J. M. Martín-Martinez, and J. D. López-González. 1984. "The Controlled Reaction of Active Carbons with Air at 350°C-II. Evolution of Microporosity." *Carbon* 22 (2): 123–30. https://doi.org/10.1016/0008-6223(84)90199-4.

- Rodríguez-Reinoso, F., M. Molina-Sabio, and M. T. González. 1995. "The Use of Steam and CO2 as Activating Agents in the Preparation of Activated Carbons." *Carbon* 33 (1): 15–23. https://doi.org/10.1016/0008-6223(94)00100-E.
- Rojo, M., D. Álvarez-Muñoz, A. Dománico, R. Foti, S. Rodriguez-Mozaz, D. Barceló, and P. Carriquiriborde. 2019. "Human Pharmaceuticals in Three Major Fish Species from the Uruguay River (South America) with Different Feeding Habits." *Environmental Pollution* 252:146–54. https://doi.org/10.1016/j.envpol.2019.05.099.
- Rouquerol, F., Rouquerol, J., et al. 2015. *Adsorption by Powders and Porous Solids, Principles, Methodology and Applications*. 2nd ed. Academic Press. http://library1.nida.ac.th/termpaper6/sd/2554/19755.pdf.
- Sabater, Sergio, Helena Guasch, Ramón Moreno, Anna Romaní, and Isabel Muñoz. 2008.

 Calidad y Cantidad de Agua: El Estado Ecológico de Los Sistemas Acuáticos

 Continentales. Aguas Continentales: Gestión de Recursos Hídricos, Tratamiento y

 Calidad Del Agua.

 http://s9c21adfc2988c5cf.jimcontent.com/download/version/1445896795/module/7866
 296786/name/aguas continentales csic.book 109 com.pdf.
- Sabio, E., E. González, J. F. González, C. M. González-García, A. Ramiro, and J. Gañan. 2004. "Thermal Regeneration of Activated Carbon Saturated with P-Nitrophenol." *Carbon* 42 (11): 2285–93. https://doi.org/10.1016/j.carbon.2004.05.007.
- Sahoo, Tapas Ranjan, and Benedicte Prelot. 2020. Adsorption Processes for the Removal of Contaminants from Wastewater. Nanomaterials for the Detection and Removal of Wastewater Pollutants. Elsevier Inc. https://doi.org/10.1016/b978-0-12-818489-9.00007-4.
- Sajid, Muhammad, Sineen Bari, Muhammad Saif Ur Rehman, Muhammad Ashfaq, Yin Guoliang, and Ghulam Mustafa. 2022. "Adsorption Characteristics of Paracetamol Removal onto Activated Carbon Prepared from Cannabis Sativum Hemp." *Alexandria Engineering Journal* 61 (9): 7203–12. https://doi.org/10.1016/j.aej.2021.12.060.
- Santos, Danilo H.S., José L.S. Duarte, Josealdo Tonholo, Lucas Meili, and Carmem L.P.S. Zanta. 2020. "Saturated Activated Carbon Regeneration by UV-Light, H2O2 and Fenton

- Reaction." *Separation and Purification Technology* 250 (May): 117112. https://doi.org/10.1016/j.seppur.2020.117112.
- Savige, WE, and JA Maclaren. 1966. Oxidation of Disulfides, With Special Reference To Cystine. The Chemistry of Organic Sulfur Compounds. Pergamon Press Inc. https://doi.org/10.1016/b978-0-08-011062-2.50019-x.
- Scaria, Jaimy, and P.V. Nidheesh. 2022. "Pre-Treatment of Real Pharmaceutical Wastewater by Heterogeneous Fenton and Persulfate Oxidation Processes." *Environmental Research* 217 (October 2022): 114786. https://doi.org/10.1016/j.envres.2022.114786.
- Schmidt, Jeremy J. 2019. *Valuing Water. Water Politics*. https://doi.org/10.4324/9780429453571-2.
- Serna-Carrizales, Juan Carlos, Ana I. Zárate-Guzmán, Angélica Aguilar-Aguilar, Angélica Forgionny, Esther Bailón-García, Elizabeth Flórez, Cesar F.A. Gómez-Durán, and Raúl Ocampo-Pérez. 2023. "Optimization of Binary Adsorption of Metronidazole and Sulfamethoxazole in Aqueous Solution Supported with DFT Calculations." *Processes* 11 (4). https://doi.org/10.3390/pr11041009.
- Sevilla, Marta, and Robert Mokaya. 2014. "Energy Storage Applications of Activated Carbons: Supercapacitors and Hydrogen Storage." *Energy and Environmental Science* 7 (4): 1250–80. https://doi.org/10.1039/c3ee43525c.
- Shmidt, J. L., A. V. Pimenov, A. I. Lieberman, and H. Y. Cheh. 1997. "Kinetics of Adsorption with Granular, Powdered, and Fibrous Activated Carbon." *Separation Science and Technology* 32 (13): 2105–14. https://doi.org/10.1080/01496399708000758.
- Sing W.S.W, Everett D.H., Haul R.A.W., Moscou L., Pierotti R.S., Rouquerol J., and Siemieniewska T. 1985. "International Union of Pure and Applied Chemistry Physical Chemistry Division Commission on Colloid and Surface Chemistry Including Catalysis, Reporting Physisorption Data for Gas/Solid Systems with Special Reference to the Determination of Surface Area and Porosity Reporting Physisorption Data for Gas/Solid Systems-with Special Reference to the Determination of Surface Area and Porosity."
- Singh, Ashok K. 2016. "Nanoparticle Ecotoxicology." In *Engineered Nanoparticles*, 343–450. Elsevier. https://doi.org/10.1016/b978-0-12-801406-6.00008-x.

- Skoog, Douglas, James Holler, and Timothy Nieman. 2001. *Principios de Análisis Instrumental 5^a Edición (Skoog, Holle.Pdf.* Edited by Concepción Fernández Madrid. 5ta. Vol. 1. Madrid: McGraw-Hill.
- Sohrabi, Mehdi, Ebrahiminezhad. 2020. Multi-Function and Fateme "Novel Polycarbonate/Activated-Carbon-Fabric Individual/Environmental Radon Twin Badges." 134:106332. Radiation Measurements https://doi.org/10.1016/j.radmeas.2020.106332.
- Son, Dong Jin, Chang Soo Kim, Jun Won Park, Jae Ho Lee, Soo Hyung Lee, Sun Kyoung Shin, and Dong Hwan Jeong. 2022. "Fate Evaluation of Pharmaceuticals in Solid and Liquid Phases at Biological Process of Full-Scale Municipal Wastewater Treatment Plants." *Journal of Water Process Engineering* 46 (October 2021): 102538. https://doi.org/10.1016/j.jwpe.2021.102538.
- Spessato, Lucas, Karen C. Bedin, André L. Cazetta, Isis P.A.F. Souza, Vitor A. Duarte, Lucas H.S. Crespo, Marcela C. Silva, Rodrigo M. Pontes, and Vitor C. Almeida. 2019. "KOH-Super Activated Carbon from Biomass Waste: Insights into the Paracetamol Adsorption Mechanism and Thermal Regeneration Cycles." *Journal of Hazardous Materials* 371 (December 2018): 499–505. https://doi.org/10.1016/j.jhazmat.2019.02.102.
- Srivastava, Vimal Chandra, Indra Deo Mall, and Indra Mani Mishra. 2006. "Equilibrium Modelling of Single and Binary Adsorption of Cadmium and Nickel onto Bagasse Fly Ash." *Chemical Engineering Journal* 117 (1): 79–91. https://doi.org/10.1016/j.cej.2005.11.021.
- Stoeckli, H, P Rebstein, and L Ballerini. 1990. "On the Assessment of Microporosity in Active Carbons, a Comparison of Theoretical and Experimental Data." *Carbon* 28 (6): 907–9. https://www.unhcr.org/publications/manuals/4d9352319/unhcr-protection-training-manual-european-border-entry-officials-2-legal.html?query=excom 1989.
- Stuart, Barbara H. 2005. Infrared Spectroscopy: Fundamentals and Applications. Infrared Spectroscopy: Fundamentals and Applications. Vol. 8. https://doi.org/10.1002/0470011149.
- Suzuki, Motoyuki. 1994. "Activated Carbon Fiber: Fundamentals and Applications." *Carbon* 32 (4): 577–86. https://doi.org/10.1016/0008-6223(94)90075-2.

- Tang, Chengli, Dongmei Hu, Qianqian Cao, Wei Yan, and Bo Xing. 2017. "Silver Nanoparticles-Loaded Activated Carbon Fibers Using Chitosan as Binding Agent: Preparation, Mechanism, and Their Antibacterial Activity." Applied Surface Science 394:457–65. https://doi.org/10.1016/j.apsusc.2016.10.095.
- Terzyk, Artur P. 2003. "Further Insights into the Role of Carbon Surface Functionalities in the Mechanism of Phenol Adsorption." *Journal of Colloid and Interface Science* 268 (2): 301–29. https://doi.org/10.1016/S0021-9797(03)00690-8.
- Thomas, Fabien, Bénédicte Prélot, Frédéric Villiéras, and Jean-Maurice Cases. 2002. "Electrochemical Properties of Solids at the Aqueous–Solid Interface and Heterogeneity of Surface." *Comptes Rendus Geoscience* 334 (9): 633–48. https://doi.org/10.1016/s1631-0713(02)01800-x.
- Thommes, Matthias, and Katie A. Cychosz. 2014. "Physical Adsorption Characterization of Nanoporous Materials: Progress and Challenges." *Adsorption* 20 (2–3): 233–50. https://doi.org/10.1007/s10450-014-9606-z.
- Thommes, Matthias, Katsumi Kaneko, Alexander V. Neimark, James P. Olivier, Francisco Rodriguez-Reinoso, Jean Rouquerol, and Kenneth S.W. Sing. 2015. "Physisorption of Gases, with Special Reference to the Evaluation of Surface Area and Pore Size Distribution (IUPAC Technical Report)." *Pure and Applied Chemistry* 87 (9–10): 1051–69. https://doi.org/10.1515/pac-2014-1117.
- Thorburn Burns, Klaus Müller, Reiner Salzer. 2014. Thorburn Burns, Klaus Müller, R. S. (2014) Important Figures of Analytical Chemistry from Germany in Brief Biographies From the Middle Ages to the Twentieth Century. Springer Cham Heidelberg New York Dordrecht London. Doi: 10.1007/978-3-319-12151-2 ISBN.I.
- Torres-Canas, Fernando, Ahmed Bentaleb, Marie Föllmer, Julien Roman, Wilfrid Neri, Isabelle Ly, Alain Derré, and Philippe Poulin. 2020. "Improved Structure and Highly Conductive Lignin-Carbon Fibers through Graphene Oxide Liquid Crystal." *Carbon* 163:120–27. https://doi.org/10.1016/j.carbon.2020.02.077.
- Tratado de la cuenca del Plata. 1969. *El Tratado de La Cuenca Del Plata*. Brasil. https://cicplata.org/es/el-tratado-de-la-cuenca-del-plata/.

- Tröger, Rikard, Stephan J. Köhler, Vera Franke, Olof Bergstedt, and Karin Wiberg. 2020. "A Case Study of Organic Micropollutants in a Major Swedish Water Source Removal Efficiency in Seven Drinking Water Treatment Plants and Influence of Operational Age of Granulated Active Carbon Filters." *Science of the Total Environment* 706 (xxxx): 135680. https://doi.org/10.1016/j.scitotenv.2019.135680.
- Tuinstra, F, and JL Koenig. 1970. "Raman Spectrum of Graphite." *Journal of Chemical Physics* 53 (3): 1126–30. https://doi.org/10.1063/1.1674108.
- UN-A/RES/70/1. 2016. "Transforming Our World: The 2030 Agenda for Sustainable Development." https://doi.org/10.1201/b20466-7.
- UNESCO, and UN-Water. 2020. *United Nations World Water Development Report 2020:*Water and Climate Change. Unesco.

 https://aquadocs.org/handle/1834/42227%0Ahttps://unesdoc.unesco.org/ark:/48223/pf0
 000372985/PDF/372985eng.pdf.multi.
- United Nations, General Assembly. 2010. "The Human Rights to Water and Sanitation." *Research Handbook on Economic, Social and Cultural Rights as Human Rights*. Vol. 1249. https://doi.org/10.4337/9781788974172.00019.
- Velasco, Leticia F., Rocio J. Carmona, Juan Matos, and Conchi O. Ania. 2014. "Performance of Activated Carbons in Consecutive Phenol Photooxidation Cycles." *Carbon* 73:206–15. https://doi.org/10.1016/j.carbon.2014.02.056.
- Vergunst, Theo, Marco J.G. Linders, Freek Kapteijn, and Jacob A. Moulijn. 2001. "Carbon-Based Monolithic Structures." *Catalysis Reviews Science and Engineering* 43 (3): 291–314. https://doi.org/10.1081/CR-100107479.
- Walker, P L, Frank Rusinko, and L G Austin. 1959. "Gas Reactions of Carbon." *Advances in Catalysis* Volume 11:133–221.
- Wandelt, Klaus. 2016. Surface and Interface Science. Surface and Interface Science. Vol. 6. https://doi.org/10.1002/9783527680580.
- Wang, Jianlong, and Xuan Guo. 2020. "Adsorption Kinetic Models: Physical Meanings, Applications, and Solving Methods." *Journal of Hazardous Materials* 390 (January): 122156. https://doi.org/10.1016/j.jhazmat.2020.122156.

- Wang, K., R. Li, J. H. Ma, Y. K. Jian, and J. N. Che. 2016. "Extracting Keratin from Wool by Using L-Cysteine." *Green Chemistry* 18 (2): 476–81. https://doi.org/10.1039/c5gc01254f.
- Wang, Yan, Daniel C. Alsmeyer, and Richard L. McCreery. 1990. "Raman Spectroscopy of Carbon Materials: Structural Basis of Observed Spectra." *Chemistry of Materials* 2 (5): 557–63. https://doi.org/10.1021/cm00011a018.
- Wang, Yifan, Ning Wang, Mei Li, Maomao Bai, and Hongbo Wang. 2022. "Potassium Ferrate Enhances Ozone Treatment of Pharmaceutical Wastewaters: Oxidation and Catalysis." *Journal of Water Process Engineering* 49 (October 2021): 103055. https://doi.org/10.1016/j.jwpe.2022.103055.
- Wigmans, T. 1989. "Industrial Aspects of Production and Use of Activated Carbons." *Carbon* 27 (i): 13–22.
- Wilkinson, John L, Alistair B A Boxall, Dana W Kolpin, Kenneth M Y Leung, Racliffe W S Lai, Donald Wong, Romaric Ntchantcho, et al. 2022. "Pharmaceutical Pollution of the World 's Rivers" 119 (8): 1–10. https://doi.org/10.1073/pnas.2113947119/-/DCSupplemental.Published.
- Wojciechowska, E, A Włochowicz, and A Wesel/ucha-Birczyn'ska. 1999. "Application of Fourier-Transform Infrared and Raman Spectroscopy to Study Degradation of the Wool Fiber Keratin." *Journal of Molecular Structure* 511–512:307–18. https://doi.org/10.1016/S0022-2860(99)00173-8.
- Yang, Yi, Yaqin Ji, Yuzong Gao, Zi Lin, Yu Lin, Yuan Lu, and Liwen Zhang. 2022. "Antibiotics and Antimycotics in Waste Water Treatment Plants: Concentrations, Removal Efficiency, Spatial and Temporal Variations, Prediction, and Ecological Risk Assessment." *Environmental Research* 215 (P1): 114135. https://doi.org/10.1016/j.envres.2022.114135.
- Yang, Zhewei, Huajun Guo, Xinhai Li, Zhixing Wang, Zhiliang Yan, and Yansen Wang. 2016. "Natural Sisal Fibers Derived Hierarchical Porous Activated Carbon as Capacitive Material in Lithium Ion Capacitor." *Journal of Power Sources* 329:339–46. https://doi.org/10.1016/j.jpowsour.2016.08.088.

Zhang, Yanhong, Changqing Zhu, Fuqiang Liu, Yuan Yuan, Haide Wu, and Aimin Li. 2019. "Effects of Ionic Strength on Removal of Toxic Pollutants from Aqueous Media with Multifarious Adsorbents: A Review." *Science of the Total Environment* 646:265–79. https://doi.org/10.1016/j.scitotenv.2018.07.279.



"Before the beginning, there was chaos. All sounds but none heard; all shapes but none seen.

Darkness pursuing darkness for an endless age. When the moment was true, out of chaos emerged the sleeping giant Pan Koo. Upon awakening, he was angered by the void and shattered it with a blow. That which yields floated upward while the unyielding sank, forming the Heavens and Earth."

Spring moon

Bette Bao Lord

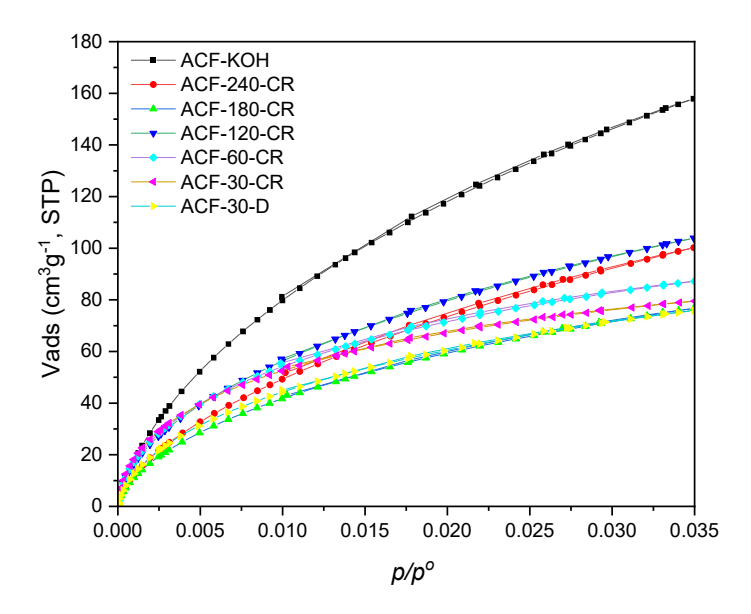


Figure AI.1 Carbon dioxide adsorption/desorption isotherms at 0 °C of samples.

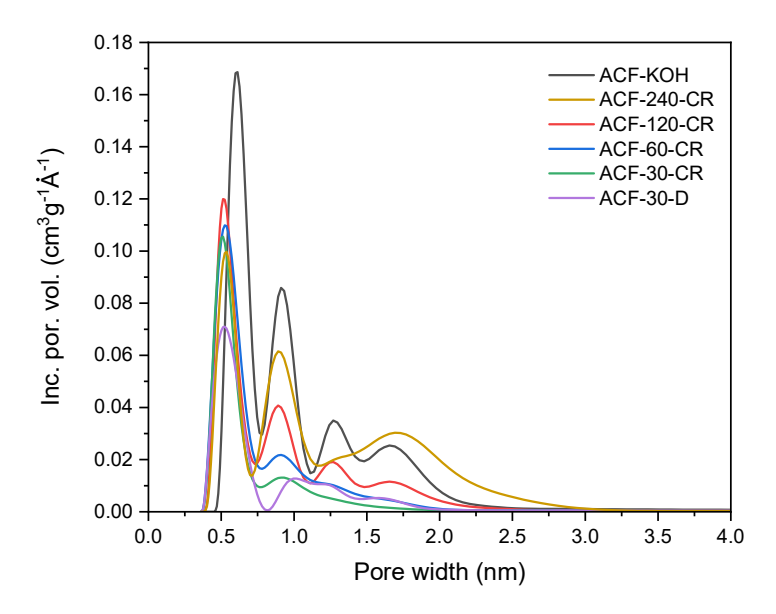


Figure AI.2 Pore size distribution of samples.

Development of Table 6.8 (Chapter VI, section 6.3.3) expression.

$$\frac{d\alpha}{dt} = \left(\frac{k_1 e^{\left(-\frac{E_a}{RT}\right) P_{CO2}}}{1 + k_2 e^{\left(-\frac{E_2}{RT}\right) P_{CO}} + k_3 e^{\left(-\frac{E_3}{RT}\right) P_{CO}}}\right) (1 - \alpha)^n$$

n=1, in this case, the reaction proceeds under chemical reaction control (Chapter II, section 2.5.3.1).

n = 0.67, the reaction is under diffusion control (Chapter II, section 2.5.3.1).

An apparent constant is defined as follows:
$$K_{ap} = \left(\frac{k_1 e^{\left(-\frac{E_a}{RT}\right)p_{CO2}}}{1 + k_2 e^{\left(-\frac{E_2}{RT}\right)p_{CO}} + k_3 e^{\left(-\frac{E_3}{RT}\right)p_{CO2}}}\right)$$

$$\frac{d\alpha}{dt} = K_{ap}(1-\alpha)^n \to \frac{d\alpha}{(1-\alpha)^n} = K_{ap} * dt$$

For n = 1:

$$\int_0^{0.22} \frac{d\alpha}{(1-\alpha)} = \int_0^{30} K_{ap} * dt \rightarrow -In|1 - 0.22| = 30 K_{ap} \rightarrow K_{ap} = 0.008 \; (min^{-1})$$

For n = 0.67:

$$\int_0^{0.44} \frac{d\alpha}{(1-\alpha)^n} = \int_0^{30} K_{ap} * dt \rightarrow -\frac{(1-\alpha)^{1-n}}{(1-n)} \bigg|_0^{0.44} 30 K_{ap} \rightarrow K_{ap} = 0.017 \; (min^{-1})$$

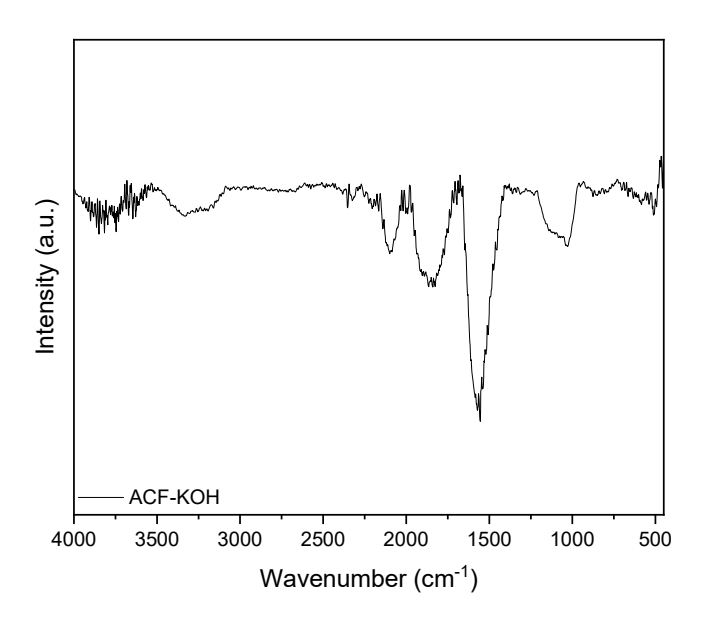


Figure AI.3a Infrared spectrum of ACF-KOH sample.

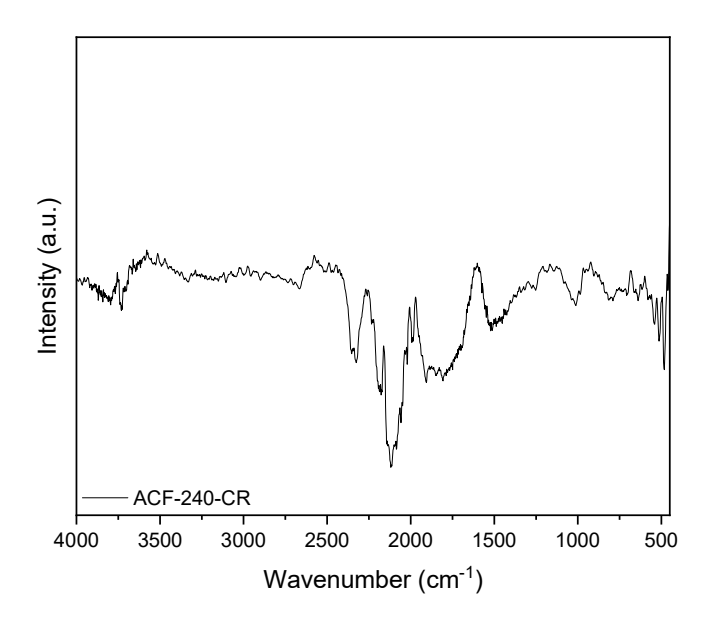


Figure AI.3b Infrared spectrum of ACF-240-CR sample.

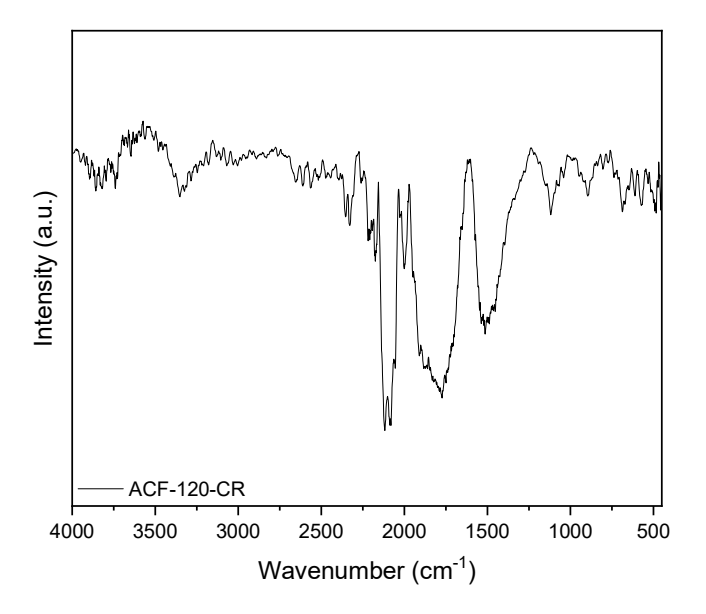


Figure AI.3c Infrared spectrum of ACF-120-CR sample.

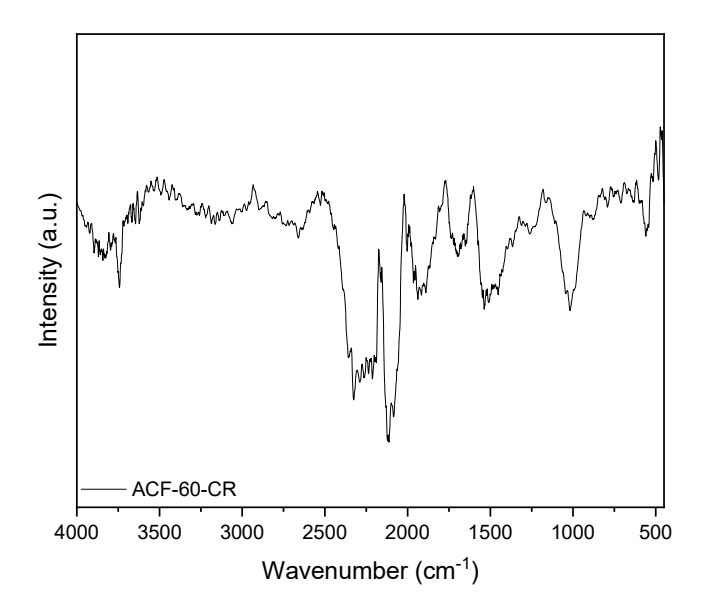


Figure AI.3d Infrared spectrum of ACF-60-CR sample.

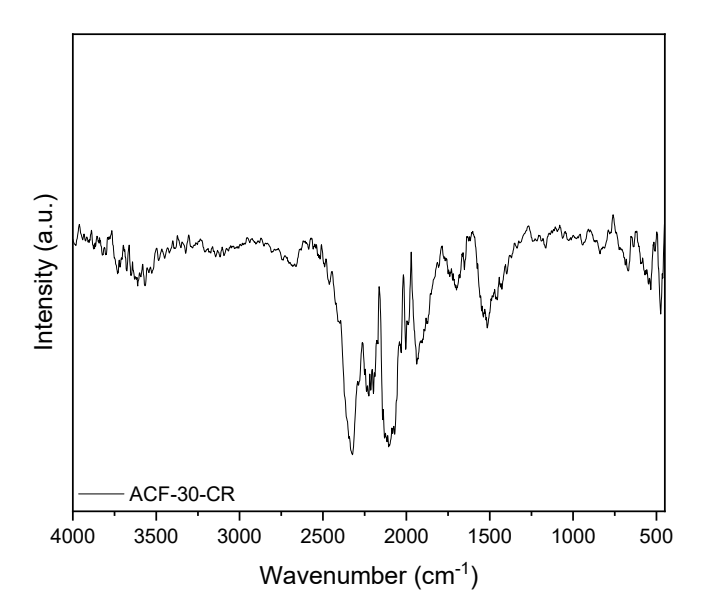


Figure AI.3e Infrared spectrum of ACF-30-CR sample.

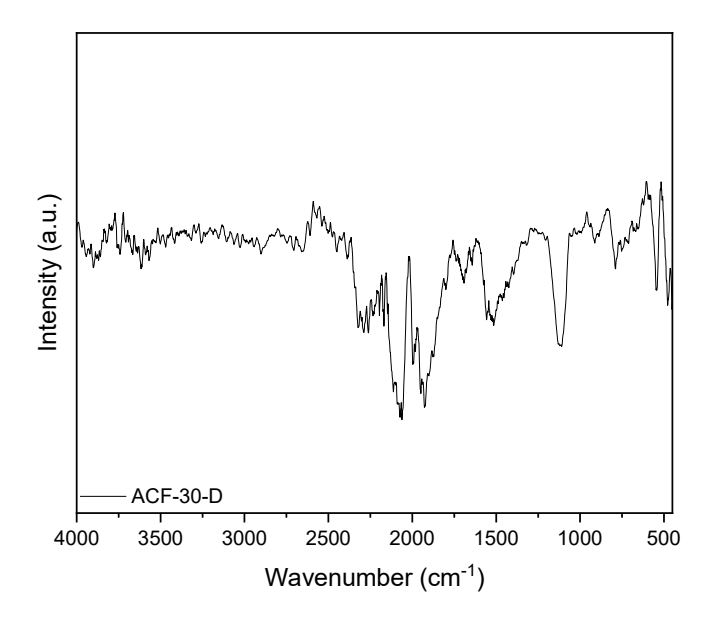


Figure AI.3f Infrared spectrum of ACF-30-D sample.

Reynolds equation : $Re = \frac{4Q\delta}{\mu\pi D_i}$

Table AI.1 Parameters used in the calculation of the dimensionless Reynolds number.

T (°C)	D (Kgm ⁻³)	$Q (m3s^{-1})$	μ (Pa.s)	Di (m)	Re (10 mLmin ⁻¹)	Re(200 mLmin ⁻¹)
875	0.613	1.67E-07	3.92E-05	5.75E-02	5.79E-02	1.16E+00

Table AI.2 SMX adsorption isotherms data (average data from three experiments).

ACF-KOH		ACF-240-CR		ACF-120-CR		ACF-60-CR	
Ce	qe	Ce	qe	Ce	qe	Ce	qe
(mmolL ⁻¹)	(mmolg ⁻¹)						
8.01E-4	0.4537	0.00175	0.30891	0.006	0.10148	5E-6	0.24826
0.00317	0.67359	0.00629	0.57704	0.02569	0.38214	0.00581	0.48
0.00788	0.90323	0.01945	0.83521	0.02925	0.2814	0.04455	0.60577
0.01265	1.14879	0.05584	1.0711	0.08291	0.7621	0.07134	0.66837
0.02124	1.35935	0.10036	1.27635	0.11673	0.93033	0.22293	0.6863
0.0476	1.62594	0.16211	1.48803	0.18802	1.02995	0.32965	0.70456
0.06235	1.70776	0.18801	1.58392	0.21372	1.12841	0.4383	0.70534
0.07995	1.73238	0.24186	1.87734	0.32377	1.1879	0.53651	0.70012
0.09774	1.76357	0.30865	1.89695	0.4307	1.2043	0.6474	0.70629
		0.36815	1.90239	0.51975	1.20407	0.74295	0.71468

ACF-	30-CR	ACF-30-D			
Ce	qe	Се	qe		
(mmolL ⁻¹)	(mmolg ⁻¹)	(mmolL ⁻¹)	(mmolg ⁻¹)		
0.04696	0.10879	2.51E-4	0.06598		
0.11996	0.13818	2.51E-4	0.11483		
0.14437	0.14821	0.00226	0.22066		
0.25101	0.17304	0.00251	0.31773		
0.3193	0.19921	0.00629	0.40754		
0.41116	0.21113	0.02112	0.47771		
0.51598	0.22074	0.03722	0.51753		
0.6117	0.22276				
0.7152	0.21962				
0.8002	0.22489				
0.9152 0.22123					

Table AI.3 MNZ adsorption isotherms data (average data from three experiments).

ACF-KOH		ACF-240-CR		ACF-120-CR		ACF-60-CR	
Се	qe	Ce	qe	Ce	qe	Ce	qe
(mmolL ⁻¹)	(mmolg ⁻¹)						
0.00918	0.22588	0.04242	0.51589	0.007	0.22423	0.0013	0.24738
0.02933	0.42763	0.07405	0.72334	0.02254	0.44199	0.02492	0.42944
0.05023	0.62419	0.14315	0.95515	0.06187	0.603	0.08985	0.53492
0.07447	0.77215	0.19422	1.06561	0.10145	0.74963	0.13479	0.68101
0.11919	0.9472	0.30407	1.11291	0.17683	0.80499	0.18156	0.80093
0.15431	1.08388	0.35257	1.16186	0.28408	0.86587	0.28436	0.8471
0.2627	1.15837	0.37955	1.14237	0.33384	0.87944	0.40491	0.86631
0.32654	1.16093	0.4208	1.20028	0.38625	0.8855	0.5105	0.86985
0.38045	1.19699	0.46395	1.20121	0.4383	0.89077	0.5964	0.8626
0.41905	1.1969	0.5138	1.19997	0.4901	0.89637	0.69095	0.86628

ACF-	30-CR	ACF-30-D			
Ce	qe	Ce	qe		
(mmolL ⁻¹)	(mmolg ⁻¹)	(mmolL ⁻¹)	(mmolg ⁻¹)		
0.00125	0.19087	0.00194	0.11027		
0.0507	0.33918	0.01005	0.21335		
0.1231	0.44175	0.03138	0.2781		
0.20105	0.50022	0.05009	0.34118		
0.26955	0.52509	0.0943	0.38697		
0.3097	0.53655	0.31767	0.51644		
0.3398	0.53672	0.57447	0.57651		
0.3959	0.53783	0.84472	0.62427		
0.4924	0.53698				
0.5233 0.53805					

Table AI.4 AMP adsorption isotherms data (average data from three experiments).

ACF-30-D					
Ce	qe				
(mmolL ⁻¹)	(mmolg ⁻¹)				
0.64718	2.31167				
0.96017	2.81625				
1.3872	3.28105				
1.62857	3.84089				
2.29697	4.99372				
3.00516	5.93879				
3.8154	6.13658				
4.5125	6.21547				
5.5245	6.31255				

Table AI.5 Kinetic fitting comparison for SMX (0.4 mmolL-1) adsorption onto ACF obtained under chemical and physical activation (D and CR methods) and different times for CR control.

	Units	ACF-KOH	ACF-240-CR	ACF-120-CR	ACF-60-CR	ACF-30-D
PFO model						
k_1	min ⁻¹	0.0011	0.0009	0.0025	0.0032	0.0038
adj-R ²		0.9025	0.7542	0.9325	0.9342	0.9268
X^2		0.543	0.4673	0.1398	0.0164	0.0130
RSS		1.3987	1.9853	2.1354	0.0432	0.0437
PSO model						
k_2	g mmol ⁻¹ min ⁻¹	0.2354	0.2471	0.0435	0.0231	0.0073
adj-R ²		0.9997	0.9999	0.9993	0.9989	0.9968
X^2		0.0256	0.0281	0.0541	0.0481	0.5843
RSS		0.0015	0.0113	0.0003	1.2546	0.0086
Diffusion model						
\mathbf{k}_3	mmolg ⁻¹ min ^{-1/2}	0.0038	0.0041	0.0023	0.0021	0.0013
adj-R ²		0.3245	0.6210	0.8349	0.9531	0.9831
X^2		0.0005	0.0008	0.0219	0.3513	1.2582
5RSS		0.0013	0.0011	0.3571	0.0866	0.7318



"¿Por qué se turba tanto tu ánimo-dijo el Maestro-, que así acortas el paso? ¿Qué te importa lo que allí murmuran? Sígueme y deja que hable esa gente. Sé firme como una torre, cuya cúspide no se doblega jamás al embate de los vientos: el hombre de quien bulle pensamiento sobre pensamiento siempre aleja de sí el fin que se propone; porque el uno debilita la actividad del otro."

La divina comedia

Canto quinto

Dante Alighieri

Articles in peer-reviewed journals

- Pina, A.C., A. Amaya, J.S. Marcuzzo, A.C. Rodrigues, M.R. Baldan, N. Tancredi, and A. Cuña. 2018. "Supercapacitor Electrode Based on Activated Carbon Wool Felt." *C* 4 (2): 24. https://doi.org/10.3390/c4020024.
- Pina, A.C., N. Tancredi, C.O. Ania, and A. Amaya. 2021. "Stabilisation of Sheep Wool Fibres under Air Atmosphere: Study of Physicochemical Changes." *Materials Science and Engineering: B* 268 (June). https://doi.org/10.1016/j.mseb.2021.115115.
- Pina, A.C., N. Tancredi, M. Baldan, J. S. Marcuzzo, and A. Amaya. 2018. "CO2 Capture and Biomethane Obtention Using Activated Carbon Filter of Animal Origin." *MRS Advances* 3:3589–3600. https://doi.org/doi.org/10.1557/adv.2018.588.

Colaborations

- Castro, Y., C. Hernández, A.C. Pina, D. Míguez, and M.E. Casco. 2024. "Evaluación de La Eficiencia Del Biochar de Bambú En La Eliminación de Microcistina-LR Del Agua." INNOTEC 27 (February). https://doi.org/10.1590/S1517-707620210002.1264.
- Blanco, G.C., M.G.C Munhoz, A.C. Rodrigues, A. Cuña, A.C. Pina, J.S. Marcuzzo, and M.R. Baldan. 2021. "Process of Converting Human Hair into Hollow Carbon Filament for Electrochemical Capacitor." Revista Materia 26 (2). https://doi.org/10.1590/S1517-707620210002.1264.

Research diffusion articles

- Pina, A.C. 2024. "Carbón Activado." Indufarma, September 2024. https://indufarma.com.uy/indufarma-setiembre-2024/.
- Pina. A.C., A. Amaya, and N. Tancredi. 2022. "Contaminantes de Origen Farmacéutico En cursos de Agua, Un Nuevo Enfoque Un Problema Sin Fronteras." Indufarma, 2022. https://indufarma.com.uy/indufarma-julio-2022/.
- Pina, A.C., A. Amaya, and N. Tancredi. 2024. "Contaminantes Emergentes, Un Riesgo Para El Medio Ambiente y La Salud." Indufarma, July 2024. https://indufarma.com.uy/indufarma-julio-2024/.
- Pina, A.C., S. Franzosi, F. Rovella, C. Testorelli, and M. Casco. 2024. "Soluciones Innovadoras: Removiendo Contaminantes Emergentes Con Materiales Sustentables." Indufarma, June 2024. https://indufarma.com.uy/indufarma-mayo-2024/.



"Tal vez lo que parecía relegado a ciertas páginas e imágenes, territorio de la infancia, ámbito exclusivo de los sueños, aún fuese posible de algún modo."

La carta esférica

Arturo Pérez-Reverte

International oral expositions

Ana Claudia Pina, Néstor Tancredi, Alejandro Amaya, Conchi Ania, "Emerging pollutants adsorption under competitive conditions", WCCE11-CIBIQ2023-GS06-Global Symposium on Removal of Emerging Contaminants, Asociación Argentina de Ingenieros Químicos, 4 – 8 June 2023, Bs. As. Argentina. Oral exposition.

Alejandro Amaya, Leticia Botta, Nicolás Tizze, Natalia Gorga, Mercedes Méndez, Lucía Feijo, Ana Claudia Pina, "Increment of CO₂ adsorption capacity of nanostructured wool activated carbon fibres by nitrification", 2nd. Advanced Materials Science World Congress 2021, 14 – 15 June 2021, Berlin, Germany. Oral exposition (presented by Alejandro Amaya).

Ana Claudia Pina, Nestor Tancredi, Alejandro Amaya, Conchi O. Ania, "Développement de fibres de carbone nano poreuses (FCN) et leur application à l'adsorption compétitive de contaminants d'origine pharmaceutique", Société Francophone d'Etude des Carbones (SFEC), online event, November and December 2020, www.carbon-on.fr.

Ana Claudia Pina, Lucía Feijó, Leticia Botta, Mariana Gerón, Nestor Tancredi, Conchi O. Ania, Alejandro Amaya, "Studies on CO₂ adsorption kinetics on nanoporous carbon fibers", 9èmes journées de l'Association Française de l'Adsorption, 29 – 31 January 2020, Ecole des Ponts Paris-Tech, Champs-sur-Marne, France.

Ana Claudia Pina, Nestor Tancredi, Alejandro Amaya, Conchi O. Ania, "Kinetic and thermodynamic aspects of coadsorption of antibiotics onto activated carbon fibres", Beyond Adsorption II, July 20 2019, New York, USA.

Ana Claudia Pina, Alicia Gómez-Berenguer, Nestor Tancredi, Alejandro Amaya, Conchi O. Ania, "Competitive adsorption of pharmaceutical compounds on activated carbon fibers", Le Studium Conferences, Water micropollutants: from detection to removal, 26 – 28 November 2018, Orléans, France.

Ana Claudia Pina, Nestor Tancredi, Alejandro Amaya, "Assessment of activated carbon fibre from wool as Paracetamol adsorbent", Le Studium Conferences, Water micropollutants: from detection to removal, 26 – 28 November 2018, Orléans, France.

Ana Claudia Pina, Nestor Tancredi, Alejandro Amaya, "Fibras adsorbentes de alta porosidad a partir de lana", 41 RIA Reunión Ibérica de Adsorción - 3er Simposio Iberoamericano de Adsorción, 5 – 7 September 2018, Gijon, Spain.

Ana Claudia Pina, Jossano Marcuzzo, Nestor Tancredi, Alejandro Amaya, "Wool activated carbon felt for Carbon Dioxide capture and Biomethane obtention", 7th International Conference on Carbon for Energy Storage and Environment Protection, 23 – 26 october 2017, Lyon, France.

International posters expositions

Ana Claudia Pina, Andrés Cuña, Mirian Casco, "Nitrogen-doped activated carbon materials from biomass residues and their application as supercapacitor electrode", The World Conference on Carbon 2023, 16 – 21, Cancún, México. Poster.

Ana Claudia Pina, Kana Maiga, Nestor Tancredi, Alejandro Amaya, Conchi O. Ania, "Competitive adsorption of pharmaceutical compounds on wool-derived activated carbon fibres", Colloque Francophone du Carbone 2020, 21 – 24 September 2021, Murol, France.

Ana Claudia Pina, Nestor Tancredi, Conchi O. Ania, Alejandro Amaya, "Activated carbon fibres from a natural source and their use for the competitive adsorption of pharmaceuticals", The World Conference on Carbon, 14 – 19 July 2019, Lexington, Kentucky, USA.

Ana Claudia Pina, Nestor Tancredi, Alejandro Amaya, "Activated carbon fibre from wool for Paracetamol adsorption", The World conference on Carbon, 1 – 6 July 2018, Madrid, Spain (presented by Alejandro Amaya).

Ana Claudia Pina, Jossano Marcuzzo, Andrés Cuña, Aline Rodrigues, Mauricio Baldan, Nestor Tancredi, Alejandro Amaya, "Supercapacitor electrode based on activated carbon wool felt", 7th International Conference on Carbon for Energy Storage and Environment Protection, 23 – 26 October 2017, Lyon, France.

Regional expositions

Ana Claudia Pina, Marco Adamiak, Mirian Casco, "Nueva estrategia para preparar materiales carbonosos dopados con nitrógeno a partir de residuos de biomasa de la industria uruguaya", 4to. Simposio Iberoamericano de Adsorción IBA-4, 3 – 5 May, Potrero de los Funes, San Luis, Argentina. Oral exposition.

Ana Claudia Pina, Nestor Tancredi, Alejandro Amaya, Conchi O. Ania, "Competitive adsorption of pharmaceutical compounds onto nanoporous carbon fibres: effect of pH and ionic strength", 13th Brazilian Meeting on Adsorption – EBA13, from November 30th to December 3rd 2020, Fortaleza, Brazil. Oral exposition.

Alejandro Amaya, Laura García, Nestor Tancredi, Jossano Marcuzzo, Ana Claudia Pina, "Obtención de fibra de carbón a partir de lana de Alpaca", Taller Latinoamericano de Materiales de Carbono TLMC3, 28 – 30 de noviembre 2018, Bogotá, Colombia. Poster (presented by Alejandro Amaya).

Laura García, Ana Claudia Pina, Nestor Tancredi, Alejandro Amaya, "Análisis termogravimétricos de la preparación de fibras de carbón activado a partir de lana", Taller Latinoamericano de Materiales de Carbono TLMC2, 16 – 18 November 2016, Termas de Chillán, Chile. Oral exposition France (presented by Alejandro Amaya).

National expositions

Sofia Franzosi, Fiorella Rovella, Camila Testorelli, Mirian Casco, Ana Claudia Pina, "Desarrollo de materiales adsorbentes a partir de biomasa para la remoción de contaminantes emergentes en cuerpos de agua", 8vo Encuentro Nacional de Química, Torre de las Comunicaciones de Antel, 18 – 21 October 2023, Montevideo. E-Poster (presented by Sofía Franzosi).

Ana Claudia Pina, Conchi Ania, Néstor Tancredi, Alejandro Amaya, "Materiales sustentables para el desarrollo de fibras de carbón activado (FCA)", II Encuentro de Investigadores en Ciencias de Materiales, 20 – 21 April 2023, Montevideo. Poster

Ana Claudia Pina, Conchi Ania, Néstor Tancredi, Alejandro Amaya, "Dispersión asociada a la preparación del material en la caracterización textural de carbones activados a partir de lana", 7mo Congreso Uruguayo de Química Analítica, Facultad de Ingeniería, 26 – 28 October 2022, Montevideo. Poster

Ana Claudia Pina, Conchi Ania, Néstor Tancredi, Alejandro Amaya, "Fibras de carbón activado para la remoción de residuos de medicamentos en cursos de agua", Encuentro Potabilización de agua: calidad de agua y aplicación de carbón activado, Latu, 25th March 2022, Montevideo. Oral exposition.

Leticia Botta, Lucía Feijó, Natalia Gorga, Nicolás Tizze, Ana Claudia Pina, Alejandro Amaya, "Funcionalización de fibra de carbón activado a partir de lana para la obtención de biometano y el secuestro de CO₂", 7mo Encuentro Nacional de Química, Torre de las Comunicaciones de Antel, 03 – 05 November 2021, Montevideo. Poster (presented by Leticia Botta).

Mariana Gerón, Claudia Rodríguez, Alejandro Amaya, Ana Claudia Pina, "Comparación de fibras nanoporosas de carbón de origen natural. Obtención y propiedades", 6to Encuentro Nacional de Química, Torre de las Comunicaciones de Antel, 16 – 18 October 2019, Montevideo. Poster (presented by Mariana Gerón).

Claudia Rodríguez, Ana Claudia Pina, Alejandro Amaya, "Validación de un método analítico de cuantificación conjunta de paracetamol y cafeína mediante UVHPLC", 6to Encuentro Nacional de Química, Torre de las Comunicaciones de Antel, 16 – 18 October 2019, Montevideo. Poster (presented by Claudia Rodríguez).

Ana Claudia Pina, Laura García, Nestor Tancredi, Alejandro Amaya, "Captura de CO₂ y obtención de biometano utilizando fieltro de carbón activado (FCA) de origen animal", Primer encuentro de jóvenes investigadores en ciencias de materiales, 13 – 14 April 2018, Montevideo, Uruguay. Poster.

Laura García, Ana Claudia Pina, Nestor Tancredi, Alejandro Amaya, "Parámetros cinéticos involucrados en la obtención de fibras de carbón activado a partir de lana de oveja", 5to Encuentro Nacional de Química, Torre de las Comunicaciones de Antel, 18 – 20 October 2017, Montevideo. Poster (presented by Laura García).

Ana Claudia Pina, Laura García, Jossano Marcuzzo, Nestor Tancredi, Alejandro Amaya, "Aplicación de espectroscopía de Infrarrojo (FTIR), Raman (FTR) y Masa (MS), para la evaluación de cambios fisicoquímicos durante la obtención de carbón activado a partir de fieltro de lana de oveja", 5to Encuentro Nacional de Química, Torre de las Comunicaciones de Antel, 18 – 20 October 2017, Montevideo. Poster.



"La science, mon garçon, est faite d'erreurs, mais d'erreurs qu'il est bon de commettre, car elles mènent peu à peu à la vérité."

L'île mystérieuse

Jules Verne



Figure 1. Pristine wool fibre



Figure 2. SF-300-120



Figure 3. ACF-30-D



Figure 4. ACF-30-CR



Figure 5. ACF-60-CR



Figure 6. ACF-120-CR



Figure 7. ACF-180-CR



Figure 8. ACF-240-CR



Figure 9. ACF-KOH



Figure 10. Wool without stabilisation